1998

Near band edge optical properties of MBE GaAs and related layered structures

Tania Marie Silver
University of Wollongong

NEAR BAND EDGE OPTICAL PROPERTIES OF MBE GaAs AND RELATED LAYERED STRUCTURES

A thesis submitted in fulfilment of the
requirements for the award of the degree of

DOCTOR OF PHILOSOPHY

from

THE UNIVERSITY OF WOLLONGONG

by

TANIA MARIE SILVER

B.Sc. (Hons) - University of Wollongongong
B. App. Sc. - Capricornia Institute of Technology

Department of Physics
1998

DECLARATION

This is to certify that the work presented in this thesis has not been submitted to any other University or Institution for the award of a degree.

T.M. Silver

ACKNOWLEDGMENTS

I would like to sincerely thank all of the people who helped me along the way with the research and writing of this thesis:

The University of Wollongong, for enabling me to do the research by providing me with financial support through a fellowship and opportunities for part time work.

My supervisors, Dr. P. E. Simmonds and Dr. A. D. Martin, for their patience, encouragement and valuable guidance, during my struggles with the interesting but challenging problems they set me.

Other members of the University of Wollongong Physics Department, especially Dr. R. E. M. Vickers for useful FORTRAN subroutines and valuable advice in dealing with MacIntosh computers and Dr. Paul Nulsen for advice on numerical methods.

The technical officers Peter Ihnat, N.A. McLean, Dale Hughes and Peter Anthony. Without their efforts in assembling and repairing the experimental apparatus none of the research would have been possible.

My fellow graduate students, Tracey A. Fisher and Michael Lerch, who provided invaluable help and support, particularly in my struggles with baulky equipment.

Dr. A. A. Williams of ANSTO who hydrogenated and annealed samples, as well as all the crystal growers who furnished the raw materials for the research.

My husband and sons, John, Andrew and Martin Silver, for putting up with all the problems a mature age student in the family brings, and providing practical help and support.

All the members of the University of Wollongong Physics Department, academics, general staff and postgraduate students for friendship, help and many fascinating arguments in the common room.

TABLE OF CONTENTS

DECLARATION ..... (ii)

ACKNOWLEDGEMENTS ..... (iii)

ABSTRACT ..... (xi)

PUBLICATIONS ..... (xiii)

PREFACE ..... (xv)

CHAPTER 1-OVERVIEW OF BAND STRUCTURE OF GaAs AND $Al_xGa_{1-x}As$ BULK AND LAYERED STRUCTURES 1

1.1 Bulk GaAs and $Al_xGa_{1-x}As$ Band Structures 1

1.1.1 The Zincblende Structure 1

1.1.2 Bloch Functions and Origins of Band Structure 2

1.1.3 Calculation of the Energy Bands 6

1.1.4 Strain and Temperature Effects on Band Structure 9

1.2 Band Structure of Quantum Wells and Superlattices 10

1.2.1 Quantum Wells and Superlattices 10

1.2.2 2-D and 3-D Density of States 12

1.2.3 Envelope Functions and Energy Quantization 13

1.2.4 Bulk and 2-D Excitons 17

1.2.5 Dimensionality and Wave Function Properties 20

CHAPTER 2-HYDROGEN PASSIVATION OF DEFECTS AND IMPURITIES 21

2.1 Overview of Defects and Impurities 21

2.1.1 Nature of Defects and Their Energy Levels 21

2.1.1.1 Shallow Impurity States: the Effective Mass Approximation 24

2.1.1.2 Deep Defect and Impurity States 25

2.1.2 Defects and Impurities at Dislocations 27

2.1.3 Defects and Impurities at the Surface and

Interfaces....28
2.2 Hydrogen Passivation of Defects and Impurities....31
2.2.1 Overview of Hydrogenation....31
2.2.2 Methods of Hydrogenation and Diffusion....32
2.2.3 Electrical and Optical Effects of Hydrogenation....33
2.2.3.1 Hydrogen Passivation of Deep Defect States....34
2.2.3.2 Hydrogen Passivation of Shallow Impurities....35
2.2.3.2 Reactivation of Levels After Annealing....36
2.2.3.4 Hydrogen Passivation at the Surface....37
2.2.3.5 Hydrogen Passivation at Dislocations....38
2.2.3.6 Hydrogen Passivation at Interfaces....40
2.2.4 Microscopic Structure of Passivated Complexes....41
CHAPTER3-OPTICAL PROPERTIES OF BULK AND LAYERED GaAs AND $Al_xGa_{1-x}As$ SAMPLES AT THE BAND EDGE....42
3.1 The Dielectric Function, Optical Constants and Reflectance....42
3.1.1 Dielectric Function and Green's Function Approaches....42
3.1.2 Material Dispersion and the Dielectric Function....44
3.1.2.1 The Purely Classical Model of $e_r(l)$....44
3.1.2.2 The Semiclassical Model of $e_r(l)$....45
3.1.2.3 The A Parameter....46
3.1.3 The Optical Constants....47
3.1.4 Reflectance at an Interface....48
3.1.5 The Optical Transfer Matrix....50
3.1.6 Quantum Confinement in the Semiclassical Model....51
3.1.7 Phase Effects and the Dead Layer....52
3.1.8 Nonlocality and Polariton Effects in Reflectance....54
3.1.8.1 The Full Andreani Nonlocal Transfer Matrix....56
3.2 Transition Probability, Absorption, Quantum Mechanical Oscillator Strength....59

3.2.1 Fermi's Golden Rule....59
3.2.2 Band to Band Absorption....59
3.2.3 Excitonic Absorption....62
3.2.4 Oscillator Strength....63
3.2.4.1 Short definitions of Oscillator Strength....63
3.2.4.2 Detailed Calculations of Oscillator Strength....64
3.3 Transition Linewidth....69
3.3.1 Inhomogeneous or Gaussian Broadening....69
3.3.1.1 Excitons Localised on Well Width Fluctuations....71
3.3.1.2 The Stokes Shift....72
3.3.2 Lorentzian or Homogeneous Broadening....73
3.3.2.2 Acoustic Phonon Scattering....74
3.3.2.3 Longitudinal Optical Phonon Broadening....75
3.3.2.4 The Intrinsic Radiative Linewidth....75
3.3.2.5 Temperature Effects on Radiative Lifetime....76
3.4 Photoluminescence (PL)....78
3.4.1 Thermalisation and Formation of Excitons....78
3.4.2 Radiative and Nonradiative Lifetimes....79
3.4.3 Important Types of Recombination in PL....80
3.4.4 PL Replica Lines....82
3.4.5 PL Involving the KP and g-line Defects....82
3.4.6 Photoluminescence Excitation and Selective Excitation....86
3.4.7 Temperature Dependence of Photoluminescence....88
3.4.8 Thermally Activated Processes in PL....89
CHAPTER 4-EXPERIMENTAL TECHNIQUES....91
4.1 MBE Growth of Samples....91
4.2 Method of Collecting Reflectance Spectra....93
4.3 Method of Collecting Photoluminescence Spectra....98
4.3.1 Collecting PLE Spectra....101

4.4 Hydrogenation and Annealing of Samples 102

CHAPTER 5-OSCILLATOR STRENGTH AND OTHER REFLECTANCE PARAMETERS OF SHALLOW QUANTUM WELLS

..... 103

5.1 Introduction 103

5.2 The Samples 104

5.3 Summary of Previous Work on the Samples 105

5.3.1 The 20/50 Shallow Quantum Wells 105

5.3.2 The 20/20 Shallow "Superlattices" 107

5.4 5K Reflectance Spectra 108

5.4.1 Reflectance Features Arising from the QWs 109

5.4.2 Low Energy Features in the Reflectance Spectra 111

5.4.3 Fitting the Reflectance Spectra 111

5.5 5K Photoluminescence Spectra 117

5.6 Reflectance and PL Spectra at Higher Temperatures 119

5.6.1 Changes in Transition Energy 119

5.6.2 Changes in Transition Linewidth 120

5.6.3 Changes in Oscillator Strength 123

5.7 Conclusions 123

5.7.1 Transition Linewidths and Local/Nonlocal Models 123

5.7.2 Oscillator Strength per Unit Area 125

5.7.3 The Shallow "Superlattices" and Single QW 127

5.7.4 Conclusions on Temperature Dependence 128

Appendix to Chapter 5 128

CHAPTER 6-HYDROGEN PASSIVATION OF DEFECT BOUND EXCITONIC LINES IN MBE GaAs 129

6.1 Introduction 129

6.2 The Samples 130

6.3 Photoluminescence Results 130

6.3.1 5K PL of the As Grown Samples 130
6.3.2 5K PL Spectra of the Hydrogenated and Annealed Samples 133
6.3.3 Temperature Dependence of the PL Spectra 134
6.3.4 Magnetophotoluminescence Results 135
6.4 Selective Excitation Results 136
6.4.1 Selective Excitation and the Substrate 136
6.4.2 Selective Excitation of A°X 137
6.4.3 Selective Excitation into the DAP Band and PLE 138
6.5 Conclusion 139
6.5.1 Evidence for Sample Inhomogeneity 140
6.5.2 Evidence for No Significant Donor Passivation 141
6.5.3 Evidence for No Significant Passivation of Simple Acceptors 141
6.5.4 Passivation of KP and g-line defects 143
6.5.5 The Question of Donor Related Excitonic Lines 144
6.5.6 The Proposed Model 145
CHAPTER 7-HYDROGEN PASSIVATION STUDIES OF BULK AND LAYERED GaAs AND $Al_xGa_{1-x}As$ STRUCTURES 147
7.1 General Introduction 147
7.2 Characteristics of the Samples 147
7.3 Experimental Results on MBE $Al_xGa_{1-x}As$ Layers 148
7.3.1 Introduction 148
7.3.2 5K Photoluminescence Results 149
7.3.3 Effects of Hydrogenation and Annealing 150
7.3.4 Conclusions on $Al_xGa_{1-x}As$ Samples 150
7.4 Experimental Results on Hydrogenated QW Samples 152
7.4.1 Introduction 152
7.4.2 Low Temperature PL of the As Grown Samples 153

7.4.3 Effects of Hydrogenation and Annealing 154
7.4.4 Effects of Hydrogenation on Temperature Dependence 155
7.4.5 Conclusions on Hydrogenated QWs 156
7.5 Experimental Results on Hydrogenated Short Period Superlattices 157
7.5.1 Introduction
7.5.2 Overview of the Samples 158
7.5.3 Photoluminescence Results at 5K 159
7.5.4 Effects of Hydrogenation 162
7.5.5 Temperature Dependence of PL Intensity 163
7.5.6 Conclusions on Hydrogenated Superlattices 163
REFERENCES 167

ABSTRACT

The research reported in this thesis involves two main strands, both concerned with optical properties near the band edge. One involves studies of reflectance from shallow quantum wells, while the other is concerned with hydrogen passivation studies of MBE bulk GaAs and $Al_xGa_{1-x}As$ and GaAs related layered structures. For the reflectance work the structures employed were very high quality undoped MBE grown multi-quantum wells consisting of 25 periods of a 20 nm GaAs well and a 50 nm or 20 nm $Al_xGa_{1-x}As$ barrier, with x=0.01, 0.02 or 0.045. Low temperature reflectance spectra of such samples are extremely sharp and detailed, ideal for the study of transition parameters such as oscillator strength per unit area and transition linewidth. Spectra were consistent with full quantum confinement of excitons for all samples. Parameters were extracted by simulation of the reflectance spectra until a very close fit was achieved using both a local, semiclassical model and the full nonlocal transfer matrix of Andreani [146,147]. Both methods were in agreement on oscillator strength per unit area, but analysis by means of the nonlocal method was necessary to achieve accurate fits of excitonic transition linewidth where the intrinsic broadening associated with the radiative lifetime of photocreated excitons was comparable in magnitude to that due to all other sources of broadening. Such an outcome has been theoretically predicted. Transition linewidths were as sharp as 53 meV FWHM, as sharp as any reported. Oscillator strengths per unit area were consistently larger than theoretically predicted, ranging for the E_{11h} transition from 51±7 to 80±4 × $10^{-5}Å^{-2}$, depending on x. The acoustic coefficient of broadening was found to be 3.0±0.4 meV/K for the E_{11h} transition and 4.5±0.4 meV/K for E_{11l}.

One aspect of the hydrogenation work involved the study of MBE *p*-type GaAs samples with strong 'KP' lines passivated by hydrogen and donor excitonic PL

lines that were undetectable before hydrogenation, but strong afterwards. Selective excitation and other experiments revealed that isolated shallow acceptors were not being passivated, and a model was developed to explain the findings. Another aspect involved the passivation of short period superlattices. It was discovered that hydrogen only improves PL efficiency when free carriers are prevented from migrating out of the superlattice by confinement in a double heterostructure or by disorder. The $\exp(T/T_o)$ temperature dependence results give evidence that quenching of PL intensity as the temperature is raised is caused by phonon assisted tunneling or hopping of localized excitons or carriers to sites where nonradiative recombination is likely to occur.

PUBLICATIONS

1. "Low Temperature Magnetophotoluminescence Investigations of the 2-D Hole System in *p*-type GaAs-AlGaAs Heterojunctions"
   A.G. Davies, E.E. Mitchell, R.G. Clark, P.E. Simmonds, T.M. Silver, D.A. Ritchie, J.E.F. Frost, M. Pepper and G.A.C. Jones; in Proceedings of the Todai 1993 Symposium and the 4th ISSP International Symposium on Frontiers in High Magnetic Fields, Tokyo, 1993 *Physica* **B201**, 397 (1994).

2. "Magneto-optics as a Probe of the Two-Dimensional Hole System"
   A.G. Davies, E.E. Mitchell, R.G. Clark, P.E. Simmonds, T.M. Silver, D.A. Ritchie, M.Y. Simmons, M. Pepper and G.A.C. Jones; in Proceedings of the 22nd International Conference on the Physics of Semiconductors, Vancouver, 1994 **2**, D.J. Lockwood, ed. (World Scientific, Singapore, 1995), p. 1460.

3. "Far-Infrared Photoconductivity and Photoluminescence of Beryllium in Gallium Arsenide"
   R.A. Lewis, P.E. Simmonds, T.M. Silver, T.S. Cheng, M. Henini and J.M. Chamberlain; in Proceedings of an International Conference on Shallow-Level Centers in Semiconductors, Amsterdam, 1996, C.A.J. Ammerlaan and B. Pajot, eds. (Singapore, World Scientific, 1997) p. 257.

4. "Quality Assessment of Gas Metal Arc Welding Systems using Frequency Domain Techniques"
   F.G. De Boer, R. Schünemann, M. Siminski, T.M. Silver and J. Norrish; to be presented at the 6th International IASTED

Conference on Robotics and Manufacturing, Banff, Canada, July 26-29, 1998.

5. "The Application of Artificial Neural Networks for Parameter Estimation and Quality Assessment for Robotic Gas Metal Arc Welding"
Q. Xu, F.G. de Boer, J. Norrish and T. Silver; to be presented at the Engineering, Mathematics and Applications Conference, Adelaide, July 13-16, 1998.

PREFACE

The research conducted for this thesis was concerned with optical transitions near the band edge in GaAs and $Al_xGa_{1-x}As$ bulk and layered samples. There are two main aspects to the work: optical parameters as determined by reflectance from shallow quantum wells and hydrogen passivation of bulk and layered structures. The first three chapters of the thesis provide a theoretical background and set the research results in context. Chapter 1 is an overview of the 3-D and 2-D band structure of GaAs and $Al_xGa_{1-x}As$ as it applies to bulk samples, quantum wells and superlattices. Chapter 2 briefly introduces defects and impurities in GaAs and $Al_xGa_{1-x}As$. Most of this chapter provides a short review of the subject of hydrogen passivation, in order to put the research results of Chapters 6 and 7 in context.

Chapter 3 deals with optical properties. The dielectric function, optical constants and reflectance are first introduced to provide a theoretical background for the semiclassical optical approach used in modelling reflectance in Chapter 5. There is then a discussion of quantum mechanical absorption and oscillator strength and transition linewidth, also relevant to chapter 5. The final section of Chapter 3 is concerned with photoluminescence (PL), which was used in all aspects of the research, and PL associated with 'KP' and 'g-line' defects as background to Chapter 6. Chapter 4 deals with experimental methods.

The research results are reported in the final three chapters. Chapter 5 reports on reflectance from shallow quantum wells, while Chapters 6 and 7 cover the hydrogen passivation of bulk MBE GaAs and $Al_xGa_{1-x}As$, as well as quantum wells and superlattices.

CHAPTER 1

OVERVIEW OF BAND STRUCTURE OF GaAs AND $Al_xGa_{1-x}As$ BULK AND LAYERED STRUCTURES

1.1 BULK GaAs AND $Al_xGa_{1-x}As$ BAND STRUCTURES

1.1.1 The Zincblende Structure

The elemental semiconductors C (diamond), Si, Ge and a-Sn belong to group IV of the periodic table. They are all covalent and crystallize in the diamond structure, an fcc (face-centered cubic) lattice with a basis of 2, with the basis atoms positioned so that it is possible to think of the diamond structure as consisting of two interpenetrating fcc lattices displaced from each other by one fourth of a body diagonal. The III-V compounds, including GaAs, AlAs, InSb, GaP, InAs and others, crystallize in the zincblende structure, which is the same as the diamond structure except that the two basis atoms and hence the two interpenetrating fcc sublattices are of different elements, one belonging to group III of the periodic table and the other to group V, as is shown in Figure 1.1(a). Each atom is tetrahedrally bonded to four other atoms belonging to the other element. $Al_xGa_{1-x}As$ is also of this structure with the mole fraction x of group III Al atoms randomly replacing the the group III Ga atoms. The III-V compounds are partly covalent and partly ionic, with the ionic character arising from the different electronegativities of the elements from groups III and V which cause the pairs of shared valence electrons represented by the bonds in Figure 1.1(a) to spend more time near one type of nucleus than the other. Coulomb attraction then arises between the now oppositely charged ions.

Zincblende Lattice

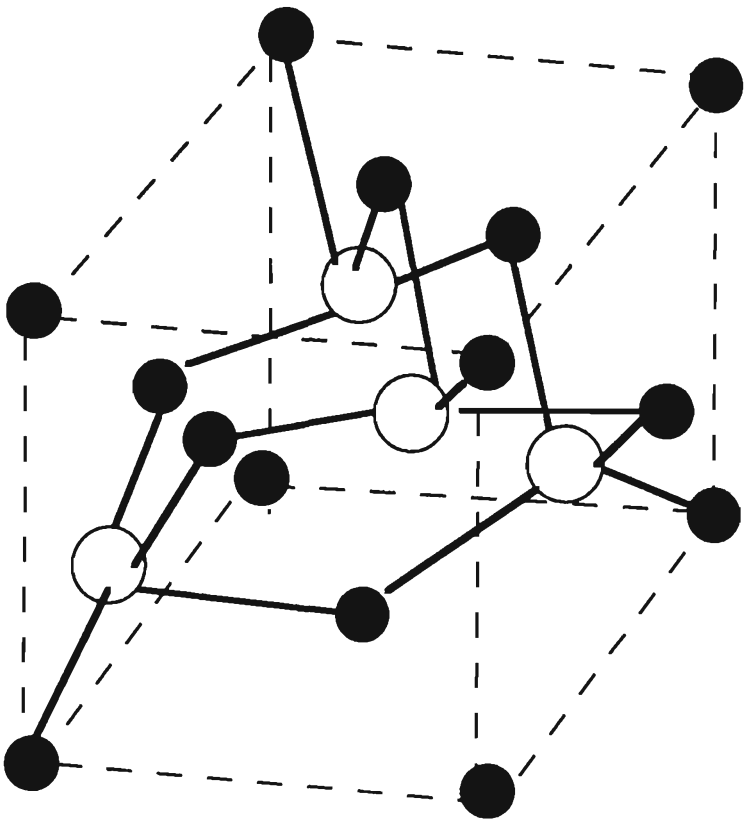

Brillouin Zone for
Zincblende Lattice

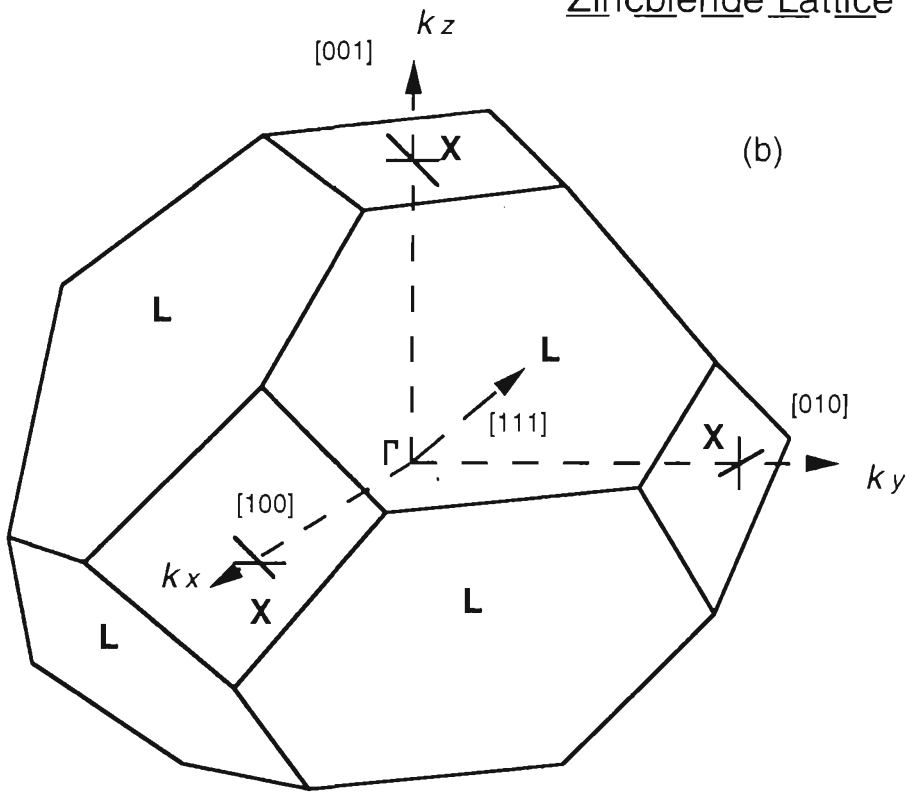

Figure 1.1 (a) GaAs crystallizes in the Zincblende structure, consisting of two interpenetating fcc lattices of Ga and As. In AlGaAs Al atoms are randomly substituted for some Ga atoms. (b) Brillouin Zone for the Zincblende structure. Symmetry points from Figure 1.2 are shown. L and X points are at the Zone edges in equivalent directions. From [1] Chapter 8.

The Brillouin Zone for the zincblende structure is illustrated in Figure 1.1(b). The Brillouin Zone is the unit cell for the reciprocal lattice vector defined in k-space (wave vector space). The structure of the Brillouin Zone is uniquely determined by the structure of the real lattice, as is described in any elementary text on Solid State Physics, e.g. [1,2,3]. The significant of the symmetry points illustrated is described in the next section.

1.1.2 Bloch functions and the origins of band structure

There are important differences in the behavior of delocalized conduction electrons or Bloch electrons in metals and semiconductors from the behavior of completely free electrons. The lattice imposes a periodic potential on the electrons so that

$$V(\mathbf{r}+\mathbf{R}) = V(\mathbf{r}) \tag{1.1}$$

where **R** is a direct lattice vector

According to the Bloch theorem (as defined in e.g. [3] *Chapter 5*) the Schrödinger equation for this type of potential has the state function solution $\psi_k(\mathbf{r})$ such that

$$\psi_k(\mathbf{r}) = e^{i\mathbf{k}\cdot\mathbf{r}} u_k(\mathbf{r}) \tag{1.2}$$

where $u_k(\mathbf{r})$ is a function having the same translational symmetry as the direct lattice.

The state function describing a conduction electron orbital is thus a travelling wave with wave vector **k** and an amplitude oscillating periodically with the cells of the lattice. If the right hand side of (1.2) is substituted in Schrödinger's equation and $e^{i\mathbf{k}\cdot\mathbf{r}}$ eliminated from both sides then an eigenvalue equation of $u_k(\mathbf{r})$ results whose solutions give the band structure or E-k relationship for the particular crystal.

$$\left[-\frac{\hbar^2}{2m}\left(\nabla + i\mathbf{k}\right)^2\right] u_k(\mathbf{r}) = E_k u_k(\mathbf{r}) \tag{1.3}$$

For each value of **k** there will be a large number of solutions to (1.3) each giving rise to a separate energy E_1, E_2,...E_n. Since **k** varies continuously so do the energy levels, with each giving rise to an energy band where the *band index* is given by the subscript. Note that only the lowest bands are occupied by electrons. The Bloch electron state functions will then have sinusoidal wave solutions in the allowed bands and decaying exponential solutions in the forbidden gaps.

The crystal lattice scatters the electron wave so that if **k** points to the right in one dimension the scattering introduces a new wave travelling to the left whose wave vector magnitude is $k' = k - 2\pi/a$ where a is the lattice constant. The amplitude of the reflected wave is given by perturbation theory and is small at small k, so that near $k = 0$, the electron behaves essentially as a free electron, but the reflected wave becomes more and more significant as k approaches π/a at the Brillouin zone boundary. At the zone boundary the two components result in a standing wave and the electron has zero velocity.

The band structure of GaAs is illustrated in Figure 1.2 (from Chelikowsky and Cohen [4]) for two crystal directions. Q, X and L are symmetry points, with Q located at **k**=0 and X and L at the Brillouin Zone boundaries. These symmetry points are also illustrated in Figure 1.1(b). The bands marked VB are the valence bands, which are fully occupied in pure GaAs at low temperature by the shared valence electrons occupying the bonds illustrated in Figure 1.1(a). In these conditions the lowest conduction band (marked CB) is empty, but it can be occupied especially at higher temperatures by electrons which have absorbed enough energy to be promoted into it. Conduction band electrons are delocalized, with their behaviour well described by (1.2) and (1.3). The fact that the valence bands are fully occupied in the pure material at low

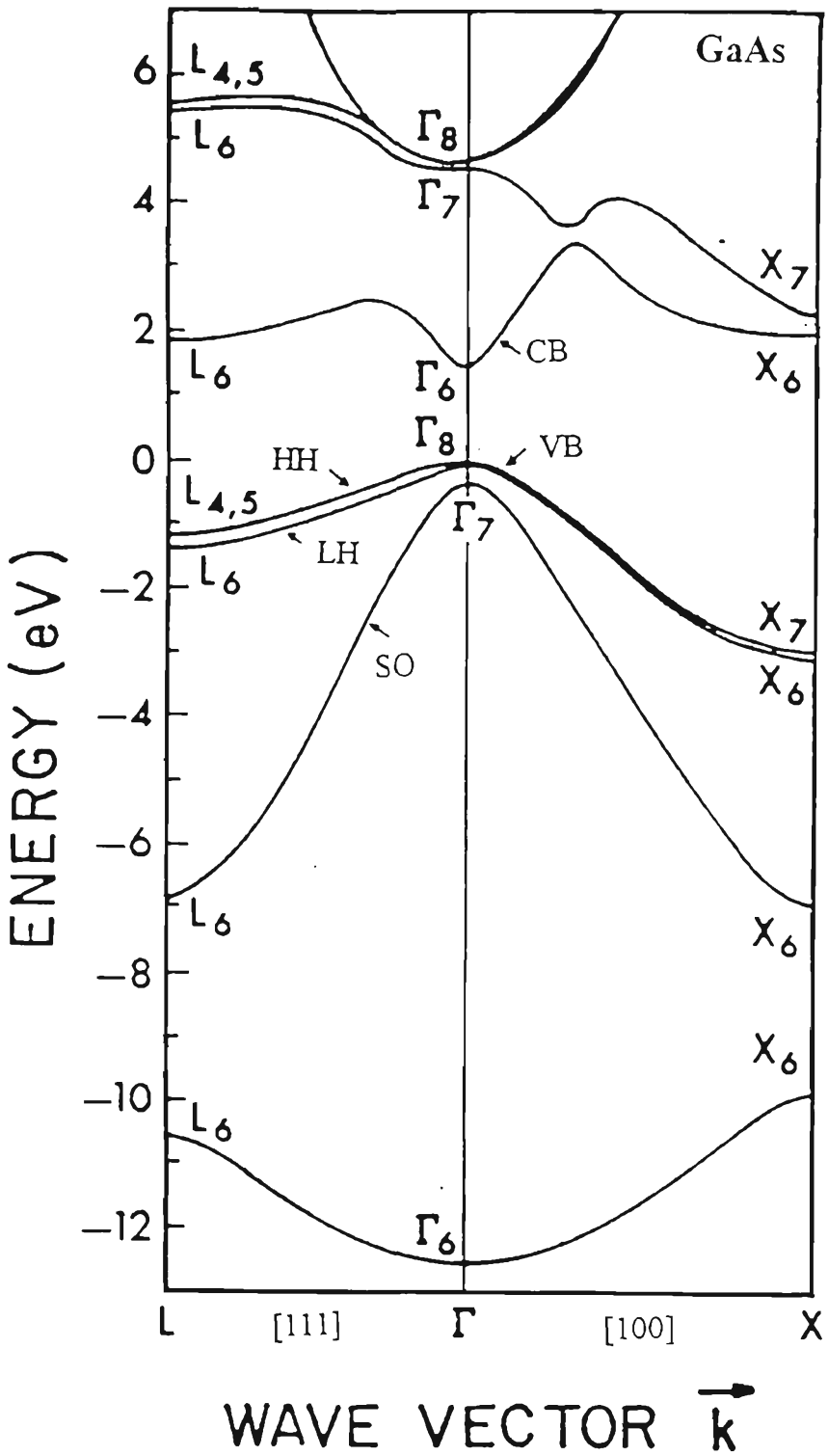

Figure 1.2 Band structure of GaAs along two crystal directions as determined by Chelikowsky and Cohen [4] using pseudopotential methods. At the point marked Γ k=0. X, and L are at the Brillouin Zone boundary and are connected to Γ by lines lying along one of the {100} directions (for X) and the {111} directions (for L). CB, VB and SO refer respectively to the conduction, valence and split-off bands. HH and LH refer to the heavy and light hole branches of the valence band, degenerate at k=0.

temperature while the conduction bands are empty with a relatively narrow forbidden gap separating the top valence from the bottom conduction band implies that GaAs is a *semiconductor*. In *conductors* such as metals the highest occupied band is always only partly filled, so that an applied electric field can always cause electrons to move through the crystal. In *insulators* the forbidden gap above the top valence band is so wide that normally electrons can never become delocalized. Note also that only the valence and conduction bands are shown. The lowest occupied bands, which can be well described by tight-binding wave functions, are localized around the individual lattice sites, and do not need to be considered in determining the electronic and optical properties of GaAs.

Transitions of electrons into states of different **k** are only possible when crystal momentum is conserved. The most common mechanism is through emission or absorption of a *phonon* or quantized lattice vibration. Because the electrons couple most strongly to the longitudinal optical or LO mode, hot electrons in polar materials relax most quickly by emitting LO phonons. In GaAs these phonons have an energy of 36.7 meV and an emission time of 130 fs [5]. Further cooling to the CB band edge at **k**=0 requires 100-200 ps and is achieved by the emission of acoustic phonons [6].

It can be shown that the force exerted on an electron in an energy band by that electron's interaction with the lattice potential can be subsumed in the *effective mass* m*. Where an external force F_i (weak enough to preclude interband transitions) is applied to a carrier with wave vector **k** in an energy band E_n an acceleration effective mass (as defined in e.g. [1] *Chapter 8*) can be derived such that

$$\left(\frac{1}{m^*}\right)_{i,j} = \frac{1}{\hbar^2}\frac{\partial^2 E}{\partial k_i \partial k_j} \quad i,j = x,y,z$$

$$\frac{dv_i}{dt} = \left(\frac{1}{m^*}\right)_{i,j} F_j \qquad (1.4)$$

As far as motion under the influence of the force is concerned the electron behaves like a free electron whose *effective mass* is given by (1.4). Note that the effective mass is a second order tensor whose elements vary inversely with the curvature of the band containing the electrons. The effective mass may be anisotropic and depends on the direction of the external force. Another useful definition of effective mass in the study of semiconductors is the energy effective mass (as defined in e.g. [7] *Chapter 2*)

$$E_n(k) = \frac{\hbar^2 k^2}{2m_E^*} \qquad (1.5)$$

This effective mass may also be anisotropic. For the conduction band in GaAs and $Al_xGa_{1-x}As$ the effective mass is essentially isotropic near **k**=0. (1.4) and (1.5) only coincide for parabolic bands.

When a partially filled band has only a few vacant orbitals it makes sense to deal with the motion of the vacant orbitals rather than with the motion of enormous numbers of electrons. It is possible to show (e.g. [1] *Chapter 8*) that the current in response to an applied electric field in an almost filled band is the same as the current would be in an almost empty band with electrons equal in number to the number of vacancies in the almost filled band, but with positive charge +e and a positive effective mass m_h^*. The h is for *hole* which is the name given to these fictitious positive particles. The vacancies or holes can be considered as occupying the top of a band where the effective mass is negative, so the absence of negative effective mass can be treated as positive effective mass of equal magnitude. It is thus possible to treat the behavior of holes in a valence band in a comparable way to the way

the behavior of electrons in a conduction band as it is discussed above. Electrons and holes are collectively known as *free carriers.*

In Figure 1.2 the three valence bands in GaAs labelled HH, LH and SO contain holes of different effective mass, called heavy, light and split-off holes. The band directly above the highest valence bands is called the conduction band (CB) because the ones above it are usually empty. It is these four bands that need to be primarily considered in determining optical properties. GaAs is a direct gap semiconductor because the highest part of the highest valence band (the deepest valley or band edge for holes) is (in k-space) directly below the lowest part or band edge of the conduction band (at $\mathbf{k}=0$). As x is increased in $Al_xGa_{1-x}As$ the forbidden gap between the valence and conduction bands widens so that [8]

$$E_g(x) = E_{g\,GaAs} + 1.447x - 0.15x^2 \qquad (1.6)$$

where x is the aluminum mole fraction

$E_g(x)$ is the $Al_xGa_{1-x}As$ band gap in eV between the conduction and valence bands at k=0 as a function of x

$E_{g\,GaAs}$ is the comparable band gap of pure GaAs at that temperature

The shape of the bands themselves also change with increasing x so that the conduction band moves away from the valence bands more quickly at the Γ symmetry point than at the X point. For $x > 0.43$ the conduction band minimum is at the X point rather than the Γ point and the semiconductor is now of indirect gap type, since the hole and electron band edges are no longer at the same **k**.

1.1.3 Calculation of the Energy Bands

A number of numerical methods have been developed to calculate the energy bands. For semiconductors the most common methods include the following.

The tight-binding (TB) approximation which modifies wave functions appropriate to isolated atomic orbitals by terms reflecting interactions with nearest neighbor atoms is only suitable for low lying narrow bands. The more generally applicable methods include the orthogonalized plane-wave method (OPW) [9,10], the pseudopotential method [11,12] and the $\mathbf{k}\cdot\mathbf{p}$ method of E.O. Kane [13,14]. In the first two methods a wave function is expanded in plane waves. Modifications have to made because otherwise the sheer number of plane waves required for the expansion would be computationally impossible. (The problem is that the wave function has atomic orbital like oscillations near the atomic sites and a long wavelength plane wave like component in the interstitial areas.) The pseudopotential method was the one used in calculating Figure 1.2.

The $\mathbf{k}\cdot\mathbf{p}$ method is a semi-empirical method used to determine band structure near band extrema. It relies on the fact that the wave function for any $\mathbf{k}$ can be written in terms of the wave function for any other, although the method is simpler if it is written in terms of a band extremum at $\mathbf{k}_o$. (In the case of GaAs the one at $\mathbf{k} = 0$ is the main one considered.) If the energy and momentum matrix elements are known for all the bands at the extremum then the energies for all $\mathbf{k}$ are completely determined. By applying a Hamiltonian, a matrix eigenvalue equation for any point $\mathbf{k}$ can be written in the $\mathbf{k}_o$ representation. To simplify computations and numbers of parameters which must be experimentally determined, the bands are divided into classes depending on whether states in that band interact strongly or weakly with the states in the band of interest. In practice bands within 3 eV at $\mathbf{k}_o$ will be included. Interactions with weakly interacting bands are 'removed' by perturbation theory and the remaining 'renormalized' interaction matrix must be exactly diagonalized. The CB near $\mathbf{k} = 0$ can be approximated by a

parabolic equation, but the **k·p** method allows a correction term to be added for the remaining nonparabolicity.

The calculation is done explicitly for electrons in the conduction band in [7] *Chapter 2* and equations are derived for the effective masses of the conduction band CB and three valence bands HH, LH and SO very near the k=0 extremum or band edge.

$$\frac{1}{m_c} = \frac{1}{m_o} + \frac{4P^2}{3\varepsilon_o} + \frac{2P^2}{3(\varepsilon_o + \Delta)} \qquad (1.7)$$

where m_c is the effective mass of an electron in the conduction band near k=0, m_o is the rest mass of the free electron, e_o is the band gap of the semiconductor, $2m_oP^2 = E_p$, the "empirical" Kane matrix element ~22-25 eV for the entire III-V family, $\Delta = \Delta_{s\text{-}o}$ the energy split between the split-off (SO) and other valence bands, which can be experimentally determined. As k increases

$$\frac{m_c(\lambda)}{m_c(0)} = \frac{(\lambda + \varepsilon_o)(\lambda + \varepsilon_o + \Delta)(\varepsilon_o + 2\Delta/3)}{\varepsilon_o(\varepsilon_o + \Delta)(\lambda + \varepsilon_o + 2\Delta/3)} \qquad (1.8)$$

where g is the energy above the band edge. The empirical formula is sometimes given

$$m^*(E) = m^*(0)(1+a(E)) \qquad (1.9)$$

where E is the energy above the band edge for the band in question and a the nonparabolicity, which for the CB in GaAs has a range of values quoted from 0.8 to 1.3, e.g. [15]. The nonparabolicity term is used as a simple convention in calculating subband levels in quantum wells, which are discussed later in this chapter. Values for band edge effective masses for electrons and holes in the conduction and valence bands in GaAs and $Al_xGa_{1-x}As$ are given in e.g. [16].

1.1.4 Effects on Band Structure of Strain and Temperature

Strain changes the energy band structure as calculated in the previous sections by changing the lattice size and symmetry, thus changing the symmetries in k-space, resulting in new energy levels and effective masses and a possible lifting of degeneracies between bands, such as that seen between the heavy and light hole bands in Figure 1.2. The topic is discussed in [17] *Chapter 1.* Strain can result from an externally applied force, or can be built in when one semiconductor is grown on top of another with a different lattice constant. The present work did not deal with deliberately strained samples, although it was necessary to mount samples carefully to avoid introducing it unintentionally.

There are also energy band changes that occur as the temperature is raised. The fundamental process involved is the shrinkage of the GaAs bandgap. The bandgap shrinkage is partly due to the volume expansion of the crystal as the temperature rises and partly due to electron-phonon interaction effects, as discussed in [17] *Chapter 1.* Grilli et al. [18] did high precision photoluminescence measurements in order to accurately determine the GaAs fundamental energy gap $E_G(T)$ and compare it with the semi-empirical formulas in use. They found that the best fit below 77K was given by the formula developed by L. Viña, S. Logothetidis and M. Cardona [19]

$$E_G(T) = E_G(0) - \frac{2a_B}{\exp(\Theta / T) - 1} \qquad (1.10)$$

where a_B = 10.4±1.1 meV

Θ = 102.4±5.7 °K reflecting an average phonon frequency

$E_G(0)$ = 1519.2±0.2 meV [20]

Grilli et al. found that (1.10) was as good as the standard Varshni formula between 77K and 280K, with neither giving an ideal fit. For these higher temperature results new parameter values must be used

a_B = 43.3 meV

Θ = 202 K

1.2 NATURE AND BAND STRUCTURE OF LOW DIMENSIONAL LAYERED STRUCTURES

1.2.1 Quantum Wells and Superlattices

A *heterostructure* is created when one semiconductor is grown on top of another with a different band structure. This is usually only practical when the crystal parameters are similar enough that any mismatch can be accommodated by strain (to avoid problems due to interface imperfections). The mismatch between AlAs and GaAs is only 0.13% at room temperature [21] so mismatch effects can be neglected in GaAs/Al_xGa_{1-x} heterostructures. Because the band structures are not the same, a free electron or hole in a sample containing a heterostructure will see a deeper valley on one side of the interface than on the other (the barrier) and will be trapped on one side of the interface when it loses sufficient energy, since there are allowed energies for valence and conduction band particles on the deeper valley side that lead to nonpropagating solutions on the barrier side. Another way of describing this is to say that there is a potential barrier at the interface with a height depending on the bandgap offset ΔE_g together with its partitioning between the conduction and valence bands. ($\Delta E_g = |E_g^A - E_g^B|$ where the heterostructure is composed of semiconductors A and B.)

When heterostructures are grown closely back to back the result is a *quantum well*. (QW), which consists of a thin layer of semiconductor A sandwiched between (usually) thicker layers of semiconductor B. If there are a number of A and B layers the result is a multi-quantum well (MQW) or a superlattice (SL). In a multi-quantum well the carriers have an

insignificant probability of tunneling out of the wells where they are trapped, while in a superlattice they are able to tunnel readily through the intervening layers of barrier material. Figure 1.3 gives schematic diagrams to illustrate quantum wells and superlattices. If the same layers are wells for both electrons and holes then the QW system is defined as Type I and recombination occurs in the wells. If different layers are wells for electrons and holes then the QW system is defined as Type II and recombination occurs at the interfaces. Only Type I $GaAs/Al_xGa_{1-x}As$ QW systems are considered in this thesis. In this case approximately 60% of the band offset is associated with the conduction band and 40% with the valence bands [22].

The essence of a quantum well (QW) is that free carriers are restricted in their motion through a solid, with free plane wave-like motion only in 2 dimensions and motion in the third dimension being restricted to a well defined region and showing energy and wave-function quantizations. [23] *Chapter 1*. The electronic states of a quantum well thus demonstrate quasi-two-dimensional behavior, "quasi" because the wave-function has physical extent in the confinement direction (conventionally called z) and thus the electron or hole particle motion is not entirely restricted to a plane. For very wide wells, on the order of several hundreds of nm, the optical and electronic properties are largely indistinguishable from the bulk. As the well becomes narrower and narrower the wave functions come more and more under the influence of the potential at the interfaces. A standard quantum mechanical treatment ([7] *Chapter 1*, [23] *Chapter 1*) shows that a discrete spectrum of energies results, with only wavefunctions of certain energies allowed, and that there is always at least one bound wavefunction regardless of the shallowness of the potential barrier at the interfaces. It also becomes possible to approximate the density of states and other behavior with 2-D equations.

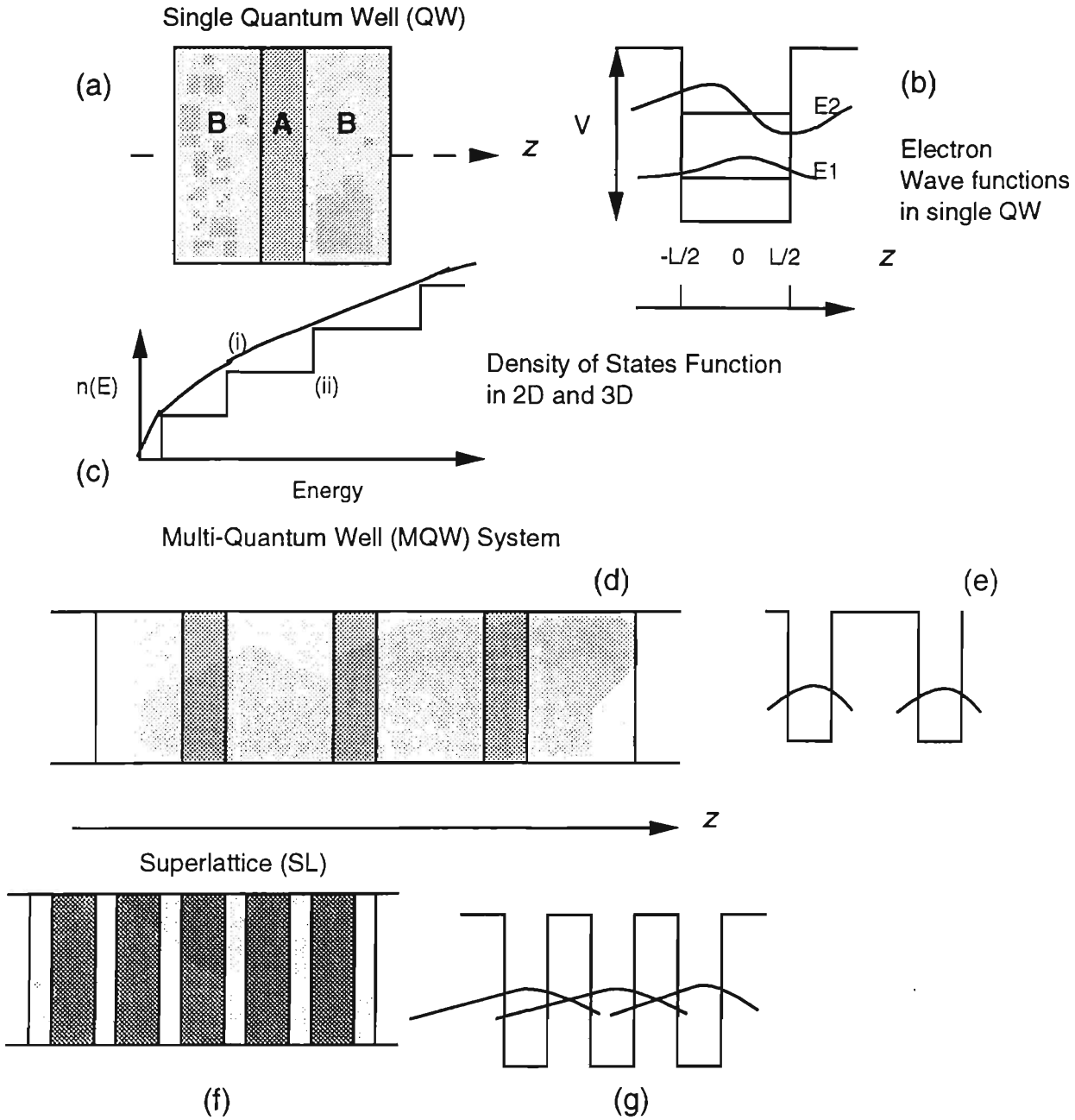

Figure 1.3 (a) Quantum Well: A has a deeper band edge for electrons and/or holes than B (b) Electron energy levels and wave functions in QW (c) (i) density of states for bulk (ii) density of states for QW (d) Multi-Quantum Well system (e) Wavefunctions are localized in MQW (f) Superlattice: narrower barrier layers allow individual well wave functions to overlap, giving a resultant delocalised wave function (not shown). The energy sublevels in a QW expand into an energy miniband due to coupling between the wells. Some figures after [7] Chapter 3 and [17] Chapter 5.

It follows from the definition of a quantum well that it ought to be possible to approach bulk behavior from a quantum well situation in three ways, either by making the well very wide, as mentioned above, by making it very narrow (to approach the situation of the bulk barrier) [24] or by reducing the height of the potential barrier at the interfaces, (i.e. by making the bandgaps of the well and barrier materials more and more similar). In this last case we have a *shallow quantum well* or possibly a shallow superlattice. Goossen, Cunningham and Jan [25] suggest that a quantum well be defined as shallow when the total band offset is on the order of 25 meV or less so that the barriers are lower than the thermal energy at room temperature. Feldmann et al. [26] studied quantum well systems with an Al content up to and including $x = 0.08$ under the rubric of the shallow quantum well and defined a deep quantum well as one with $x > 0.2$ in its barriers.

1.2.2 Density of States - 2D vs. 3D

By treating the free electrons in the Bulk or 3D situation as a free electron Fermi gas, it is possible to show (e.g. [1] *Chapter 6*) that the density of states or number of orbitals (possible wavefunctions) per unit energy range is

$$D(E) = \frac{V}{2\pi^2}\left(\frac{2m^*}{h^2}\right)^{3/2} E^{1/2} \qquad (1.11)$$

where E is the electron energy above the bottom of the energy band, m* is the effective mass of the electron in the crystal, and V is the volume of the crystal. In the absence of excitonic effects due to the interaction between electrons and holes the absorption spectrum would reflect the density of states. It can be seen that D(E) tends to zero as E tends to zero. Within an allowed energy band (1.11) shows that there is no further restriction on allowed energies in a bulk crystal.

In the quantum well it can be shown (e.g. [17] *Chapter 5*) that it follows from the energy quantization in the growth direction that the density of states in the conduction band can be expressed as a "staircase" with each step consisting of a subband with a step height of $m^*/\pi\hbar^2$ (assuming a unit area of quantum well in the *x-y* plane) so

$$D(E) = \sum_n \rho_n(E) \quad \text{where n is the subband index} \qquad (1.12)$$

$$\rho_n(E) = m^*/\pi\hbar^2 \quad E \geq E_{nz}$$

$$= 0 \qquad E < E_{nz}$$

Figure 1.3 (c) shows the 2-D and 3-D density of states.

Note that a new subband appears every time $E \geq E_{iz}$, i an integer, although there is no limit to the maximum energy of a given subband, so long as the z 'component' of that energy remains the same. Note also that there is no dependence on energy in the density of states function and that the density of states function is finite even at the bottom of the 2D level. This implies that all dynamical phenomena such as scattering, optical absorption and gain remain finite at low temperatures and kinetic energies, [23] *Chapter 1*. As with the discrete energy spectrum the density of states situation is more complicated for the valence band due to degeneracy and interband coupling.

1.2.3 Envelope functions and energy quantization in the z direction

Where heterostructure hole and electron states are built from the same extrema in the well and barrier materials' bulk Brillouin Zones (Q for GaAs wells in $Al_xGa_{1-x}As$ barriers for $x < 0.4$), the wave functions can be appropriately modeled by Gerald Bastard's [7] envelope function approach. In this model wave functions are composed of Bloch functions having the same periodicity as the lattice (as in the bulk) and assumed to be the same in both well and barrier, modulated by a slowly varying envelope function whose solutions are given by the one-dimensional time independent

Schrödinger equation. This is needed to account for the lack of translational invariance associated with the existence of the quantum well interfaces. Where a number of band edges are under consideration the wave function is actually a sum of Bloch functions modulated by envelope functions, but if it is assumed that the envelope function is derived from a single isotropic band such as the conduction band (the Ben Daniel-Duke approximation) then to give a simple example

$$\left[\varepsilon_s + V_s(z) - \frac{h^2}{2}\frac{\partial}{\partial z}\frac{1}{\mu(z)}\frac{\partial}{\partial z} + \frac{h^2 k_\perp^2}{2\mu(z)}\right]\chi(z) = \varepsilon\chi(z) \qquad (1.13)$$

where x(z) is the envelope function (z the confinement direction)

e_s is the energy at the bottom of the conduction band in the well material

$V_s = 0$ if z is located in well material

$= WE_c$ (the conduction band offset) for z in the barrier

m(z) is the effective mass of the electron in the well or barrier as appropriate

$k_\perp$ is the wave vector in the in-plane direction

The solution of Equation (1.13) is analogous to that of the standard square well potential in elementary Quantum Mechanics. Equation (1.13) is solved by matching envelope functions (which are assumed to be finite everywhere) at layer boundaries with

$$\chi(z) \text{ and } \frac{1}{\mu(z)}\frac{d\chi}{dz} \text{ both continuous} \qquad (1.14)$$

The m(z) dependence is necessary to account for effective mass mismatch at interfaces. It can be shown ([7] *Chapter 7)* that (1.13) and (1.14) are satisfied in quantum wells by sinusoidal or cosinusoidal wave functions inside the well depending on whether the envelope function is even or odd and evanescent

exponential solutions outside the well. Where the center of the well is at z=0 and the interfaces at $z = \pm L_w/2$

$$\left.\begin{aligned}\chi_{even}(z) &= A\cos(k_w z)\\ \chi_{odd}(z) &= A\sin k_w z)\end{aligned}\right\}\ |z| \le \frac{L_w}{2} \qquad (1.15)$$

$$\chi_n(z) = B\exp\left[-k_B\left(z-\frac{L_w}{2}\right)\right]\ z \ge \frac{L_w}{2}$$
$$\chi_n(z) = B\exp\left[+k_B\left(z+\frac{L_w}{2}\right)\right]\ z \le -\frac{L_w}{2} \qquad (1.16)$$

$$\varepsilon - \varepsilon_s = \frac{h^2 k_w^2}{2m_w} + \frac{h^2 k_\perp^2}{2m_w} = V_s - \frac{h^2 k_B^2}{2m_B} + \frac{h^2 k_\perp^2}{2m_B} \qquad (1.17)$$

where k_w and k_B and m_w and m_B are the z-components of the wave vectors and the electron (in this case) effective masses in the z direction in the well and barrier respectively

To a first approximation the same equations are applicable to light and heavy hole states by substituting the valence band offset for the conduction band offset and replacing electron effective masses by the equivalent light or heavy hole masses. However, while satisfactory solutions for the conduction band can be found by using the simple one band approach discussed above, with nonparabolicity incorporated as a parameter, adequate solutions in the valence band require a model with two or three bands treated on an equal footing using a **k·p** approach as discussed in [7] *Chapter 3*. Solutions are found by matching the envelope functions and the envelope function derivatives divided by the appropriate effective masses at the interfaces as required by the continuity condition (1.14) with the result that

$$\cos\phi_w - \frac{m_B}{m_w}\frac{k_w}{k_B}\sin\phi_w = 0 \quad \text{for even states}$$
$$\cos\phi_w + \frac{m_w}{m_B}\frac{k_B}{k_w}\sin\phi_w = 0 \quad \text{for odd states} \qquad (1.18)$$
$$\phi_w = \frac{1}{2}k_w L_w$$

It is immediately seen that wave vectors are restricted as to the z component of motion and that energies will also be restricted provided that there is no in-plane component to the wave vector. Allowing for all possible in-plane wave vectors

$$E_n(k_\perp) = \varepsilon_s + E_n(0) + \frac{\hbar^2 k_\perp^2}{2m_n} \tag{1.19}$$

where $E_n(0)$ is a solution of (1.18) for zero in-plane mass and m_n is the appropriate effective in-plane mass in the well

It follows from (1.19) that there are sets of parabolic subbands and that the minimum electron energy is upshifted from the minimum in the bulk material of which the well is composed. There is a corresponding reduction in the energy of the topmost 'heavy' and 'light hole' states. The narrower the well and the higher the potential barrier (hence the greater the confinement), the greater the amount of energy shifting for both the electrons and holes.

In a superlattice condition (1.13) still applies, but the band edges and effective masses are periodic functions of z with a period d, where d is the period of the superlattice so that the envelope function can be written as a Bloch wave

$$\chi_n(z+d) = \exp(iqd)\,\chi_n(z), \quad -\frac{\pi}{d} < q \le \frac{\pi}{d} \tag{1.20}$$

In this case the envelope functions in the well and barrier layers are linear combinations of outgoing and incoming waves resulting in four linear equations for four unknowns when there is matching at the interfaces, as in the Kronig-Penney model. Solutions only exist when the associated matrix vanishes leading to the bound superlattice dispersion relations

$$\cos(qd) = \cos(k_w L_w)\cos(k_B L_B) - \frac{1}{2}\left(\xi + \frac{1}{\xi}\right)\sin(k_w L_w)\sin(k_B L_B)$$

$$\xi = \frac{k_w}{\mu_w(\varepsilon)} \frac{\mu_B(\varepsilon)}{k_B} \qquad (1.21)$$

The discrete subbands of the quantum well broaden out into minibands separated by minigaps.

1.2.4 Bulk and 2-D Excitons

Optical spectra of both bulk and layered samples are very different from what would be expected from the density of states function because account must be taken of the screened Coulomb interaction between an electron which has been promoted to the conduction band and the hole it leaves behind in the valence band. A fundamental excitation (VB→CB) in the crystal results in a so-called Wannier exciton which consists of an electron hole pair bound together through the Coulomb interaction in a hydrogen like structure. It is possible (e.g. [17] *Chapter 2*) to derive the energies and wavefunctions of the bulk exciton by solving the two particles Schrödinger equation with the electron mass m_c^*, the hole mass m_v^* and their screened Coulomb interaction. The bound state energy (for a simple 2 band model) is found to be

$$E = E_n(\mathbf{K}) = E_g + \frac{\hbar^2 K^2}{2\left(m_c^* + m_v^*\right)} - \frac{R}{n^2} \qquad (1.22)$$

where n is the principal quantum number and R the effective Rydberg

K is the center of mass wave vector of the exciton

E_g is the energy gap in the semiconductor

$$R = \frac{m_r^* e^4}{2\hbar^2 \varepsilon^2 (4\pi\varepsilon_o)^2} = \frac{m_r^*}{\varepsilon^2} x\, 13.6\, eV$$

where m_r^* is the reduced effective mass and ε is the dielectric constant in the semiconductor

There is thus a family of excitons including the ground state where n=1 and the excited states where n has a higher value. In an absorption spectrum the

excitons of $n \leq 3$ are typically seen as sharp peaks, but merge into a continuum for the higher n values. This is because as n becomes higher and higher the energies are more and more closely spaced. For GaAs the ground state binding energy for the bulk exciton has been determined to be 4.2 eV [27]. As for a hydrogenic system the bound wavefunction depends on a*, the exciton radius, where

$$a^* = a_0 \varepsilon \frac{m_0}{m_r^*} \tag{1.23}$$

with m_0 the free electron mass and a_0 the Bohr radius

For GaAs $a^* \approx 130$ Å as compared with a lattice constant of 5 Å, showing that the exciton state is weakly bound having a wave function with a large spatial extension. Using inverse Fourier transformation to study the **k** space distribution of the exciton (e.g. [17] *Chapter 2*) it is simple to show that **k** is localized near the zero point of the Brillouin Zone for both electrons and holes.

In quantum wells the degeneracy (seen in Figure 1.3 for bulk GaAs) is lifted between the two highest valence bands. (Spin degeneracy remains.) These bands have different curvatures, and the holes in them have different effective masses. There is thus a splitting in quantum wells between heavy hole (HH) and light hole (LH) density of states functions, resulting in excitons which have different masses and different transition energies. Each combination of a step in the density of states function for electrons with a step in the density of states function for light or heavy holes is associated with a family of excitons, consisting of a ground and excited states, although some combinations are not seen because the transition has zero (or very small) oscillator strength. Even in an allowed transition there are always associated nonradiative states because only one spin component can be optically active [28,29]. In absorption spectra the excitons are seen as sharp

peaks at the onset of the allowed intersubband transitions. Because of the shapes of the wave functions involved, some transitions are parity forbidden. They are nevertheless sometimes present in real spectra due to the effects of built in electric fields in the sample or other asymmetry. Unlike the situation in bulk, the excitons associated with heavy and light hole transitions are well resolved due to the different effective masses involved. Light and heavy hole excitons can be distinguished by their polarization behavior as well as their energy positions. Most notably, ground state heavy hole excitons are optically active only for in-plane polarization [30]. Bound exciton and impurity related processes are also far less significant in emission than for bulk material of similar quality, as discussed in the review article of Miller and Kleinman [31].

There are further obvious differences relating to the nature of the excitons themselves. In the quantum well situation, the width of the quantum well is typically comparable to or smaller than the 3-D exciton radius, resulting in compression of the exciton and an enhanced Coulomb interaction. This in turn results in an enhanced binding energy, up to a theoretical maximum of $4R_{3D}$. The binding energy is reduced again for very narrow wells with finite barrier heights as the wave functions increasingly leak into the barriers. It is possible to calculate the binding energies for excitons in wells of various width and barrier height using variational and other methods [32,33,34,35]. The enhanced binding energies cause quantum well excitons to persist even up to room temperature where the bulk excitons would have long since dissociated due to thermal effects. Figure 1.4 compares the absorption coefficients due to 3-D and 2-D excitons. Excitonic absorption and optical properties of excitons are discussed in Chapter 3.

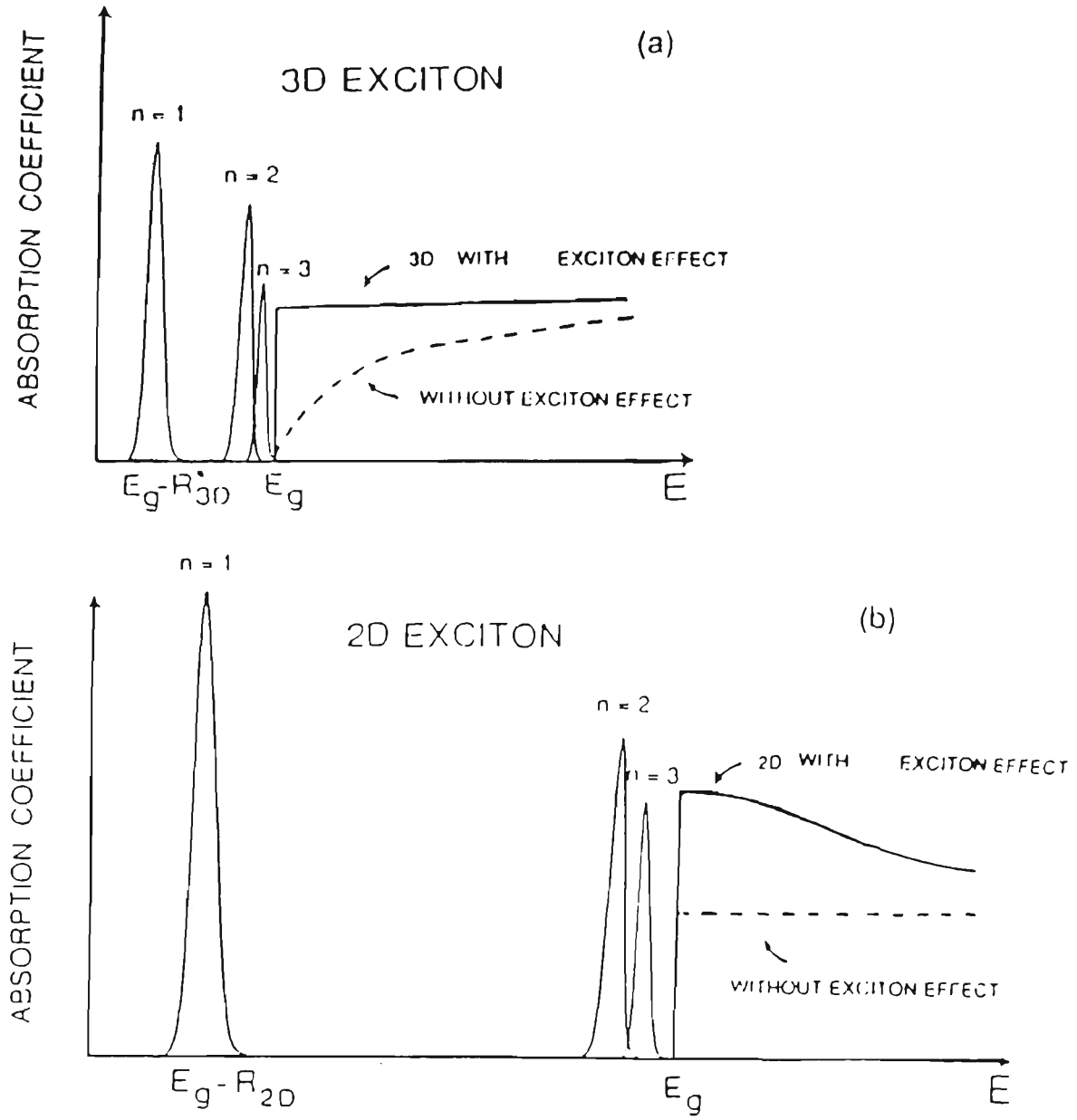

Figure 1.4 (a) shows excitonic effects on bulk absorption in GaAs or direct $Al_xGa_{1-x}As$ and (b) excitonic effects in Type I $GaAs/Al_xGa_{1-x}As$ quantum wells. In (b) it should be noted that there are usually several such families of excitons corresponding to individual steps in the density of states function. In both (a) and (b) absorption in the absence of excitonic effects is given by the dashed lines and is proportional to the 3-D or 2-D density of states functions shown in Figure 1.3(c). n=1 is the ground state. Note that the binding energy is much greater in the 2D case. Generally only the first two excited states n=2 and n=3 are visible as separate lines. Reproduced from [17] Chapter 5.

1.2.5 Dimensionality and wave function properties

It is possible to experimentally separate the QW properties which depend directly on quasi 2-D confinement from those relating to the 2-D confinement only through the wave function. This is because as a quantum well is made narrower and narrower, the wave function spills out of the well more and more, having the properties of a barrier wave function for a well of zero width. At the same time, if there is any confining potential well at all (provided that it is narrow enough), the center of mass motion of the excitons will be confined to the plane. Thus it is quite possible for a system to show bulklike behavior for those properties such as exciton binding energy and Bohr radius that are mediated through the wave functions and quasi 2-D behavior in the excitons and density of states, which are not. Brandt, Lage and Ploog [24] grew samples with 10 InAs monolayers (ml) separated by 40 ml of GaAs. Experiments showed that the monolayers were acting as quantum wells with respect to density of states, oscillator strength of transitions and exciton confinement as demonstrated by reflectivity resonances, but that the confined excitons were bulklike in their binding energy and Bohr radius.

CHAPTER 2

HYDROGEN PASSIVATION OF DEFECTS AND IMPURITIES

2.1 AN OVERVIEW OF DEFECTS AND IMPURITIES

2.1.1 Introduction of energy levels by defects and impurities

An *imperfection* is any deviation from an ideal crystalline structure. *Defects* (also called physical, native or intrinsic defects) disrupt the lattice structure without introducing any elements which are foreign to the basic crystalline structure. Point defects include vacancies, antisites, where an atom of one element occupies a site appropriate to an atom of another element, and interstitials, where an atom is crowded in between sites. There are different types of *dislocations* or line defects, which consist of a linear array of misplaced atoms in the crystal. There are also planar defects or stacking faults. All these defects naturally cause distortions in the lattice around them. *Impurities* are foreign elements introduced into the crystal structure. They can occur interstitially or substitutionally where they replace the "proper" atom at a crystal lattice point. In GaAs substrate material and in the MBE grown material studied here among the most common residual impurities are carbon, oxygen, silicon and sulfur [36,37,38].

Imperfections in the crystal structure introduce energy levels into the band structure of a semiconductor. Imperfection states are bound or localized states because the imperfection is localized, and the wave functions well away from it can be expressed as a linear combination of the eigenfunctions appropriate to the pure crystal. In many cases imperfections push band states into a forbidden gap leaving antiresonance states behind, as discussed

in [17] *Chapter 3*. These gap energy levels can be classified as shallow or deep levels. In the older view, an imperfection energy level was shallow if it was located in the forbidden gap very near to the conduction or valence band, and otherwise deep. Now the distinction is made on the basis of whether the level is principally due to a long range Coulomb interaction (shallow) or a short range defect or impurity level (deep). The introduced energy levels can have profound effects on the near band gap optical and electronic properties of the semiconductor, because of their ability to trap and assist with the recombination of excitons and free carriers. Some of these properties are desirable for device applications so both impurities and defects are often deliberately introduced.

In general substitutional impurities are usually classed as *donors* if they have more valence electrons than the atom they replace, *acceptors* if they have fewer and isovalent if the number of valence electrons is the same. Substitutional impurities which are deliberately introduced are often called *dopants*. The attraction between the donor nucleus and its extra electron (surplus to the number required for bonds with neighbouring atoms) is very weak so that a small amount of energy will easily delocalize it from the vicinity of the impurity, leaving an immobile positively charged ion behind. The same applies to the hole introduced into the lattice structure by an acceptor. It is also easily delocalized, leaving the acceptor as an immobile negatively charged ion. Semiconductors where donors (acceptors) dominate are known as n-type (p-type). In effect the presence of impurity atoms in the lattice gives rise to energy levels (filled at low temperature) in the energy gap between the valence and conduction bands. In the case of shallow donors these energy levels are close to the conduction band and close to the valence band for shallow acceptors. Introducing donors (acceptors) into a pure intrinsic semiconductor thus moves the *Fermi energy* (the

energy of the topmost filled level in the ground state of the crystal) from the middle of the band gap to a position close to the conduction (valence) band. Donors and acceptors compensate each other when both are present in a sample, because the extra electron from the donor ends up in the extra hole from the acceptor. It is possible to show (e.g. [3] *Chapter 8*) that the product of the hole and electron concentration is constant regardless of impurity concentration.

Donors (acceptors) are often deliberately introduced into semiconductors to increase the electron (hole) concentration in the conduction (valence) bands. In *modulation doping*, the advantages of the delocalized free carriers are obtained in a quantum well or the narrow gap side of a heterostructure, without the immobile ions causing scattering and compromising the pure, high mobility nature of the material. The doping is done in the wider gap barrier material, in the knowledge that the resultant free electrons or holes will migrate into the narrower bandgap material, at least until charge considerations cause the process to stop. The dopant ions are often further separated from the free carriers they liberate by an undoped spacer layer of barrier material between the heterojunction and the doped barrier. (See e.g. [23] *Chapter 2*).

In the present work shallow donors or acceptors are indicated by including the element they replace in the crystal lattice as a subscript. The most common residual shallow donors and acceptors in the present work are carbon in the form of C_{As} (acceptor) and silicon (acceptor (Si_{As}) or donor (Si_{Ga})). Sulphur is also a common residual shallow donor. Si_{Ga} occurs in some of the samples as a donor dopant.

2.1.1.1 Shallow impurity states: the effective mass approximation

It is possible to treat the wave functions of the shallow states (usually arising from impurities) as a linear combination of the unperturbed Bloch functions at the bottom of the conduction band for the donors and the top of the valence band for the acceptors. The Bloch wave functions are modulated in amplitude by slowly varying envelope functions in real space. The shallow state wave functions extend over a wide area in real space and are thus strongly localized in **k** space. If the effective mass in the (parabolic) band is isotropic it is possible to derive an estimate of the shallow donor or acceptor ionization energy by approximating the impurity potential by a hydrogen-like Coulomb potential in the so-called effective mass approximation, e.g. [17] *Chapter 3*.

Thus

$$\left[\frac{-\hbar^2}{2m^*}\nabla^2 - \frac{e^2}{\varepsilon r(4\pi\varepsilon_o)}\right]F_l(\mathbf{r}) = E_v F_l(\mathbf{r}) \qquad (2.1)$$

where ε is the dielectric constant of the material, $-e$ the electronic charge and $F_l(\mathbf{r})$ the envelope function discussed above.

$$E_n = \frac{e^4 m^*}{2\varepsilon(4\pi\varepsilon_o\hbar)^2}\frac{1}{n^2} \qquad (2.2)$$

gives the energies of the allowed ground and excited states

The approximation gives a donor ionization energy of the order of 6 meV for GaAs, and several times as large for the acceptor. The low ionization energies imply that the free carrier is weakly bound enough that donor or acceptor orbitals will overlap even at relatively low impurity concentrations. The donor or acceptor effective Bohr radius is given by [1] *Chapter 8*

$$\left.\begin{matrix} a_D \\ a_A \end{matrix}\right\} = \varepsilon_r a_o \frac{m_o}{m^*} \qquad (2.3)$$

where ε_r is the dc relative dielectric constant = 12.9 for GaAs and a_o is the hydrogen Bohr radius

For GaAs donors and acceptors this radius is of the order of 100Å, enough to cause considerable overlap even at quite low impurity concentrations, allowing hopping transport without promotion of electrons (holes) to the conduction (valence) bands.

There are small discrepancies between theory and experiment which occur because in GaAs the simple hydrogenic approximation is no longer completely appropriate in the central cell region, especially for the ground state. The actual donor and acceptor binding energies differ according to the impurity element (the chemical shift), [17] *Chapter 3*. Even with this taken into account energy levels introduced by different shallow single donors (but not acceptors) are so close that it is difficult to distinguish them.

2.1.1.2 Deep defect and impurity states

The deep state wave functions are strongly localized in real space and delocalized in **k** space, so that the effective mass theory is inappropriate. Methods appropriate for calculating the deep level wave functions and energies, such as the cluster method and the K-S Green's function method are discussed in [17] *Chapter 3*. Deep states have a strong influence on the electronic and optical properties of a semiconductor, because of their ability to trap free carriers. Recombination through traps often dominates direct band to band recombination, even if the trap concentration is quite low. It is possible to show that recombination through traps is most efficient for states in the center of the forbidden gap, e.g. [17] *Chapter 3*. Because of this property, it can be shown that a high concentration of deep traps leads to poor luminescence efficiencies and poor minority carrier diffusion length and lifetime [39].

Recombination through the deep traps generally is nonradiative and and involves the release of a number of phonons by a mechanism explained by Huang and Rhys [40]. Because the deep states are strongly localized, atomic equilibrium positions vary depending on whether the defect state is or is not occupied by an electron. (This change in equilibrium position is known as lattice relaxation.) It is possible for a conduction band electron to acquire an activation energy sufficient to cross over to an excited state where it is bound to the deep defect. When the electron reaches the crossing point it can be captured by the defect state, and causes violent lattice vibrations through the extra energy it brings to the defect or deep impurity, because the crossing point is very far from the new equilibrium. As the vibrations damp down the energy propagates away as phonons. This phenomenon only occurs in deep states, because shallow wave functions are more spread out in real space and the electron-lattice interaction is weak. It leads to an experimental situation for deep traps where the capture cross-section can be experimentally fitted [17] *Chapter 3*

$$\sigma_n = A \exp\left[\frac{-E_A}{k_B T}\right] \tag{2.4}$$

where σ_n is the capture cross-section for the trap, A is a constant characteristic of the trap, E_A is the activation energy of the trap

Some deep defects and impurities are capable of trapping more than one electron. Generally the state with the trap occupied by two electrons is of higher energy than the state with the trap occupied by one electron, because of Coulomb repulsion between the electrons. In a negative-U system the lattice relaxation energy which is released after the second electron enters the trap is greater than the Coulomb repulsive energy. Effectively, having one electron in the trap attracts another, and the new state with two electrons in it is of lower energy than the state with only one.

Linking experimentally observed deep levels with particular physical defects or defect impurity complexes is frequently very problematical. It is also clear that deep levels vary with the material and the growth technique and temperature, with some being unique to particular growth techniques. The main deep levels to be seen in the MBE and substrate materials studied in this thesis are tabulated in the review articles of Baranowski [41] and Yasuami [42] on defects in LEC GaAs material and Peaker and Nicholas [43] and Illegems [39] on MBE GaAs and Peaker and Saleemi [44] on $Al_xGa_{1-x}As$. Oxygen has been shown to behave as a deep acceptor in GaAs and to have a negative-U character [45]. It compensates shallow donors and degrades radiative efficiency [46,47,38].

2.1.2 Defects and Impurities at Dislocations

Dislocations are to be found in GaAs LEC substrate material at typical densities of 10^4 - $10^5\,cm^{-2}$, but they are not evenly distributed, forming cellular networks with cell diameters of 300 to 500 μm. A high density of dislocations tangle together to form the cell walls, but the cell interiors are largely dislocation free [48]. The dislocations also propagate into epitaxial layers so that densities found in the epitaxial layer are close to those found in the substrate [39,49] although a superlattice layer is known to block the propagation [50]. It is believed that deviations from Ga:As stoichiometry in the melt from which the substrate crystal is grown is responsible for the cellular dislocation structure. There is also evidence that dislocations can nucleate on clusters of point defects [49] and result from misfit at heterojunctions, for example when GaAs is grown on an Si substrate [51].

High dislocation densities are associated with reduced average minority carrier lifetime, to the point that the minority carrier diffusion length is limited by the average distance between dislocations [52], due to the

introduction of nonradiative recombination sites. Dislocations can be directly responsible for the presence of arsenic antisites [36], but there is evidence that the dislocations themselves are not the main source of short minority carrier lifetimes, but rather other defects and impurities that diffuse into the vicinity of dislocations from elsewhere because of their strain field [36,52,53,54]. Annealing improves the electrical behavior of GaAs LEC substrate without affecting the dislocation structure [36]. Defects and impurities associated with dislocations include precipitates formed of impurities [52] or arsenic [36] which decorate and pin the dislocations, as well as forming nonradiative regions Also to be found are various point defects causing nonradiative recombination sites [42,52,51], the EL2 defect in LEC substrate [36,55] (which may just be an arsenic antisite) and donor and acceptor impurities [52,56] including Carbon in LEC GaAs [57] and in MBE quantum well structures [58] and Silicon [53]. The cathodoluminescence measurements of Petroff et al. [54] revealed that defects responsible for the g-line and so-called KP defect lines (to be discussed in Section 3.3) which are commonly seen in MBE GaAs were concentrated near dislocations, and similar defects were observed to be associated with dislocations in InGaAs/GaAs heterostructures [59]. Stacking faults are also known to collect other imperfections in their strain field [52].

2.1.3 Defects and impurities at the surface and at interfaces

Added to the repulsive potential which would exist even at an ideal intrinsic surface due to image charges is an attractive extrinsic potential due to the ease with which so called adatoms of various impurities can attach themselves to the reconstructed surface. (Surface atoms rearrange themselves to eliminate dangling bonds and to reduce surface polarity.) Sharma [60] claims that any GaAs samples kept under normal laboratory conditions will quickly acquire an oxide layer of 20-30Å. Chemical reactions

of the adatoms with the surface layer promote native defects, especially the arsenic antisite. It is these defects that pin the surface states to the Fermi level and act as nonradiative recombination centers [61]. Carbon and Oxygen are particularly troublesome adatoms and react strongly with Al. The surface electric field arising from the adatoms and defects causes band bending and acts to ionize any excitons in the vicinity, which causes them to be heavily damped and reduces their contribution to the dielectric function. The attractive potential extends deeper into the sample than the repulsive so that an exciton approaching the surface is first attracted and then repelled. In most cases any exciton or free carrier that reaches the surface ends up recombining nonradiatively through surface states, but in some cases the potential valley produced by the interaction between the two potentials can accommodate exciton bound states, which manifest themselves in patterns of spikes in the reflectance spectrum [62]. These have been seen experimentally, but always only after some sort of surface treatment such as electron or ion bombardment [63]. The dissociation of the excitons at the surface is responsible for the 'dead layer' effects discussed in Chapters 3 and 5.

In samples without capping layers to confine the excitons, nonradiative recombination at the surface often dominates the other optical effects, since an exciton that reaches the surface is certain to fall into the Fermi level traps. The magnitude of these effects is often expressed through a surface recombination velocity [64,65]. The devastating effect of surface traps on excitons is also seen in the study of surface quantum wells [66,67].

It was observed more than 15 years ago that the luminescence from the first of a series of quantum wells was more broadened than that from the wells grown later. It was concluded that roughness was greater at a so-called

inverted interface where GaAs is grown on top of AlGaAs than in the normal or direct interface where AlGaAs is grown on top of GaAs [68]. On the basis of the extrinsic photoluminescence this was attributed to residual carbon floating on the surface of the AlGaAs during growth and condensing out at the inverted interface, interfering with normal growth. Other evidence for the inferior quality of the inverted interface comes from modulation doped structures where high mobility can only be obtained from direct and not inverted heterostructures [69] unless very special care is taken and from the fact that growing prewells or short period superlattices before (but not after) a quantum well or double heterostructure improves the carrier lifetime and hence the photoluminescence [69,70,71,72]. Gérard et al. [69] inserted AlAs and InAs monolayers into quantum wells in order to localize the excitons in particular parts of the well (in the case of the InAs) or push them away from particular parts of the well (in the case of the AlAs). They then used time resolved measurements of nonradiative lifetime and were able to prove that lifetimes were considerably shorter at the inverted interface.

DLTS and C-V studies have shown that the region surrounding an inverted interface contains a high concentration of native defects related to Arsenic vacancies, interstitials and antisites, with the concentration higher when the Aluminum concentration of the barriers is higher [73]. Hong and Wang [74] had earlier noted that the inverted interface was of lower quality if the growth temperature was low, which would have encouraged native defects. There is also evidence in the inverted interface region for Carbon [68, 58] and Oxygen [38,75]. Growth on a misoriented substrate is believed to improve interface quality because it improves the sticking probability for Arsenic at the expense of Oxygen [38,76]. The basic problem is apparently due to the fact that Aluminum has a smaller surface migration rate than Gallium and the fact that some substitutional impurities such as Oxygen are more soluble

in $Al_xGa_{1-x}As$ than in GaAs. The impurities condense out at the interface and may have effects on the surface reconstruction which tend to pin steps on the surface and interfere with the lateral propagation of the atomic layer [38,77]. This could encourage the incorporation of native defects, since in a sample that has no growth interruption, the growth of a new layer begins when the old layer is only half completed [78,79]. Krispin et al. [73] believe that the native defects could be encouraging the further incorporation of impurities.

Because the substrate is of much lower quality than the epitaxial layers, excitons and free carriers that reach it tend to recombine nonradiatively on defects, leading to a substantial interface recombination velocity, as mentioned in the previous section on the surface.

2.2 HYDROGEN PASSIVATION OF DEFECTS AND IMPURITIES

2.2.1 Overview of hydrogenation

It was recognized by the early 1950s that hydrogen had dramatic effects on the electronic properties of semiconductors. The earliest systematic work on the subject was that of Van Wieringen and Warmoltz [80] in 1956. The effects essentially involved the passivation of energy levels introduced by defects and impurities, as well as effects on surface reconstruction. The early work was mostly done on Silicon. Chevallier et al. [81] first demonstrated the hydrogen passivation of donor dopants in *n*-type GaAs samples in 1985, and in the following year Johnson et al. [82] demonstrated 1986 the first hydrogen passivation of acceptor dopants in *p*-type GaAs. See Pankove and Johnson [83] for more historical background.

2.2.2 Methods of hydrogenation and diffusion into samples

There are a number of methods for deliberately introducing hydrogen into a semiconductor sample during growth [84]. With existing samples a number of methods will work, including electrochemical methods and immersing in water. The two commonest and most effective methods involve ion implantation and immersion in a gas plasma generated by a radio frequency glow discharge with the sample held at an elevated temperature (for GaAs typically 150-300C [85]) to encourage diffusion [86]. Ion implantation is associated with considerable surface damage, caused by the ion bombardment displacing lattice atoms. The rf plasma method is also capable of causing surface damage because of ions with energies over the damage threshold of 15 eV produced at the edge of the plasma. There is also some evidence of new volume defects induced by hydrogenation [87]. Surface damage associated with hydrogenation is in fact well known and the resulting defects include As vacancies and interstitials and Ga precipitates [88,89,90,91,92]. The surface damage from high energy ions can be minimized by locating the sample in a "downstream" environment where it is shielded from direct bombardment by energetic protons or negative hydrogen ions [93]. Diffusion is typically to a depth of several microns, depending on the processing conditions and the doping levels in the sample.

Hydrogen normally diffuses interstitially [94], but there is evidence it can diffuse preferentially down dislocations and grain boundaries in polycrystalline material, as is discussed in Section 2.2.3.5. The diffusion profiles, which are determined by SIMS and C-V measurements, depend on the plasma conditions and the sample temperature during the hydrogenation process, but there are distinctly different profiles for n- and p-type samples [95]. It has also been found [96] that introduction of a heavily n-doped cap near the surface of a GaAs sample inhibits diffusion regardless of the sample

type, but that a *p*-doped cap has no such effect. Reverse bias annealing (RBA) experiments in Zn doped *p*-type GaAs hydrogenated Schottky diodes indicate the drift of a positively charged monatomic species [97]. It is now generally accepted that hydrogenation occurs through the diffusion of H^+ ions in *p*-type material. Similar experiments have been performed in *n*-type material [98,99] and the results are consistent with the diffusion of hydrogen as H^- ions in *n*-type material. According to some workers [91,100] the SIMS data is better fit by assuming that H diffuses in a neutral state in undoped and *n*-type material. They accept that hydrogen diffuses as H^- in $Al_xGa_{1-x}As$. See Pavesi [94] for further references on this question.

First principle calculations ([101,102,103] and references in [94]) indicate that H^+, which acts as a deep donor, is the stable charge state for *p*-type GaAs. It prefers to stay in a high valence charge region near the bond center. H^-, which acts as a deep acceptor, is the stable charge state for *n*-type GaAs and prefers the low valence charge region near a tetrahedral site. Note that this charge state is the one supported by the RBA experiments. Which charge state is the one of lowest energy depends on the Fermi energy, but H° is never the state of lowest energy. Thus hydrogen acts as a negative-U centre.

2.2.3 Electrical and optical effects of hydrogenation

Hydrogen incorporated during GaAs sample growth in an H_2 atmosphere can reduce the incorporation of residual impurities, including carbon and oxygen, and raise the minority carrier diffusion length and (usually) the PL efficiency [84,94,104]. Hydrogenation of an existing sample can suppress electronic states due to dangling bonds associated with defects and impurities that are already present, regardless of whether they are shallow or deep, donors or acceptors. This suppression is described as passivation rather

than compensation, because a neutral pair is created, consisting of the hydrogen atom plus the imperfection. In the case of shallow impurities this reduces the carrier concentration because the impurity can no longer be ionized, so cannot contribute a free carrier to the conduction or valence band. The passivation also increases the mobility because the impurity remains neutral and cannot act as an ionized scattering center. In compensation donors (acceptors) reduce the carrier concentration that would otherwise exist because of the dominant acceptors (donors) in the sample by recombination through a Donor Acceptor Pair (DAP) mechanism at the cost of decreasing the mobility due to the introduction of new ionized scattering centers [105].

The extent of the hydrogen passivation can be virtually complete. Yang et al. [106] were able to establish through electrolyte electroreflectance and PL measurements on a GaAs/$Al_xGa_{1-x}As$ resonant tunneling structure that over 96% of the shallow donors were passivated in their sample after hydrogenation and that the density of deep levels was reduced by a factor of 300. Hydrogenation is reversible on annealing at a suitable temperature, with the thermal energy causing the hydrogen-imperfection complex to dissociate, and at even higher temperatures driving the hydrogen out of the sample.

2.2.3.1 Hydrogen Passivation of Deep Defect and Impurity States

The majority of deep level traps to be found in GaAs and $Al_xGa_{1-x}As$ can be passivated by hydrogen [107]. Individual defect levels revealed as substantially or completely passivated by DLTS and C-V measurements include EL2 in bulk GaAs [108,109,110,111], EL2, EL3 and EL6 [112], M1, M3 and M4 in MBE GaAs, accompanied by improvements in PL efficiency and no change in mobility due to deep level passivation [113,114], M1 and M4 (but

not M3) in MBE GaAs [104], several electron traps found in LPE GaAs material [115] and 'DX' impurity centers in Si-doped MBE $Al_xGa_{1-x}As$ [116]. See further references in Murray [85] and Pavesi [94].

2.2.3.2 Hydrogen Passivation of Shallow Impurities

All shallow donors and acceptors are passivated by hydrogen in GaAs [107], and passivation of most of them has also been demonstrated in $Al_xGa_{1-x}As$ [94]. Techniques for demonstrating passivation include SIMS with deuterium used as a more detectable surrogate for hydrogen and/or electrical C-V or Hall effect measurements (Johnson et al. [82] for Zn in GaAs, Pearton, Dautremont-Smith et al. [117] for Si, Zn,S,Se,Te,Sn,Ge in GaAs, Pan et al. [118] for Carbon in undoped GaAs, Pan et al. [119] for Si in high purity GaAs accompanied by a narrowing of the donor bound exciton line in PL and an increase in mobility, Leitch [99] for Se in GaAs, Jalil et al. [120] for Si in GaAs, with significant increase in mobility reported along with passivation, Chevallier [81] for Si in GaAs, Nabity [116] for Si in $Al_xGa_{1-x}As$). Pearton, Dautremont-Smith et al. [96] report that for Zn acceptor doped GaAs there is a strong dependence of passivation efficiency on the initial dopant concentration.

Local vibrational mode (LVM) spectroscopic measurements in the infrared also show deletions of lines seen in the as grown sample and the generation of a new pattern of lines reflecting new bonds formed in hydrogen-impurity complexes (Ashwin et al. [121], Davidson et al. [122,123] for Carbon (in GaAs and AlAs doped samples), Newman [124] for Carbon in GaAs, Chevallier et al. [125] for Si in GaAs, Pajot et al. [126] for Zn in GaAs, [127] for Si, Zn, Be in GaAs, Nandhra [128] for Be in GaAs). Details of these patterns give clues to the nature of the bonds involved. See further references in Murray [85] and

Pavesi [94], although see Pavesi et al. [129] for evidence that the deep levels were preferentially passivated in their samples.

Some studies have considered the issue of passivation of samples that are already heavily compensated. Murray [85] reports work done by him and co-workers on GaAs doubly doped with Si (a donor) and Be (an acceptor) and then hydrogenated. It was found that only the majority dopant could be passivated no matter what the conditions. Passivation stopped when the material became semi-insulating. Similar results in compensated samples are reported in Chevallier et al. [130].

2.2.3.3 Reactivation of deep and shallow levels after annealing

Shallow donor or acceptor activity is completely recovered after annealing at temperatures lower than those needed for some deep levels. Pearton, Dautremont-Smith et al. [114] measured carrier concentration as a function of annealing temperature and were able to derive equations giving the dissociation energy for each donor (or acceptor) as a function of annealing time and annealing temperature. In general donor activity was restored around 400C and dissociation energies were slightly above 2 eV. The estimates of the dissociation energies were later revised down on the basis of measurements involving reverse bias to prevent retrapping to between 1.2 and 1.5 eV in GaAs, depending on the donor or the acceptor, with Si_{Ga} 1.25±0.05 eV, Si_{As} 1.45±0.10 eV, C_{As} 1.35±0.10 eV, with the actual binding energy (as opposed to the migration energy) component 0.4 to 1.0 eV. There was no clear distinction in energy between donors and acceptors as a group [107]. It was found from other studies that athermal reactivation of shallow donors and acceptors could take place if minority carriers were injected into the sample optically or by other methods, [131] and references in [107]. It is

believed that these carriers react with the hydrogen ion bound to dopants to produce neutral hydrogen.

There is sometimes disagreement about the temperatures required to reactivate the deep traps after passivation. Dautremont-Smith et al. [113] found that the deep M series traps they studied were not reactivated after a 5 min. anneal at 400C or 500C, adequate to reactivate shallow impurities, but did begin to reappear after a 5 min. anneal at 600C. Omel'yanovskii et al. [109] similarly found that a high annealing temperature was necessary to reactivate EL2, but this is disputed by Conibear et al. [111] and Cho et al. [112] who found that annealing temperatures as low as 250C began to reactivate this defect. Nabity et al. [116] found that the DX center in $Al_xGa_{1-x}As$ recovered its activity at about 400C, the same temperature as the shallow impurities. This is expected since the DX defect level is widely believed to be due to a simple donor accompanied by some lattice relaxation. Mehta et al. [132] shows that the Al-O-C defect is reactivated after 5 min. annealing at 500C. The concept of a temperature window in which deep levels remain passivated and shallow donors and acceptors are reactivated would only seem to be firmly established in epitaxial GaAs where EL2 and DX defect levels are not seen.

2.2.3.4 Hydrogen passivation at the surface

The defects at the surface are also vulnerable to hydrogen passivation. They act as nonradiative recombination centers and can dramatically reduce photoluminescence in surface quantum wells, as was discussed above through their effects on the surface recombination velocity and band bending. A large number of studies [61] show that hydrogenation is effective in removing surface oxides and reducing the concentration of surface states thus reducing the surface recombination velocity, which

improves electrical characteristics of devices such as the surface leakage current. Because of the improvement in photoluminescence (PL) yield with the passivation of surface states, *in situ* PL monitoring and surface vibrational spectroscopy technique is used in some of these studies to follow the progress of the hydrogenation treatment. The hydrogen treatment is often followed by nitridation or other processes to stabilise the passivation against water vapor and oxygen molecules in the air. Sometimes it is desirable to passivate the surface, but not the bulk shallow donors or acceptors. Yoon et al. [133] found that surface passivation is stable on annealing for 60 min. at 400C in vacuum, a high enough temperature to reactivate any passivated shallow impurities. Despite the reduction in surface states, passivated uncapped samples were shown to improve in PL efficiency far less than capped ones, where (in the latter case) migration of free carriers and excitons to the surface is completely prevented [113].

2.2.3.5 Hydrogen passivation at dislocations and grain boundaries

When epitaxial GaAs is grown on a Si substrate, numerous threading dislocations and microtwin defects appear to accommodate the mismatch. The dislocations are responsible for the appearance of nonradiative areas and problems with electrical as well as optical properties. When such samples are hydrogen passivated the electrical characteristics improve. Pearton, Wu et al. [51] noted that the reverse breakdown voltage of Schottky diode structures made using this technique was improved by a factor of 2.5 after hydrogenation, still far inferior to a comparable diode made using a GaAs substrate and hence lacking the dislocations. Because characteristics within 0.5 mm of the surface were the same whether the substrate was GaAs or Si, the improvement in the GaAs on Si samples after hydrogenation was attributed to passivation of the dislocations. It is not clear whether the

dislocations were passivated directly or just the defects and impurities in their vicinity.

Hsieh et al. [89] also studied GaAs on Si samples and found through C-V and Hall effect measurements that the passivation depth was greater than for GaAs grown on a GaAs substrate, and reduced again when the defect concentration was reduced by high temperature annealing. They attribute the greater passivation depth in GaAs on Si samples to easier hydrogen access through the threading dislocations and microtwin defects. TEM examination of sample cross sections showed dark patches formed along dislocations down to the passivation depths observed in C-V profiles. They concluded that the threading dislocations were acting as line sources of hydrogen during plasma exposure. A number of similar findings have been made on hydrogen moving in through dislocations and grain boundaries in silicon [134]. Gal, Tavendale et al. [135] also report hydrogen passivation of defect states caused by misfit dislocations in InGaAs/GaAs heterostructures. In their case photoluminescence bands attributed to recombination in the defect states were strongly reduced after hydrogen passivation.

Pearton and Tavendale [136] found that hydrogenation of surface barrier diodes made from polycrystalline GaAs showed reductions in reverse leakage currents after hydrogenation by a factor of up to 50. There was a correlation between average grain size and the amount of improvement, with the smallest grain sizes associated with the greatest improvement. It was concluded that hydrogen preferentially diffuses down the grain boundaries, passivating the defects associated with them.

2.2.3.6 Hydrogen passivation at interfaces

In view of the high concentration of defects and impurities often seen in the vicinity of interfaces as discussed in Section 2.1.3, it would be expected that hydrogen would also be found concentrated in their vicinity after passivation. This was observed in SIMS by Polyakov et al. [137] using deuterium as a surrogate for hydrogen. They could not deal directly with quantum wells because their resolution was not sufficient, but the effect occurred at junctions between thicker layers of $Al_xGa_{1-x}As$ of differing Al mole fraction x.

Narrower wells or short period superlattices where interface states are likely to be relatively more important are more likely to show increased photoluminescence yield after hydrogen passivation [132,138,139]. The explanation involving interface defects is supported in the case of short period superlattices by calculations on a Kronig-Penney model which show a decreasing quantum efficiency correlated with an increasing probability that an electron will be found at an interface [139]. Position of a well in a sample can also affect the response to hydrogenation. As was mentioned in Section 2.1.3, the first in a series of quantum wells to be grown is often of lower quality with more defects and impurities at the interfaces. Botha and Leitch [140] found that these wells were more likely to show linewidth narrowing and increases in PL efficiency after hydrogenation. Wells grown near the surface are likely to have their quality reduced due to plasma damage during hydrogenation and are likely not to show any improvement in PL efficiency. Botha and Leitch also noted that improvements in the PL response due to hydrogenation began to fall off as the the sample temperature was increased above 100K. They attributed this to thermal activation of plasma induced defects.

2.2.4 Microscopic structure of passivated complexes

The structures of some of the passivated complexes have been established, especially those involving shallow impurities [141,142]. For Group IV donors, such as Si_{Ga}, in GaAs or $Al_xGa_{1-x}As$ the complex structure was originally proposed by Pajot, Newman et al. [127] on the basis of LVM spectra and supported by the cluster calculations of Briddon and Jones [143]. It involves the donor atom being five-fold coordinated and bonded directly to the hydrogen atom which is located in an antibonding position along a trigonal axis. For Group IV acceptors in GaAs or $Al_xGa_{1-x}As$, such as C_{As} or Si_{As}, a model has been proposed by Chevallier et al. [144] on the basis of LVM studies where the hydrogen atom is bonded directly to the acceptor in a bond centered (BC) site between the acceptor and one of its Ga or Al neighbors. These models are illustrated in Figure 2.1. The structure for the sulfur donor has not yet been definitely established [142], nor the structures for most deep defects.

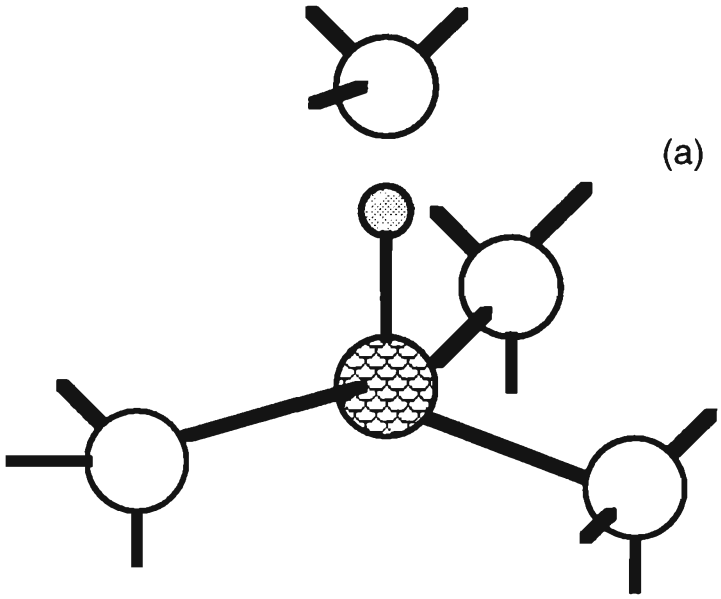

Passivation of Group IV Acceptor e.g. C

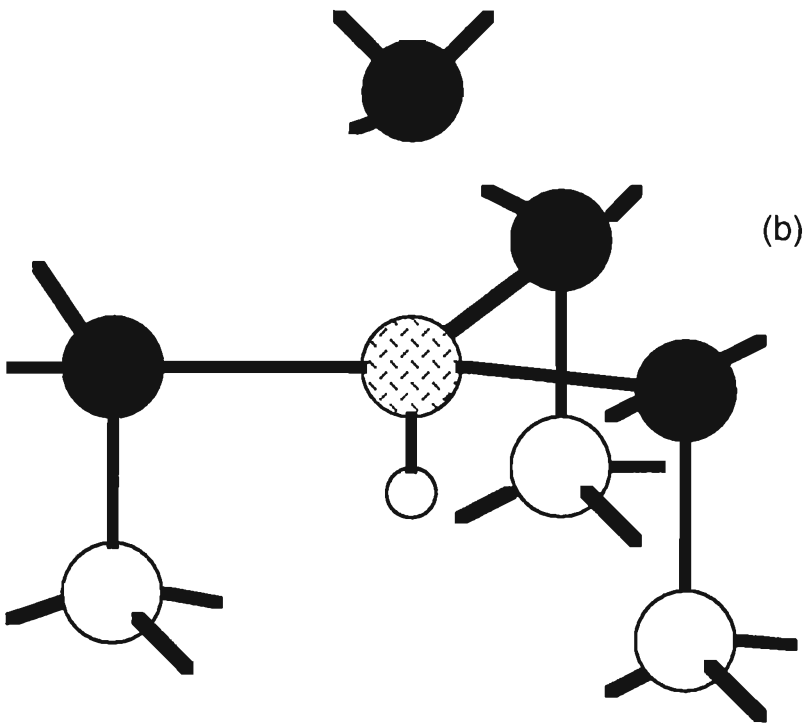

Passivation of Group IV Donor e.g. Si

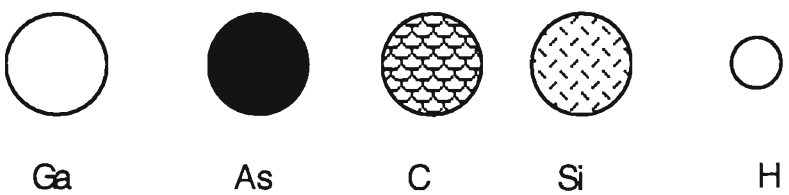

Figure 2.1 The mechanism of hydrogen passivation of Group IV impurities in GaAs has been well established. (a) shows the passivation of acceptors (b) of donors. After Chevallier, Clerjaud and Pajot [141].

CHAPTER 3

OPTICAL PROPERTIES OF BULK AND LAYERED GaAs AND $Al_xGa_{1-x}As$ SAMPLES AT THE BAND EDGE

3.1 THE DIELECTRIC FUNCTION, OPTICAL CONSTANTS AND REFLECTANCE

Chapter 3 introduces the theoretical background employed in planning and interpreting the experimental work reported in Chapters 5, 6 and 7. Photoluminescence (PL) (discussed in Section 3.4) was employed in all aspects of the present work, while the dielectric function and optical constants (Section 3.1) are of crucial importance for efficiently simulating the reflectance spectra reported in Chapter 5, as well as for the interpretation of those spectra. It is theoretically possible to avoid the use of the dielectric function in describing optical properties in favor of a full quantum mechanical approach, but as is discussed in Section 3.1.1 for quantum wells, this is not always desirable in practice.

3.1.1 The Dielectric Function and Green's Function Approaches to Optical Properties of Quantum Wells

There are two basic approaches to the optical properties of quantum wells. In one, the full quantum mechanical *material* approach, the Green's function for the coupled exciton-electromagnetic modes to be found in the quantum well structure is considered as the interband elementary excitations of the crystal. In this approach the main focus is on the quantum well structure and its degrees of freedom. (See D.S. Citrin [145] and references therein for theoretical papers using this approach.) In the other approach, the semiclassical *optical* approach, the main focus is on the electromagnetic field and the light transmitted and reflected by the structure, given an

incident electromagnetic wave. It involves the use of linear dispersion theory and is formulated in terms of transfer matrices. (See L.C. Andreani [146,147], Chen, Cingolani et al. [148], Tassone, Bassani and Andreani [149] and other references in Citrin [145].) The work is ultimately based on the classical theory formulated by Paul Karl Drude, W. Voight and Hendrik Antoon Lorentz in the nineteenth and early twentieth centuries ([150] *Chapter 7*).

Citrin [145,151] demonstrated the completely complementary nature of the two approaches. For example, transfer matrices which are formally the same arise in both approaches, but the interpretations differ. In the optical approach the transfer matrix gives the amplitude and phase of the transmitted and reflected electric field across the structure. In the Green's function approach, the transfer matrix gives the amplitudes and phases of the modes of the vacuum-field fluctuations on opposite sides of the quantum well structure. While the two approaches are equivalent, certain problems are more conveniently dealt with by using one rather than the other. Citrin [145] demonstrated that the material approach is better for spontaneous emission problems, while the optical approach is better for calculations of reflectivity and transmission spectra. It must be pointed out, however, that parameters must sometimes be used in the optical approach for quantities that arise naturally from the fully quantum mechanical approach [145,153]. It is the optical approach which forms the theoretical basis for the interpretation of the present work on shallow quantum well reflectivity reported in Chapter 5, and the Green's function material approach will not further considered.

3.1.2 Material Dispersion and the Relative Dielectric Function $\varepsilon_r(\omega)$

The relative dielectric function $\varepsilon_r(\omega)$ is characteristic of a particular medium. If the medium is nondispersive, the dielectric function becomes the dielectric constant, and the medium responds in the same way whatever the frequency of the incident light wave. In the classical optical model, the response of a dispersive medium is treated as arising from the way in which the molecules behave as classical simple harmonic oscillators driven by the incident electromagnetic wave. The oscillators have resonant frequencies associated with the binding forces in the molecules and the atoms they contain. As the frequency of the incident light wave is increased to approach a resonance from below, the oscillators absorb and re-emit radiation, which slows the propagation of light through the medium. As the resonance is passed and the frequency of the incident light wave moves far above it, there is no absorption of radiation. The refractive index is real and independent of frequency until the next resonance is approached, tending to 1 above the highest resonances. This is one reason why light pulses containing a range of frequencies spread out as they pass through an optical fiber.

3.1.2.1 The Purely Classical Model of $\varepsilon_r(\omega)$ Near a Resonance

With free charges (not relevant to the present reflectance work), it is possible to neglect restoring forces, but with other types of polarizability it is necessary to account for the forces that restore particles displaced by the applied field back to their unperturbed position. The derivation from the equations of motion of the particles in question is very well known, e.g. [150] *Chapter 7*, [153] *Chapter 13*. The complex dielectric function for oscillators of mass m is given by (in SI units)

$$\tilde{\varepsilon}_r(\omega) = \frac{\varepsilon(\omega)}{\varepsilon_o} = \varepsilon_b + \frac{Ne^2 / mV}{\varepsilon_o(\omega_o^2 - \omega^2 - i\Gamma\omega)} \tag{3.1}$$

where N is the number of oscillators, e is the charge assiociated with each oscillator, V is the volume containing the oscillators, ε_o is the permittivity of free space, Γ is the broadening and equal to the damping constant per unit mass from the equations of motion, ω_o is the resonant frequency, with ω_o^2 equal to the stiffness per unit mass from the equations of motion, and ε_b the background dielectric constant used to account for the effects of oscillators with distant resonant frequencies.

As a resonance is approached from a lower frequency, the real part of the refractive index will increase (normal dispersion), until it is within a distance Γ of the resonance frequency (the region of anomalous dispersion). The refractive index will then decrease from its maximum to its minimum value, and will then increase after that to a value determined by the background dielectric constant. The situation is illustrated in Figure 3.1. The resonant frequency is located between the maximum and the minimum values of the refractive index. Resonances too closely spaced to be comfortably accommodated using a background constant can be accomodated with a summation.

$$\tilde{\varepsilon}_r(\omega) = \varepsilon_b + \sum_j \frac{f_j e^2 / m\varepsilon_o)}{\omega_j^2 - \omega^2 - i\Gamma_j\omega} \tag{3.2}$$

where $f_j = N_j/V$ is the classical oscillator strength, here the number of oscillators per unit volume having the resonance with the characteristic frequency ω_j and the damping Γ_j.

3.1.2.2 The Semiclassical Model of $\varepsilon_r(\omega)$

In practice, purely classical calculations cannot accurately predict the correct resonant frequencies, even with the Lorentz field correction ([151] *Chapter 7)*, because quantum mechanical calculations are necessary to deal

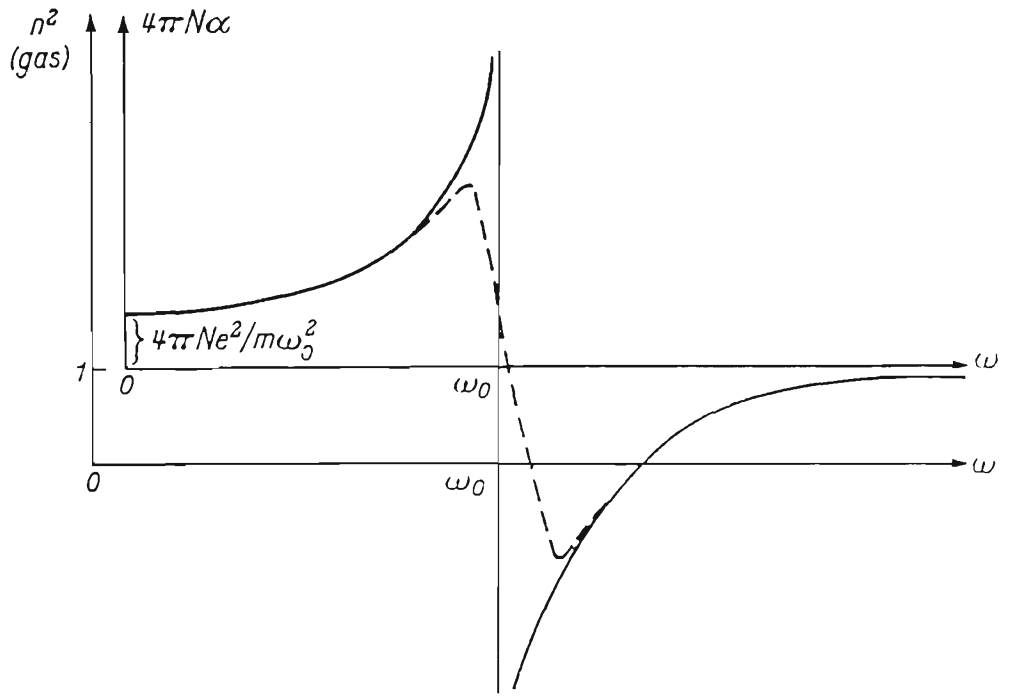

Figure 3.1 Material dispersion near a resonance. Reproduced from Born and Wolf [157] *Chapter 2.* $4\pi N\alpha = \varepsilon_r(\omega) - \varepsilon_b$ where $\varepsilon_r(\omega)$ is given by equation (3.1) in the present work. Here ε_b and V are assumed to equal 1. n is the refractive index and is discussed in Section 3.1.3. $\varepsilon_r(\omega)$ is only real and equal to n^2 when there is no damping, i.e. $\Gamma = 0$. This situation is illustrated by the solid curve. The dashed curve shows the effect on n^2 when damping is introduced. Note that the resonant frequency occurs midway between the maximum and the minimum of n^2.

with the band structure of solids, and with the magnitude of the absorptions, as discussed below. Quantum mechanics using perturbation theory leads to expressions similar to (3.1) and (3.2) where the resonant frequencies are those associated with transitions between quantum states, $\Gamma \propto 1/\tau$ where τ is the lifetime of the upper quantum state, and the oscillator strength is replaced by its quantum mechanical equivalent, which depends on the transition probability, the probability that a transition will occur between the two quantum states in question, as discussed below. It follows that the form of (3.2) can be retained with the numerator in the fraction replaced by a parameter A_j depending on the (quantum mechanical) oscillator strength and ω_o^2 and Γ having their quantum mechanical meanings. The quantum mechanical parameters must come from an accurate quantum mechanical theory of excitons [28,29,145, 154]. Quantum mechanical oscillator strength is discussed in Section 3.2.4 and transition linewidths in Section 3.3. The parameter A is usually defined in terms of energy so that

$$\tilde{\varepsilon}(E) = \varepsilon_b + \sum_j \frac{A_j}{E_j^2 - E^2 - i\Gamma_j E} \qquad (3.3)$$

The simple semiclassical approach using equation 3.3 is the one of those used in the present work (reported in Chapter 5) to model reflectance from shallow quantum wells. The energy position of an excitonic transition, the damping and the oscillator strength are used as parameters to be fitted, but compared with those arising from quantum mechanical calculations.

3.1.2.3 The A Parameter for quantum wells

It remains to relate the oscillator strength per unit area as defined in Andreani and Pasquerello [29] to the parameter A used in this work in the form given in equation (3.3) A is defined in Gil et al. [155] as $A_{\alpha\beta}=4\pi\Phi_{\alpha\beta}\hbar^2\omega^2_{\alpha\beta}$ with $4\pi\Phi_{\alpha\beta}$ the excitonic polarizability for the transition $\alpha\beta$. Andreani and Pasquerello [29] give the relationship between the parameter

A for a transition and their oscillator strength per unit area $f_{xy}{}^{A}$ as (in SI units)

$$A = \frac{e^2\hbar^2}{\varepsilon_o m_o}\frac{f_{xy}^{A}}{L} \tag{3.4}$$

with A in J^2 and L the width of the quantum well.

Andreani and Pasquerello [29] claim that the results of Gil et al. [155] are in good agreement with theirs when the conversion of parameters is made. Gil et al. discuss the case of the lowest ground state heavy and light hole excitons in a 79 Å GaAs quantum well in thick $Al_{0.32}Ga_{0.68}As$ barriers. They quote A as 12,000 $(meV)^2$ for the heavy hole and 5000 $(meV)^2$ for the light hole. Applying (3.4) gives an oscillator strength of 69×10^{-5} $Å^{-2}$ for the heavy hole exciton and 29×10^{-5} $Å^{-2}$ for the light hole exciton in almost perfect agreement with Figure 7 in Andreani and Pasquerello [29]. Zhang et al. [156] also use the parameter A as in Gil et al. [155], but derive an equivalent to (3.4) which is smaller by a factor of 2. This causes the oscillator strengths derived from a given A parameter to be a factor of 2 smaller than those to be derived from (3.4).

3.1.3 The Optical Constants

In this semiclassical approach excitonic behavior is accounted for in the dielectric function. The optical theory as a whole is based on Maxwell's equations and the material equations relating current density to the electric vector, electric displacement to the electric vector, and magnetic induction to the magnetic vector. Any standard text on Optics (e.g. [150,157]) gives the derivation of the complex refractive index ñ from Maxwell's equations and its relationship to the dielectric function .

$$\tilde{n}(\omega) = (\tilde{\varepsilon}_r(\omega))^{\frac{1}{2}}\mu_r^{\frac{1}{2}} \tag{3.5}$$

where μ_r is the relative magnetic permeability of the medium ($\mu_r = 1$ where the medium is nonmagnetic, as is the case with the materials studied in the present work.)

At any given frequency

$$\tilde{n} \equiv n + i\kappa \tag{3.6}$$

where n is called simply the refractive index and κ the extinction coefficient. The relationship between the absorption coefficient α and extinction coefficient at a particular frequency is given by

$$\alpha = 2(\omega / c)\kappa \tag{3.7}$$

where c is the velocity of light in vacuum

It is simple to derive n and κ at a particular frequency if the real and imaginary parts ε' and ε'' of the dielectric function are known.

$$\varepsilon'^2 + \varepsilon''^2 = n^4 - 2n^2\kappa^2 + \kappa^4 + 4n^2\kappa^2 = (n^2 + \kappa^2)^2 \tag{3.8}$$

$$n^2 = [(\varepsilon'^2 + \varepsilon''^2)^{1/2} + \varepsilon']/2 \qquad \kappa^2 = [(\varepsilon'^2 + \varepsilon''^2)^{1/2} - \varepsilon']/2 \tag{3.9}$$

If the lattice and electical properties of a material are known and incorporated in the dielectric function, it is thus possible to derive the optical constants n and κ, and is then possible to derive more observable optical properties, such as the reflectivity. Note that in some bulk crystals (but not the ones studied in the present work) the dielectric function and hence $\tilde{n}$ can be direction or polarization dependent due to anisotropy.

3.1.4 Reflectance at an Interface and the Optical Constants

The plane of incidence of light incident on an interface is specified by the wave vector of the incident ray and the normal to the interface. Where the electric vector **E** of the incident light is entirely perpendicular to the plane of incidence (and hence parallel to the interface) the light is polarized in the TE (Transverse Electric) mode. Any standard text on optics (e.g. [150,157])

gives the derivation from Maxwell's equations of the first Fresnel equation for the ratio of the perpendicular components of the electric vector of the reflected and incident rays. This ratio is defined as the amplitude reflection factor $\rho_\perp$.

$$\rho_\perp = \frac{n_2 \cos\theta_i - n_1 \cos\theta_t}{n_2 \cos\theta_i + n_1 \cos\theta_t} \qquad (3.10)$$

where the n_1 refers to the refractive index of the medium containing the incident and reflected wave and n_2 to the medium containing the transmitted wave. If the incident wave is normal to the interface then $\theta_i = \theta_t = 0$. If we then take the general case where n is complex.

$$\rho_\perp = \frac{\tilde{n}_2 - \tilde{n}_1}{\tilde{n}_2 + \tilde{n}_1} \qquad (3.11)$$

In the TM (Transverse Magnetic) polarization mode **E** is parallel to the plane of incidence, while the magnetic vector **H** is perpendicular to the plane of incidence and parallel to the interface. There are actually two modes under the TM rubric: L (Longitudinal) when **E** is parallel to the interface and Z when **E** is perpendicular to the interface [149]. The Z mode is obviously not excited when the direction of propagation is itself perpendicular to the interface, as is the case with normal incidence, since **E** must be perpendicular to the direction of propagation. Again it is possible to derive the second Fresnel equation for TM mode

$$\rho_\parallel = \frac{n_2 \cos\theta_t - n_1 \cos\theta_i}{n_2 \cos\theta_t + n_1 \cos\theta_i} \qquad (3.12)$$

which can again be generalized to the case where n is complex. In the case of normal incidence (assuming that ñ is not polarization dependent) $\rho_\parallel = \rho_\perp =$ (3.12). The relative intensity of reflected light in the TM and TE orientations is given by R where $R_\parallel = |\rho_\parallel|^2$ and $R_\perp = |\rho_\perp|^2$. If there is no polarization dependence in ñ, then at normal incidence $R_\perp = R_\parallel = R$, the reflectivity. In the special case where the first medium containing the incident and reflected waves is air or vacuum then $n_1 = 1$ and $k_1 = 0$, where n_1 and k_1 are the real and imaginary parts of $\tilde{n}_1$. Let $\tilde{n}_2 = n + ik$. Then in this case

$$R = \left|\frac{n-1+i\kappa}{n+1+i\kappa}\right|^2 = \frac{(n-1)^2+\kappa^2}{(n+1)^2+\kappa^2} \qquad (3.13)$$

3.1.5 The Optical Transfer Matrix

It is possible to derive a characteristic transfer matrix for a medium which will completely determine the propagation of a plane monochromatic wave through that medium, and by multiplying the transfer matrices associated with the individual layers, it is possible to derive a transfer matrix characteristic for an entire layered structure. For normal incidence it is only necessary to consider the TE case. For normal incidence in a nonmagnetic homogeneous material, Born and Wolf [157] *Chapter 1* use Maxwell's Equations to solve for the components of **M** the transfer matrix to yield

$$\mathbf{M} = \begin{bmatrix} \cos(\tilde{n}z2\pi/\lambda) & -i\sin(\tilde{n}z2\pi/\lambda)/\tilde{n} \\ -i\sin(\tilde{n}z2\pi/\lambda)\tilde{n} & \cos(\tilde{n}z2\pi/\lambda) \end{bmatrix} \qquad (3.14)$$

Born and Wolf also show that for a stack of dielectric layers it is possible to derive a characteristic matrix for the stack by multiplying the matrices for the individual layers

$$\mathbf{M}_{z_N} = \mathbf{M}_1(z_1)\mathbf{M}_2(z_2-z_1)\ldots\mathbf{M}_N(z_N-z_{N-1}) \qquad (3.15)$$

As is the case with the matrix for the single layer, the amplitudes of the electric and magnetic vectors of the incident, reflected and transmitted waves are all determined by this characteristic matrix.

Once the characteristic matrix of a structure is known it is possible to calculate the reflectivity. Assuming that **M** is of the type represented in (3.14) and has elements m_{ij} with light entering from free space or air, then the reflection coefficient ρ is given by

$$\rho = \frac{(m_{11}+m_{12}\tilde{n})-(m_{21}+m_{22}\tilde{n})}{(m_{11}+m_{12}\tilde{n})+(m_{21}+m_{22}\tilde{n})} \qquad (3.16)$$

where $\tilde{n}$ is the complex refractive index of the substrate below z_N.

$R = |\rho|^2$ = reflectivity.

3.1.6 Quantum Confinement in the Semi-classical model of QW reflectance

In a purely classical approach, the well excitons and free carriers are treated as particles in a box, spending all of their time in the well and none in the barriers. In fact, unless the potential difference between the well and the barrier is infinite, there is penetration of the exciton wavefunction into the surrounding barriers, implying that there is definite probability of the exciton or free carrier being found in the barrier rather than the well, provided that a suitable measurement has been made, e.g. [23,7] or any textbook on quantum mechanics.) The situation is illustrated in Figure 1.3(b) in Chapter 1. The penetration into the barrier increases as the potential difference between the well and the barrier decreases and is thus greatest for shallow quantum wells. Simmonds et al. [158] calculate that for the deepest electron and hole levels in their GaAs wells in $Al_xGa_{1-x}As$ barriers with x = 0.01 there was a 25% probability that the electron would be found in the barrier and a 14% chance for the hole. The exciton confinement would depend on that of the hole. For comparable wells with 4.5% Al in the barriers the probabilities fall to 5% and 3% respectively.

Reflectivity associated with exciton transitions including penetration into the barriers has been fully modelled by Andreani [146,147] and Citrin [145]. Humlíček et al. [159] claim that it can be successfully modelled in a semi-classical approach by simply increasing the effective width of the well or layer. Chen [160] calculated the theoretical reflectivity of excitons from a single GaAs quantum well enclosed in 30% Al AlGaAs barriers and found no significant differences appeared when ideal confinement was assumed, versus the the situation when penetration into the barriers was fully modelled.

In the present work, the effect of barrier penetration was considered by increasing the effective well width by an appropriate amount for a given exciton oscillator strength. Although there were some small phase effects there were no significant differences from assuming ideal confinement.

3.1.7 Phase Effects and the 'Dead Layer'

Because the electric and magnetic field vectors of propagating light oscillate with the frequency, this means that two parallel waves with the same frequency and the same initial phase angle will not necessarily remain in phase if they must cover different optical paths. Since the wavelength of light depends on the refractive index of the medium, what counts for optical path between points A and B is how far the light wave would have traveled in a vacuum during the time it actually takes to get from A to B in the medium. The optical path difference is defined

$$\Delta = \mathbf{k}_1 . \mathbf{r} - \mathbf{k}_2 . \mathbf{r} \qquad (3.17)$$

where $|\mathbf{k}_i| = n_i 2\pi / \lambda_o$, n_i is the refractive index in the medium

λ_o is the wavelength of the light in vacuum

Δ is the difference between the distances traversed by the two separate waves in reaching a particular point in units of wavelength in vacuum, corrected by the refractive indices of the media involved. It is possible to show that the resultant intensity from the two parallel waves is

$$I = I_1 + I_2 + 2\sqrt{I_1 I_2}\cos\Delta \qquad (3.18)$$

See Guenther [150] or any text on optics. It is obvious that if there are series of parallel interfaces separating separate media with light reflected and transmitted at each one that there will be constructive or destructive interference between them depending on the final term of (3.18). Thus the shape of a resonance in a reflectance spectrum depends dramatically on optical path difference. In a multi-quantum well the light reflected from a

given interface will generally be out of phase with the light reflected from the surface or from other interfaces in the structure. Thus each of the wells contributes a different lineshape to the total reflectivity profile, apart from the changes due to changes in light penetration depth. The center of the lineshape associated with a transition is dominated by the front quantum well, while complicated interference effects appear in the wings [161]. For this reason fitting the center of the lineshape is given priority, since the shape of the wings is very sensitive to the details of the layered structure. Figure 5.6 in Chapter 5 shows the dramatic effect of optical path differences on the reflectance spectra of single and multi-quantum well samples with GaAs wells and 2% Al in the $Al_xGa_{1-x}As$ barriers.

Phase effects at the surface can be simulated by adding an exciton free layer or 'dead layer' (without a resonance at the position of the GaAs bulk exciton) to GaAs, thus changing the relative phase of the light reflected directly from the surface with respect to the light reflected from the interface between the exciton free layer and the bulk GaAs [162]. By increasing the depth of the layer it is possible to show the effects of all possible phase differences, and for GaAs the cycle repeats itself every 1110 Å [163]. Simple measurements of peak height or the like without reference to phase would reveal little about the optical parameters.

The 'dead layer' is physically justified by the exclusion of excitons from an effective Bohr radius of the surface by image charges [162,164] and are heavily damped to a much greater depth due to nonradiative traps and electric fields at the surface as discussed in Section 2.1.3. Due to differences in defect concentrations the depth of the dead layer is highly sample dependent [162]. While the dead layer actually grades off in an exponential way [62] and varies with frequency [165], good reflectance fits can be

achieved by using a simple dead layer model. The dead layer required for matching theoretical and experimental spectra is always greater than the diameter of the exciton, although Fischbach et al. [166] were able to reduce the effective thickness of the dead layer in GaAs bulk samples to approach the GaAs exciton diameter by using high laser illumination on the surface in order to reduce the band bending while the reflectance spectrum was being measured.

3.1.8 Nonlocality and Polariton Effects in Reflectance

Polaritons are coupled mode excitations which classically can be considered to result from two oscillatory modes in a polar crystal having very similar frequencies and wavelengths. Far from the intersection point of the pure modes on a dispersion diagram, there is little admixture between the modes, but near it the oscillators, say the pure photon and pure exciton (with an intersection point near the fundamental absorption edge of the crystal), can no longer vibrate independently, but vibrate together in two different modes at two new frequencies, much like two mechanical harmonic oscillators connected by a spring. The new dispersion relationship, which can be calculated theoretically and has been verified experimentally [167], can be considered as relating to the polariton, an exciton/photon hybrid mode. Excitonic polariton effects can in practice be taken into account through the dielectric function, which can be modified in a phenomenological way to take account of damping through interaction of the exciton polariton with phonons, impurities and other defects.

In the bulk sample the excitonic polaritons are stationary states, which in a perfect infinite crystal would oscillate back and forth between photon-like and exciton-like properties forever. There is no true radiative decay, with what appears to be radiative decay of free excitons being due to

thermalization of the exciton resulting in escape from the crystal and conversion of the excitonic polariton to a photon. This makes the effective radiative lifetime in the bulk proportional to the crystal size [168]. There is radiative recombination of bound excitons. In the quasi-2D system there are two kinds of polariton modes which are separated by the photon dispersion. the surface modes which are analogous to the bulk excitons and the radiative modes. The surface polaritons are nonradiative because energy and momentum conservation forbid coupling to the incident light. They can only be excited by very specialized techniques, involving attenuated total reflection or a grating on a sample. The radiative modes are the ones observed in experiments such as the ones described here. The lack of translational invariance along the growth direction introduces a radiative decay channel for excitons with $k<k_o$, the wave vector of the incident light [169]. Experimental radiative lifetimes can be on the order of 100 times shorter in good quantum wells than in good bulk samples [170]. The solutions for the radiative modes are not stationary states, but mostly resonances of the Fano type, where there is coupling between an exciton and the continuum of a lower lying excitonic state [30].

The issue of local and nonlocal dielectric behavior is discussed in Hopfield and Thomas [164]. The semiclassical model discussed above is based upon the concept of local dielectric behavior. This implies that the dielectric polarization within a volume of radius r_o ($r_o<<l$) depends only on the electric field within the volume. This further implies that electromagnetic waves are the only significant energy transport mechanism. In real materials there often are other means of energy transport, such as transport by electrons or excitons and the dielectric function must be modified to deal with them. The term nonlocality is used for situations where the local approximation is not justified. Hopfield and Thomas show that one type of

nonlocality, spatial dispersion, can be dealt with in semiclassical terms by including coupling between the oscillators. They derive a new dielectric function that closely resembles (3.2) but contains an additional k^2 dependent term in the denominator. The solution results in two roots k_1 and k_2 that satisfy the equation. This means that for a wave of frequency ω incident on an interface there will be two transmitted waves of the same frequency and same direction, but wave vectors of different magnitude. In the exciton polariton context they can be considered to be polaritons on different branches of the dispersion curve, and hence possessing different wave vectors, but the same frequency. The separate wave vectors imply that each transmitted wave will experience a different refractive index. The interference of these two waves should produce effects on the optical transmission and reflectivity. Evangelisti, Fischbach and Frova [162] have shown that in bulk GaAs, spatial dispersion effects will be masked for linewidths greater than about 0.1 meV. For thin layers (several times the exciton radius) highly anisotropic spatial dispersion is seen with polariton waves propagating in the layer plane, but oscillating in the confinement direction [171,165]. None of the samples studied in the present work show evidence of spatial dispersion effects.

3.1.8.1 The Full Andreani Nonlocal Transfer Matrix for Quantum Well Reflectance

In quantum wells there are two sources of nonlocality (apart from the spatial dispersion discussed above) associated both with the layered structure of the sample and with the fact that the excitonic radius in the well is of the order of the well thickness. Spatial dispersion itself can be neglected for thin quantum wells because polariton propagation can only occur in the well plane, with the well width far narrower than the relevant wavelength of light. A nonlocal optical transfer matrix approach to deal with quantum

wells and layers was derived by Tredicucci et al. [171] (for thin films), the TE mode for quantum wells and thin films by Kosobukin [172], while a more complete approach including both TE and TM modes is to be found in Citrin [145] and Andreani [146,147]. Humlíček et al. [159] includes an effective dielectric constant based on a nonlocal treatment of a GaAs layer between two MQW structures.

The following equations enable the reflectivity of multi-quantum well structures to be fit using a full nonlocal approach, which should be valid even for very narrow linewidths. Andreani [146] derives the transfer matrix of a quantum well period in the TE and TM polarizations. Only the TE is necessary for work at normal incidence.

$$T^{TE} = \frac{1}{\Delta_T}\begin{pmatrix} \exp(ik_z L)(\Delta_T - i\Gamma_T) & -i\Gamma_T \exp(ik_z L_b) \\ i\Gamma_T \exp(-ik_z L_b) & \exp(-ik_z L)(\Delta_T + i\Gamma_T) \end{pmatrix} \qquad (3.19)$$

where $\Delta_T = \omega - \omega_{ex} - \Delta\omega_\alpha + i\gamma$

with ω the energy of the incident light, ω_{ex} the energy of the excitonic transition, $\Delta\omega_\alpha$ the radiative shift, which can be subsumed in the transition energy when it is entered as a parameter and γ is the energy linewidth due to all sources of scattering apart from the intrinsic linewidth (discussed in Section 3.3 on linewidth)

$k_z \simeq k_o$ the photon wavevector = $n\omega/c$ where n is the background refractive index and c is the speed of light in vacuum

L is the length of the MQW period

L_b is the width of the barrier within the period

Γ_T is the intrinsic radiative linewidth, which is directly proportional to the oscillator strength per unit area ($\Gamma_T = \Gamma_o$ discussed below for normal incidence)

The transfer matrix for the entire MQW can be derived by multiplying the transfer matrices for the individual periods, as explained above. The

coefficient of reflection for the multi-quantum well $r^s_{QW} = -T_{21}/T_{22}$, the ratio of the corresponding matrix elements. For the total structure [149]

$$R = \left|r^s_{tot}\right|^2 = \left|\frac{r^s_{12} + r^s_{QW}\, e^{i\phi}}{1 + r^s_{12} r^s_{QW}\, e^{i\phi}}\right|^2 \qquad (3.20)$$

where $r^s_{12} = (n-1)/(n+1)$ where n is the background refractive index and Φ is the phase given by $2k_oD$ with D the depth of barrier required to produce the given phase shift, as discussed in Section 3.2.7.

In the case of a single quantum well [149,168] (3.19) and (3.20) give the result

$$R(\omega) = \left(\frac{n-1}{n+1}\right)^2 - \frac{8n}{(n+1)^2} \times \frac{(\gamma+\Gamma_o)\cos(k_o\ell) + (\omega_o-\omega)\sin(k_o\ell)}{(\omega_o-\omega)^2 + (\gamma+\Gamma_o)^2} \qquad (3.21)$$

where the variables have the same meanings as in (3.19) and (3.20) except that ℓ=L+2D , with D the thickness of the top barrier, and Γ_o is the intrinsic radiative linewidth where $k_{||} = 0$. In SI units

$$\Gamma_o = \frac{he^2}{4\pi\varepsilon_o n m_o c} f^A_{cv} \qquad (3.22)$$

h is omitted where Γ_o is defined as a decay rate rather than an energy broadening. Where the local approximation is legitimate, an entire MQW structure may be fit as if it came from a single homogeneous layer, with the effective oscillator strengths found through a local fit used to determine the corresponding oscillator strength for a single quantum well by multiplying by the ratio of the quantum well width to the quantum well period [146], also Ivchenko et al. [173] where the LT splitting is used as a surrogate for the oscillator strength.

As will be shown in Chapter 5 (3.19) and (3.20) often deliver results equivalent to the local approach, but not where narrow transition linewidths are combined with large oscillator strengths. In the context of a quantum well, the local approach is formally justified when the transition linewidth is much greater than $2\Gamma_o/(k_oL)$ where Γ_o is the radiative decay rate for an

exciton with zero in-plane momentum, L is the width of the quantum well and $k_0 = n\omega_0/c$, the photon wavevector in the material. In the case of multi-quantum wells, L is replaced by the length of a well/barrier period. (Γ_0 is proportional to the oscillator strength and is of the order of 0.025 meV for a typical lowest energy quantum well excitonic transition [168]. Surveying the literature, most papers based on quantum well reflectance do ignore nonlocality, e.g. [155,161,163,174,175,176,177,178,179] and this is probably justified due to the relatively large transition linewidths in most work.

3.2 TRANSITION PROBABILITY, ABSORPTION AND QUANTUM MECHANICAL OSCILLATOR STRENGTH

3.2.1 Fermi's Golden Rule

The probability per unit time that an electron will make a transition between initial state $|i\rangle$ and final state $|f\rangle$ can be derived from time dependent perturbation theory and appears in the form of Fermi's Golden Rule [180]

$$W_{ab,em} = \frac{2\pi}{\hbar}\sum_{\lambda}\sum_{i,f}\left|\left\langle f\left|H^{ab,em}\right|i\right\rangle\right|^2 \delta\left(E_{f,\lambda} - E_{i,\lambda}\right) f(\varepsilon_i)[1 - f(\varepsilon_f)] \qquad (3.23)$$

where W is the total transition rate between atomic energy levels E_i and E_f with the energies in the delta function representing the total energies of the initial and final states including the energy of the radiation field; H is the interaction Hamiltonian = $-(e/mc)\mathbf{A}\cdot\mathbf{p}$ where $\mathbf{A}$ is the vector potential and $\mathbf{p}$ the momentum; ab and em refer to absorption and emission; $f(\varepsilon_i)$ is the probability that the initial state at energy ε_i is occupied and the final factor gives the probability that the final state is unoccupied, since transitions are always from an occupied to an unoccupied state

3.2.2 Band to Band Absorption

The absorption coefficient $\alpha(\omega)$ is defined such that

$$I = I_o \exp(-\alpha(\omega)x) \qquad (3.24)$$

where I is the intensity of light of frequency ω remaining after it has penetrated a distance x while I_o is the intensity at x=0

Strictly speaking for quantum wells and superlattices x is replaced by $\mathcal{L}$, the length over which the quantum well or superlattice bound state is well defined ([7] *Chapter 7*).

The absorption coefficient depends on the transition probability discussed in the previous section. The interaction Hamiltonian takes on different forms for the bulk and the quantum well case due to the wave functions involved. Under the electric dipole approximation in Bastard's approach ([7] *Chapter 7*) the interaction Hamiltonian in the quantum well case reduces to

$$H^{ab.em} = \frac{ieF}{2m_o\omega}\varepsilon \cdot \mathbf{p} \tag{3.25}$$

where F is the magnitude and ω the radial frequency of the electromagnetic wave involved in the absorption or emission; $\boldsymbol{\varepsilon} \cdot \mathbf{p}_{if}$ describes the interaction of an electromagnetic wave with polarization $\boldsymbol{\varepsilon}$ with an electron excited between states i and f

The band to band absorption coefficient can be defined for quantum wells as

$$\alpha(\omega) = A\sum_{i,f}\frac{1}{m_o}\left|\varepsilon \cdot \mathbf{p}_{if}\right|^2 \delta(\varepsilon_f - \varepsilon_i - \hbar\omega)\left[f(\varepsilon_i) - f(\varepsilon_f)\right] \tag{3.26}$$

where in SI units $A = \pi e^2/(n\varepsilon_o c m_o \Omega \omega)$ with n the refractive index and Ω the volume over which absorption takes place

The sum over $f(\varepsilon_i)$ - $f(\varepsilon_f)$ depends on the density of states as well as the Fermi-Dirac distribution so that in quantum wells the sum over $[f(\varepsilon_i)$ - $f(\varepsilon_f)]$ describes the 2-D density of states function between the initial and final states. For direct band to band transitions in the bulk it can be shown that (e.g. [17] *Chapter 2*) absorption is related to the band gap E_g

$$\alpha(\omega) \propto \frac{1}{\omega}\left(\hbar\omega - E_g\right)^{\frac{1}{2}} \tag{3.27}$$

In case of a rectangular type I quantum well (such as the ones discussed in this thesis) the transition between the ground state heavy hole and electron subbands is given by ([7] *Chapter 3*)

$$\alpha_{HH_1 \to E_1}(\omega) = \frac{e^2 E_p}{4\varepsilon_o nc\, m_o \omega \hbar^2 L} \mu^* \left| \left\langle \chi_1^{(h)} \middle| \chi_1^{(e)} \right\rangle \right|^2 Y\left[\hbar\omega - E_g - E_1 - HH_1\right] \qquad (3.28)$$

comparing (3.26) and (3.28)

$$\frac{1}{m_o} |\varepsilon \cdot \mathbf{p}_{if}|^2 = \frac{E_p}{4} \left| \left\langle \chi_1^{(h)} \middle| \chi_1^{(e)} \right\rangle \right|^2 \qquad (3.29)$$

where E_p is a Kane [13] matrix element $\approx$ 23 meV for members of the III-V family of semiconductors. The χ functions are the quantum well envelope functions discussed in Section 1.2.3 and $\langle \chi_1^{(h)} | \chi_1^{(e)} \rangle$ represents their overlap integral. (In superlattices $|\langle x_i^{(h)} | x_f^{(e)} \rangle|^2$ varies as 1 + cos qd where q is the superlattice wave vector and d the period.) L is $\mathcal{L}$ the length over which the bound state is well defined. μ^* is the reduced effective mass of the hole and the electron so that $(\mu^*)^{-1} = (m^*_e)^{-1} + (m^*_h)^{-1}$ (in III-V semiconductor heavy hole transitions $\mu^* \approx m^*_e$ because the hole mass is so much larger) Y is the step function associated with the staircase 2-D density of states and describing the onset of absorption at $E_g + E_1 + HH_1$. Note that the quantum well fundamental absorption edge is blueshifted above the bulk edge by $E_1 + HH_1$ as determined by the 2-D density of states function. It can easily be shown that when (3.28) is substituted into (3.24) with appropriate numerical values for III-V semiconductors for the various factors that the attenuation by passage through a single quantum well is only of the order of 0.6% ([7] *Chapter 7*).

Certain selection rules follow ([7] *Chapter 7*) from the overlap integral of the envelope functions and the dipole matrix element. The most important results are (i) that $E_n HH_m$ transitions are predicted to be three times as intense as those involving light hole subbands (twice as intense when valence band mixing is included in the calculation, as discussed below) (ii)

for light propagation in the layer plane the polarization e_z is forbidden for E_nHH_m transitions but not those involving light holes (iii) the in-plane wave vector is conserved in optical transitions (as is the superlattice wave vector q) (iv) for type I symmetrical quantum wells such as those discussed in this work the envelope function overlap integral $\langle x_n | x_m \rangle$ is only nonzero if n+m is even and thus the envelope functions are not of opposite parity with respect to the center of the well, with transitions much stronger when n=m. Note that a strong electric field can change the overlap integral and allow an otherwise forbidden transition to occur.

3.2.3 Excitonic Absorption

Bastard ([7] *Chapter 7*) shows that for quantum wells the excitonic absorption transitions (involving direct creation of excitons by resonant absorption) can be written in terms of the envelope functions and the hydrogenic exciton amplitude wave function $\beta(\mathbf{r})$ whose square expresses the probability of finding the hole and electron with total wave vector $\mathbf{K} \sim 0$ and separated by an in-plane position vector $\mathbf{r}$. The result for the E_1HH_1 transition (neglecting any valence subband mixing) is

$$\alpha(\omega)_{HH_1 \to E_1} = \frac{\pi e^2 E_p}{2ncm_o\omega\mathcal{L}} \left| \langle \chi_1^{(h)} | \chi_1^{(e)} \rangle \right|^2 \sum_v |\beta_v(0)|^2 \delta(\hbar\omega - E_v) \qquad (3.30)$$

where n is the refractive index for the well material and E_p is the Kane matrix element (~ 23 meV for most III-V materials) which is related to the momentum matrix element between the band edge Bloch functions, with the summation over the exciton ground and excited states, and E_v is the transition energy for a particular excitonic state

The excitonic absorption in a quantum well obeys the same polarization and selection rules as the band to band quantum well absorption. It follows that only excitons with wave vectors which put them very near to $\mathbf{K}=0$ are able to recombine radiatively. Since the $\beta(\mathbf{r})$ wave functions are radial, the exciton

eigenstates are labelled with radial quantum numbers n and only nS states can be optically created. $|\beta_\upsilon|0|^2$ represents the probability of an electron in state υ being separated from a hole by a zero in-plane position vector while having a total wave vector $\mathbf{K}\approx 0$. (Broadening due to interface roughness and other disorder always give rise to a finite momentum width near $\mathbf{K}=0$ where allowed transitions can occur.) Because of the enhancement of binding energies for excitons discussed in Section 1.2.4 excitonic transitions have a strongly enhanced absorption coefficient over a narrow frequency range.

For resonant excitonic absorption in the bulk it can be shown ([17] *Chapter* 2) that

$$\alpha'(\omega) = \alpha(\omega)\pi x e^{\pi x} / \sinh(\pi x)$$
$$x = \sqrt{R/(\hbar\omega - E_g)} \qquad (3.31)$$

where $\alpha'(\omega)$ is the bulk excitonic absorption; $\alpha(\omega)$ is the bulk band to band absorption; R is the effective Rydberg

It follows that for large energies the bulk and excitonic absorption coefficients converge and that for excitonic absorption the absorption coefficient no longer tends to zero close to the absorption edge at the top of the forbidden gap. Excitonic absorption in the bulk and in the quasi 2-D situation is illustrated in Figure 1.4 in Chapter 1.

3.2.4 Oscillator Strength

3.2.4.1 Short definitions of oscillator strength

For historical reasons and reasons of convenience in dealing with dielectric functions, the oscillator strength parameter (oscillator strength per unit volume for the bulk, and oscillator strength per unit area for quantum wells) is often used. It can be defined (e.g. [181]) for the quantum well case (in SI units) in terms of the integrated absorption $A_{n,m}$ of a transition

$$A_{n,m} = \int \alpha(E)dE = \frac{\pi e^2 \hbar}{2\varepsilon_o n m_o c} \frac{f_{xy}^A}{L} \qquad (3.32)$$

where $A_{n,m}$ is the integrated absorption for the transition indicated by n,m; n is the refractive index of the well material; L is the width of the quantum well; f_{xy}^A is the oscillator strength per unit area (f_{xy}^A/L is replaced by f_{osc}^V the oscillator strength per unit volume in the bulk case)

In Bastard's notation ([7] *Chapter 7*) the oscillator strength per unit area for the ground state heavy hole transition in a quantum well is given by

$$f_{xy}^A = \frac{E_p}{\hbar\omega} \left| \left\langle \chi_1^{(h)} \middle| \chi_1^{(e)} \right\rangle \right|^2 |\beta_{1s}|0||^2 \qquad (3.33)$$

Although the notation differs most definitions of oscillator strength quoted in published work (e.g. [156,182,183,184]) treat it as a product of factors related to the exciton transition energy, the overlap integral between the envelope functions of electrons and holes in the z direction, the value of the in plane wave function for $\rho = 0$ (with its square giving the probability that the electron and hole will be found at the same position) and the optical transition matrix element between the conduction and valence bands.

The oscillator strength for a transition in a real quantum well is actually an average function, because the excitons experience different environments due to the influence of different effective well widths and localization on defects in the same well [181,185]. Zhang et al. [156] derives an expression showing that the oscillator strength per unit area decreases with increasing temperature. The magnitude of the effect is too small to be experimentally observable in the present work.

3.2.4.2 Detailed calculation of oscillator strength

The calculation of the oscillator strength and binding energy of the exciton depends on the exciton model used. Winkler [154] has a discussion of these

models, which make use of envelope functions in the effective mass approximation (discussed in Section 1.2.3). The early models used a simple one band approach for both electrons and holes and neglected valence band mixing and subband coupling as in equation (3.30) above. An improvement came with models using a 4×4 Luttinger Hamiltonian for the valence band states and incorporating valence band mixing and coupling between excitons belonging to different subbands. The widely accepted model of Andreani and Pasquerello [28,29] belongs in this category, also including nonparabolicity of the conduction band and the difference in dielectric constants between well and barrier materials. Winkler claims that even greater accuracy can be obtained by using an 8×8 Hamiltonian including both the electron and hole subband states, although results for binding energy and oscillator strength are very close to those of Andreani and Pasquerello [28,29]. Winkler's model is also distinguished by the fact that it considers the envelope function problem in momentum rather than position space, so that the Schrödinger equation becomes a set of coupled integral equations which can be solved to arbitrary accuracy by means of a quadrature method. This automatically gives correct boundary conditions at interfaces, eliminates spurious solutions and is equivalent to the Green's function approach.

Andreani and Pasquerello [29] give a detailed expression for the theoretical quantum mechanical oscillator strength per unit area for excitons in quantum wells. The following equation automatically generates the correct selection rules observed in experiment. A similar expression is to be found in Winkler [154].

$$f_{xy}^{A} = \frac{2}{m_o E_g}\left|\sum_s \left\langle u_c \middle| \varepsilon \cdot \mathbf{p} \middle| u_v^s \right\rangle \times \sum_{jv} a_{ijv} \int \frac{d\mathbf{k}_{\parallel}}{(2\pi)^{3/2}} h_v(k_{\parallel}) \times e^{i(m-s)\alpha} I_{ij}^{s}(k_{\parallel})\right|^2 \qquad (3.34)$$

where m_o is the mass of the free electron

E_g is the transition energy

u_c and u^s_v are bulk Bloch functions for the conduction and valence bands at k=0, with s the spin index of the hole. ε is the polarization vector of the incident light and **p** the momentum operator. $<u_c|\varepsilon \cdot \mathbf{p}|u^s_v>$ are matrix elements between the bulk band-edge Bloch functions and an otherwise possible oscillator strength will disappear unless the corresponding matrix element is nonzero. It is this condition that causes states with $m = \pm 3/2$ (even light hole states) to have zero oscillator strength for light polarized along the growth direction [28].

The factors after the second summation sign represent the product of an expansion of the in-plane radial wave function over the various subbands of the exciton in k-space together with the overlap integral I^s_{ij} between envelope functions of conduction and valence subbands. The exponential represents a phase factor with m a quantum number representing the projection of the total angular momentum along the growth direction (taken as z) and s the spin index . The integral containing the exponential over α will only be nonzero if m=s, so at most one spin component, the one with zero orbital angular momentum, can be optically active [28].

The overlap integral is defined

$$I^s_{ij}(k_\parallel) = \int dz\, c_i(z)\, v^s_{jk_\parallel}(z) \qquad (3.35)$$

This overlap integral condition assigns zero oscillator strength to transitions where the conduction and valence states have opposite parities. It is this condition which forbids the $E_{12h}(1s)$ exciton. Forbidden transitions can become allowed in real samples where there is an electric field or other asymmetry along the z direction.

Although expressions for the oscillator strength per unit area may appear similar, it is clear that different authors are calculating it in different ways.

with the source of discrepancy possibly the optical transition matrix element M or $\langle u_c|\varepsilon \cdot \mathbf{p}|u^s_v\rangle$, depending on exactly which basis states are considered [186]. Thus, although Zhang et al. [156] have the standard relationship between the reflectance parameter A discussed below and the integrated absorption also seen in Andreani and Pasquerello [29], they define the oscillator strength in such a way that the oscillator strength calculated from a given parameter A is a factor of 2 smaller than it would be if calculated by the method given in Andreani and Pasquerello. There are also discrepancies in the literature on the relationship between integrated absorption and oscillator strength per unit area, with Masselink et al. [182] using a formula that reduces the oscillator strength calculated on the basis of an integrated absorption by a factor of 2 compared with that derived by other authors such as Masumoto et al. [181] and Grousson et al. [187]. When Andreani and Pasquerello [29] compare their theoretical oscillator strengths with those in Masselink et al., they double the published values to compensate for the discrepancy in the two definitions of oscillator strength. The present work relies for comparison on the Andreani and Pasquerello definition of oscillator strength per unit area which corresponds in fact to the standard definition derived from a semiclassical dielectric function.

Winkler [154] claims close agreement between his calculations and those of Andreani and Pasquerello [28,29] for exciton binding energies and oscillator strengths per unit area. Both the oscillator strengths and the binding energies depend on the electron-hole wavefunction overlap reflecting the confinement of the excitons, so both tend to be larger for small well widths and high barriers, with the differences due to barrier height becoming relatively less significant for wider wells, especially for the oscillator strengths. Oscillator strength is predicted to fall off again for very narrow wells (less than 10Å) due to the smaller overlap as wavefunctions penetrate

into the barriers. For wells much wider than 10Å, the wavefunction overlap does not change much with further widening so that the reduction in oscillator strength also becomes slower [156]. Heller et al. [184] do predict a reduction in oscillator strength for shallow quantum wells on the basis of variational calculations. For very wide wells (greater than $3a_B$ where a_B is the effective Bohr radius of the exciton) the oscillator strength is predicted to go through a minimum and start increasing again as it passes into a regime where the binding energy is greater than the quantization energy. In this regime the oscillator strength depends directly on the film thickness [188]. An accurate model of excitonic effects also makes a difference to oscillator strength ratios. When the effect of valence band mixing is properly included, the ratio of oscillator strengths between heavy and light hole excitons becomes close to 2 rather than 3 as previously reported [29].

In determining oscillator strengths, it is necessary to be aware that it is not possible to assign an oscillator strength belonging to an excitonic resonance to a single electron-hole subband pair. Because of Coulomb mixing, exciton states are always linear combinations of different electron-hole subband pairs, especially in wider quantum wells where the subbands are closer together. Winkler [154] was able to separately calculate the contribution to the oscillator strengths of the peaks in a quantum well absorption spectrum of the different hole subbands, and found that the HH1 subband strongly contributes to the oscillator strength of the higher lying peaks, even where they are assigned to other subbands.

D.S. Citrin [189] disputes the applicability of equation (3.32) for transitions with very narrow linewidths where the intrinsic radiative broadening Γ_0 and Γ, the broadening from other sources, are of comparable magnitude. In this case he shows that the perturbative approximation based on Fermi's Golden

Rule starts to break down and the area under the absorption peak depends explicitly on Γ and not the oscillator strength. He predicts that a signature of this effect will be an anomalously small absorption by the lowest-lying heavy hole exciton peak compared with the features due to higher-lying levels where Γ is larger and the perturbative approach applies well.

In some of the literature, as in Ivchenko et al. [173,178,179], the longitudinal-transverse splitting ΔE_{LT}, the long range part of the electron-hole exchange interaction, is used as a surrogate for the oscillator strength. This is valid for the bulk and for superlattices, where ΔE_{LT} is proportional to the oscillator strength, but not for isolated quantum wells where it vanishes for $\mathbf{k}=0$. Fits of reflectivity data for quantum wells do not give the real longitudinal-transverse splitting, but simply a parameter related to the oscillator strength [30].

3.3 TRANSITION LINEWIDTH

The broadening or linewidth of an exciton in a quantum well can be discussed in terms of two components, the Lorentzian or homogeneous and the Gaussian or inhomogeneous broadening, with the names reflecting the mathematical functions needed for modelling an excitonic resonance in absorption where one type of broadening dominates.

3.3.1 Inhomogeneous or Gaussian Broadening

The damping constants γ or Γ in the dielectric function and transfer matrix equations discussed in Section 3.1 relate to the homogeneous broadening. Excitons in quantum wells have finite phase coherent lifetimes in a particular k state due to scattering from phonons, other excitons and free carriers, interface fluctuations and neutral and ionized impurities and defects [190]. Γ is inversely proportional to this lifetime, and increases

with temperature due to the greater population of phonons as the temperature is increased. This type of broadening can be accounted for in the Lorentzian framework discussed above. The homogeneous broadening is somewhat greater in a real well than in an ideal one, largely due to the impurity and defect related scattering, including scattering off interface roughness.

Inhomogeneous broadening is only to be found in real wells. It is caused by statistical fluctuations in potential at interfaces due to well width fluctuations on a scale less than the exciton diameter [191] as well as alloy broadening. Because there is a normal distribution of such fluctuations, the inhomogeneous broadening must be accommodated within a Gaussian framework. It is not temperature dependent [192]. Chand and Chu [77] were able to observe the fluctuations directly in the form of waviness in interfaces observed in TEM (Transmission Electron Microscopy). They noted that in GaAs on $Al_xGa_{1-x}As$ interfaces the amount of waviness tended to increase as x got larger, although the amount of waviness also depended on the purity of the Aluminium source. Roughness is greater when the interface has a high concentration of defects and impurities and when the Al content of the barrier is high, as discussed in Section 2.1.3.

The inhomogeneous broadening may be modelled by convolving the Lorentzian dielectric function (3.3) with an appropriate Gaussian [193]

$$f_G = \frac{1}{\sqrt{2\pi}\Gamma_G} e^{-[E_0-\langle E_0\rangle]^2/2\Gamma_G^2} \qquad (3.36)$$

where f_G is a Gaussian function with the expectation value of the transition energy as the mean and the Gaussian broadening Γ_G as the standard deviation. Note that the HWHM of a Gaussian peak is 1.18 standard deviations.

Humlíček et al. [193] derive the convolution in the form

$$\varepsilon_{LG}(E) \approx \varepsilon_{\infty} + \frac{\sqrt{\pi}F}{2E_o\Gamma_G}\left[w\left(\frac{E-\langle E_o\rangle}{\Gamma_G}+i\frac{\Gamma_L}{2\Gamma_G}\right)-w\left(\frac{E+\langle E_o\rangle}{\Gamma_G}+i\frac{\Gamma_L}{2\Gamma_G}\right)\right] \quad (3.37)$$

where Γ_L is Γ in (3.3) with the subscript to distinguish it from the Gaussian broadening, F is a parameter proportional to the oscillator strength and w(z) is the complex probability function

$$w(z) = \frac{i}{\pi}\int_{-\infty}^{\infty}\frac{e^{-t^2}}{z-t}\,dt \quad (3.38)$$

where z is a complex number with a positive imaginary part

In Chapter 5 it will be shown that the reflectance of the shallow quantum wells with the lowest potential barriers can be adequately simulated without any assumption of Gaussian broadening, but that an improved fit for one of the samples can be achieved through modelling with equations (3.37) and (3.38).

3.3.1.1 Excitons Localised on Well Width Fluctuations

Excitons can be scattered and migrate between regions of different effective well widths and different average effective well widths. At low temperature it is much easier for excitons to lose energy than to gain it, so they can end up trapped in the wider regions of the well and at interface defects of one kind or another, and in fact the majority of the excitons in the quantum well can end up trapped in this way. The localized excitons are very much less vulnerable to scattering and decay processes due to their smaller extent and relative immobility, although it is possible for them to transfer between sites through tunneling and phonon assisted transfer [194,195]. Relatively weak impurity related photoluminescence in quantum wells as opposed to bulk is partly related to the fact that excitons tend to be quickly localized on interface fluctuations and rendered unable to easily migrate to donor or acceptor impurities [196]. Free carriers can also be separately localized on

interface fluctuations and then form excitons when they are delocalized later [197,198].

All else being equal, the effect of localized excitons tends to be greater in narrower quantum wells, because the excitons "spend more time" near the interfaces and because energy differences resulting from interface fluctuations are greater. The density of localized excitons tends to be very low in good quality wide quantum wells, especially ones wider than 150Å [183,199,200,201]. Because of local minima, mobile and localized states are to be found at all energies across the exciton resonance. This is supported by time resolved and resonant excitation [202,203], four wave mixing [191] and resonant combined with nonresonant excitation [204]. Raman scattering and degenerate four wave mixing [190,205], and resonant and time delayed PL [202] show that homogeneous linewidth increases as the energy is raised across the inhomogeneous linewidth, resulting in a mobility edge where a formerly localized exciton acquires enough energy to become delocalized and scatter. (See also Hegarty et al. [206,207], Minami et al. [208] and references in the review paper of Miller and Kleinman [31].

3.3.1.2 The Stokes Shift

An important parameter related to localization and inhomogeneous broadening is the Stokes shift. This is the energy difference between the peak in the PLE (Photoluminescence Excitation) or absorption spectrum corresponding to a given excitonic resonance with the peak in the corresponding PL spectrum. The Stokes shift was first attributed to excitons relaxing into lower energy localized states at interface fluctuations and then radiatively recombining there [196,209,210]. This mechanism implies a correlation between low inhomogeneous broadening and a low Stokes shift. It was later recognized that migration to wider islands on a scale larger than

an exciton diameter also play a role, even though the excitons do not count as delocalized in terms of dephasing mechanisms [211]. On the basis of theoretical considerations, Humlíc̆ek et al. [193] suggested that in good quantum well structures a Stokes shift can appear as a consequence of the thermal population of an inhomogeneously broadened exciton band, so that there is no need to postulate interface trapping. This was confirmed by Gurioli et al. [212].

3.3.2 The Lorentzian or Homogeneous Broadening Γ_h

Homogeneous broadening is primarily caused by various types of scattering which can change the direction or magnitude of the exciton's momentum, cause it to gain or lose energy, or even cause it to ionize and disappear, as in the case of a collision with a longitudinal optical phonon. Homogeneous broadening always also includes a small contribution Γ_o related to the lifetime of the upper quantum state involved in the transition, the time required for the distribution function of electrons and holes to be re-established after the transition [195]. The inverse of the homogeneous decay rate is known as the dephasing time.

Following e.g. Srinivas et al. [183,213,214], the homogeneous broadening can be divided into several components

$$\Gamma_h = \Gamma_I + \gamma T + \frac{\Gamma_{LO}}{\exp(\hbar\omega_{LO} / k_B T)} + \Gamma_{spin} + \Gamma_{MB} + \Gamma_o \qquad (3.39)$$

The first term refers to homogeneous broadening due to scattering of excitons off impurities in the quantum well. Scattering can occur off neutral [215] and especially ionized impurities [216,217] and excitons bound to such impurities. This term can also subsume homogeneous broadening due to scattering off interface fluctuations [151,218]. Note that spatial inhomogeneities within a quantum well contribute to Lorentzian as well as Gaussian broadening [151]. The fourth term refers to spin-flip scattering

[213] and is on the order of 0.025 meV. Γ_{MB} refers to many body effects: exciton-exciton and exciton-free carrier scattering [219,220,221]. Since the present samples are high quality and undoped, all of these sources of broadening are assumed in the present work on reflectance from shallow quantum wells reported in Chapter 5 to be either insignificant or not showing temperature dependence. These sources of broadening are, however, partly responsible for the extrapolated zero temperature broadening seen in Figure 5.14. The other sources of broadening are of more importance and are discussed separately. Higher excitonic states might also need to have a term included to cover broadening due to Fano type resonances. Fano broadening occurs when a discrete excitonic state has an energy overlap with continuum states for a lower index exciton. Extremely rapid scattering can result [222].

3.3.2.2 Acoustic Phonon Scattering

γT, the second term in (3.39), refers to acoustic phonon scattering. Lee, Koteles and Vassell [216] show that this term is a sum of separate terms reflecting scattering from piezoelectric and deformation potential mechanisms, both of which are directly proportional to the temperature. Lee, Koteles and Vassell derive the expressions for both types of acoustic phonon scattering and show that both are directly proportional to the temperature. Both expressions have a complicated dependence on the masses of the exciton involved and the hole and electron that make it up. A strong mass dependence is also seen in the derivation of Takagahara [223,224]. See also Oberhauser et al. [218] and references therein for further theoretical calculations.

There is no disagreement about acoustic phonon broadening being directly proportional to temperature, at least above 5K, but there is disagreement

about whether the mass dependence should result in γ being smaller for light hole excitons than it is for heavy hole ones. Lee, Koteles and Vassell predict an approximately 20% smaller temperature coefficient γ due to this sort of scattering for light hole than for heavy hole excitons in their calculation for a typical quantum well, which was apparently supported by experiment. Takagahara [225] suggests that the dominant effect should be opposite to this because phonons can mediate the transfer from the light to the heavy hole subband.

3.3.2.3 Longitudinal Optical Phonon Broadening

The third term in (3.39) allows for the contribution of longitudinal optical-phonon scattering, which begins to be significant above 80K. Lee, Koteles and Vassell [216] also determine the transition rate from which Γ_{LO} in equation (3.39) is derived. There is a dependence on the hole mass of the exciton and their calculations for excitons in typical deep quantum wells show the LO phonon broadening to be nearly 50% less for a light hole exciton than for a heavy hole exciton. LO phonon broadening is not significant below about 80K. A full derivation of the linewidth due to optical phonon broadening occurs in Rudin and Reinecke [226]. They include both bulk and interface modes of the optical phonon and show that the linewidth coefficient Γ_{LO} is a function of electron and hole mass together with well width, reaching a maximum in narrow wells of less than 50Å and declining after that. They claim good agreement with published experimental results for Γ_{LO} for GaAs/$Ga_xAl_{1-x}As$ systems, which range between 5.5 and 12 meV.

3.3.2.4 The Intrinsic Radiative Linewidth

The intrinsic radiative linewidth (Γ_o, the last term of (3.39)) was first calculated for quantum wells by Eiichi Hanamura [227]. His basic approach was adopted in Andreani, Tassone and Bassani [168]. D.S. Citrin [151] has

since verified the calculation of Andreani, Tassone and Bassani by showing that a full Green's function calculation leads to the same results in the case of wide wells with a low density of localized states. Where the populated states are primarily bound by interface fluctuations a model characterized by a finite coherence area such as that of Eccleston et al. [228] better approximates the Green's function results. The Andreani, Tassone and Bassani approach is clearly justified for very clean, wide shallow quantum wells.

Andreani, Tassone and Bassani [168] use Fermi's Golden Rule and sum the elementary oscillator strength in a volume limited by the wavelength [229] to derive the intrinsic radiative decay rate at 0K of the heavy hole exciton as (in SI units using formulation in Srinivas [183]):

$$\tau_q^{-1} = \frac{e^2}{4\pi\varepsilon_o} f_{xy}^A \frac{\pi}{nm_o c} \times \begin{cases} k_o / (k_o^2 - q^2)^{1/2}, T \bmod e \\ (k_o^2 - q^2)^{1/2} / k_o, L \bmod e \\ 0, \quad |q| > k_o \end{cases} \qquad (3.40)$$

where q is the exciton in-plane momentum, $k_o \equiv n\omega/c$ the photon wave vector in the semiconductor, and n is the refractive index in the well material, and f_{xy}^A is the oscillator strength per unit area discussed in Section 3.2. If the wave vector is taken along the x axis in the xy plane then the L, T and Z modes are the states polarized along the x, y and z directions. The Z mode does not exist for the ground-state heavy hole exciton. It does for the light hole, but not at normal incidence.

The intrinsic linewidth is related to the exciton lifetime or decay time by the energy uncertainty principle. Andreani, Tassone and Bassani [168] calculate τ_o, the decay time given by (3.40) for zero in-plane momentum, as 25 ps for a ground state heavy hole exciton in a 100Å $GaAs/Al_xGa_{1-x}As$ quantum well with an oscillator strength of 50 x 10^{-5}Å^{-2}. This decay time would actually be halved if only the optically active state were considered [151], so that

Deveaud et al. [219] were able to measure τ_o in a very good single quantum well as 10 ± 4 ps. If $\Gamma_o = \hbar / \tau_o$, with scattering and other intrinsic processes neglected, then the intrinsic radiative linewidth for $k_{||} = 0$ excitons is 25μeV, using the 25 ps value for τ_o.

3.3.2.5 Temperature Effects on the Radiative Lifetime

The homogeneous linewidth is actually always much greater than $\hbar / \tau_o$ and the dephasing time smaller than τ_o because the decay rates calculated in the previous section assume that the free excitons are (1) quantum mechanically spatially coherent over the entire well, (2) temporally coherent on time scales giving energy spreads small compared with the energy range allowed for radiative polaritons and (3) with scattering of excitons sufficiently rapid so that the exciton population remains thermal while radiative decay is taking place [151]. In fact as mentioned above there is scattering not only among the excitons themselves, but with phonons, free carriers, impurities and interface fluctuations. Assumption (3) is only justified for T > 5K [168]. At low temperature optical phonons can be neglected and thermalization of excitons is caused by inelastic scattering events with acoustic phonons. When T >> 1K only a small fraction of the excitons have $k_{||} < k_o$, and have a radiative decay channel open to them, as discussed in Section 3.2.8. Andreani, Tassone and Bassani [168] derive an expression for the radiative decay time below 80K where optical phonon broadening becomes significant by averaging over (3.40) over the Boltzmann distribution

$$\tau(T) = \frac{3M k_B T}{\hbar^2 k_o^2} \tau_o \qquad (3.41)$$

where M is the mass of the exciton and other factors as defined above. For a heavy hole exciton in a 100Å $GaAs/Al_{0.4}Ga_{0.6}As$ quantum well $\tau(T) = 34T$ ps. This is in agreement with experimental results using resonant excitation [229,230].

3.4 PHOTOLUMINESCENCE

3.4.1 Thermalisation and Formation of Excitons After Absorption

Spontaneous emission at a particular frequency is proportional to the transition probability at that frequency given in equation (3.23). Because the emission process is symmetrical to absorption all of the same selection rules are obeyed. ([7] *Chapter 7*) Because transition times for direct band to band recombination are longer than relaxation times, most photoluminescence (PL) is comprised of light emitted during recombination from lower energy states.

Clérot et al. [6] elucidated the details of the relaxation process with their experiments on coupled quantum wells. Because transitions are vertical in direct semiconductors, most free carriers excited by the absorption of incident light (unless the excitation is resonant) will initially be hot, with high k values in the conduction band. The processes involving loss of energy to LO phonons and formation of excitons occur far more rapidly than radiative recombination. The fastest process is emission of a LO phonon, which occurs in 200 fs. The result is that the hot electrons and holes rapidly lose energy (with some forming into excitons, as discussed below) and then thermalize down through further interactions with phonons and collisions with excitons and free carriers until they reach their respective band edges where they form a Fermi gas in quasi-equilibrium. This quasi-equilibrium can be characterized by quasi-Fermi levels and an equilibrium temperature [231]. Photoluminescence may occur as a result of recombination from the band edges.

If there are lower energy defect or impurity states available excitons and free carriers will thermalize down to them and recombine there. Because of

thermalization PL spectra are often dominated by impurity related recombination, even though the associated densities of states are often smaller then those in the conduction and valence band by several orders of magnitude ([7] *Chapter 7*). Frequently most recombination is nonradiative due to capture of free carriers by deep defects as discussed in Section 2.1.1.2. Direct band to band recombination of free carriers is negligible compared to excitonic recombination below 50K [232] and of less important than excitonic processes below about 115K [233].

Exciton formation time in GaAs quantum wells is on the order of 20 ps [6,234,235]. At low temperature in high quality material most radiative recombination involves excitons. As discussed above, excitons cannot radiatively recombine unless their center of mass wave vector is within a homogeneous linewidth of $\mathbf{K} = 0$, but the excitons are likely to be hot at the time of formation. Once the excitons or free carriers have reduced their energy to below that of an LO phonon, on the order of 36 meV, they can only lose energy by emission of acoustic phonons and collisions, so that it requires 100-200 ps to reach the band edges. Once there, the effective radiative lifetime depends on the transition probability as discussed above, as well as on the temperature. A higher temperature means more scattering of the quasi-equilibrium free carriers into higher $\mathbf{k}$ nonradiative states and more scattering and dissociation of excitons and thus longer radiative lifetimes [235]. For localised excitons, the effective lifetime also depends on the coherence length of the exciton ([3] *Chapter 16*).

3.4.2 Radiative and Nonradiative Lifetimes and Quantum Efficiency

Recombination channels can be characterized by a recombination rate for that channel averaged over the occupation of all states. The sum of the rates

of all the radiative recombination channels is the radiative recombination rate, whose inverse is the radiative lifetime τ_R. There is also a total nonradiative recombination rate and lifetime τ_{NR}. The quantum efficiency is defined

$$\eta = \frac{\tau_R^{-1}}{\tau_R^{-1} + \tau_{NR}^{-1}} \tag{3.42}$$

The nonradiative recombination rate is the sum of the bulk rate and the surface rate given by the surface or interface recombination velocity mentioned in Section 2.1.3. For the bulk rate, e.g. [113]

$$\frac{1}{\tau_{NR\,(bulk)}} = \sum_i N_{ti}\sigma_i v_t \tag{3.43}$$

where N_{ti} is the density of traps of species i

σ_i is the capture cross section of traps of species i at the given temperature

v_t is the minority carrier thermal velocity

Since a fully occupied trap cannot capture more particles it is possible to saturate the traps if the excitation intensity is high enough.

3.4.3 Important Types of Recombination in Photoluminescence

Energies at which the following processes occur in 4K undoped GaAs are tabulated in Pavesi [236].

(a) Bound Exciton (BE) Recombination A defect or impurity attracts and binds a free carrier which then attracts and binds a free carrier of the opposite sign forming a bound exciton. The exciton collapses and recombines in the normal way giving off a photon whose energy is reduced below that of the free exciton (discussed in Section 1.2.4) by the binding energy between the exciton and the impurity or defect. The bound exciton lifetime is of the order of 1 ns, with a capture time less than 1 ns [237]. D°X represents an

exciton bound to a neutral donor and A°X an exciton bound to a neutral acceptor. D^+X represents an exciton bound to an ionized donor. There is no evidence that excitons bind to ionized acceptors in most semi-conductors, a combination that is theoretically predicted to be unstable [180]. The special case of excitons bound to 'KP' and 'g-line' defects which is important for the samples discussed in Chapter 6 is treated below in Section 3.4.5.

(b) Free to Bound (FB) Processes In the eA° process a conduction band electron radiatively recombines with a neutral acceptor. D°h is the recombination of a valence band hole with a neutral donor. For eA° Eagles [238] theoretically calculated the lineshape

$$S(\omega) \propto y^{1/2} \exp(-y)$$

$$y = \frac{\hbar\omega - E_g + E_I}{k_B T} \qquad (3.44)$$

where E_I is the energy separation of the acceptor level and the valence band edge

It follows from (3.44) that linefitting can enable the electron equilibrium temperature to be calculated.

(c) Donor Acceptor Pair (DAP) Processes [180,239] Where there is overlap of a donor and acceptor effective Bohr radius it is possible for an electron which is weakly bound to a neutral donor to recombine with an acceptor hole. The result of DAP processes is a band in the PL spectrum because the characteristic energy of the photon emitted depends on the pair separation (Coulomb energy) as well as the binding energy of the acceptor and donor. The band narrows and its peak shifts to higher energies (typically about 1 meV per excitation decade in GaAs) as the laser excitation is increased and the more distant pairs with longer recombination times saturate. Heavier counterdoping also increases the peak energy because there are then more

close pairs. In GaAs, emission energies of the sharp isolated lines expected where pairs are close all lie above the band gap and cannot be seen, with the DAP band observed in PL being due to more distant pairs [180,239]. The energies of the excitation peaks are given by [180]

$$h\nu = E_G - (E_A + E_D) + \frac{e}{4\pi\varepsilon r} \qquad (3.45)$$

where hυ is the transition energy

E_G is the bandgap

E_A and E_D are the acceptor and donor binding energies

r the separation of the donor acceptor pair excited

3.4.4 PL Replica Lines

In a good quality spectrum or under selective excitation phonon replicas of lines may also be seen, as well as two-hole and two-electron replicas of exciton lines. Two-hole (two-electron) replicas occur when an acceptor (donor) bound exciton recombines leaving the acceptor (donor) in a low-lying excited state, with the energy separation of the transition from the principal bound exciton line being characteristic of the impurity [240]. Phonon replicas occur when a recombination occurs with part of the energy given off as a phonon and part as a lower energy photon. Because of the lower probability of this happening the replica peak will be relatively small and separated from the main line in a PL spectrum by the phonon energy.

3.4.5 Photoluminescence Involving the KP Defect and the g-line Defect in MBE GaAs Samples

The 'KP' and 'g-line' defects are of particular interest in the present work because it involves a class of bulk samples (discussed in Chapter 6) in which they are strongly present. They are manifested in the 4K photoluminescence spectra of some (but not all) MBE grown GaAs bulk samples as a spectrum of up to 60 separate lines from 1.50 up to 1.511 eV, with

the related broader d_n bands running from between 1.47 and 1.49 eV [241]. PL associated with the KP and g-line defects can be seen in Figure 6.1 in Chapter 6, as well as many other spectra illustrated in that chapter. These lines were first reported by Künzel and Ploog [242] in *p*-type nominally undoped MBE samples grown with an As4 arsenic source. Rao et al. [243] reported them as existing but strongly reduced in n-type samples or samples grown at higher temperatures. Briones and Collins [244] and Skromme et al. [245] found that the relative intensities of the KP lines and the presence or absence of the d_n bands depends strongly of the growth conditions. Some workers use the term KP lines loosely to include the usually strong line at 1.511 eV which is known as the g-line, but because of differences in behavior it is better to treat the g-line separately.

Briones and Collins [244] were the first to suggest that the KP lines were due to excitons bound to defect complex acceptors and that the d_n lines were FB and DAP transitions involving the same defect complex acceptors whose bound excitons are seen in the KP series. Competing models were those of Reynolds et al. [246] who interpreted the KP lines as DAP transitions and the isoelectronic bound exciton model of Beye et al. [247]. The bound exciton character of the KP lines and the correlation with the d_n lines are supported by the polarized PL and selective excitation measurements of Skolnick, Tu and Harris [248] and the high resolution selective excitation and time resolved PL measurements of Charbonneau and Thewalt [249]. It also became clear that the KP defect could not be a simple point defect or impurity, largely because the polarized PL and PLE measurements indicated that most KP lines (but not the g-line) were strongly polarized parallel to a <110> direction, implying that the defect must have a well-defined symmetry axis.

Eaves and Halliday [250] first explained the KP PL emissions as due to excitons bound to acceptor pairs at different separations. Skolnick et al. [251, 252] extended this model so as to be consistent with important spectroscopic results. The extended model involves the exciton being bound to neutral acceptor pairs as in Eaves and Halliday, although with some differences in detail, or to a double acceptor - isoelectronic pair, and includes a theory of the transitions involved intended to be completely compatible with the spectroscopic evidence. Because of the polarization dependent behavior, the defect complexes must be preferentially incorporated in particular orientations with both members of the pair on the same sublattice, while the precisely reproducible energies and the large number of lines suggests pairs with a limited number of possible separations determined by the crystal lattice. The suggestion is made that the second defect in the pair will usually encounter the first one embedded in a growth step and can approach most closely along the step normal which thus determines the orientation. Cheng, Stavola et al. [253,254] report evidence from infrared absorption in carbon doped MOMBE GaAs of a similar axially aligned defect consisting of a pair of carbon acceptor atoms stabilized by a hydrogen atom. They deny that this defect is in fact the KP defect because it dissociates at temperatures below those used for MBE growth.

While the nature of the KP defect is not resolved, there is considerable evidence that residual impurities are involved, particularly Carbon. Rao et al. [243] noted that their first undoped sample grown in a newly installed MBE system was completely lacking in KP lines. Skromme et al. [245] found that growth conditions that favored the incorporation of Carbon also favored the appearance of KP lines in the spectrum of the sample. Akimoto et al. [255] found that KP lines became more intense when the amount of CO in the background increased and attributed the KP lines to carbonyls incorporated

on arsenic sites. Briones and Collins [244] also implicated Carbon together with As and Ga vacancies. Makita et al. [256] found that KP lines could be introduced into very pure MBE samples that did not show them by implanting both C^+ and O^+ ions, with both types of ions necessary to produce the effect. Another suggestion [249] that might show the necessary axial symmetry was a B_{As}- N_{As} defect. The problem is that Boron is not a major residual impurity in MBE systems, while Carbon and Oxygen are.

The g-line transition at 1.511 eV (at 4K) is distinguished from the lower energy axial KP line transitions by a shorter lifetime (1.2 ns vs. 2.4 for the KP lines [241]) and a complete absence of polarization sensitive behavior. It is also present under the widest range of growth and doping conditions, even those which inhibit the axial KP lines. Reynolds and Collins ([257] *Chapter 8*) present a theory of the g-line as due to a DAP transition involving a double donor (possibly an arsenic antisite) and a deep neutral acceptor complex or a double acceptor (possibly a gallium antisite) and a neutral donor complex. Most authors [241,258,259] favor a bound exciton recombination, with the exciton bound to a neutral acceptor complex defect involving involving carbon acceptors and an isoelectronic defect. Leroux et al. [259] proposed that the isoelectronic center is N_{As} after discovering that there were considerable amounts of N in their nominally undoped samples. They suggest that since N is more electronegative than the As it replaces there is an interaction between a C_{As} acceptor and a nearby N atom acting as a hole repulsive isoelectronic center. The net effect is to lower the transition energy of the bound exciton to 1.511 eV. In GaP N_P is well known to bind excitons [141]. Makita et al. [256] found that by implanting with C^+ ions the g-line could be brought up in very pure samples that lacked it. Oxygen was not necessary as it was for the axial KP lines.

3.4.6 Techniques Involving Resonantly Excited Photoluminescence: Photoluminescence Excitation and Selective Excitation (SE)

In conventional photoluminescence spectra, where the excitation wavelength is constant and the detection wavelength is scanned, only the lowest energy states are usually in evidence because thermalization to a lower energy state is faster than radiative recombination. In photoluminescence excitation spectra it is the excitation wavelength that is scanned while the detection wavelength is constant. By locating the detection wavelength on a peak that appears in the photoluminescence spectrum and scanning the laser through the excited state transitions of higher energy, it is possible to produce an excitation spectrum similar to an absorption spectrum. If enough free carriers or excitons resonantly excited to the higher state can thermalize down to the detection states before recombining, then there will be measurable increase of PL intensity at the detection wavelength. The thermalization often proceeds down through a cascade of states, and it is necessary that for all of them recombination directly from that state is not much faster than thermalization down to the detection level. The magnitude of the PL increase observed also depends on the rates for the competing processes, and is thus not always directly comparable to the magnitudes observed in absorption spectra. Some transitions associated with higher energy states may appear as dips in the spectrum or not at all because they have no way of efficiently transferring free carriers or excitons to the detection states. ([7] *Chapter 7*).

Selective excitation spectra are PL spectra with the excitation energy tuned to resonantly excite a particular state or transition. The intensity of the lower lying peaks depending on a cascade of excitons or free carriers from the resonantly excited state is expected to be proportional to the

concentration of the species involved in the original transition, without free carrier or exciton trapping or diversion into competing states being a consideration.

In selective excitation of the DAP band only pairs at particular separations are directly excited, since the characteristic energy of a DAP recombination is a function of the pair separation. The laser energy is chosen to produce a pair consisting of a neutral donor and an acceptor in an excited hole state at a given separation. Shallow or effective mass acceptors show a quasi-hydrogenic pattern of excited hole states with energy separation between the ground 1s and excited states depending on the nature of the particular acceptor [258]. Because the separations between pairs vary continuously (within the constraints of the lattice) a given laser energy will actually produce a series of peaks representing a whole ladder of excited states, 2p(3/2), 2s(3/2), 2p(5/2) etc. The pair separation involved in producing each of these peaks is different and meets the condition that the energy required for the transition represented by the peak is equal to the laser energy. The energy pattern of such states will be characteristic of the particular acceptor, and similar to what is seen in PLE spectra of DAP transitions [260]. The relaxation time of the hole is typically much shorter than the DAP recombination time so that the excited acceptor is quickly de-excited to its ground state subsequently emitting a photon of a characteristic recombination energy [261]. The situation is illustrated in Figure 3.2.

A selective excitation spectrum involving the DAP band is superimposed on a broad DAP band especially in *p*-type samples. The band owes its existence to the fact that a continuum of neutral acceptors already exists prior to excitation. Another characteristic of these processes is that there is no sharp resonance in the photon energy required to excite the spectra as there is for

Selective Excitation of Donor Acceptor Pairs

Laser neutralizes ionized pairs and excites acceptor to hole state given by bold solid line at that pair separation.

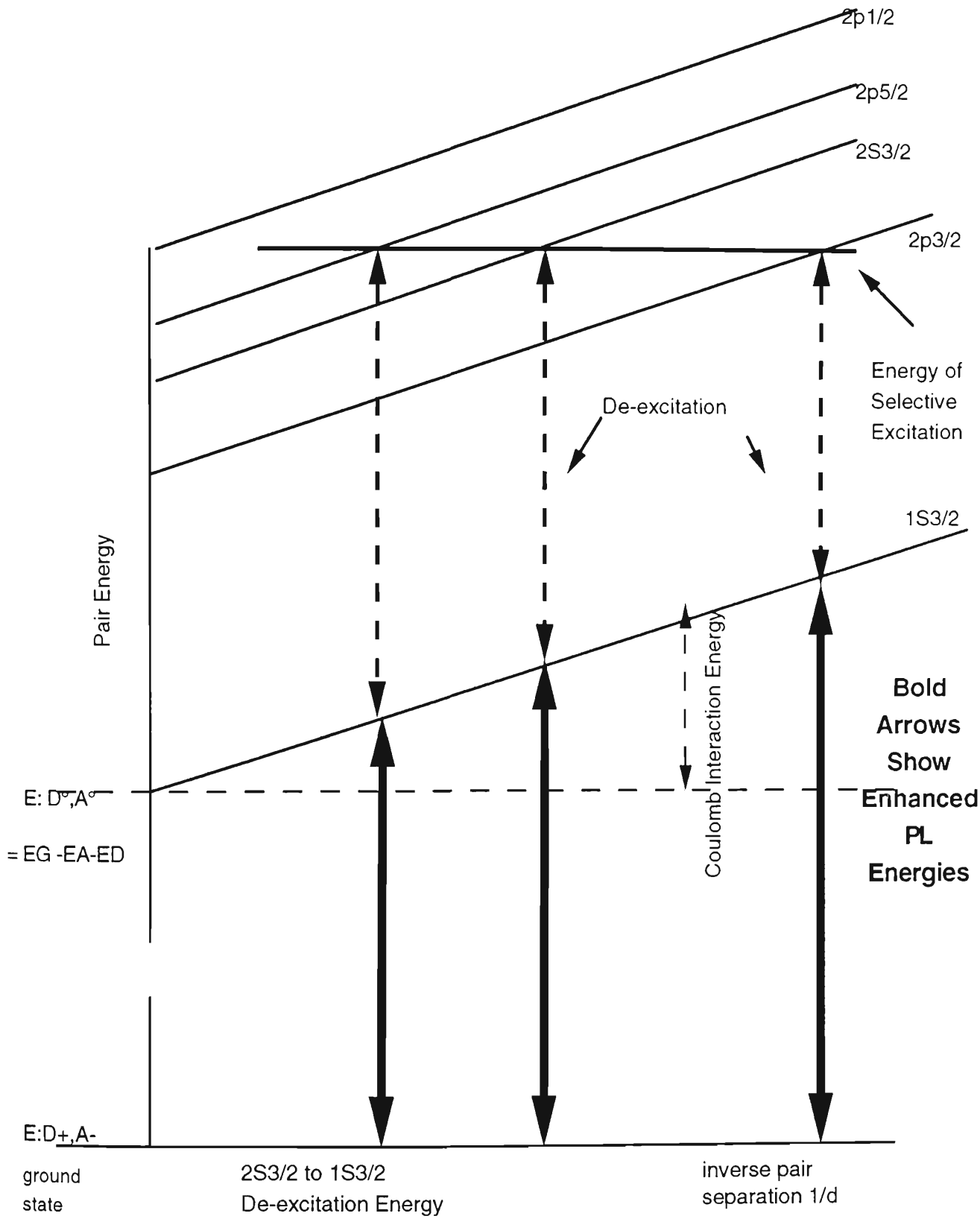

Figure 3.2 **Selective excitation of donor acceptor pairs. The 2S3/2 to 1S3/2 de-excitation energy is 17.8 meV for Carbon, 25.2 meV for Silicon and 19.7 meV for Beryllium [258].**

the two-hole and phonon replicas of excitonic transitions. Changing the energy of the excitation will simply result in the excitation of a pattern of new pairs, closer together or further apart.

3.4.7 Temperature Dependence of Photoluminescence

As the temperature is raised a quenching of PL integrated intensity is usually observed. This is illustrated in Figure 5.13 for excitons in shallow quantum wells. Such a quenching is due to several factors. For quantum wells excitons can only couple with photons when they have energies within the effective homogeneous linewidth of $\mathbf{K} = 0$. The thermalized distribution of excitons ceases to be so strongly peaked near $\mathbf{K} = 0$ as the temperature rises and becomes more spread out so that the density of excitons that are candidates for radiative recombination becomes smaller [235]. There are also changes in the transport properties of free carriers. The minority carrier diffusion length increases with temperature leading to greater losses at nonradiative centers at the surface or substrate [239]. At low temperatures mobility increases with temperature [262] so that excitons and majority carriers are also more likely to escape to the surface or substrate. Bulk nonradiative recombination rates are typically also proportional to the carrier thermal velocity and the capture cross sections of the individual traps, e.g. [113]. These trap capture cross sections are frequently thermally activated, as shown in equation (2.4). Because the confinement of excitons and free carriers in good quality quantum wells prevents them from reaching the surface or bulk traps, their PL is quenched less rapidly than in bulk.

Quenching of PL intensity also results from the thermal dissociation of free and bound excitons. For free excitons the dissociation process becomes significant above 30K and can be approximated by a thermally activated

process [263,264]. The dissociation of excitons can create free electrons and holes that screen the Coulomb attraction binding other excitons and cause them to dissociate in turn ([7] *Chapter 7*), although this effect is small at low temperatures. More importantly, free carrier recombination probabilities are substantially smaller than the probabilities for low temperature excitons [180]. For donor bound excitons and the DAP band it is clear that the quenching is due to ionization of the donor above 10K [180]. At higher temperatures it is observed that eA° quenches at a rate consistent with the ionization of the acceptor [239].

3.4.8 Thermally activated processes in photoluminescence

As discussed in Section 3.3.1.1, thermally delocalized excitons have a much greater chance of being captured by traps and recombining nonradiatively. Thus the delocalisation and consequent quenching is expected to have a standard mobility edge and obey an activated or Arrhenius type temperature dependence containing the Boltzmann factor $\exp(-E_A/kT)$. Thus, e.g. Zucker et al. [265]

$$N_t = \frac{1}{1 + CTe^{-\frac{E_b}{kT}}} \tag{3.46}$$

where N_t is the number of trapped excitons, C is a fitting parameter and E_b the binding energy of the exciton to the imperfection.

Where there is transport by tunneling or hopping of localized excitons to sites where nonradiative recombination is likely to occur it has been shown [266,267] that

$$\frac{p_{nr}}{p_r} = \frac{I_o}{I(T)} - 1 = \frac{A \exp(T / T_o)}{1 + (B - A)\exp(T / T_o)} \tag{3.47}$$

where A and B are constants and p_{nr} and p_r are the respective probabilities of nonradiative and radiative recombination

If B~A, corresponding to all the recombination being nonradiative at high temperature then

$$\frac{p_{nr}}{p_r} = A \exp(T / T_o) \tag{3.48}$$

(3.48) is used by Minami et al. [208] to account for the temperature dependent behavior of photoluminescence from a short period GaAs/AlAs superlattice.

CHAPTER 4

EXPERIMENTAL TECHNIQUES

4.1 MBE GROWTH OF SAMPLES

Layered structure semiconductor samples of the quality standard studied in this work owe their existence to the modern epitaxial growth technologies which make possible the growth of thin layers with very low concentrations of residual impurities and native defects, as well as nearly monolayer smooth interfaces. These qualities are frequently essential when semiconductor devices are being grown. Shallow GaAs/$Al_xGa_{1-x}As$ quantum well modulators for instance are ineffective unless the background impurity concentration is less than 1×10^{15} cm^{-3} [268]. In the case of GaAs the highest quality material with the lowest concentrations of residual impurities and defects to date tends to be consistently produced by older Liquid Phase Epitaxy (LPE) methods, although the best samples grown by Molecular Beam Epitaxy (MBE) can approach these concentrations. Where MBE definitely has the advantage is that its relatively low growth temperatures and shuttered Knudsen cells allow controlled and abrupt changes in layer composition and doping. It is difficult to grow layers of less than 100Å by LPE techniques [269]. All of the samples reported on in the present work are MBE grown GaAs and $Al_xGa_{1-x}As$ bulk and layered structures.

Molecular Beam Epitaxy is essentially a vacuum evaporation technique adapted to the growth of single crystals. A carefully prepared substrate is introduced into an ultra-high vacuum chamber (with base pressures $\leq 5 \times 10^{-11}$ Torr) containing Knudsen effusion cells which are basically separately heated inert crucibles containing the solid or liquid source materials for growth. The temperature is regulated to be appropriate for the rate of

growth so that the solid and gaseous phases are in equilibrium within the cell and a beam of evaporated atoms emerges from a small orifice to be deposited on the heated, rotating substrate. The atoms attach themselves to existing lattice sites and therefore under appropriate conditions continue the crystal structure of the substrate. Fast acting shutters enable the beam to be stopped and started quickly enough to produce virtually monolayer flat interfaces between layers. The heating arrangements allow the system to be outgassed at temperatures as high as 1600C for empty Knudsen cells and 1000C for the substrate holder to enable impurities to be baked out. The Knudsen cells are also separated by a liquid nitrogen baffle to minimize chemical and thermal cross-contamination, and only sources of very high purity are used. GaAs is normally grown at substrate temperatures between 550-650C, a relatively low growth temperature compared to other growth techniques, which results in negligible interdiffusion between layers.

Because of the ultra-high vacuum, beam and growth monitoring devices can be easily incorporated within the MBE system. The most common monitoring technique involves reflection high-energy electron diffraction (RHEED). The oscillations in the RHEED pattern enable monolayer growth to be monitored [270].

Jan et al. [268] suggest that a substrate growth temperature of 600C which is close to the optimum for GaAs is also suitable for growing shallow quantum wells (total band offset on order of 25 meV or less) [25]. With no preferential desorption at this temperature of either Gallium or Aluminum, the sample composition is determined by the growth rates of the two compound semiconductors, GaAs and AlAs, with the GaAs growth rate 1 ± 0.01 monolayer/sec and the AlAs growth rate determined by [271]

$$x = \frac{[AlAs]}{[AlAs] + [GaAs]} \tag{4.1}$$

where x is the Al mole fraction and the quantities in brackets are the respective growth rates

The melt temperatures then required for the necessary growth rate are experimentally determined.

Layered structure GaAs/$Al_xGa_{1-x}As$ samples are usually grown with a GaAs buffer between the substrate and the epilayer or layered structure of interest and a GaAs capping layer. The purpose of the capping layer is to protect the underlying $Al_xGa_{1-x}As$ barrier which would otherwise degrade easily in air. In a GaAs/$Al_xGa_{1-x}As$ multi-layer sample, the buffer is a layer of GaAs of the order of 1 micron or more in thickness which is grown directly on top of the substrate. The purpose of the buffer is to improve the quality of the layers grown on top of it by acting as a sacrificial layer to receive impurities which tend to be incorporated early in the growth process and by shielding the higher layers from the substrate and its defects and impurities [148].

4.2 METHOD OF COLLECTING REFLECTANCE SPECTRA

Figure 4.1 shows the experimental set-up. The light source is a 12V 100W Philips auto headlamp bulb (Model 7023 FCR A1/215). Output of light is reasonably constant over the range of frequencies considered, with the shape of the mirror response discussed below mostly determined by the response of the spectrometer. The light source sits in a fan cooled Oriel mount, with power supplied by a Sorensen DCR80-33B power supply, which enables power to be supplied in either constant current or constant voltage mode. For the spectra discussed here the lamp was run at a constant 7.5 to 8A, in order to achieve a high constant output of light while spectra are being taken. The light from the lamp is collected and collimated by a large

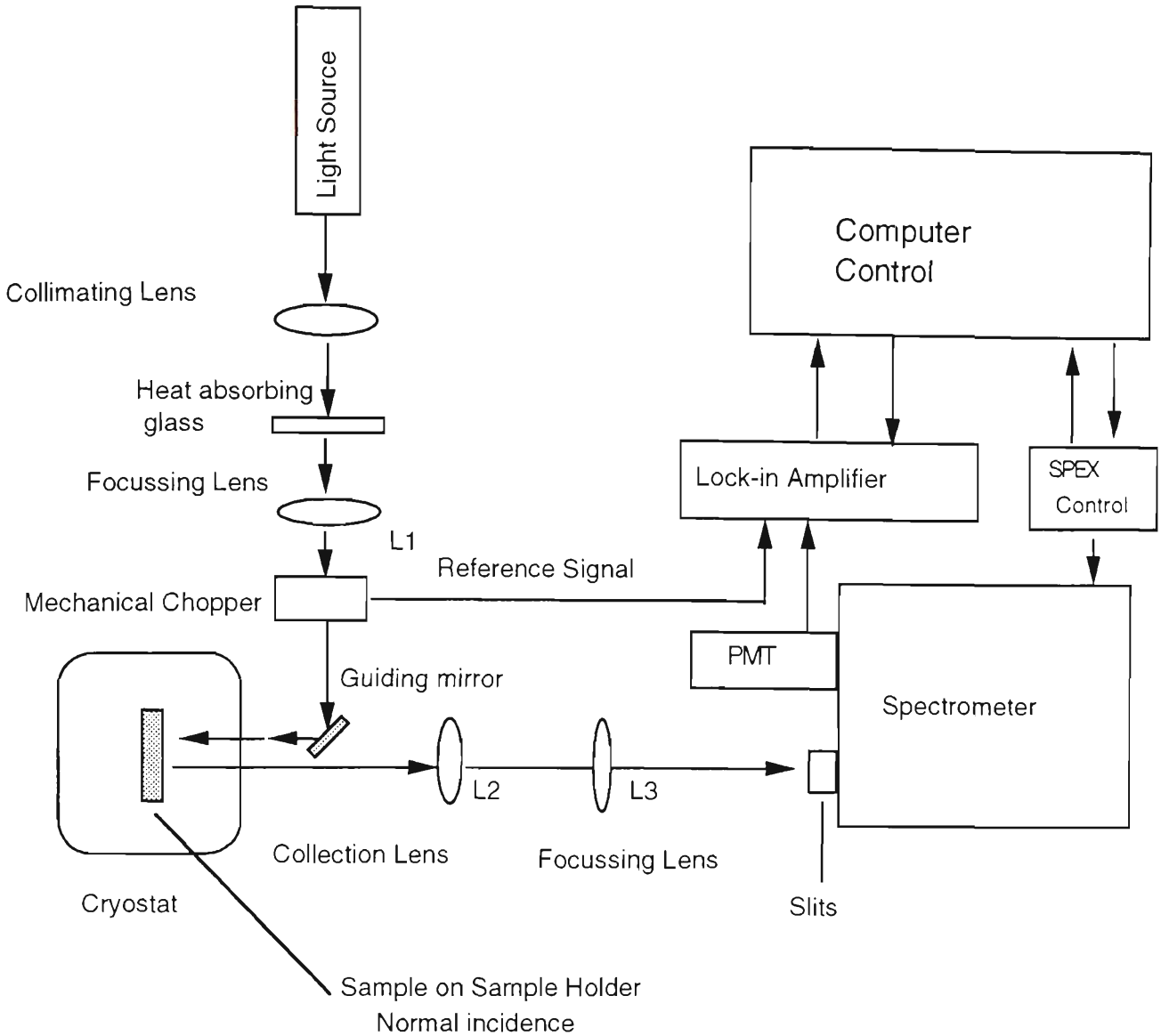

Figure 4.1 **Schematic diagram of optics for collecting reflectance spectra. Light reflected at normal incidence from a sample kept at low temperature is dispersed by a grating spectrometer and detected by a GaAs photomultiplier tube.**

diameter 8.25" (21 cm) focal length lens. It then passes through a sheet of heat absorbing glass, which reduces the intensity of the light by a factor of about 30% at 600nm and considerably more at longer wavelengths, but is used because it absorbs in the infrared and minimizes heating of the sample. The light then passes through a 20 cm focal length lens and a Stanford Research Systems SR540 chopper run between 375 and 500 Hz. The chopper provides a reference signal to the lock-in amplifier. The light finally reaches a small mirror which directs it through the cryostat window where it strikes the sample at near normal incidence.

The cryostat (Oxford Instruments Model MD404) contains a central sample space surrounded by the liquid helium reservoir, vacuum spaces and a liquid nitrogen shield. The pressure in the vacuum space is kept below 10^{-5} Torr using a turbomolecular pump. The sample space is filled with a helium exchange gas at a pressure of about 160 Torr, which is cooled as liquid helium drips through a heat exchanger from the helium reservoir, with the drip rate controlled by a needle valve For 77K measurements the helium reservoir is filled with liquid nitrogen. For a range of temperatures up to room temperature, the helium can is filled with liquid helium or nitrogen as appropriate and the temperature in the cryostat regulated by an Oxford Instruments CLTS temperature sensor and a heating element which is controlled by a digital three term temperature controller (Oxford Instruments DTC2). This system maintains stability within ± 1K over this temperature range (as determined by the energy shift of a sharp quantum well transition and hence the GaAs host material bandgap with temperature as given by equation (1.10)), if the helium and heat flows are properly balanced. The sample is mounted from one corner in order to avoid strain with 'Cowgum' petroleum rubber solution on a blackened copper sample holder and optical access is through Indium sealed sapphire windows in the

cryostat tailpiece. The cryostat is slightly tilted to eliminate the problem of light reflected from the crysotat windows reaching the spectrometer slits.

The light reflected from the sample is collected by a 6.5" (16.5 cm) focal length plano-convex lens (L2 in diagram) placed so that the sample is at its focal length in order to collimate the light arriving from the cryostat window. The lens has an f number of f/2.8. This f number defines the collection angle of the lens. The lens is not perfectly matched to the light output cone of the cryostat window, which is defined approximately by f/1 (ratio of distance of sample to cryostat window to window diameter), but collecting enough light is not a problem in this work. The light collimated by L2 is focussed onto the spectrometer slits by L3, a 5" (12.7 cm) plano-convex focal length lens with f/3.5. The lens is not well matched to the spectrometer which is f/9, from a light collection point of view, but the short focal length lens was selected and placed so as to fully illuminate the collimating mirror of the spectrometer in order to obtain maximum resolution. The magnification of the image of the sample on the slits is given by the ratio of the focal length of L3 to that of L2.

The spectrometer used is a SPEX 1704 with a 1 m focal length and a Model 1501 grating blazed at 5000Å and containing 1200 grooves/mm, using a Czerny Turner mount. For this arrangement the fundamental grating equation [272] is

$$m\lambda = d(2\sin\alpha\cos\beta) \qquad (4.2)$$

where m is the order of the principal maximum
λ is the wavelength of light, d is the grating spacing
α = angle of incidence = $\theta + \phi$ where $\phi = 4°54'$, $\beta = \theta - \phi$
θ = grating rotation measured from direct image position

The spectrometer is operated in first order. The theoretical resolving power is given by

$$R_T = \frac{\lambda}{\Delta\lambda} = m\,N \qquad (4.3)$$

where m is the order of diffraction and N is the total number of grating grooves.

Here m = 1 and N = 1200 grooves/mm × 102 mm. For a typical wavelength on the order of 8150Å, the minimum resolution is theoretically 0.07 Å. In practice, the resolution is limited by the slit width and the focal length of the instrument. The manufacturer provides tables of the reciprocal linear dispersion at various wavelengths, and the spectral bandpass is determined by multiplying the slit width by the appropriate value. The reflectance spectra discussed here were taken with a slit width of 20-40μm and hence a spectral bandpass of 0.3Å or 0.05 meV at worst, assuming a slit height no greater than 1 cm, as was the case in all the present work. The efficiency of the grating is at a maximum at its blaze wavelength of 5000Å and falls off to 50% of the maximum at 3300 Å and 10,000Å on either side. In practice spectral range is limited by the photomultiplier tube rather than by the grating. The spectrometer was calibrated before every run on the 8136.406Å line from a neon lamp.

Dispersed light passes out of the exit slits of the spectrometer and into a GaAs photomultiplier tube (RCA C31034A). The spectral response of this tube is reasonably flat between 2700Å and 8700Å, but falls off rapidly at longer wavelengths. It is thermo-electrically cooled with a dark count typically in the range of 50 cps at -20°C and a typical current gain of 3×10^5. The current output of the photomultiplier tube is connected to the current input of a Stanford Research Systems Model SR510 lock-in amplifier. The reference signal is provided by the chopper discussed previously.

Overall controll of data collection was provided by a MacIntosh SE computer running FORTRAN programs written by the author. The starting and end points of the spectrum in Angstroms are entered into the SPEX control along with the increment at which data is to be collected. The computer triggers the spectrometer to move to the next data collection point and then collects the magnitude of the photomultiplier current at that point from the lock-in amplifier. It then triggers a move to the next collection point. The reflectance spectrum is displayed on the monitor as it is being collected and the output of the program is a file giving photomultiplier current as a function of wavelength.

Software was also written to correct gathered spectra by the 'mirror response' of the system. An Al mirror was mounted in the same way as a sample and the reflectance spectrum collected in the normal way, giving a broad Gaussian response down to the cut-off of the photomultiplier tube. Reflectance spectra are corrected to give the same relative response as they would if the mirror response were flat by dividing the current at a particular wavelength by the mirror response at that wavelength. To assure a good fit of weak features several identical spectra were successively taken under the same conditions so that an averaged spectrum could be produced with noise reduced. The error estimates given in Chapter 5 refer to how great a change in the relevant parameter was needed before the fit is significantly changed. These errors are greater than the small day to day changes between experimental spectra, apart from the rare situation when the spectrometer shifts out of calibration during a run.

4.3 METHOD OF COLLECTING PHOTOLUMINESCENCE SPECTRA

Figure 4.2 shows the experimental set-up showing two alternative optical paths depending on the laser in use. There are three sources of light for excitation. One is a Model 106-2 Spectra-Physics HeNe laser with a power output of 18mW, emitting in the red at 633nm. The second is a 25W Spectra-Physics Model 2040 Argon Ion Laser lasing strongly at 488 nm and 514.5 nm. The third is a tunable Spectra-Physics model 3900 Titanium doped Sapphire (Ti:S) laser, pumped by the argon ion laser. This Ti:Sapphire laser was also used for the photoluminescence excitation measurements described later. It is [273] tunable in the red and near infrared between 650 nm and 1.1 mm using four different sets of cavity mirrors and rotation or replacement of a birefringent filter for different parts of this range. Output power is approximately 20% of the power output of the pumping laser and there is less than 1% RMS noise and 3% drift over a 2 hr period at constant temperature. Spectral linewidth is < 40 GHz. The laser produces a well collimated beam (divergence only 1.0 mrad) at a diameter of 0.95 mm. Although the power is reasonably stable at any given wavelength there is variation in power over the range provided by the mirror set. This can be largely corrected for through the use of a Spectra-Physics Model 373 Dye Laser Stabilizer, and is most important for the PLE measurements discussed later.

The intensity distribution of the laser output is Gaussian [274] throughout the optical system and given by

$$I(r) = I_0 \exp(-2r^2 / r_0) \qquad (4.4)$$

where r is the radial distance from the center of the beam and r_0 is the beam waist radius, the radius at which the intensity has dropped to I_0/e^2

A guiding mirror M2' (M1 and M2 for the Ti:Sapphire or argon ion laser) directs the beam down the optical bench. No collimating lens is used but the

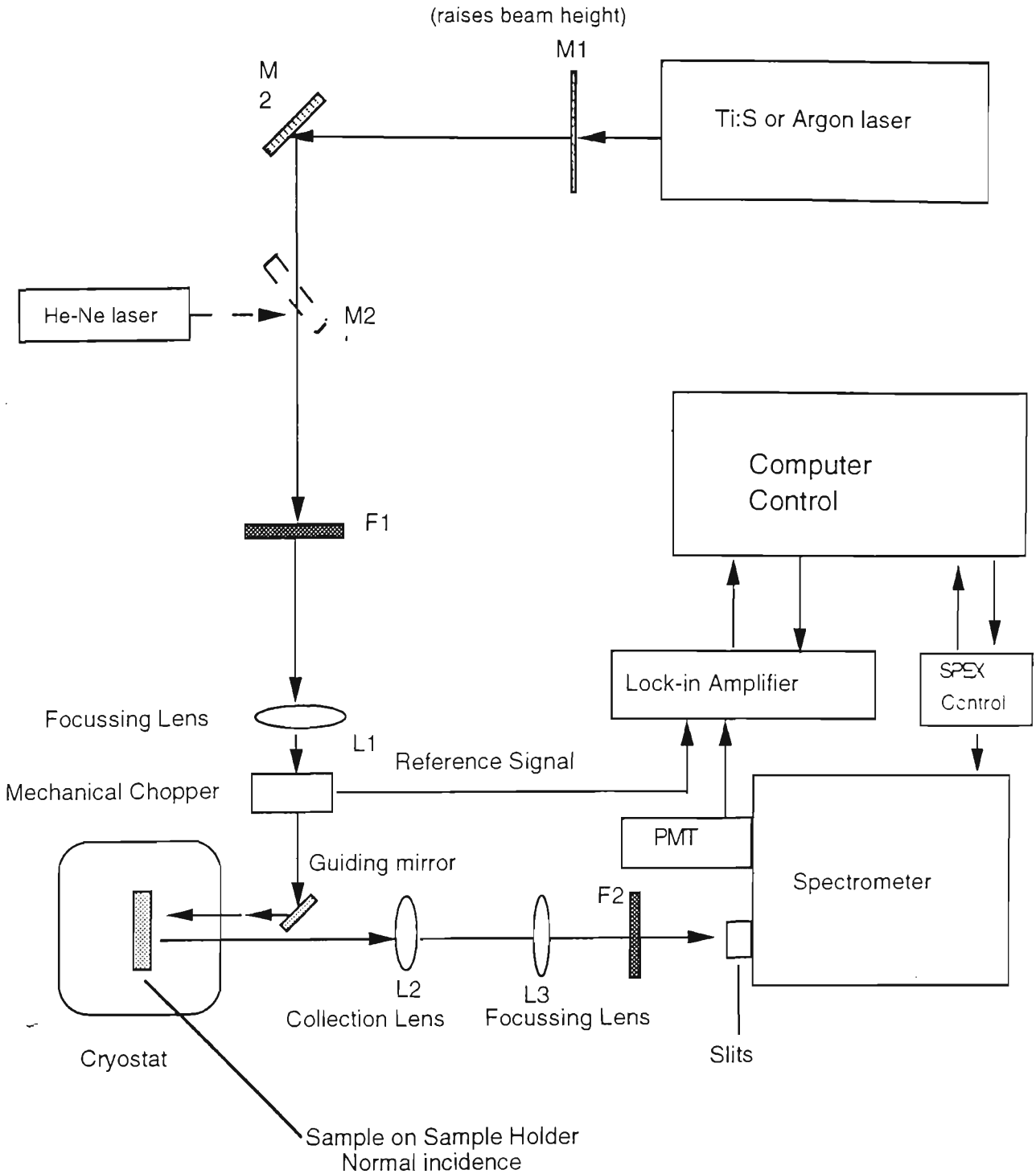

Figure 4.2 Schematic diagram of optics for collecting photoluminescence spectra. PL excited by laser is dispersed by a grating spectrometer and detected by a GaAs photomultiplier tube. M refers to mirrors and F to optical filters.

beam size is controlled by an iris. The beam first passes through a set of filters (F1 in Figure 4.2) which include an Edmunds Scientific notch filter (for the HeNe laser only) to prevent extraneous wavelengths from the laser impinging on the sample and neutral density filters to reduce the beam intensity and avoid sample heating or excess free carrier or exciton density. Beam power after the F1 filters is monitored by means of a Spectra-Physics model 404 power meter. The chopper is used as described in the previous section on reflectance. Lens L1 (focal length 20 cm) is placed so that the sample is at its focal length when the distance to the guiding mirror M3 from L1 is added to the distance from M3 to the sample. L1 thus focusses the laser beam onto the sample. The spot size on the sample [274] is determined by

$$D = \frac{4\lambda_{laser}}{\pi} \cdot \frac{f_{L1}}{w} \qquad (4.5)$$

where D is the diameter of the spot
f_{L1} is the focal length of L1
w is the width of the beam at the position of L1 ≈ 1 mm

For the present setup D = 160μm at best. Defocussing can be used to further reduce the power density on the sample. The guiding mirror M3 directs the laser beam onto the sample at an angle to the normal to minimize reflections of the laser beam reaching the spectrometer slits from the sample or the cryostat windows. The system is aligned by passing the laser beam through two irises set at the same height and approximately 1 m apart on the optical bench between the laser and the cryostat.

The cryostat and collection lens L2 are as described in Section 4.2. The focussing lens L3 (focal length f_{L3} 50 cm, f/6.7) is placed so that the spectrometer slits are at its focal length, with fine adjustment made by moving the lens to maximize the PL signal from a strong peak. The magnification on the slits of the sample PL spot is about 3 for the present work. Filter F2 (used with the HeNe laser only) absorbs shorter wavelengths of light than about 6450Å, in order to block scattered laser light. Alignment

between the cryostat window and the spectrometer slits is dealt with by scattering a laser beam off a bare copper sample holder. The light will be scattered in the same direction as the photoluminescence and is clearly visible. L3 is removed from the bench and L2 is adjusted so that a uniform disk of scattered light is centered over the slits and does not increase or decrease in size as it passes down the optical bench. Once L2 is correctly aligned, L3 is adjusted so that the disk is focussed down onto the slits. Fine adjustments are made as explained above. The spectrometer is as described in the previous section.

Two different types of detector were in use for photoluminescence measurements. The first type, the GaAs photomultiplier tube was used for most measurements in the visible. It was also used for measuring reflectance spectra and has been described in the previous section. The second detector was a liquid nitrogen cooled North Coast Ge EO-817L photodiode primarily intended for measurements in the infrared, with its range between 6000Å and 17,000Å. In actual measurements we found the response to be reasonably flat between 9000Å and 13,600Å, where it was limited by the response of the grating spectrometer. It is less sensitive in terms of signal to noise ratio and less flat in the visible than the GaAs photomultiplier tube. The Ge detector is also more sensitive to cosmic rays, especially muons, than the GaAs photomultiplier tube and needs to be used with a special spike suppressing circuit containing a muon filter supplied together with the detector and (in the present case) a Princeton Applied Research Model 128A lock-in amplifier. The spike suppression circuit works by detecting the leading edge of a large noise spike and gating and holding the output of the detector for a preset time. The output of this circuit was first directed to an A/D converter incorporated in the Stanford Research Systems SR510, so that data could be collected on the computer in the normal way. Because of lack of dynamic

range this was replaced by a DC to AC chopper circuit [275] designed so that the SR510 lock-in amplifier would see the output of the Ge detector circuit as suitable input, with a voltage controlled oscillator supplying the reference signal. The computer programs for controlling this system were written by the author. Despite the spike suppression circuit, multiple identical spectra needed to be taken sometimes for the purposes of comparison and elimination of negative going noise spikes.

The rest of the system, the spectrometer and the computer control used with the GaAs photomultiplier tube are as described in the previous section.

4.3.1 Collecting Photoluminescence Excitation (PLE) Spectra

The same equipment and methods are used for collecting PLE spectra as is used for collecting photoluminescence spectra using the tunable Ti:Sapphire laser. The only difference is that a SPEX Model 1871 Minidrive stepping motor is connected to the micrometer screw which drives the birefringent filter inside the Ti:Sapphire laser. Stepping the screw changes the output wavelength before each data collection burst, while the grating spectrometer is set for detection at a constant wavelength. The stepping motor and data collection are under computer control using a program written by the author. The micrometer screw is not calibrated in wavelengths, but only in divisions, and the laser output over the range of interest must be frequently calibrated using the calibrated grating spectrometer. A polynomial fit to the calibration enables the data output to be given directly in terms of eV.

4.4 HYDROGENATION AND ANNEALING OF SAMPLES

Where hydrogenation was indicated, samples were cleaved and sections sent to ANSTO (Australian Nuclear Science and Technology Organization) at the

Lucas Heights Research Laboratories to be hydrogenated by (the late) A.J. Tavendale and A.A. Williams in a RF plasma for 1 hr at 300C. The hydrogenation procedure was developed by A.J. Tavendale of ANSTO and involved positioning the samples on a heated stage downstream from a continuously pumped 27 MHz, 0.5 W, 0.5 Torr hydrogen plasma [97,136].

Annealing of hydrogenated samples to restore the activity of shallow impurities was carried out in an Argon atmosphere with 4% hydrogen in an annealing furnace at ANSTO by A.A. Williams. The temperatures and annealing times employed were varied and will be listed as appropriate when the individual samples are discussed.

CHAPTER 5

OSCILLATOR STRENGTH AND OTHER REFLECTANCE PARAMETERS OF SHALLOW QUANTUM WELLS

5.1 INTRODUCTION

Reflectance studies of very high quality shallow $GaAs/Al_xGa_{1-x}As$ quantum well samples, such as the ones discussed in this chapter, have important advantages in the study of oscillator strengths and transition linewidths. The extremely sharp and detailed structure arising from confined excitonic transitions in low temperature reflectance spectra reduce the uncertainties in oscillator strength per unit area and linewidth which are often a problem in interpreting reflectance spectra from deeper quantum wells. (Shallow quantum wells have a total band offset of about 25 meV or less such that the barriers are lower than the thermal energy at room temperature [25].) Reflectance techniques also avoid the problems with sample preparation characteristic of absorption techniques, and unlike Photoluminescence Excitation (PLE) allow qualitative measurements of the relative intensities associated with the various transitions.

Very precise and consistent values for the oscillator strengths, transition linewidths and energy positions for the exciton transitions occurring in the quantum wells were obtained by means of close fits of reflectance spectra using both a local, semiclassical model and the nonlocal transition matrix method of Andreani [146,147]. Results were fully consistent with the quantum confinement of electrons, holes and excitons even in the samples where x (the mole fraction of Al in the barriers) was only 0.01. Excitonic transition energies were always consistent with each other and the positions established by previous PLE measurements. Oscillator strengths per unit

area were consistent from day to day regardless of sample temperature or fitting formula, and significantly larger than the values predicted by theory. Some QW excitonic transition linewidths were as sharp as any previously reported.

Analysis by means of the nonlocal method of Andreani [146,147] was necessary to achieve accurate fits of excitonic transition linewidth where the intrinsic broadening associated with the radiative lifetime of photocreated excitons was comparable in magnitude to that due to all other sources of broadening. Such an outcome has been theoretically predicted. The temperature coefficient of thermal broadening for temperatures below 70K was determined for the two lowest energy quantum well transitions to be $3.0\pm0.4\ \mu eV/K$ for E_{11h} and $4.5\pm0.4\ \mu eV/K$ for $E_{11\ell}$, with no discernable dependence on barrier height.

5.2 THE SAMPLES

The present samples are very high quality MBE grown 25 repeat multi-quantum well (MQW) samples, with 20 nm GaAs wells and either 20 nm (20/20 samples) or 50 nm (20/50 samples) $Al_xGa_{1-x}As$ barriers. x, the mole fraction of Al in the barriers ranges from 0.01 to 0.045. A full description is given in Table 5.1. They were grown at the Defense Research Agency (DRA) initially as part of a collaboration with the University of Sheffield and were initially studied there from the point of view of photoluminescence and photoluminescence excitation before being passed on for the present reflectance studies. The present measurements complement the previous work reported in Simmonds et al. [158] on the same shallow quantum well samples and in the doctoral dissertation of Wendy I. Tagg [276] so this work needs to be summarized first. In reporting this and the later reflectance work the quantum well transitions are labelled as follows: E_{nmh} or $E_{nm\ell}$. n

Table 5.1. **Structure of Shallow Multi-Quantum Well Samples. All layers are nominally undoped. Samples grown by Dr. G.W. Smith of the DRA in collaboration with workers at the the University of Sheffield.**

Sample Name x for $Al_xGa_{1-x}As$ layers	GWS482# & GWS280* x = 0.045	GWS479# & GWS359* x = 0.02	GWS485# & GWS360* x = 0.01
GaAs capping layer	200 Å	200 Å	200Å
$Al_xGa_{1-x}As$ barrier	500Å#, 200Å*	500Å#, 200Å*	500Å#, 200Å*
25 Periods MQW			
GaAs well	200 Å	200 Å	200 Å
$Al_xGa_{1-x}As$ barrier	500Å#, 200Å*	500Å#, 200Å*	500Å#, 200Å*
GaAs buffer	10000 Å	10000 Å	10000 Å
GaAs substrate	undoped	undoped	undoped

Comparison Samples

Sample Name x in $Al_xGa_{1-x}As$ barriers	GWS463 (Single QW) x = 0.02	GWS507 (Barrier only) x = 0.02
GaAs capping layer	200Å	200Å
$Al_xGa_{1-x}As$ barrier	5000Å	2000Å
GaAs QW	200Å	none
$Al_xGa_{1-x}As$ barrier	5000Å	none
GaAs buffer	10000Å	10000Å
GaAs substrate	undoped	undoped

refers to order from the bottom of the quantum well of the corresponding electron subband furnishing the exciton electron. There are separately numbered subbands for light and heavy holes in quantum wells, with m referring to the order of the parent hole level,. and h or ℓ standing for heavy or light hole.

5.3 SUMMARY OF PREVIOUS WORK ON THE PRESENT SAMPLES

5.3.1 The 20/50 Shallow Quantum Well Samples

Simmonds, Birkett, Skolnick et al. [158] used very high resolution spectroscopic studies to determine binding energies in $GaAs/Al_xGa_{1-x}As$ shallow quantum wells in the 20/50 MQW systems described in Table 5.1. The x values used were x=0.045 (GWS482), x=0.02 (GWS479) and x=0.01 (GWS485). Equation (1.6) implies band gap discontinuities for these x values at 5K of 65 meV, 29 meV and 14 meV respectively. They established that the excitons associated with the quantum wells in these samples were unquestionably of quasi 2-D rather than bulk (3-D) character, as was theoretically predicted. PLE spectra showed several fully confined levels for both electrons and holes in all samples.

The particular interest of Simmonds et al. was in determining the exciton binding energies and their variations with confinement. They determined the binding energies from the energy separations of 1s and 2s exciton states of the E_{11h} and $E_{11\ell}$ transitions in PLE spectra at low temperatures, after correcting for the 2s binding energy. Transitions were identified in the spectra by comparison with the results of three-band $\mathbf{k \cdot p}$ calculations realized in a computer model written by D.M. Whittaker of the University of Sheffield. Circular polarization experiments also served to definitely

determine light and heavy hole features, which respond differently to polarized light in PLE spectra. They confirmed the identification of the E_{11h} 2s peaks by using low magnetic fields as well as circular polarization, with the 2s peaks showing an upshift in transition energy with magnetic field while the neighboring E_{12h} (1s) peak shows a splitting with little displacement of the center of gravity. Allowing 1.1 meV for the binding energy of the 2s exciton, they found the binding energy of the 1s heavy hole exciton to be 7.0 meV for the sample with x = 0.045, 6.4 meV for the sample with x =0.02 and 5.9 meV for the sample with x = 0.01. Comparable light hole values were 0.1 meV smaller. All of these values are significantly above the 4.2 meV observed for 3D excitons in bulk GaAs, providing further evidence of quantum confinement, although the shallow quantum well binding energies are smaller than the binding energies observed for excitons in deep quantum wells The experimental binding energies were in close agreement with theoretical calculations using variational techniques employing non-separable wavefunctions and adapted for the fact that in a shallow quantum well the Coulomb interaction is of the same order as the confinement potential.

Simmonds et al. also observed increasing quenching of the PLE response due to below barrier QW continuum transitions as x was decreased. This made weak transitions more prominent relative to the background in the PLE spectrum. The phenomenon was attributed to the weaker confinement allowing photocreated carriers to migrate to the substrate or surface more readily. Feldmann, Goossens et al. [26] found that it only takes 21 ps for free carriers to tunnel out of a shallow quantum well, and escape can be much faster (down to 5.5 ps) if the barrier height is reduced by an electric field or the temperature is high enough to allow phonon assisted escape.

5.3.2 The 20/20 Shallow "Superlattices"

The 20/20 samples are described in Table 5.1 and are identical to the ones discussed in Simmonds et al. [158] apart from the fact that the barriers are only 20 nm wide instead of 50 nm wide. These samples are described in the doctoral dissertation of Wendy I. Tagg [276] as shallow superlattices. The reduction in barrier width seen in these samples is theoretically sufficient to allow wavefunctions to penetrate the barriers into adjoining quantum wells, thus causing a significant broadening of the transition levels into mini-bands. This broadening is greatest for the samples with the smallest aluminum content in the barriers. Miniband widths of up to 2 meV for the electron and the light hole in the x=0.01 sample were calculated using a three band **k·p** model realized in a computer program written by D.M. Whittaker of the University of Sheffield. The minibands associated with x=0.045 barriers are already so small that it was recognized that even theoretically the sample should have virtually no superlattice character [276]. PLE spectra of these samples were taken by Wendy I. Tagg and are described in her dissertation. She attributes increased broadening seen in the x=0.01 and x=0.02 samples with respect to their sister samples with 50 nm barriers to miniband effects. There may indeed be some interwell coupling that is responsible for the broadening, but it is believed that none of the samples can be considered as superlattices in practice. This is because there is no significant difference in measured transition energies and separations between the "superlattice" samples and the corresponding wider barrier samples. The discrepancy between theoretical and experimental results is likely to be due to the disruptive effect of electric fields on the miniband structure. That such fields are present is confirmed by the appearance of the parity forbidden E_{12h} peak in PLE and reflectance spectra.

5.4 5K REFLECTANCE SPECTRA

Figures 5.2-5.4 show the 5K 20/50 reflectance spectra taken by the author in association with 5K PLE and PL spectra taken by Simmonds et al. [158]. The excitonic transitions identified in PLE are mostly also visible in reflectance, with E_{11h} at 1.5182 eV for x=0.01, 1.51965 eV at x=0.02 and 1.5214 eV for x=0.045. The corresponding $E_{11\ell}$ energies are 1.51945 eV, 1.5215 eV and 1.5240 eV. The basic lineshapes are described by the classical model for reflectance due to a simple harmonic oscillator, but the principal transitions show considerable extra structure on the wings of the transitions due to interference effects between the layers. The linewidths are very narrow (down to 0.126 meV for E_{11h} for x=0.01) but become broader as x is increased. The 20/20 spectra shown in Figures 5.6 and 5.7 each agree closely in fitted parameters with the 20/50 sample where x is the same, as does the single QW spectrum shown in Figure 5.6. Apparent differences are due to the different phase shifts between reflectance from the surface and the QW interfaces, and in some cases broader linewidths in the 20/20 sample spectra (and for the single QW).

Some of the higher energy transitions appear in PLE but are washed out in reflectance, especially in GWS482 (x=0.045). This is due to small oscillator strengths as well as the quenching of continuum transitions discussed by Simmonds et al. [158]. The positions of the transitions that do appear support the conclusions of Simmonds et al. with respect to binding energies and the 2-D nature of the transitions. (These positions are tabulated for E_{11h} in Table 5.2 and for all the transitions in Table I of the appendix to this chapter.) Figure 5.5 shows all the 20/50 samples offset for comparison. The theoretical baseline reflectance for each of these samples is approximately 30% and the zeroes are indicated.

Figure 5.6 shows the 5K reflectance spectra of the x=0.02 samples. A spectrum of the same 20/50 sample shown in Figure 5.3 is displayed together with the spectrum of the comparable 20/20 sample and the spectrum of a 20 nm single QW enclosed in 500 nm x=0.02 barriers. The x=0.01 and x=0.045 20/20 and 20/50 samples are shown together for comparison in Figure 5.7. Apparent differences in the spectra are primarily due to interference effects caused by differences in optical path between the surface and the quantum well interfaces in each of the samples, although differences in linewidth play some role.

The following schematic diagram of a quantum well in the x = 0.01 sample GWS485 shows the principal transitions that occur in the well.

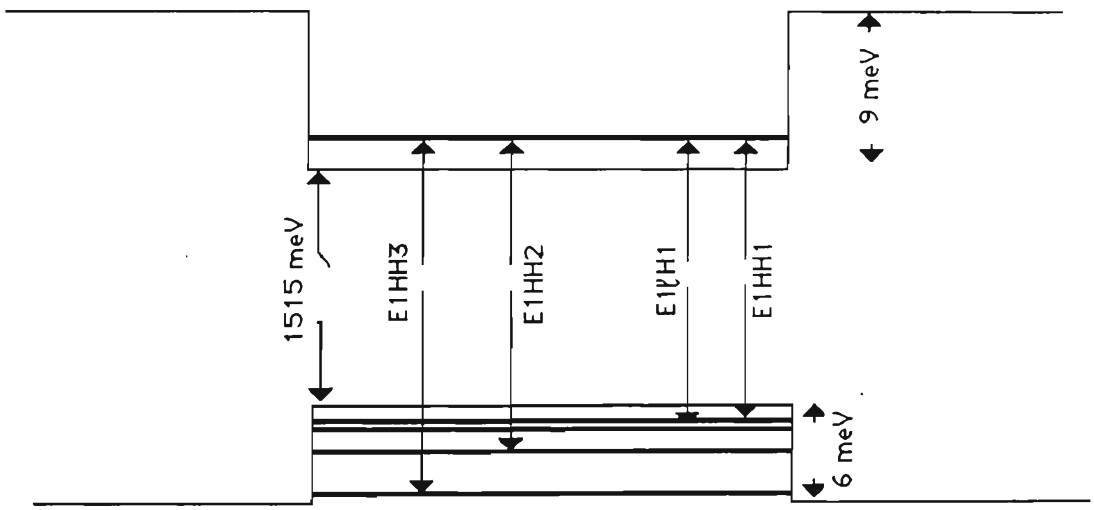

20 nm GaAs well set between 50 nm 1% barriers. Labels show how electrons combine with holes from various levels to form excitons whose recombination peaks are seen in PLE spectrum. Free electrons and holes readily tunnel out at low T.

Figure 5.1 **Schematic of shallow QW transitions.**

5.4.1 Reflectance Features Arising from the Quantum Wells

The transitions labelled in Figures 5.2 - 5.4 have their origins in the quantum wells, apart from the bulk buffer GaAs exciton and the very high energy

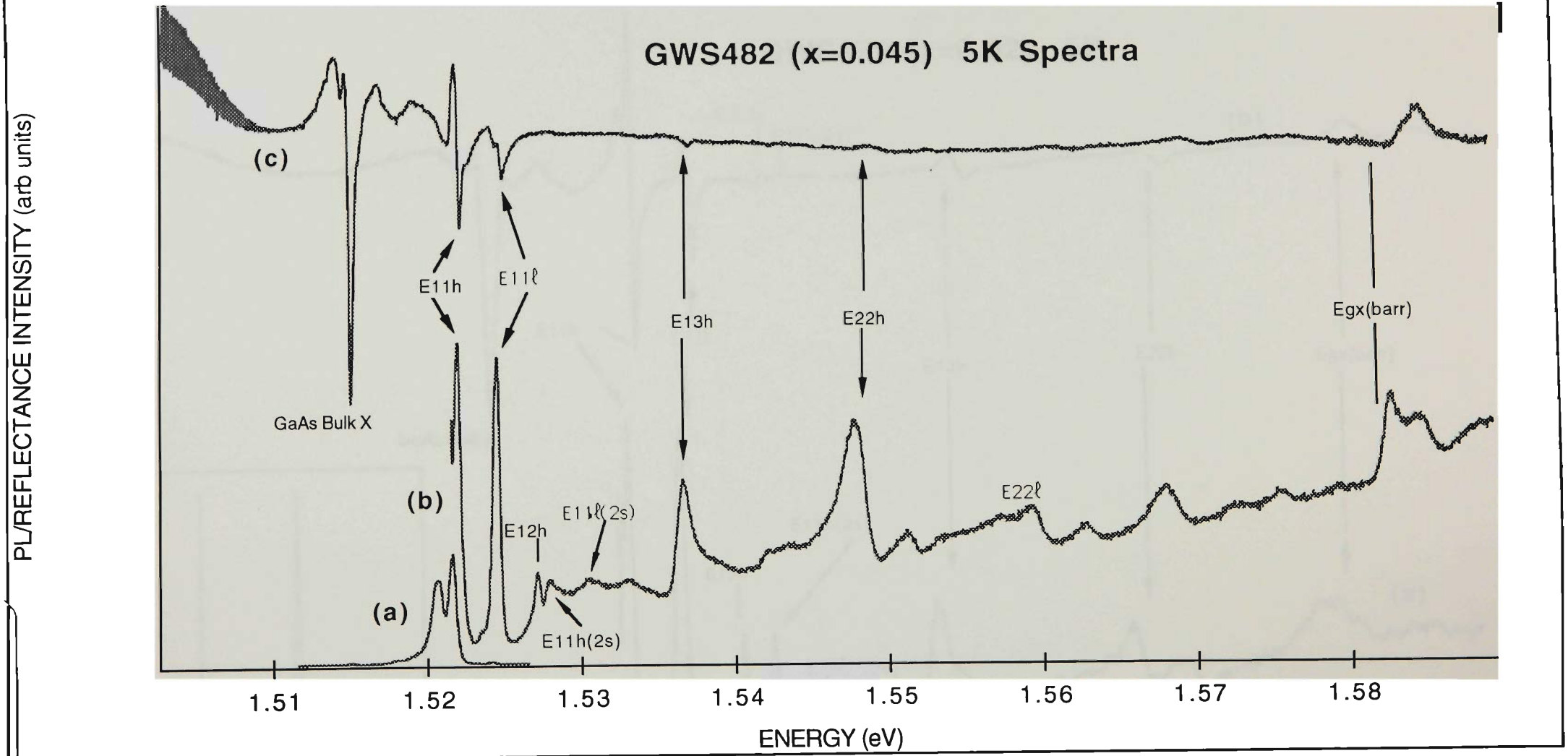

Figure 5.2 GWS482 has wide and shallow 20 nm quantum wells between 50 nm $Al_{0.045}Ga_{0.955}As$ barriers. (a) 5K PL spectrum showing peaks related to E_{11h} exciton with lower energy peak showing extrinsic recombination in the wells (b) 5K PLE spectrum reveals higher transitions as does (c) the 5K reflectance spectrum. Note the very small Stokes shift. Egx(barr) is due to transitions in the barriers. Reflectance spectra are offset, Figure 5.5 shows the true zeroes. (a) and (b) from Simmonds et al. [158].

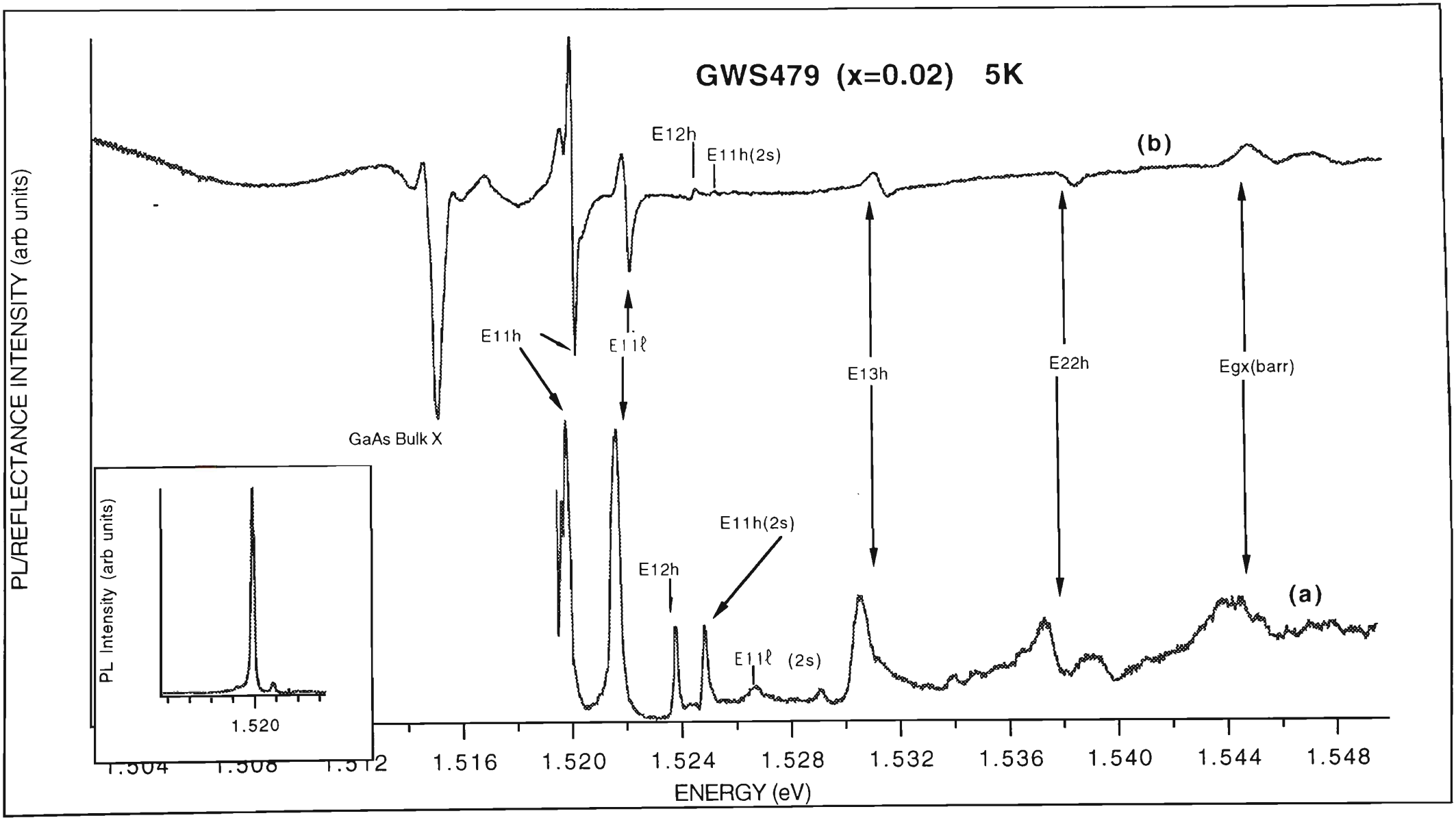

Figure 5.3 GWS479 has 20 nm GaAs wells and 50 nm $Al_{0.02}Ga_{0.98}As$ barriers (a) 5K PLE and (b) 5K reflectance Inset shows 5K PL spectrum showing two lowest transitions in the wells. PLE and PL spectra from Simmonds et al. [158].

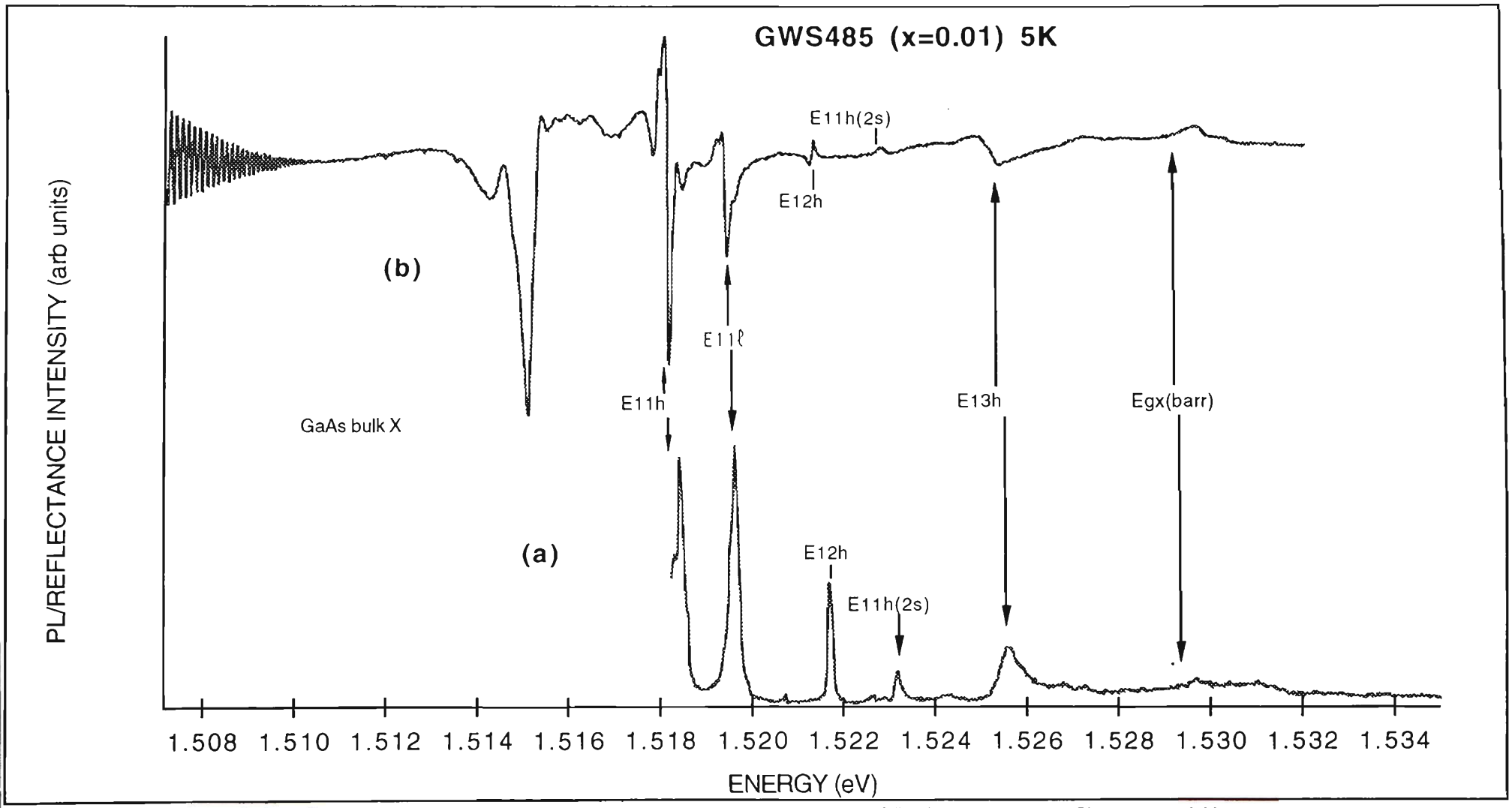

Figure 5.4 GWS485 has 20 nm GaAs wells and 50 nm $Al_{0.01}Ga_{0.99}As$ barriers (a) 5K PLE from Simmonds et al. [158] (b) 5K reflectance. The PL spectrum of this very shallow quantum well sample is very weak. Higher energy states seen in Figures 5.1 and 5.2 are absent due to the lack of confinement. Note that the parity forbidden E_{12h} transition is phase reversed with respect to the principal transitions.

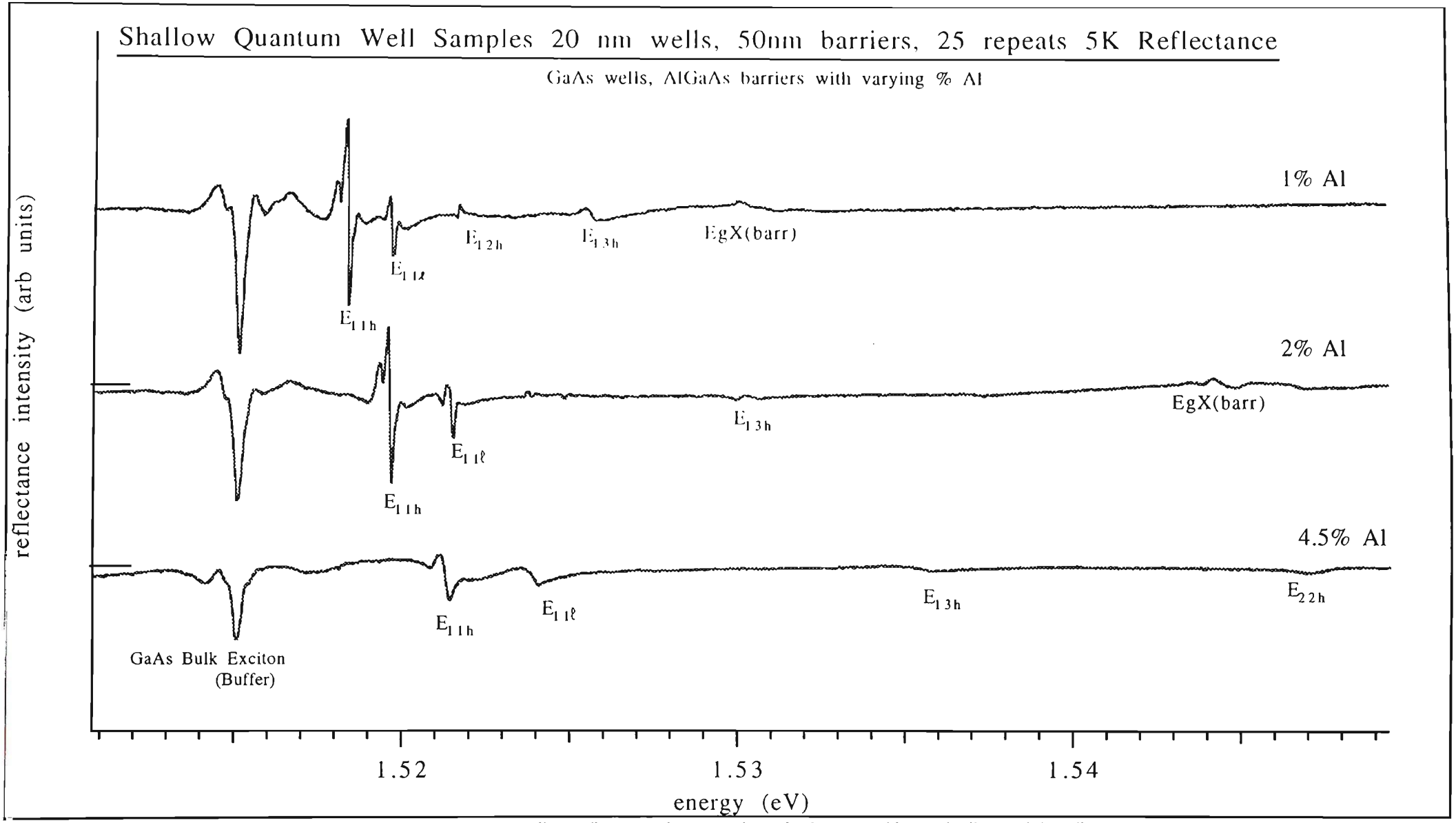

Figure 5.5 Reflectance spectra for the 3 20/50 samples. The baseline reflectance is approximately the same (theoretically 30%) for all spectra. Upper two have been offset with zeroes indicated on the y axis. Note that transitions are broadened and shifted up in energy as the Al content of the barriers is increased. All principal absorption transitions are observed in the reflectance spectra.

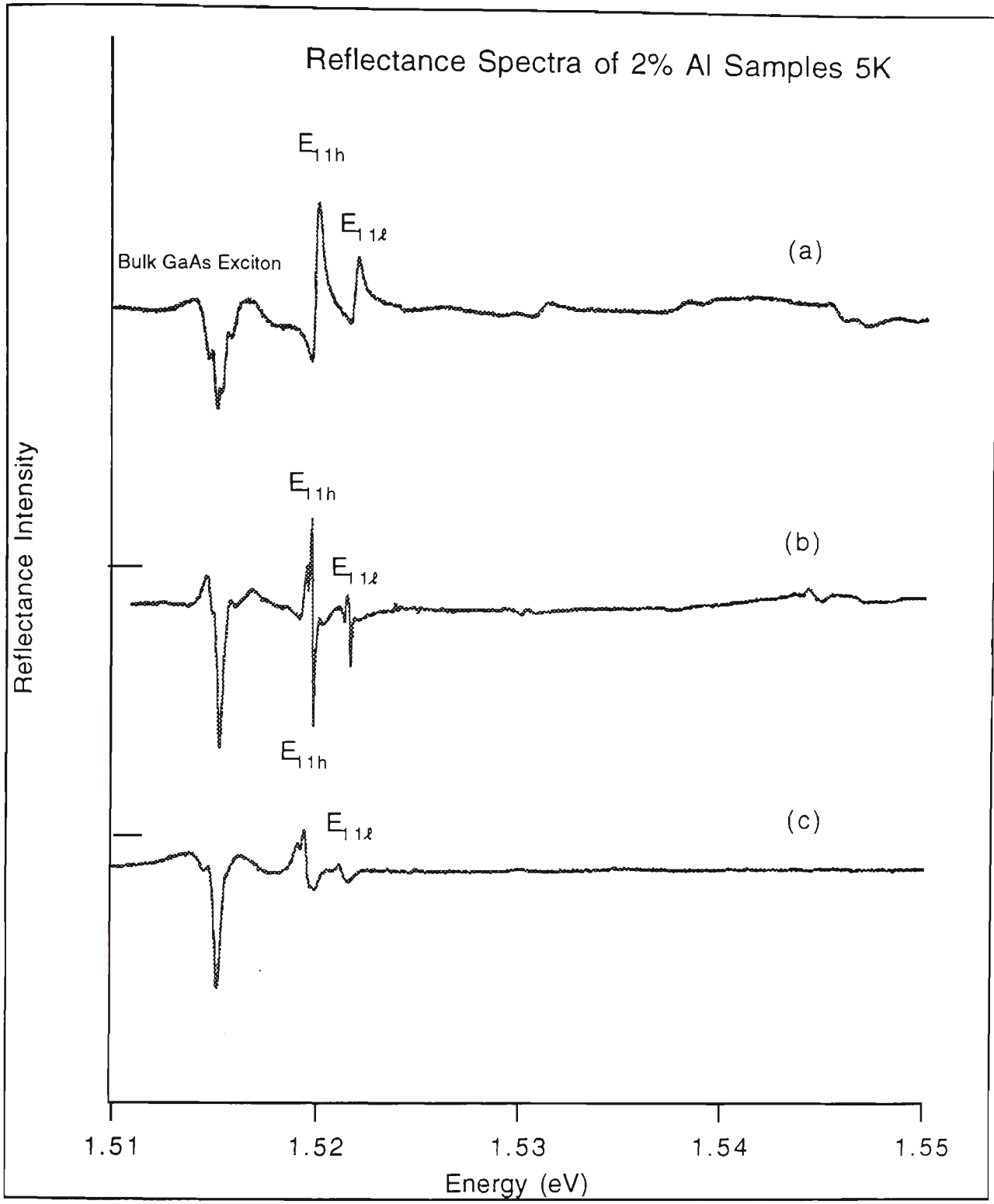

Figure 5.6 All x=0.02 samples agree in oscillator strength. Apparent differences are due to differences in linewidth and especially differences in phase because of differing optical path differences between the surface and the QW interfaces in each sample. (a) GWS463 is a 20 nm single QW (b) GWS479 is a 20/50 MQW. A detailed spectrum is shown in Figure 5.3 (c) GWS359 is a 20/20 MQW. The other 20/20 samples are also phase reversed with respect to the comparable 20/50 samples. Upper two spectra are offset with the zeroes indicated on the y axis.

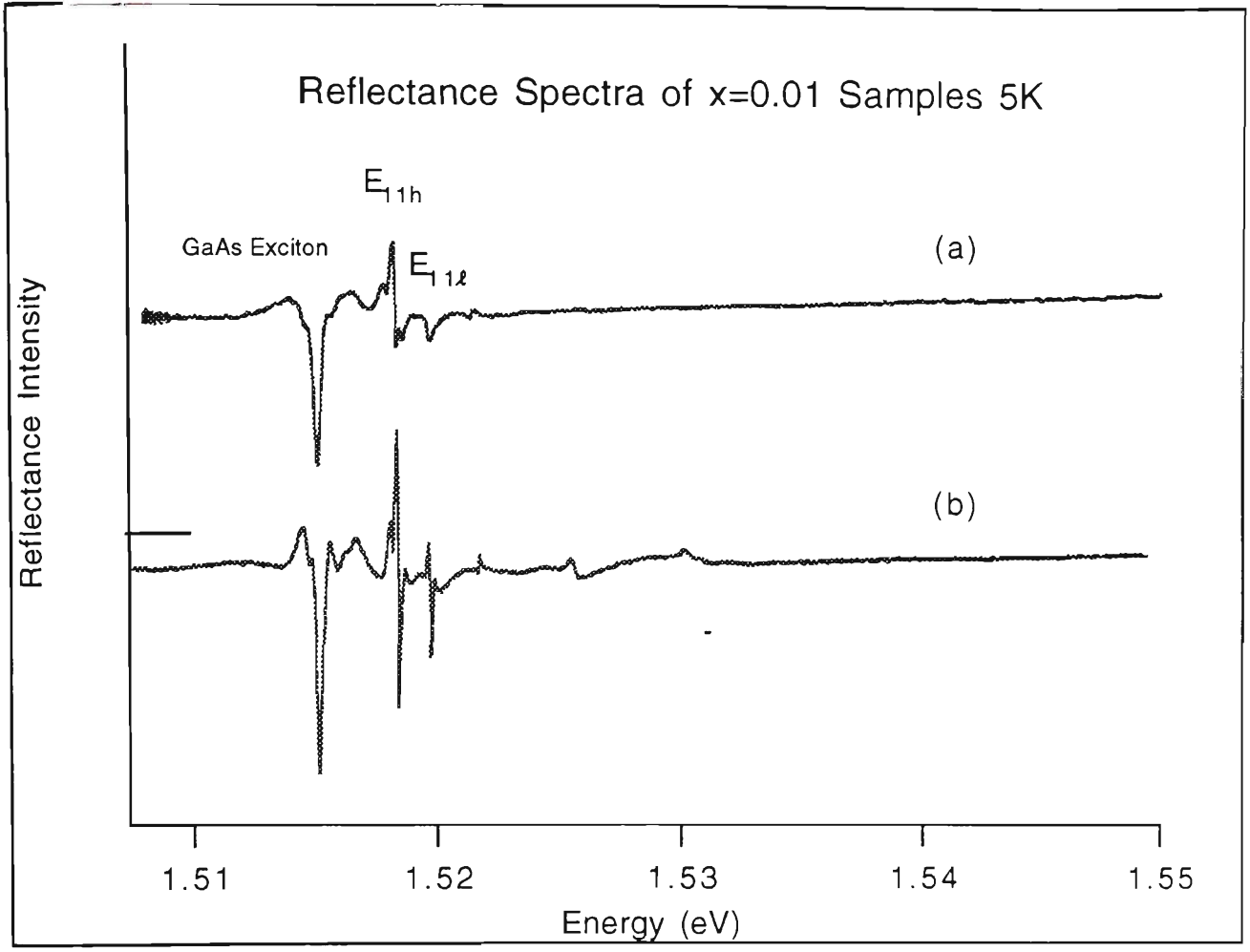

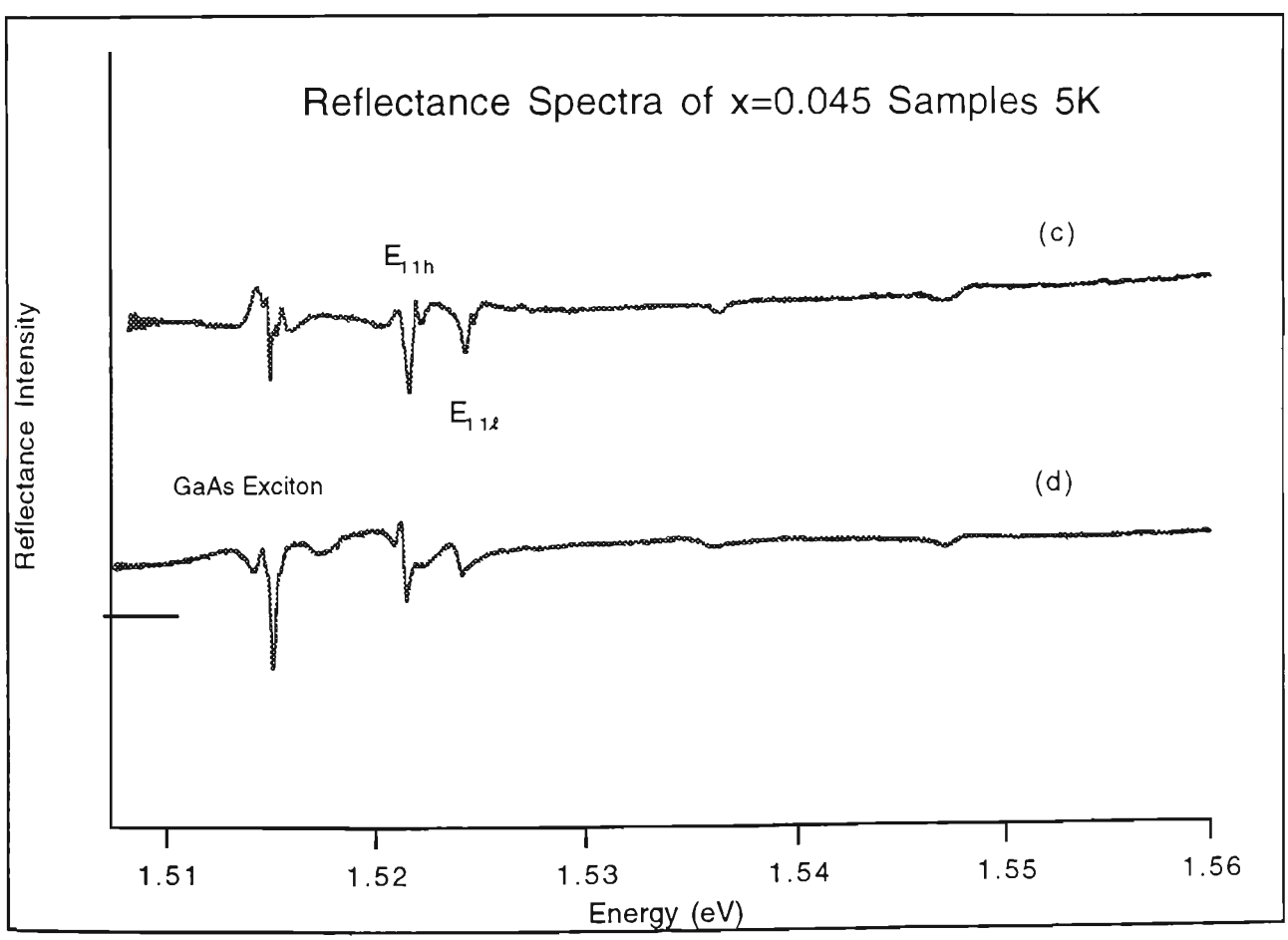

Figure 5.7 20/20 samples shown with comparable 20/50 samples. Zeroes of upper traces indicated on y axis. (a) GWS360 20/20 x=0.01 (b) GWS485 20/50 x=0.01. Figure 5.4 contains a labelled high resolution spectrum. (c) GWS280 20/20 x=0.045 (d) GWS482 20/50 x=0.045. Figure 5.2 contains a labelled high resolution spectrum. Apparent differences between (c) and (d) are entirely due to phase. (a) also has broader linewidths than (b)

transitions shown as occurring in the $Al_xGa_{1-x}As$ barriers. The phase difference between the reflectance features of the bulk exciton and the higher transitions is due to the optical path differences between the surface and the relevant regions which give rise to the reflected waves and lie at different depths in the sample, as well as electric fields caused by different residual impurity and defect concentrations in the buffer and the first barrier layer [175]. In the PLE spectra in Figures 5.2-5.4 the strong apparent oscillator strengths of the lowest light hole peak and some of the higher transitions relative to what is seen in the companion reflectance spectrum are artifacts of the PLE process, possibly associated with overabsorption effects. The E_{12h} transition is parity forbidden and requires the presence of electric fields to be manifested. It can be seen in the x=0.01 reflectance spectrum that the E_{12h} transition is phase reversed with respect to the allowed lower transitions. The 2s transitions are due to excited excitonic states of the E_{11h} and $E_{11\ell}$ transitions. Asymmetric higher energy peaks in the PLE spectra are due to Fano type resonances with continua or excited states of excitons with lower labels.

Note that that there are confined subbands for both electrons and holes, even at the low x value of 0.01. There are more confined levels in standard deep QWs, but it can be seen in Figure 5.5 and the earlier figures that higher electron and hole levels drop out as the well becomes shallower in accordance with theoretical predictions, so that two electron levels are seen when x = 0.045, but only one when x is smaller. Figure 5.5 shows the reflectance spectra of the different 20/50 samples displayed together, showing the greater upshifting and broadening of the transitions as x is increased and the potential barriers raised at the interfaces.

5.4.2 Low Energy Features in the Reflectance Spectra

The reflectance spectra shown in the figures include oscillations at low energy due to interference arising from reflectance from the back of the sample of light with energies below the GaAs bandgap. There is also a strong but distorted transition feature in the correct energy position to represent the bulk GaAs exciton in the GaAs buffer layer between the substrate and the quantum wells. This transition does not appear in the PLE spectra because it is below the detection energy. Similar lineshape distortion of the bulk exciton is seen in earlier reported spectra (e.g. Pearah et al. [277]) and is explained by Novikov et al. [278] on the basis of photoreflectance and differential photoreflectance measurements on epitaxial GaAs layers as due to electric fields set up by residual impurities and defects at the buffer/substrate interface. This effectively shifts the position of the bulk exciton to a higher energy near the interface with the substrate, causing interference with the normal exciton generated in other regions of the buffer. The observed distortion varied from spot to spot in these samples, but was not affected by the polarization of the incident light, as it probably would be if the distortion were due to level splitting caused by strain on the sample. The distortion is also seen in reflectance spectra of the comparison sample GWS507. This sample only contains a buffer and an x=0.02 barrier, so it only shows bulk transition features.

5.4.3 Fitting the Reflectance Spectra

Reflectance spectra must be fitted to a theoretical description to be interpreted. This is because light reflected from the surface of the sample interferes constructively or destructively with waves reflected from the interfaces between the various layers. Differences in optical path between the reflected waves can result in radically different line shapes (phase

shifts) for oscillators with the same parameters. (The subject of phase is discussed in Section 3.1.7)

Fitting in the present work is done by simulation using the various lineshape formulas with certain variables treated as adjustable parameters until there is a good match with the corresponding experimental spectrum. Allowance is made using optical transfer matrices for interference effects between the layers of the sample. As discussed in Sections 3.1.7 there is always a surface layer into which excitons are assumed not to penetrate, and thus a phase shift due to differing optical path between layers reflected directly from the surface and rays reflected from the bottom of the exciton free dead layer where the refractive index is changing. This phase shift is simulated by assuming a dead layer on top of the sample and adjusting its depth until a satisfactory match is assumed. Most attention is given in fitting to the region of principal reflectance modulation close to the transition energy (corresponding to the center of the absorption line), since the fit on the wings of the transition is less perfect, because there is less absorption of light and sampling occurs to a greater depth.

Several formulas for the dielectric function for use in calculating reflectance have been discussed in Sections 3.1 and 3.3.1, which use oscillator strength (or a parameter related to it), linewidth, transition energy position and phase shift as adjustable parameters. The main lineshape formulas are repeated here for convenience.

1. Semiclassical formula:

$$\tilde{\varepsilon}(E) = \varepsilon_b + \sum_j \frac{A_j}{E_j^2 - E^2 - i\Gamma_j E} \tag{3.3}$$

Γ_j is the phenomenological homogeneous broadening (comparable to FWHM) associated with transition j. The parameter A is defined in the work of Gil et al. [155], where it was given as $A_{\alpha\beta}=4\pi\Phi_{\alpha\beta}\omega^2_{\alpha\beta}$ with $4\pi\Phi_{\alpha\beta}$ the excitonic polarizability for the transition $\alpha\beta$. This definition is appropriate for reflectance from bulk samples. For quantum wells A is defined in SI units as

$$A = \frac{e^2\hbar^2}{\varepsilon_o m_o}\frac{f^A_{xy}}{L} \tag{3.4}$$

where L is the width of the quantum well in and $f_{xy}{}^A$ is the oscillator strength per unit area appropriate for normal incidence

The relationship between A and the integrated absorption coefficient $A_{n,m}$ whose relationship to the oscillator strength per unit area is given in (3.32) is $A = 2nc\hbar A_{n,m}/\pi$, with n the background refractive index.

2. Andreani [146] full non-local transfer matrix for the reflectance effects of a transition:

$$T^{TE} = \frac{1}{\Delta_T}\begin{pmatrix} \exp(ik_z L)(\Delta_T - i\Gamma_o) & -i\Gamma_o \exp(ik_z L_b) \\ i\Gamma_o \exp(-ik_z L_b) & \exp(-ik_z L)(\Delta_T + i\Gamma_o) \end{pmatrix} \tag{3.19}$$

where terms are as described in Section 3.1.8.1. It should be noted here that Γ_O is the intrinsic radiative linewidth (HWHM), which is directly proportional to the oscillator strength per unit area and γ is the energy linewidth (HWHM) due to all sources of (homogeneous) scattering apart from the intrinsic linewidth. The transfer matrix for the entire MQW can be derived by multiplying the transfer matrices for the individual periods. The coefficient of reflection for the multi-quantum well $r^s_{QW} = -T_{21}/T_{22}$, the ratio of the corresponding matrix elements. Γ in (3.3) is equivalent to 2γ, with Γ_o neglected. The relationship between Γ_o and the oscillator strength per unit area is given by (3.22).

3. Humlíček et al. [193] formula convolving a Lorentzian lineshape derived from a semiclassical formula such as (3.3) with a Gaussian for cases where inhomogeneous broadening is significant:

$$\varepsilon_{LG}(E) \approx \varepsilon_{\infty} + \frac{\sqrt{\pi}F}{2E_{o}\Gamma_{G}} i\left[w\left(\frac{E-\langle E_{o}\rangle}{\Gamma_{G}} + i\frac{\Gamma_{L}}{2\Gamma_{G}} \right) - w\left(\frac{E+\langle E_{o}\rangle}{\Gamma_{G}} + i\frac{\Gamma_{L}}{2\Gamma_{G}} \right) \right] \quad (3.37)$$

$\varepsilon\infty$ is the background dielectric constant, F is a parameter proportional to the oscillator strength, Γ_L is the Lorentzian broadening, equivalent to the FWHM of the absorption peak (equivalent to Γ in (3.3)) and the Gaussian broadening Γ_G is the standard deviation of the Gaussian function in the convolution. The FWHM of this Gaussian is equivalent to 2.36 Γ_G.

w(z) is the complex probability function

$$w(z) = \frac{i}{\pi}\int_{-\infty}^{\infty} \frac{e^{-t^2}}{z-t}\,dt \quad (3.38)$$

where z is a complex number with a positive imaginary part

Table 5.2 gives the parameters extracted from the fits in the case of the E_{11h} transition. Parameters deduced from the fits for all the transitions observed appear in Table I in the Appendix to this chapter. Table II in the Appendix gives a comparison of reflectance and PL linewidths, while Table III gives linewidth and oscillator strength results reported in the literature. In all the tables reporting the present work errors express the extent to which a parameter can be changed without markedly degrading the fit between the experimental and theoretical results.

Apart from GWS482, all the other samples can be satisfactorily fit without explicitly taking inhomogeneous broadening into account, by the use of the local semiclassical formula, as in equation (3.3), or the nonlocal Andreani transfer matrix most appropriate for extremely narrow linewidths, as in equations (3.19) and (3.20). Both the local and nonlocal methods give equivalent results within the errors for the transition energy and the

Table 5.2 Parameters extracted from local and nonlocal fits of shallow quantum well spectra for the E_{11h} transition. Data for all transitions observed and explanatory notes are in Table I of the appendix to this chapter. Γ_0 is intrinsic radiative broadening, γ other homogeneous broadening. GWS482 has a convolution fit, with Γ_G the Gaussian component, Γ_L the Lorentzian.

	Transition Energy (PL and PLE)	Transition Energy (Reflectance Fit) (meV)	Γ Linewidth (eq. to FWHM) local fit (meV)	Γ Linewidth (eq. to FWHM) nonlocal fit $\Gamma=2\gamma+2\Gamma_0$ (meV)	A local fit parameter $(meV)^2$	Oscillator Strength per unit area $(Å^{-2}\times10^{-5})$
GWS479 20/50 SL (x=0.02)	1519.65	1519.65±0.1	0.11±0.005	0.17±0.02 [γ:0.05±0.005, Γ_0:0.037±0.005]	5100±400	74±6
GWS485 20/50 SL (x=0.01)	1518.3	1518.20±0.05	0.06±0.005	0.126±0.006 [γ:0.035±0.002,Γ_0: 0.028±0.001]	3500±500	51±7
GWS280 20/20 SL (x=0.045)	1521.5	1521.74 ±0.05	0.25±0.02	0.35±0.03 [γ:0.14±0.01, Γ_0:0.034±0.002]	5000±500	73±7
GWS359 20/20 SL (x=0.02)	1519.5	1519.4±0.1	0.19±0.03	0.32±0.03 [γ:0.12±0.01, Γ_0:0.038±0.002]	5200±500	76±6
GWS360 20/20 SL (x=0.01)	1518.3	1518.3±0.1	0.12±0.02	0.17±0.03 [γ:0.06±0.01, Γ_0:0.025±0.002]	3500±500	51±7
GWS463 20 nm single QW (x=0.02)	1519.9±0.05	1519.8±0.1	0.21±0.02	0.31±0.03 [γ:0.12±0.01, Γ_0:0.037±0.002]	5200±500	76±6
GWS482 20/50 SL (x=0.045)	1521.95	1521.4 ±0.1	0.30±0.02 [Γ_L : 0.12±0.01, Γ_G :0.12±0.01]	not fitted	5500±500	80±4

oscillator strength. Figure 5.8 and 5.9 show various local and nonlocal fits of reflectance spectra of the 20/50 ml samples, while Figure 5.10 shows local and nonlocal fits of the same reflectance spectrum of a 20/20 sample. The local and nonlocal formulas also give equivalent results for the total transition linewidth where the intrinsic radiative linewidth Γ_o is small with respect to other sources of broadening. This can occur either where transitions are broad or where transitions are sharp, but have a very small oscillator strength per unit area forcing Γ_o to be small in relation to other sources of broadening. The E_{12h} transition seen in spectra of GWS485 (x=0.01) is an example of this second case. For very narrow strong transitions such as E_{11h} in GWS485, Γ_o can no longer be neglected and nonlocal methods are necessary to determine the correct linewidths. Here the nonlocal formula results in a fit with significantly larger total linewidths as can be seen in Table 5.2.

In the case of low temperature spectra of GWS482, a sample with x=0.045 barriers, a good fit for the $E_{11\ell}$ transition could not be achieved without the use of the Humlíček et al. [193] local convolution formula embodied in equations (3.37) and (3.38) which explicitly takes account of inhomogeneous broadening. The reflectance transitions are sufficiently broad in this sample that it is reasonable to neglect Γ_o and use the local approximation. Fits are best when it is assumed that the broadening is approximately 50% inhomogeneous. Figure 5.11 illustrates this fit. The superiority of the convolution formula for the sample with the highest Al content is expected, since the additional broadening occurring as the Al content of the barriers is increased should be inhomogeneous. It is not clear why the E_{11h} transition, which is narrower and should show the effect of inhomogeneous broadening more clearly does not show a superior result when the convolution fit is used, and it is always possible that the superior fit for the light hole transition is

simply due to a quirk. However, when a low temperature PL spectrum of this sample is fit using a PL simulation program the best fits are also achieved by assuming that the broadening is 40% to 60% inhomogeneous.

In some of the other samples such as GWS280 and GWS463 linewidths are broad enough that inhomogeneous broadening can reasonably be suspected. There is no significant difference with these samples between a convolution fit with Gaussian equal to Lorentzian broadening or a fit assuming that the broadening is purely homogeneous. Whether there is a visible difference between the two simulations seems to depend on the 'dead layer' phase parameter.

The convolution algorithm also provided a method of testing the extent to which the narrowest transitions in the reflectance spectra were resolution limited, since a question arises as to how much of the apparent linewidth of a transition is in fact due to the spectral bandpass associated with the spectrometer slit width. (Spectral bandpass is discussed in Chapter 4.) The effect of this can be simulated by assuming that the effect of the slits is to convolve the essentially Lorentzian function of a narrow transition with a Gaussian. Linefits demonstrated that the very worst case spectral bandpass with the narrowest transitions will at most contribute 0.01 meV to the observed broadening.

Much of the additional structure seen on the wings of the reflectance spectra transitions can be theoretically reproduced as a natural consequence of interference effects between the layers arising from the principal transitions alone. There is no need to assume the involvement of bound excitons, impurities or the like as in Pearah et al. [277]. These interference effects on the wings of transitions often cause fitting difficulties because

they are very sensitive to the details of the layered structure. This point is illustrated in Figure 5.8. A better fit can often be achieved by assuming that the transitions are very much broadened in the well nearest the substrate. Doing this does not affect the fitting parameters, and as has been discussed in Section 2.1.3, there is evidence that the first grown of a series of wells is often of lower quality. For reasons which are not clear the nonlocal fit is often better on the wings of transitions than the local, as can be seen in Figure 5.10.

Attempts to fit the GaAs bulk exciton reflectance reveal an anomalously high oscillator strength in the 1% and 2% Al samples compared to the bulk GaAs results of Sell et al. [279] and Evangelisti, Fischbach and Frova [162]. These authors give an excitonic polarizability $4\pi\alpha$ of 1.6×10^{-3} (when energies are in meV). Since for the fitting parameter A discussed above, $A = 4\pi\alpha E_o^2$, in theory A = 3670 $(meV)^2$ for the bulk exciton. Reflectance fits and direct comparisons of percentage of light reflected did give results in this neighborhood for GWS482 (x=0.045 in barriers), although distortion of the lineshape was very severe. Fits ranged from A=8000 to A=10,000 $(meV)^2$ for the x=0.01 and x=0.02 samples. The reason for the apparent high oscillator strengths is unknown.

5.5 5K PHOTOLUMINESCENCE SPECTRA

Photoluminescence spectra were taken in the course of the present work for comparison with reflectance results. At 5K only the E_{11h} and the $E_{11\ell}$ level were visible, although higher transitions did appear as levels were thermally populated at higher temperatures. For GWS482 (x=0.045 barriers) a double peak structure appeared (as seen in Figure 5.2). The lower energy peak does not appear in the 20/20 sister sample and disappears as the

temperature is raised. It has thus been assigned to recombination through impurities in the well or at the interfaces. Apart from this, all of the peaks (including the higher energy peak of the doublet seen in GWS482) showed an asymmetrical structure, with a good fit of the experimental peak only possible by treating the asymmetrical structure as the result of the overlap of two narrow peaks spaced between 0.2 and 0.3 meV apart as seen in the inset of Figure 5.8, with the lower energy peak having lower intensity. The existence of the lower energy peak component in the PL spectrum, which shows no analogue in PLE or reflectance, is attributed to interface roughness or statistically insignificant areas in the sample where the well is wider than the nominal value, allowing excitons to be trapped before radiative recombination.

The simulation program allowed the peaks to be simulated with either Gaussian or Lorentzian lineshapes or with hybrid lineshapes with any fraction of Gaussian or Lorentzian character. Broad peaks resulting from high intensity excitation were best fit as Gaussians. The Gaussian/Lorentzian character of the peaks taken at low excitation (below $0.5W/cm^2$) varied among the samples. GWS485 (20/50, x=0.01 barriers) and GWS479 (20/50, x=0.02 barriers) were best fit as pure Lorentzians or as hybrids with no more than 20% Gaussian broadening. GWS482 (20/50, x=0.045 barriers) was best fit with between 40% and 60% Gaussian character. These results were also supported by the reflectance fits where the x=0.01 and x=0.02 samples could be satisfactorily fit without including any inhomogeneous broadening, whereas a convolution fit produced better results for the x=0.045 sample. Photoluminescence was strongly quenched in GWS360 (20/20, x=0.01 barriers). In general the PL results for the 20/20 samples resembled those for the sister 20/50 samples, with asymmetrical peaks at the E_{11h} position.

The PL peak positions for all the samples agreed with the fitted reflectance positions within 0.3 meV at the very most, and there was also fairly reasonable agreement between the FWHM of the PL peak (taken at low excitation) and the theoretical total broadening ($2\gamma + 2\Gamma_o$) of the reflectance transition as determined by the nonlocal fit. Linewidth results for PL, PLE and reflectance are tabulated in Table II in the Appendix to this chapter. It should be noted that PL linewidths are expected to be broader than reflectance linewidths due to transition mechanisms involving impurities and interface roughness. Note also that the PLE linewidth may be wider than than the PL linewidth due to overabsorption effects.

5.6 REFLECTANCE AND PHOTOLUMINESCENCE SPECTRA AT HIGHER TEMPERATURES

Figure 5.12 shows the typical changes observed in reflectance spectra as the temperature is increased, mainly consisting of the shift of transitions to lower energies and linewidth broadening. As will be explained below, the oscillator strength parameter does not decrease with increasing temperature, despite appearances. Figure 5.13 shows the typical changes expected in a photoluminescence spectrum with increasing temperature. These include the shift of transitions to lower energies and linewidth broadening, which are both also seen in reflectance. In addition, PL intensities are reduced and some of the higher energy transitions which are observed in reflectance become visible. The latter is due to thermal population of the higher electron and hole energy levels in the quantum wells and recombination from those levels.

5.6.1 Changes in transition energy position with temperature

As the temperature is raised, the excitonic transitions occur at lower energies. The fundamental process involved is the shrinkage of the GaAs

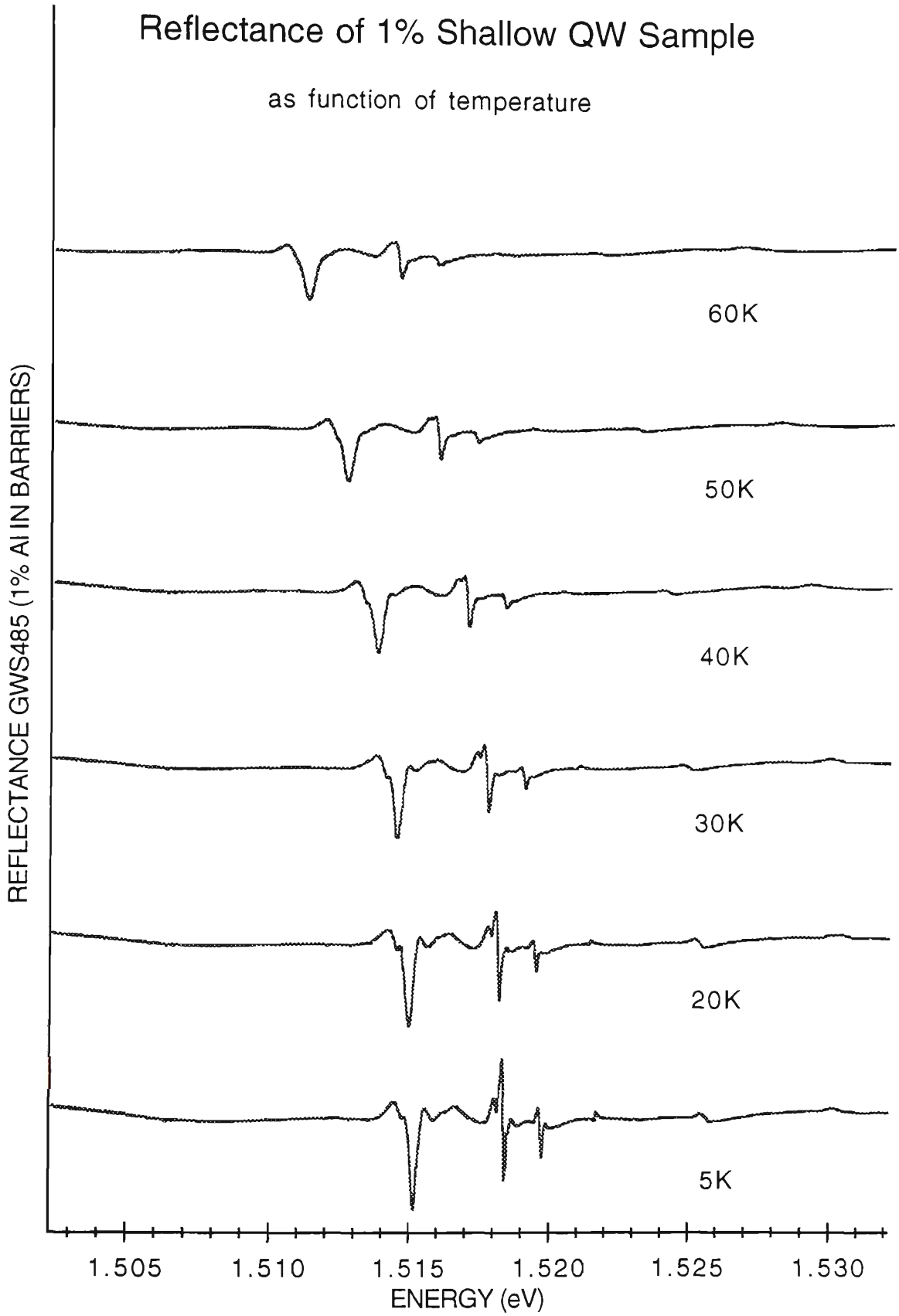

Figure 5.12 Transitions are broadened and shifted to lower energies as the temperature is increased. The spectra are offset to show the changes, with the baseline reflectance the same for all. Despite appearances the oscillator strength parameter needed to achieve a good fit does not change with temperature.

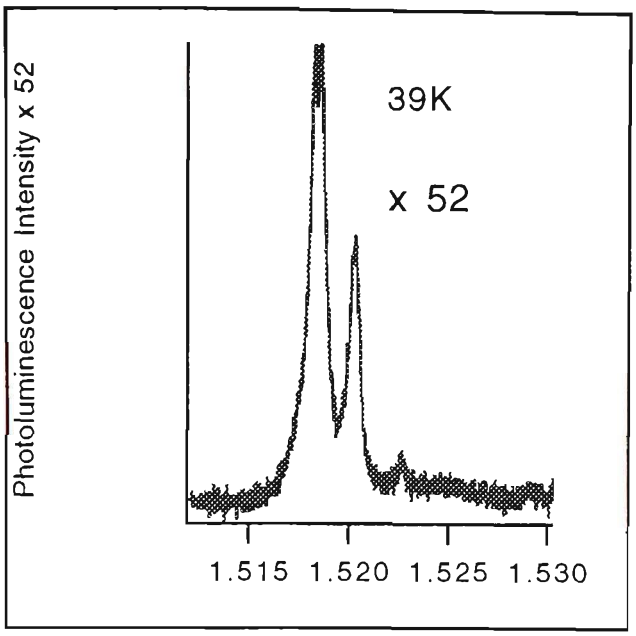

Figure 5.13 Typical changes in a PL spectrum as the temperature is increased. Note reduced PL intensity and higher transitions showing that higher energy subbands are being thermally populated as the temperature increases. Note also that the transition linewidths broaden with temperature.

host material bandgap, which is responsible for the energy position temperature dependence of the transitions in the quantum wells [18,156]. The shifts are as expected with the change in temperature. Temperature dependence of the bandgap is discussed in Section 1.1.4.

5.6.2 Changes in transition linewidth

As was explained in Section 3.3, the excitonic transitions broaden as the sample temperature is raised, due principally to the linear temperature dependence associated with acoustic phonon scattering and the exponential temperature dependence associated with optical phonon scattering. The temperature dependent broadening would normally only apply to homogeneous broadening. For GWS482 (x=0.045 barriers) where inhomogeneous broadening is significant, fitting was done by retaining the 5K value of the Gaussian broadening and broadening the Lorentzian component until a fit was achieved. Due to the greater linewidths and the greater uncertainties involved with fitting an extra parameter, uncertainties are greater in the fits for this sample, especially for $E_{11\ell}$ where the fit was difficult in any case.

Below 70K to 80K the only significant source of broadening with temperature is expected to be acoustic phonon scattering. As seen in (3.39) and the discussion in Section 3.3.2.2 broadening due to this type of scattering is theoretically predicted to be linear. The experimental results in this temperature range are in fact linear, as can be seen in Figure 5.14 where the fitted experimental linewiths are plotted against the temperature, with the slope of the linear fits giving the linear scattering coefficient γ.

The linear scattering coefficient γ is determined to be 3.0±0.4 μeV/K for E_{11h} and 4.5±0.4 μeV/K for $E_{11\ell}$. See Table IV in the appendix to this chapter for

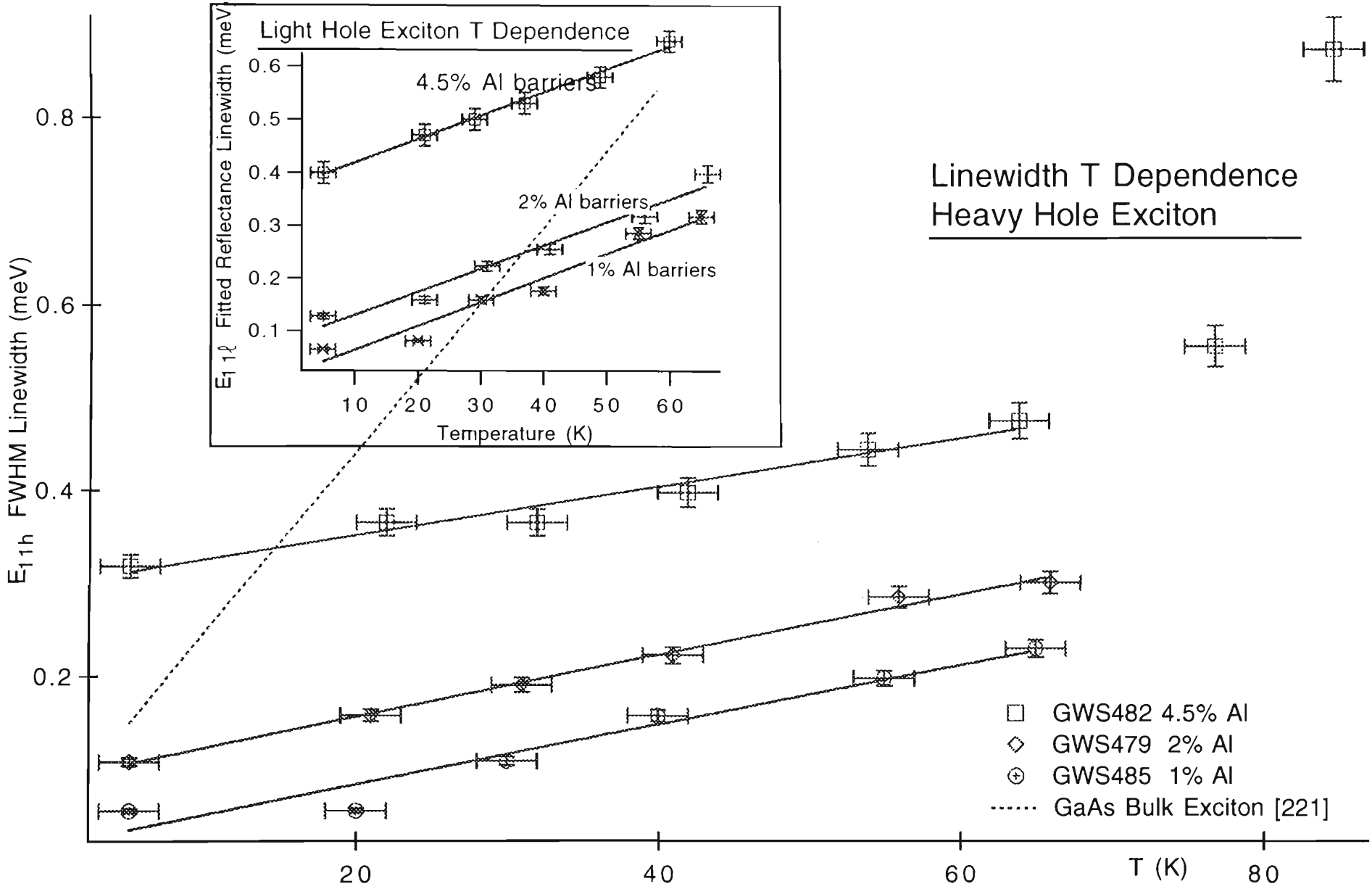

Figure 5.14 Linewidth temperature dependence in reflectance of the 20/50 ml shallow QW samples.

earlier published values for γ in quantum wells and in bulk. The uncertainties for the present light hole result are determined on the basis of the two shallower samples. The results for GWS482 (4.5% Al in the barriers) agree (fitted coefficient 4.3 μeV/K) but the uncertainty is on the order of ± 1 μeV/K. The present results are in general agreement with published values for deep quantum wells (Lee, Koteles and Vassell [216], Schultheis et al. [222], Srinivas et al. [214], Vinattieri et al. [234]) and much smaller than the Schultheis et al. [222] value for bulk GaAs (but comparable with the 7 μeV/K value reported in Humlíček et al. [159] for an epitaxial capped layer).

Previous theoretical and experimental published values for γ differ as to whether there is a significant difference between the coefficients for light and heavy holes and if so, which one should be larger. Lee, Koteles and Vassell [216] believed that the mass dependence of the scattering should imply that the coefficient should be smaller for light holes, while Takagahara [225] placed more stress on the phonon mediated transfer from the light to the heavy hole band causing a larger coefficient for the light hole. Schultheis et al. [222] observed no significant difference in γ between light and heavy holes on the basis of the temperature broadening of transmission spectra. They dispute whether the differences observed by Lee, Koteles and Vassell [216] were in fact significant. Neither was any difference revealed by the temperature dependent photoluminescence measurements of Srinivas et al. [183]. The present results support Takagahara. Table I in the Appendix also shows that the present E_{11} linewidths tend to be somewhat larger than the comparable heavy hole ones at 5K, and Takagahara's reasoning would account for this as well. It may not be possible to generalize the present results to deep quantum wells. The theoretical calculations of Park and Kwon [280] show that the light and

heavy hole excitons behave in a more similar way in shallow quantum wells than they do in deep ones.

Takagahara [215,225] suggests that the temperature coefficient γ should be larger for wider quantum wells due to the smaller inter-subband energy spacing making phonon related transitions more efficient. γ should also be larger for excited states than for ground states for similar reasons and for higher index states involved in Fano resonances. (It should be noted that Schultheis et al. [222] did not find that γ was any larger for the light hole exciton involved in a Fano resonance, although the initial low temperature broadening was significantly greater in this case.) An opposite dependence of γ on well width [218, 281] is also predicted, with γ larger for smaller well widths is predicted by Schmitt-Rink et al. [281] on the basis of density of states considerations. The result of larger γ for thicker quantum wells was supported by the work of Schultheis et al. [222] using measurements of the transmission linewidth as a function of the temperature below 70K where optical phonon broadening is insignificant, but there is no clear trend in other published experimental results. The lack of variation in γ observed here where changes in potential barrier height were due to changes in Al content in the barriers suggests that changes in γ should not be expected when the confinement energy is changed by varying the well width. All results are closely linear, as were the published results, indicating the dominance of one-phonon scattering as a cause of optical dephasing, with any higher order phonon processes insignificant.

Above 70K broadening becomes superlinear, as is shown for GWS482 in Figure 5.14, and as is expected when optical phonon broadening becomes substantial. Experimental uncertainties also become much larger as broadening increases. About the 100K range for GWS485 and GWS482 (before

uncertainties in linewidth become impossibly great) a reasonable fit to the data was provided by Γ_{LO} = 10±2 meV for both E_{11h} and $E_{11\ell}$, in agreement with the results of Chen et al. [282]. The results of Chen et al. were also those in best agreement with the theoretical results of Rudin and Reinecke [226]. It was clear that the broadening with temperature was monotonic, with none of the narrowing observed between 77K and 100K that was shown in spectra for deeper quantum wells published by Zhang et al. [156].

5.6.3 Changes in oscillator strength

In the case of the present data, adequate fits could be obtained up to 150K in some cases without assuming any temperature dependence in the oscillator strength. Small decreases in oscillator strength with temperature were theoretically predicted in Zhang et al. [156], but the magnitude of the predicted effect below 150K is well within the uncertainties in the present data. Transitions do appear weaker at higher temperatures (as is seen in Figure 5.12) but this is an illusion due to the greater broadening. The fitted oscillator strength parameter does not change significantly.

5.7 CONCLUSIONS

5.7.1 Transition Linewidths and the Local and Non-local Models

The present samples produce very high quality spectra, and the principal transitions seen in the reflectance spectra are extremely sharp in the shallow multi-quantum well samples, with linewidths as narrow as the best reported in the literature, as small as 50 μeV for the E_{12h} transition in GWS485 (x=0.01). In the principal transitions in the shallower quantum wells (with x=0.01 or x=0.02 in the barriers) the intrinsic radiative broadening is comparable to the broadening due to all other sources. The light hole transitions tend to be somewhat broader than the heavy hole ones, probably

because of having an additional decay channel (LH1→HH1 intersubband energy relaxation). The energy positions of transitions in reflectance agree very well with those reported in PLE by Simmonds et al. [158] and Tagg [276], as well as the theoretical predictions on the basis of three band **k·p** calculations which they also report. The reflectance work thus lends further support to the 2-D character of the transitions. This agreement in energy position also supports the conclusions of Simmonds et al. [158] with respect to exciton binding energies.

Analysis in terms of local and non-local theoretical calculations gave equivalent results for the energy position and the oscillator strength per unit area of the various transitions. The local method gives a narrower linewidth because it cannot account explicitly for the intrinsic radiative broadening proportional to the oscillator strength discussed in Section 3.3.2.4. This narrowing becomes significant where oscillator strengths are large and transitions narrow. Table 5.2 shows that this theoretically predicted underestimation of the linewidth in the local model [168] is definitely significant in practice for the E_{11h} transition in the x=0.01 and x=0.02 samples. A comparison with Table II in the appendix shows that there is reasonable agreement between the broader total linewidths calculated for this transition in reflectance by the non-local method and the PL and PLE linewidths, bearing in mind the additional sources of broadening in PL and the problems of overabsorption in PLE. It is worth noting that the local result could be corrected in an ad hoc way by calculating the intrinsic radiative broadening Γ_o from the oscillator strength via equation (3.22) and adding $2\Gamma_o$ to the linewidth calculated by means of the local method. This would allow a comparison with PL or absorption data.

5.7.2 Oscillator strengths per unit area

The oscillator strengths per unit area determined from the reflectance fits are considerably larger than the detailed theoretical calculations of Andreani and Pasquerello [29] for a 20 nm quantum well, which estimate an oscillator strength of approximately 30×10^{-5}Å^{-2} for E_{11h} and 13×10^{-5}Å^{-2} for $E_{11\ell}$ for single quantum wells with x = 0.25. Somewhat smaller values still are predicted for shallower barriers and wider wells. In the present work the oscillator strengths for E_{11h} have been determined for the 20/50 samples as $80\pm4 \times 10^{-5}$Å^{-2} for the x=0.045 sample, $74\pm6 \times 10^{-5}$Å^{-2} for the x=0.02 sample and $51\pm7 \times 10^{-5}$Å^{-2} for the x=0.01 sample, with the light hole values smaller by a factor of about 2 as predicted by Andreani and Pasquerello. The real discrepancies are actually even larger, because oscillator strength is expected to increase with x. Apart from the shallowest quantum wells (x=0.01), the present experimental values are also larger than those predicted by Winkler [154] which estimate an oscillator strength of about 50×10^{-5}Å^{-2} for E_{11h} and 20×10^{-5}Å^{-2} for $E_{11\ell}$ for 20 nm single quantum wells with x = 0.4. Table III shows that some authors derive oscillator strengths (for 'deeper' wells) that agree closely with the present ones, especially Zhang et al. [156] and Srinivas et al. [214]. Other authors, such as Gil et al. [155] and Masselink et al. [182], agree more closely with the theoretical results predicted in Andreani and Pasquerello. Only Srinivas et al. reported samples with linewidths as narrow as ours. Due to the close, detailed and consistent fits obtained it is unlikely that the present results for oscillator strength per unit area are as large as they are simply due to experimental error. Possibly the discrepancy arises in the relationship between reflectance, oscillator strength and integrated absorption breaking down in the Citrin regime discussed below. As well as problems with the magnitude of the oscillator strength, some authors, such as Zhang et al. [156] do not find that their

experimental oscillator strengths decrease as the well width increases beyond 150Å, contrary to the theoretically predicted trend [29].

The oscillator strengths per unit area of the E_{11h} and $E_{11\ell}$ ground state transitions in the shallow multi-quantum wells do show some decrease in the present work as the proportion of Al in the barriers decreases and the wells become shallower, as was calculated by Heller et al. [184]. This decrease shows the same trend as that exhibited by the exciton binding energies, with both trends caused by reduced confinement as the wells become shallower. The ratio of the oscillator strengths of the light to the heavy hole excitons is approximately 1:2, as predicted by Andreani and Pasquerello [29].

Citrin [189] suggests that the relationship between the integrated absorption and the oscillator strength breaks down at very narrow transition linewidths, essentially because perturbation theory no longer yields the correct results. He suggests that his theory would be supported by the observation of an anomalously high oscillator strength per unit area, or integrated absorption, for an excited state with respect to its ground state obtained from the absorption spectrum. This is because the excited states are more broadened so that the perturbation theory approximation remains valid for the excited state. There is some evidence from the present work that this anomalous relationship does not appear in the present reflectance results. As explained above the fitting parameter used to determine oscillator strength per unit area from reflectance spectra is also proportional to the integrated absorption. GWS485 (x=0.01 barriers) is a good test case. The E_{11h} exciton is consistently fitted (in the non-local approximation) with a linewidth of 0.13 meV (equivalent to FWHM), of which only 0.07 meV is non-intrinsic. The 2s excited state is prominent enough to be fitted and yields a linewidth of 0.15 meV, with nearly all of it non-intrinsic (The relative

amount of non-intrinsic broadening determines whether the perturbation theory approximation is appropriate.) The oscillator strengths per unit area for the transitions are $51\pm7 \times 10^{-5}$Å^{-2} for the 1s transition and $2.5\pm0.4 \times 10^{-5}$Å^{-2} for the 2s transition, giving a ratio of approximately 1:20 for 2s:1s, which is the ratio reported in Gil et al. [155] where Γ was 3 meV for both the ground and 2s states. (See Table III in the Appendix to this chapter). At the present linewidths there is no evidence of any non-standard effects coming into play in reflectance processes.

5.7.3 The 20/20 shallow "superlattices" and the single quantum well sample

Whether a sample behaves optically as a multi-quantum well or as a superlattice depends on the relative magnitudes of the miniband width and the exciton binding energy (e.g. Fox et al. [283]) For a 'pure' superlattice where the miniband width is greater than the binding energy, the oscillator strength has been predicted and shown to be reduced from the true quantum well situation [284,285]. It is also known that coupling between wells reduces any Gaussian inhomogeneous broadening because the superlattice wavefunctions average over a larger volume [286]. With the 20/20 samples as discussed above, the theoretical miniband width is significant, especially for $x \leq 0.02$ under ideal conditions, but there is no evidence in the present work of miniband effects in the energy positions of exciton transitions. There is also no significant difference in oscillator strength per unit area between the 20/50 samples and the corresponding 20/20 samples. Apparent differences between the 20/50 and the 20/20 spectra are mostly due to phase differences and some extra broadening in transitions in the shallower 20/20 samples, possibly due to interwell coupling. It is likely that the ideal miniband structure is broken down by internal electric fields, whose presence is indicated by the parity forbidden E_{12h} transition.

The single quantum well sample GWS463 which has a 20 nm QW in 500 nm barriers where x=0.02 also agrees with the other x=0.02 samples in oscillator strength per unit area, as would be theoretically expected. There is considerable extra broadening, especially relative to the 20/50 sample, but this finding is not unreasonable. As has been explained in the Section 2.1.3, the first quantum well to be grown in a sample is often of lower quality.

5.7.4 Conclusions on temperature dependence

The energy positions of the principal excitonic transitions as a function of temperature follow the shrinkage of the GaAs bandgap. Below 70K the broadening with increased temperature of the principal transition linewidths is closely linear and is determined to be 3.0±0.4 μeV/K for E_{11h} and 4.5±0.4 μeV/K for $E_{11\ell}$, with no discernable dependence on barrier height. This broadening is consistent with acoustic phonon scattering. Table IV in the Appendix shows that there are also no clear trends in the published results for the linear temperature coefficient varying with confinement. The present discrepancy between the light and heavy hole results implies that the linear temperature coefficient is significantly larger for $E_{11\ell}$ than for E_{11h} (at least for shallow quantum wells), in agreement with the prediction of Takagahara [225]. At higher temperatures the broadening becomes superlinear, as is expected to happen due to optical phonon broadening. The optical phonon broadening coefficient is estimated to be 10±2 meV, again with no dependence on barrier height. There is no significant change in oscillator strength over the temperature range studied.

APPENDIX TO CHAPTER 5

Table I

5K Reflectance Parameters

(a) GWS482 20/50 x=0.045

Transition Label	Transition Energy (PL and Simmonds et al. from PLE peak) (meV)[1]	Transition Energy (Reflectance Fit) (meV)	Γ Linewidth (eq. to FWFM) (meV) Convolution fit parameters in brackets	A Local Fit Parameter $(meV)^2$	Oscillator Strength per unit area (Local model) $(Å^{-2}\times10^{-5})$
E_{11h}	1521.95	1521.4 ±0.1	0.30±0.02 [Γ_L : 0.12±0.01, Γ_G :0.12±0.01]	5500±500	80±4
$E_{11\ell}$	1524.55	1524.0	[Γ_L :0.20±0.01, Γ_G 0.20±0.01]	3500±500	51±7[2]
$E_{11h}(2s)$	1527.85	1528±0.5	dip too small to fit	–	–
$E_{11\ell}(2s)$	1530.35	not visible	–	–	–
E_{12h}	1527.3	prob. incl. in (2s) dip	–	–	–
E_{13h}	1536.7	1537.0±0.5	0.6±0.05	400±100	5.8±1.5
E_{22h}	1548.0	1547.5±0.5	2.5±0.4	1500±300	21.9±4
$E_{22\ell}$	1559.1	not clearly visible	–	–	–

See explanatory notes at end of Table I for references.

(b) GWS479 20/50 x=0.02 5K

Transition Label	Transition Energy (PL and Simmonds et al. from PLE peak) (meV)[1]	Transition Energy (Reflectance Fit) (meV)	Γ Linewidth (eq. to FWHM) local fit (meV)	Γ Linewidth (eq. to FWHM) nonlocal fit $\Gamma=2\gamma+2\Gamma_0$ (meV)	A local fit parameter $(meV)^2$	Oscillator Strength per unit area $(Å^{-2}\times10^{-5})$
E_{11h}	1519.65	1519.65±0.1	0.11±0.005	0.17±0.02 [γ:0.05 ±0.005,Γ_o:0.037±0.005]	5100±400	74±6
$E_{11\ell}$	1521.55	1521.5±0.1	0.13±0.005	0.14±0.02 [γ:0.055 ±0.005Γ_o:0.015±0.005]	2500±500	36±7
$E_{11h}(2s)$	1524.95	1525.35±0.05	too small to fit			–
$E_{11\ell}(2s)$	1527.75	not clearly visible	–		–	–
E_{12h}	1523.60	1524.55±0.05	0.20±0.05		100±50	1.4±0.4
E_{13h}	1530.40	1531.40±0.05	0.50±0.05		1450±200	21±3
E_{22h}	1537.10	1538.50±0.07	0.9±0.1		1900±200	28±3

(c) GWS485 20/50 x=0.01 5K

Transition Label	Transition Energy (PL and Simmonds et al. from PLE peak) (meV)[1]	Transition Energy (Reflectance Fit) (meV)	Γ Linewidth (eq. to FWHM) local fit (meV)	Γ Linewidth (eq. to FWHM) nonlocal fit $\Gamma=2\gamma+2\Gamma_0$ (meV)	A local fit parameter $(meV)^2$	Oscillator Strength per unit area $(Å^{-2}\times10^{-5})$
E_{11h}	1518.3	1518.20±0.05	0.06±0.005	0.126±0.006 [γ:0.035 ±0.002,Γ_o:0.028±0.001]	3500±500	51±7
$E_{11\ell}$	1519.65	1519.45±0.1	0.085±0.01	0.14±0.01 [γ:0.055 ±0.004,Γ_o:0.016±0.001]	2000±500	29±7
$E_{11h(2s)}$	1523.15	1522.90±0.1	0.15±0.02	0.153±0.01 [γ:0.075± 0.004,Γ_o:0.0013±0.0002]	160±30	2.5±0.4
$E_{11\ell(2s)}$	1524.35	not visible				
E_{12h}	1521.60	1521.39±0.02	0.05±0.005	0.053±0.001 [γ:0.025± 0.005,Γ_o:0.0014±0.0002]	190±30	2.7±0.3
E_{13h}	1525.50	1525.3±0.1	0.6±0.05		2400±300	35±4

(d) GWS280 20/20 x=0.045

Transition Label	Transition Energy (PL and Tagg from PLE peak) (meV)[3]	Transition Energy (from Reflectance Fit) (meV)	Γ Linewidth (eq. to FWHM) local fit (meV)	Γ Linewidth (eq. to FWHM) nonlocal fit $\Gamma=2\gamma+2\Gamma_0$[4] (meV)	Λ local fit parameter $(meV)^2$	Oscillator Strength per unit area $(Å^{-2}\times10^{-5})$
E_{11h}	1521.5	1521.74 ±0.05	0.25±0.02	0.35±0.03 [γ:0.14±0.01, Γ_o:0.034±0.002]	5000±500	73±7
$E_{11\ell}$	1523.5	1524.4±0.1	0.29±0.02	0.44±0.06 [γ:0.20±0.03, Γ_o:0.022±0.002]	2700±500	39±7
E_{12h}	1526.8	1526.9±0.1	too small to fit			
E_{13h}	1537	1536±1	0.65±0.1		2400±500	35±7
E_{22h}	1548	1547.3±0.1	0.85±0.1		3400±500	50±7
$E_{22\ell}$	1557	not visible				
$E_{33\ell}$	1568	not visible				

(e) GWS359 20/20 x=0.02 5K

Transition Label	Transition Energy (PL snd Tagg from PLE peak) (meV)[3]	Transition Energy (from Reflectance Fit) (meV)	Γ Linewidth (eq. to FWHM) local fit (meV)	Γ Linewidth (eq. to FWHM) nonlocal fit $\Gamma=2\gamma+2\Gamma_0$[4] (meV)	A local fit parameter $(meV)^2$	Oscillator Strength per unit area $(Å^{-2}\times10^{-5})$
E_{11h}	1519.5	1519.4±0.1	0.19±0.03	0.32±0.03 [γ:0.12±0.01, Γ_o:0.038±0.002]	5200±500	76±6
$E_{11\ell}$	1520.8	1521.45±0.1	0.27±0.04	0.40±0.05 [γ:0.18±0.02, Γ_o:0.018±0.002]	2500±700	36±10
E_{12h}	1523.9	1523.5±0.1	too small to fit			
E_{13h}	1530.1	1529.6±0.1	too small to fit			

(f) GWS463 2% Al Single 20 nm QW in 500nm x = 0.02 Barriers

Transition Label	Low Excitation PL above bandgap Peak energy (meV)	Transition Energy (from Reflectance Fit) (meV)	Γ Linewidth (eq. to FWHM) local fit (meV)	Γ Linewidth (eq. to FWHM) nonlocal fit $\Gamma=2\gamma+2\Gamma_0$[4] (meV)	A local fit parameter $(meV)^2$	Oscillator Strength per unit area $(Å^{-2}\times10^{-5})$
E_{11h}	1519.9±0.05	1519.8±0.1	0.21±0.02	0.31±0.03 [γ:0.12±0.01, Γ_o:0.037±0.002]	5200±500	76±6
$E_{11\ell}$	1521.9±0.05	1521.75±0.1	0.32±0.03	0.46±0.05 [γ:0.21±0.02, Γ_o:0.018±0.002]	2700±500	39±7
E_{12h}		1522.7±0.1	0.3±0.05		200±70	2.9±1
E_{13h}		1525.0±0.3	0.4±0.05		300±70	4.4±1

(g) GWS360 20/20 x=0.01

Transition Label	Transition Energy (PL and Tagg from PLE peak) (meV)[5]	Transition Energy (from Reflectance Fit) (meV)	Γ Linewidth (eq. to FWHM) local fit (meV)	Γ Linewidth (eq. to FWHM) nonlocal fit $\Gamma=2\gamma+2\Gamma_0$[4] (meV)	A local fit parameter $(meV)^2$	Oscillator Strength per unit area $(Å^{-2}\times10^{-5})$
E_{11h}	1518.3	1518.3±0.1	0.12±0.02	0.17±0.03 [γ:0.06±0.01, Γ_o:0.025±0.002]	3500±500	51±7
$E_{11\ell}$	1519.4	1519.75±0.1	0.27±0.02	0.32±0.03 [γ:0.14±0.01, Γ_o:0.020±0.002]	2000±400	32±4
E_{12h}	1521.3	1521.35±0.1	0.10±0.02	0.21±0.03[γ:0.10±0.01, Γ_o:0.0035±0.0005]	500±70	7±1

Table I Explanatory Notes

[1] Samples GWS482, GWS479 and GWS485 were discussed in Simmonds et al. [158] and PLE spectra were published. They determined that there was negligible Stokes shift between PL and PLE peak positions. Their published PLE peak positions have been shifted so that the E_{11h} peak coincides with the measured low excitation PL position of the same peak taken on the same sample spot on the same day as the present reflectance spectrum. In the case of GWS482 the spectrum taken on the same day was not as suitable for fitting, but the shift between PL and reflectance could be determined. The maximum shift observed between the published PLE results and the present PL results was 0.2 meV.

[2] It was impossible to obtain a satisfactory fit of the light hole peak in this sample until the convolution fit of Humlíček et al. [193] combining a standard local reflectance fit such as that of equation (3.3) with a Gaussian was used. This is designed to model inhomogeneous broadening, and is embodied in equations (3.37) and (3.38). Due to the greater linewidths associated with the x=0.045 samples it is reasonable to expect some inhomogeneous broadening, but it is not clear why the convolution fit only gives superior results for the light hole in this one sample. (See Figure 5.11). Because of normalization problems this fit has only been used to determine relative oscillator strengths. Γ_L is the standard Lorentzian broadening parameter seen in the local fit (equivalent to FWHM in absorption). Γ_G is the standard deviation of the Gaussian with which it is convolved. The FWHM of this Gaussian is equivalent to 2.36 Γ_G.

[3] PLE peak positions were reported for samples GWS280, GWS359 and GWS360 in Tagg [276]. These were shifted as described above so that the E_{11h} peak coincides with the measured PL result. The maximum shift required was 0.1 meV. For GWS360 the PL results were too weak for this procedure to be followed and the published results have simply been reprinted.

[4] The Andreani [146] fully nonlocal fit is embodied in equations (3.19) and (3.20) and is most appropriate for very narrow linewidths. There was complete agreement between the local and nonlocal fits on transition energy and oscillator strength even for the narrowest linewidths, but the local fit tended to underestimate the linewidth, by neglecting the intrinsic radiative broadening.

[5] As printed in Tagg [276].

Table II
Comparison of 5K Low Excitation Photoluminescence Linewidths

Note: Reflectance Linewidths are from Table I. Because of asymmetry the PL linewidth is taken as twice the energy separation between the peak and the half maximum on the high energy side. PLE data are from Simmonds et al. [158] and Tagg [276]. Low excitation here means a maximum of 0.6W/cm^2 (633 nm).

Sample	Transition	Linewidth Local Reflectance Fit (meV)	Linewidth Nonlocal Reflectance Fit (meV)	PL Linewidth FWHM (meV)	PLE Linewidth FWHM (meV)
GWS482 20/50 x=0.045	E_{11h}	0.30±0.02	0.34±0.02	0.46±0.02	0.40±0.04
GWS482 20/50 x=0.045	$E_{11\ell}$	no satisfactory fit	no satisfactory fit	too weak to measure	0.50±0.05
GWS280 20/20 x=0.045	E_{11h}	0.25±0.02	0.35±0.02	0.72±0.04	0.70±0.07
GWS280 20/20 x=0.045	$E_{11\ell}$	0.29±0.02	0.44±0.06	too weak to measure	0.70±0.07
GWS479 20/50 x=0.02	E_{11h}	0.11±0.005	0.17±0.02	0.22±0.02	0.32±0.03
GWS479 20/50 x=0.02	$E_{11\ell}$	0.13±0.005	0.14±0.02	0.30±0.02	0.39±0.04
GWS359 20/20 x=0.02	E_{11h}	0.19±0.03	0.32±0.03	0.46±0.02	0.5±0.05
GWS359 20/20 x=0.02	$E_{11\ell}$	0.27±0.04	0.40±0.05	too weak to measure	0.50±0.05
GWS463 20nm SQW x=0.02	E_{11h}	0.21±0.02	0.31±0.03	0.34±0.03	0.23±0.04
GWS463 20nm SQW x=0.02	$E_{11\ell}$	0.32±0.03	0.46±0.05	0.38±0.04	0.27±0.04
GWS485 20/50 x=0.01	E_{11h}	0.06±0.005	0.126±0.006	0.16±0.02	0.26±0.03
GWS485 20/50 x=0.01	$E_{11\ell}$	0.085±0.01	0.14±0.01	0.18±0.02	0.24±0.03
GWS360 20/20 x=0.01	E_{11h}	0.12±0.02	0.17±0.03	very weak at low excitation	0.41±0.04
GWS360 20/20 x=0.01	$E_{11\ell}$	0.27±0.02	0.32±0.03	very weak at low excitation	0.41±0.04

Table III
$GaAs/Al_xGa_{1-x}As$ Quantum Well Results in Literature

Note: Zhang et al. [156] and Masselink et al. [182] use a definition of oscillator strength that is reduced by a factor of 2 with respect to the standard relationship between the parameter A, the integrated absorption and the oscillator strength that is accepted by Andreani and Pasquerello [29] and the other authors. The published results for oscillator strength of Zhang et al. and Masselink et al. have been multiplied by a factor of 2 to make them directly comparable to the results of other authors. Theoretical results listed in boldface with 2 of the entries are from Andreani and Pasquerello [29]. The results of Masselink et al. and Gil et al. [155] are also in close agreement with Andreani and Pasquerello.

(a) Oscillator Strength Determined from Reflectance

Transition	Sample Type	Reference	Γ (meV) FWHM	A $(meV)^2$	$f_{osc}{}^A$ $(\times 10^{-5} Å^{-2})$
Bulk GaAs exciton	500 nm MBE layer between MQW structures	Humlíček et al. [193] 22K	0.15	3670 $= 4\pi\alpha E_0{}^2$ at 5K	
E_{11h}	SQW x=0.28 3nm well	Zhang et al. [156] 7K	not given	84,300*	184±20
E_{11h}	SQW x=0.28 5nm well	Zhang et al. [156] 7K	not given	36,900*	134±20
E_{11h}	SQW x=0.28 10nm well	Zhang et al. [156] 7K	not given	14,000*	102±10
E_{11h}	SQW x=0.28 15nm well	Zhang et al. [156] 7K	not given	9,350*	102±10 **theory** 40
E_{11h}	SQW x=0.28 20nm well	Zhang et al. [156] 7K	not given	7,000*	102±10 **theory** 30
E_{11h}	SQW x=0.32 79Å	Gil et al. [155] 2K	3	12,000	69†

Table IV

Literature Values for Acoustic Phonon Temperature Coefficient of Broadening γ

Note that the broadening is that which would apply to the full linewidth

Transition	QW Well width (nm)	QW Barrier x (Al mole fraction)	Reference	γ (μeV/K)
Bulk			Schultheis, Kuhl and Honold [221]	17
E_{11h}	27.7	0.3	Schultheis et al. [222]	10
$E_{11\ell}$	27.7	0.3	Schultheis et al. [222]	10
E_{11h}	13.5	0.3	Schultheis et al. [222]	5
$E_{11\ell}$	13.5	0.3	Schultheis et al. [222]	5
E_{11h}	32.5	0.3	Srinivas et al. [183]	6±1
E_{11h}	15	0.3	Srinivas et al. [183]	3.4±1
E_{11h}	asymmetric coupled QWs (Sample A)	0.4	Veliadis et al. [217]	2.9
E_{11h}	asymmetric coupled QWs (Sample B)	0.3	Veliadis et al. [217]	3.2
E_{11h}	20	not given	Lee et al. [216]	6
$E_{11\ell}$	20	not given	Lee et al. [216]	5
E_{11h}	8	0.3	Vinattieri et al. [234]	5
E_{11h}	13	0.3	Vinattieri et al. [234]	5
E_{11h}	15	0.3	Vinattieri et al. [234]	5
Bulk (Thin Layer in SL Barriers)			Humlíček et al. [159]	7±2
E_{11h}	20	0.01,0.02,0.045	present work	3.0±0.4
$E_{11\ell}$	20	0.01,0.02,0.045	present work	4.5±0.4

Transition	Sample Type	Reference	Γ (meV) FWHM	A $(meV)^2$	$f_{osc}{}^{A}$ $(\times 10^{-5} Å^{-2})$
E_{11}	SQW x=0.32 79Å	Gil et al. [155] 2°K	4	5,000	25†
$E_{11h}(2s)$	SQW x=0.32 79Å	Gil et al. [155] 2K	3	600	3.5†
$E_{11}(2s)$	SQW x=0.32 79Å	Gil et al. [155] 2K	4	600	3.5†
E_{11h}	SQW 100Å well x=0.3	Zheng et al. [163] 4.2K	3.5	10,000	73†
E_{11h}	SQW 150Å well x=0.3	Srinivas et al. [214] 10K	0.15 **(0.08 extrinsic + 0.06 intrinsic)	N/A	120 (±30)††
E_{11}	SQW 150Å well x=0.3	Srinivas et al. [214] 10K	0.18 (0.15 extrinsic + 0.025 intrinsic)	N/A	50(±14)††
E_{11h}	MQW lw 100Å lb 75Å 20 periods x=1	Terzis et al. [174] 4.2K	not given	10,350	105†
E_{11}	MQW lw 100Å lb 75Å 20 periods x=1	Terzis et al. [174] 4.2K	not given	9,200	93†
E_{11h}	MQW lw 103Å lb 75Å 18 periods x=1	Terzis et al. [174] 4.2K	not given	15,000	110†
E_{11}	MQW lw 103Å lb 75Å 18 periods x=1	Terzis et al. [174] 4.2K	not given	8,500	62†
E_{11h}	SQW 150Åwell x=1	Terzis et al. [174] 4.2K	not given	6,000	65†
E_{11}	SQW 150Åwell x=1	Terzis et al. [174] 4.2K	not given	5,000	55†

*Deduced from oscillator strengths per unit area via equation (3.4) †Deduced from A parameter via equation (3.4)
**Photoluminescence linewidth (FWHM) also 0.15 meV. ††Deduced from intrinsic broadening via equation (81)

(b) Oscillator Strength Determined from Absorption

Transition	Sample	Reference	f_{osc}^{A} ($\times 10^{-5}$ Å^{-2}) †
E_{11h}	32Å well in SL barriers eq. to x=0.25 AlGaAs	Grousson et al. [187]	140
E_{11l}	32Å well in SL barriers eq. to x=0.25 AlGaAs	Grousson et al. [187]	32
E_{11h}	10nm SQW well x=0.3	Grousson et al. [187]	61
E_{11l}	10nm SQW well x=0.3	Grousson et al. [187]	22
E_{11h}	40Å SQW x=0.25	Masselink et al. [182] 3K	94±12
E_{11h}	90Å SQW x=0.25	Masselink et al. [182] 3K	48±4
E_{11h}	100Å SQW x=0.25	Masselink et al. [182] 3K	50±4
E_{11h}	120Å SQW x=0.25	Masselink et al. [182] 3K	40±4
E_{11h}	150Å SQW x=0.25	Masselink et al. [182] 3K	38±4

Transition	Sample Characteristics	Reference	Integrated Absorption (cm^{-1} eV)	f_{osc}^{A} ($\times 10^{-5}$ Å^{-2}) †
E_{11h}	30Å SQW, 40Å AlAs barriers	Masumoto et al. [181]	1120±10	110±2
E_{11h}	83Å SQW, 93Å AlAs barriers	Masumoto et al. [181]	250±10	67±3
E_{11h}	108Å SQW, 36Å AlAs barriers	Masumoto et al. [181]	200±10	70±4
E_{11h}	154Å SQW, 131Å AlAs barriers	Masumoto et al. [181]	120±10	60±5
E_{11h}	254Å SQW, 122Å AlAs barriers	Masumoto et al. [181]	100±10	83±8

†related to integrated absorption by equation (3.32).

CHAPTER 6

HYDROGEN PASSIVATION OF DEFECT BOUND EXCITONIC LINES IN MBE GaAs

6.1 INTRODUCTION

Initial studies were made [287] on high purity epitaxial MBE GaAs samples displaying strong photoluminescence (PL) lines associated with 'KP' and 'g' defect complex bound excitons from two different sources. (KP and g defects are discussed in Section 3.4.5) These particular PL lines were strongly quenched after hydrogen passivation treatment. There was apparently substantial Donor Acceptor Pair (DAP) PL, but donor bound excitons were unobservable in the PL spectra of the As Grown samples, yet became very prominent after hydrogen passivation; on the other hand shallow acceptor bands were either enhanced with respect to excitonic PL or little changed, suggesting that there was little passivation of isolated acceptors. By contrast, C-V (Capacitance-Voltage) measurements [288] showed reductions in carrier concentration of at least an order of magnitude after hydrogenation.

The present work was undertaken in an attempt to resolve the puzzles relating to changes with hydrogenation in shallow donor and acceptor concentrations in these samples through detailed measurements on two of the samples, using techniques involving PL at different temperatures, PLE (Photoluminescence Excitation), magnetophotoluminescence and PL involving selective excitation of neutral acceptor bound excitons (A°X) and DAP. The evidence suggests that the PL spectra of these samples before and after hydrogenation can be largely explained by the preferential hydrogen passivation of the KP and g-line defects, which are concentrated in definite regions of the sample, probably around dislocations, and which are

responsible for efficient trapping of excitons and free carriers. These defect complexes also appear to be responsible for the suppression of donor bound exciton lines.

6.2 THE SAMPLES

The samples consist of 3μm epitaxial layers of MBE GaAs grown on a semi-insulating substrate. The crystal grower was Dr. Martin Emeny of DRA (Defense Research Agency, previously RSRE), Malvern, UK. ME122 was available in As Grown and Hydrogenated versions. ME128 had been hydrogenated and then annealed at 450C for 5 minutes, completely reversing the hydrogen passivation as explained below. A piece of this sample (referred to as ME128H) was then rehydrogenated. In what follows AsG after the sample name means the As Grown version of the sample and H the hydrogenated or rehydrogenated version. Hann after the sample name means a piece of the sample that was hydrogenated and then annealed.

6.3 PHOTOLUMINESCENCE RESULTS

6.3.1 5K PL of The As Grown Samples

Figure 6.1 shows the 5K excitonic PL typically seen in this class of sample in its As Grown state. The line identifications (which are well known) are from Pavesi [236] and from Skolnick, Halliday and Tu [251]. The bands in Figure 6.1 at 1.5073 eV, 1.5062 eV and 1.5052 eV are actually groups of excitonic lines resolved for a similar sample by Skolnick, Tu and Harris [248] and their line identifications are shown. These identifications were confirmed by polarization studies [287] of ME122 and ME128 which were done in our laboratory. A strong polarization dependence was found corresponding to that described by Skolnick, Tu and Harris for the relative intensities of the three main bands other than the g-line.

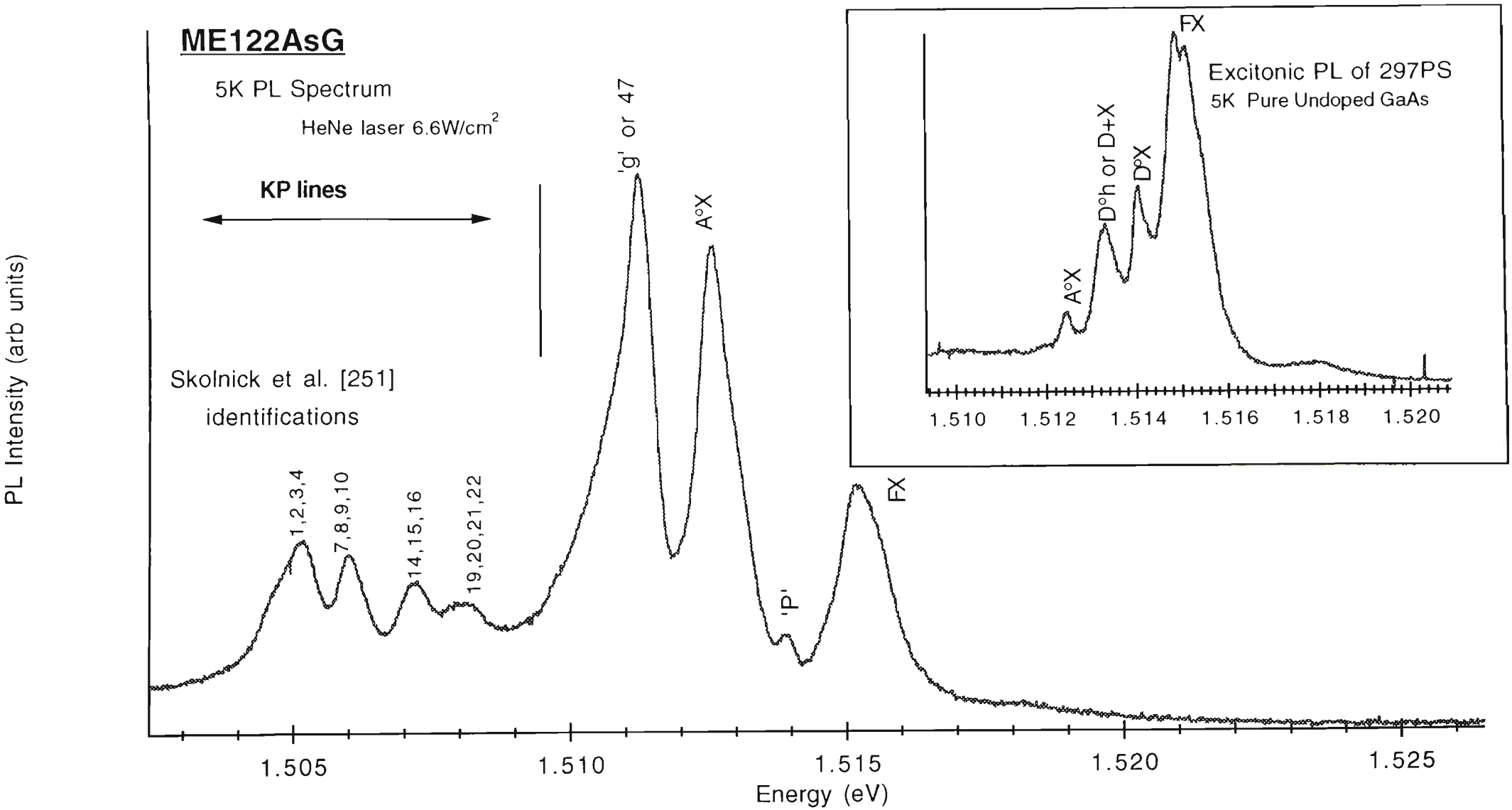

Figure 6.1. **Excitonic part of PL spectrum of a typical sample with strong KP and g lines and a low apparent donor concentration. Inset shows the corresponding part of the PL spectrum for typical high quality undoped MBE epitaxial GaAs.**

There has been some degradation in the intensity of the free exciton line from spectra taken when the samples were fresh, probably due to surface degradation. Note that the free exciton peak in this spectrum is symmetrical and lacking a dip near the absorption line center. The same is true of all the spectra taken of the other samples in this class. The absence of such a dip has been associated with a very low neutral donor concentration [289]. There is no clear evidence of any donor related excitonic lines, either here or in spectra of the other samples. The photon energy of the small line marked 'P' in Figure 6.1 does not correspond precisely to the energies of the donor related excitonic lines, and the origin of it is unknown.

The carbon impurity band in ME122AsG is shown (for low excitation) in Figure 6.4, and at higher excitation is the same as for the spectrum of the fully annealed sample shown in Figure 6.3. The lower energy part of the spectra of all the samples is dominated by eA° (caused by recombination of electrons in the conduction band and neutral shallow acceptors) and DAP peaks related to shallow carbon acceptors. The donors involved in the DAP photoluminescence are likely to be silicon or sulphur, the most common residual impurities in MBE GaAs [290]. In the ME series samples (except at the lowest laser power densities) the peaks overlap to form one smooth, broad band, which is relatively weak compared to the total excitonic PL. The carbon impurity band is stronger in a CSIRO sample that was part of the initial studies (with the eA° peak sufficiently strong to be well resolved). The identification of these peaks was confirmed by temperature dependent PL measurements discussed below for ME122 and ME128 and by magnetophotoluminescence measurements in ME122. In the ME samples at 5K the dominant peak is DAP with a smaller, narrower eA° peak superimposed so that the band maximum is at the position expected for the

maximum of eA°. In ME122 this conclusion about the relative intensities is supported both by the magnetophotoluminescence measurements and by linefits utilizing the Eagles [238] formula for eA°. In some low temperature, low excitation intensity spectra it is also possible to resolve the eA° and DAP peaks, even at zero magnetic field. There is no clear evidence of lower energy peaks related to other simple substitutional acceptors or the d_n series associated with the KP lines that was described by Briones and Collins [244] and is briefly discussed in Section 3.4.5. It should be noted that Briones and Collins were not able to observe this series in all samples that displayed KP lines.

It was initially determined from C-V measurements [288] that the active acceptor concentration was $\cong 1 \times 10^{15}$ cm^{-3} for ME122 in the As Grown state, but at least an order of magnitude lower after hydrogenation. Using low excitation spectra of ME122AsG and ME122H it was possible for the author to fit the Lorenz, Morgan and Pettit [291] formulas (also used by Schairer and Schmidt [292]) relating the lineshape of the DAP peak on the low energy side (where pairs are distant) and the position of the DAP maximum in low excitation spectra to the donor concentration. These formulas are only applicable in the low excitation limit. A linefit using the Eagles [238] formula established that the eA° luminescence was not shifting the DAP peak maximum, and this was also confirmed later by the magnetophotoluminescence spectra discussed below. From the fit, the donor concentration (at least in the part of the sample from which the PL is emitted) was measured as $7\pm3 \times 10^{12}$ cm^{-3} in ME122AsG and $4\pm1 \times 10^{12}$ cm^{-3} in ME122H. (It was not possible to do a similar fit for ME128 because the eA° peak is large enough to obscure the DAP peak maximum at low excitation.)

Intensity dependent measurements on ME122AsG and ME128Hann show little relative change in the PL spectrum over 2 orders of magnitude, except that the free exciton and A°X peaks approximately double in intensity over the range relative to the rest of the spectrum. The same changes with intensity are observed after hydrogenation (apart from a smaller relative change in A°X and the free exciton). Changes in the intensity of these peaks, the g-line and KP lines and the carbon impurity band intensities are all linear with respect to the laser intensity over the range employed, and remain so after hydrogenation and annealing.

6.3.2 5K PL Spectra of the Hydrogenated and Annealed Samples

The samples were hydrogenated following the procedure described in Chapter 4, and pieces of ME128 and ME122 were progressively annealed at 360C, 400C and 450C, each for 5 minutes. A piece of ME128AsG was also annealed by the same procedure without ever having been hydrogenated. Figure 6.2 shows the excitonic part of 5K PL spectra of ME122 taken before and after hydrogenation, while Figure 6.3 shows a 5K annealing series for this sample. The changes resulting from hydrogenation are dramatic. They include an increase in total PL intensity of up to 6 times, with a modest or nonexistent increase in the free exciton and A°X lines and the appearance of donor related excitonic lines (D°X at 1.5141 eV and D°h and/or D^+X at 1.5134 eV) of comparable magnitude to the A°X lines. In contrast, the g-line is strongly quenched and there is substantial to complete passivation of the KP defect excitonic lines. The carbon impurity band shows a relative and absolute increase in PL intensity ranging from modest to dramatic, depending on the sample. Table 6.1 shows the shifts in integrated intensity in the PL spectrum of ME122 with hydrogenation at 3 excitation levels. Similar changes were observed after hydrogenation in the GaAs buffer PL of

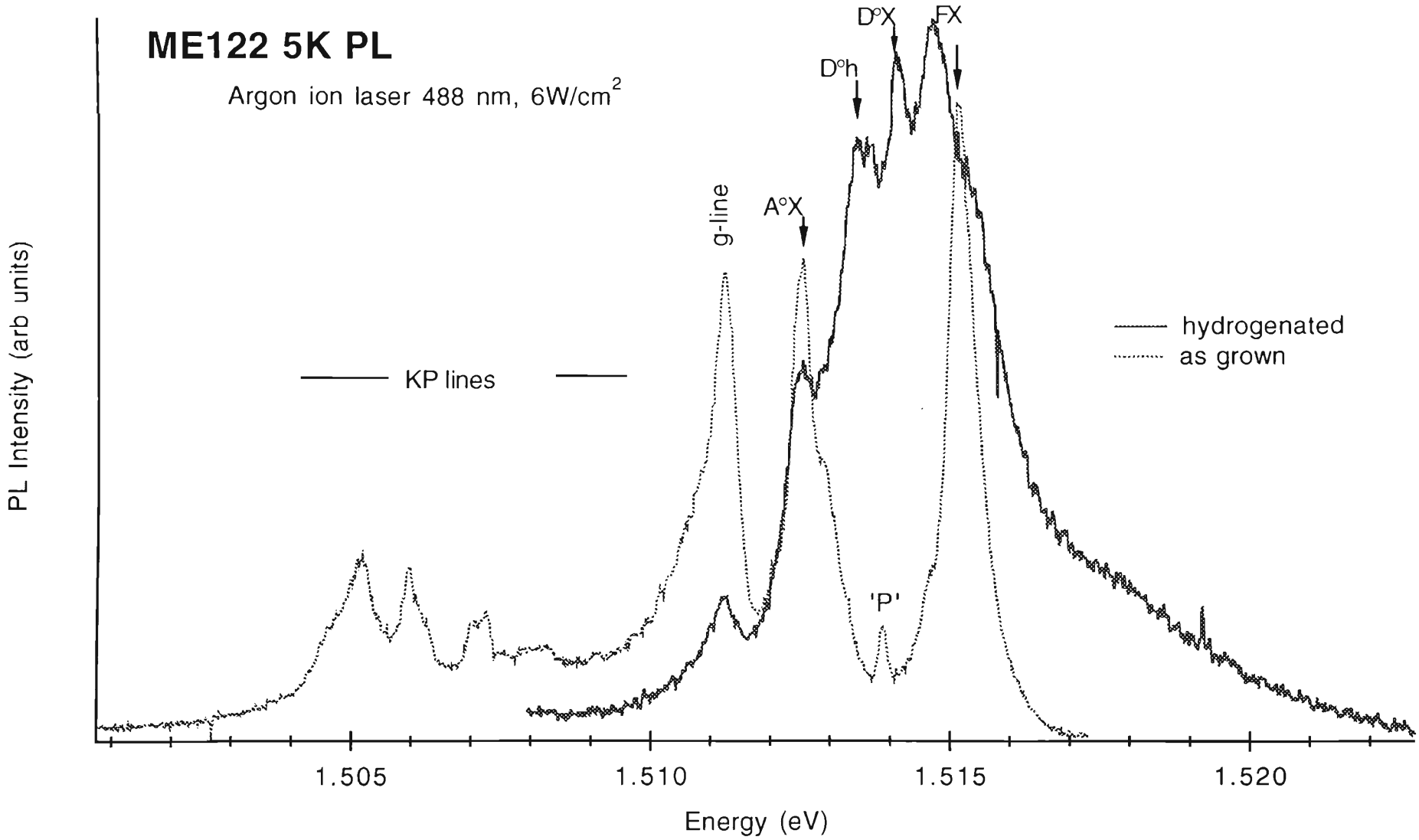

Figure 6.2 **Hydrogenation passivates the defect related bound excitons while causing the donor related excitons to prominently appear. Spectra of fresh samples taken by T.A. Fisher. Later spectra taken by the author show broadening and reduction in the FX line.**

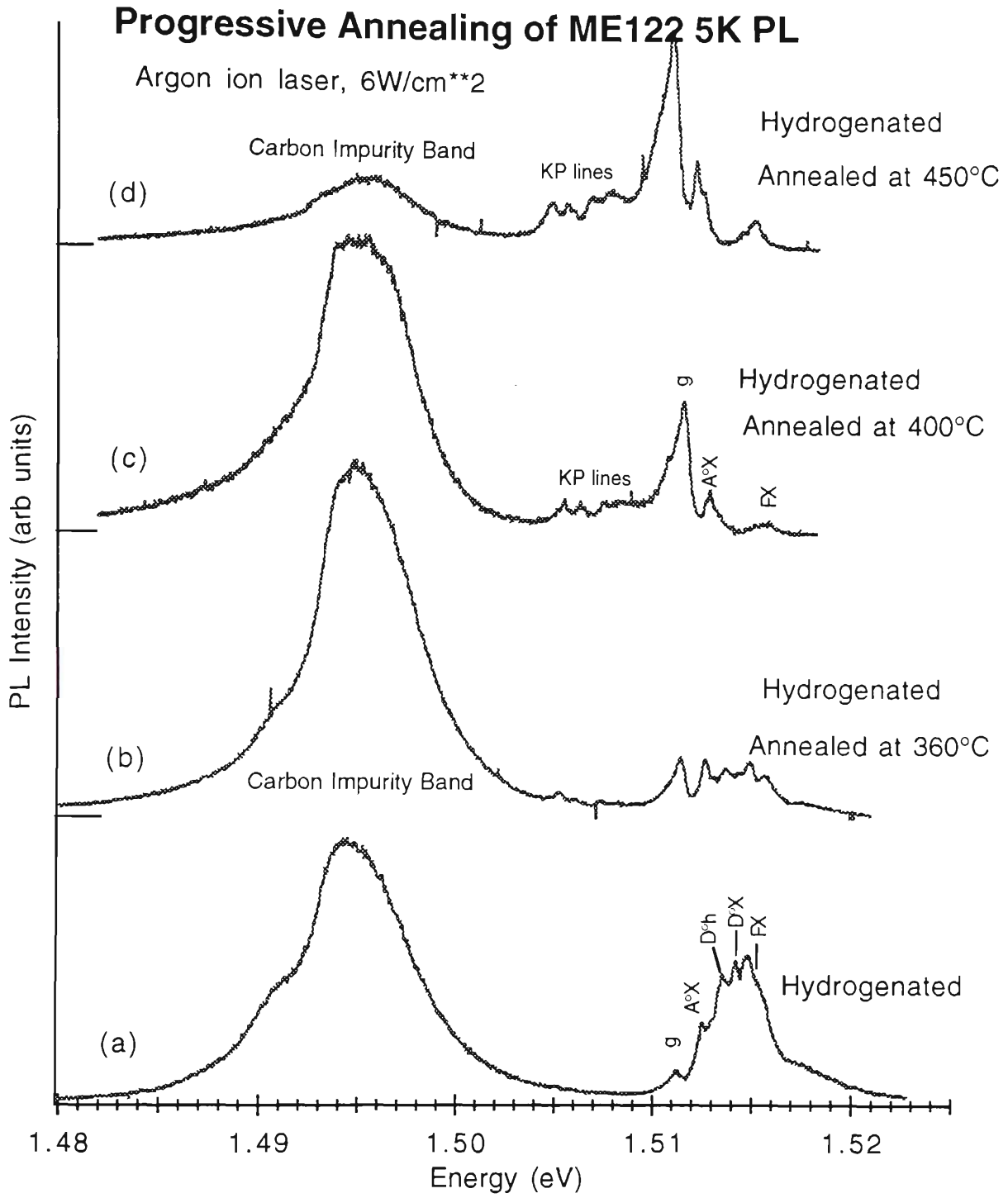

Figure 6.3 (a) shows the freshly hydrogenated sample (b) after 360C g becomes brighter and the KP lines begin to appear while the free and donor related excitons begin to quench (c) after 400C the g and KP lines are stronger while the donor related excitonic lines have disappeared and the carbon impurity band begins to quench (d) after 450C the As Grown spectrum is restored, apart from some loss of intensity and degradation of the free exciton line. Spectra taken by T.A. Fisher. ME128 shows the same changes apart from less quenching of the free exciton line.

Table 6.1 Relative Integrated PL Intensity at 5K as a Function of Laser Power (HeNe Laser at 633 nm)

Sample	Laser Power	Free/Bound Excitonic		Defect Excitonic		Total Excitonic		Carbon Impurity Band		Total PL
		relative PL	% of Total	relative PL	% of Total	relative PL	% of Total	relative PL	% of Total	
ME122 As G	38mW/cm^2	1	11.4%	4.2	48.1%	5.2	58.7%	3.6	41.3%	8.7
	507mW/cm^2	15.8	21.4%	29.1	39.4%	44.9	60.8%	28.9	39.1%	73.8
	4.75W/cm^2	94.7	24.5%	139	35.9%	234	60.4%	154	39.6%	387
ME122H	38mW/cm^2	3.6	8.9%	1.6	4.0%	5.2	13.0%	34.8	87.0%	40.0
	570mW/cm^2	44.7	10.6%	24.3	5.8%	69.0	16.3%	353	83.7%	422
	4.75W/cm^2	164	10.0%	86.9	5.3%	250	15.1%	1390	84.9%	1640

the layered samples discussed in Chapter 7, in the case of samples such as GWS28 where KP bands were observed in the As Grown samples.

The changes that occur on annealing are detailed in Figure 6.3. After annealing at 450C for 5 minutes, the As Grown spectrum is recovered, apart from a general loss of intensity and some reduction in the free exciton line. The spectrum of the comparison sample of ME128AsG that was annealed at 450C was identical to the one from ME128Hann. This suggests that the annealing process itself is responsible for the loss of brightness and degradation of the free exciton line, and that any changes due to hydrogenation itself are reversed after annealing at 450C. Nissim and Gibbons [293] have shown that annealing at these temperatures grossly degrades the surface of GaAs samples, quite apart from any damage due to hydrogenation.

6.3.3 Temperature Dependence of the PL Spectra

In general, PL intensity is expected to decrease with increasing temperature, with the exact mechanism varying with the particular line or band, as discussed in section 3.4.7. An important factor is the thermal dissociation of excitons, especially above 30K [263,264] and the thermal ionization of donors above 10K. (There are also thermal quenching mechanisms operative for the A°X line, involving the liberation of an electron or a hole and an electron [294]). At higher laser excitations, the expected temperature dependence is observed for all samples. At very low excitations, however, PL intensity actually increases for most lines and bands between 5K and 10K, as can be seen in Figure 6.4, a phenomenon which is attributed to sample inhomogeneity [263]. Above 10K normal quenching with temperature is observed.

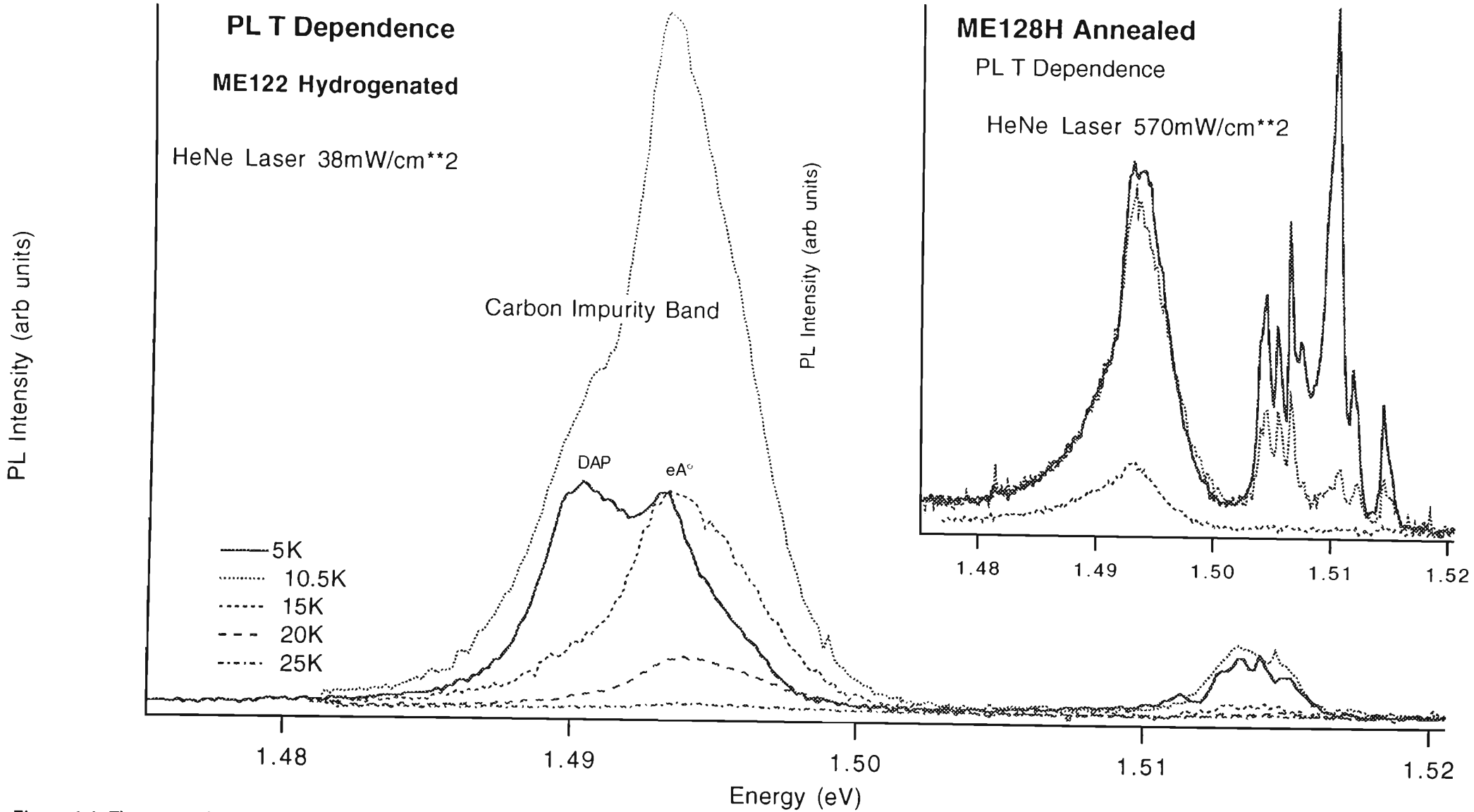

Figure 6.4 These very low excitation PL spectra of ME122H show the PL intensity increasing between 5K and 10K. Inset shows the temperature dependence of ME128Hann at a higher laser power density.

Figure 6.4 also demonstrates that the KP lines and g-line show approximately the same temperature dependence as A°X and D°X. KP lines are known to quench rapidly with temperature [54] and in the present work were found to be undetectable by 20K even at the highest power densities used (4.75 W/cm^2). Note also the narrowing of the carbon impurity band by 15K as would be expected if the lower energy section of the impurity band were assigned to DAP photoluminescence which quenches more rapidly than PL associated with eA° transitions. The very rapid quenching is further evidence of a low donor concentration.

6.3.4 Magnetophotoluminescence Results

The magnetic field dependence of the eA° band is markedly different from that of the DAP band. Because of the absence of donor related excitons in the As Grown spectra of these samples, it was thought desirable to obtain further confirmation that the band assigned to Carbon DAP was in fact that, and not a second eA° band caused by an acceptor other than Carbon. In the presence of a magnetic field an eA° band narrows and shifts upward in energy with the bottom of the conduction band (if the small shift of acceptor energy is neglected) by $0.5\hbar\omega_c$ where ω_c is the radial cyclotron frequency. The DAP band remains broad even in a high magnetic field and displays a weaker shift corresponding to the diamagnetic shift of the shallow donor energy. In order to check this point with a typical sample, magnetophotoluminescence measurements were carried out on ME122AsG and ME122H [295]. Results for the two peaks agreed closely with theory, showing that they were indeed eA°:C and DAP:C. Further support for this view is that the lower energy component identified as DAP quenches much more rapidly as the temperature is raised than the component identified as eA°, as would be expected. It can be seen when the peaks are well separated that the DAP identified band is almost entirely quenched by 12.5K. At lower temperatures

the separation of the peaks also makes it clear that hydrogenation has no significant effect on the eA°/DAP intensity ratio, as is shown in Figure 6.5.

6.4 SELECTIVE EXCITATION RESULTS

Direct Selective Excitation (SE) at photon energies below E_g into transitions associated directly with impurity states would be expected to give information on the changes in concentrations of neutral and ionized donors and acceptors without confusion from competing recombination channels, as discussed in Section 3.4.6.

6.4.1 Selective Excitation and the Substrate

There is a potentially serious problem with SE due to the low densities of states involved. With excitation at photon energies above the GaAs bandgap, absorption coefficients are so large that light can only penetrate a relatively short distance (on the order of 1 μm) into the epitaxial layer, but below the bandgap light can easily penetrate to the substrate, where Steiner et al. [296] found that it can also cause selective excitation of impurity transitions. The author was involved in work [297] on a beryllium doped GaAs sample that showed evidence of predominant beryllium acceptors in far infrared absorption and in PL with laser excitation above E_g. At the same time there was strong evidence of carbon acceptors, but not beryllium, when there was below E_g selective excitation into the donor acceptor pair band. The explanation in that case was that most of the selective excitation was occurring in the substrate where Carbon is probably the most common residual acceptor.

To gain some understanding of the effects of the substrate, the samples were turned on edge where most of the surface is substrate material and spectra taken with laser excitation both above the bandgap and directly into the DAP

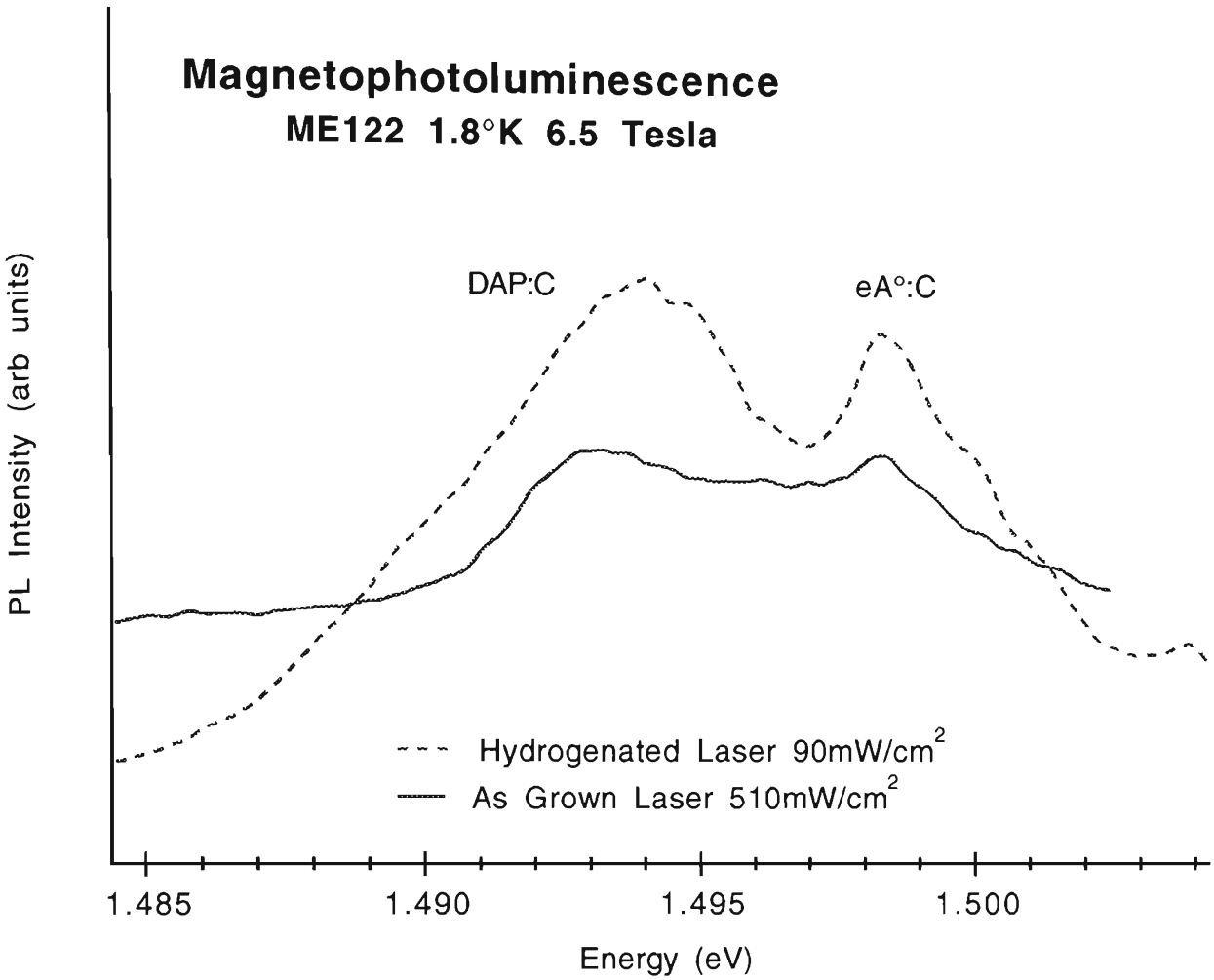

Figure 6.5 Separation of eA° and DAP bands under a magnetic field show that the eA°/DAP ratio does not change with hydrogenation. Although the laser powers are different I_{PL} is approximately the same (and the spectrum shape is not expected to be affected by the higher laser power for ME122AsG. Data smoothing was applied.

band. Normal PL spectra with laser excitation above the bandgap at power densities of up to 5W/cm^2 showed no excitonic PL of any kind, and only a very weak broad carbon impurity band. Selective excitation spectra, such as those described below, could be observed from the sample edge in both hydrogenated and as grown samples, but only with a very high excitation power density of 34W/cm^2, making it clear that the excitation was very probably from the the thin epitaxial layer. Even so, results need to be taken with caution, especially for excitation directly into the carbon impurity band, since even a very small absorption coefficient can give rise to significant absorption of radiation when the light penetrates a sufficiently thick layer.

6.4.2 Selective Excitation of A°X

Attempts were made to excite the two-hole replica and LO-phonon replica of A°X (discussed in section 3.4.6) by selectively exciting the principal A°X transition (1.5126 eV at 5K). This was done in order to determine (qualitatively) the change in the concentration of isolated neutral acceptors with hydrogenation. (C-V measurements had already indicated a reduction in overall acceptor concentration of at least an order of magnitude after hydrogenation as mentioned above.) Excitation at this energy is only capable of creating bound electron hole pairs in the vicinity of a neutral acceptor (in addition to some neutral DAP creation). At 5K ambient phonon detrapping and dissociation of the excitons are insignificant, as are nonradiative recombination through a multi-phonon cascade [237,298].

When an attempt was made to excite a two-hole replica, a satellite peak did appear at the appropriate energy, but it was not resonant with respect to the A°X energy, indicating that the satellite was more likely caused by selective excitation of DAP transitions. However, it was possible to unambiguously

observe the LO-phonon replica of A°X under resonant excitation. This replica peak represents the situation where an acceptor bound exciton recombines, emitting part of its energy as a LO phonon. The replica is thus displaced from the main A°X line by 36 meV, and its intensity under resonant excitation is expected to give a measure of the relative concentration of neutral acceptors, just as the strength of the selective DAP excitation lines are a measure of the relative concentration of ionized acceptors and donors, as discussed in Section 3.4.6. Spectra were taken from several spots on each sample and in both samples there was no significant difference (within 25%) in the height of the LO phonon replica peak above the background regardless of the hydrogenation status of the sample. In the case of ME128 the background was also the same for the hydrogenated and annealed samples, as shown in Figure 6.6. The difference in background intensity for ME122 is probably because ME122AsG never suffered surface damage due to hydrogenation or annealing and therefore has a brighter background than ME122H.

Since competing excitonic processes have been strongly reduced by the selective excitation, the lack of change in the LO phonon replica with hydrogenation seems to indicate that the concentration of isolated substititutional carbon acceptors is relatively unchanged after hydrogenation. An attempt was also made to excite an LO phonon replica of the strong g-line, but this was barely detectable in the As Grown or Annealed samples and not detectable after hydrogenation when the g-line is heavily quenched.

6.4.3 Selective excitation into the DAP band and PLE results

Selective excitation into the DAP band excited a pattern of peak separations characteristic of internal excitation energies of carbon acceptors. The

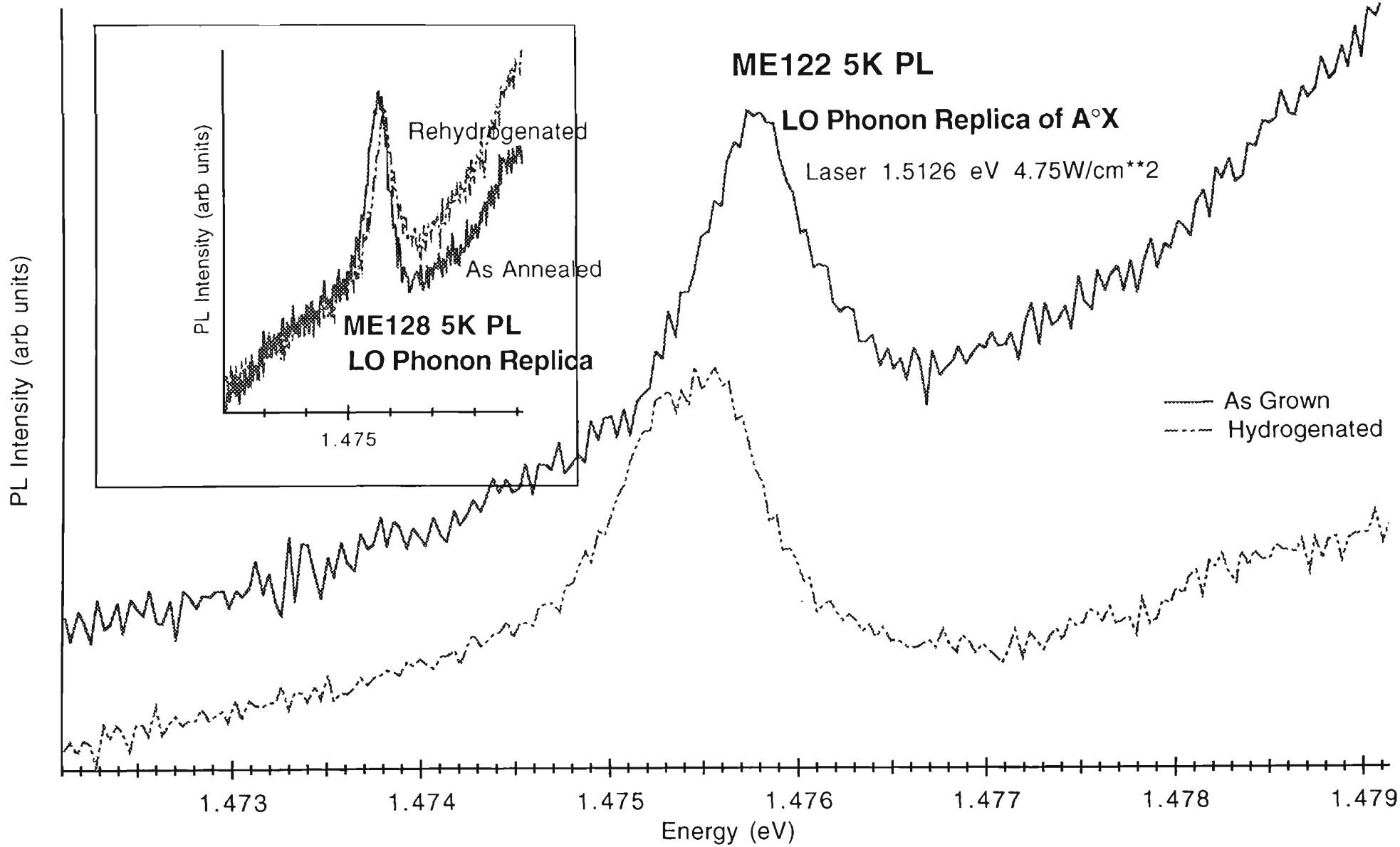

Figure 6.6 Selective excitation onto A°X gives rise to an identical LO-phonon replica regardless of hydrogenation status, suggesting that the concentration of isolated neutral carbon acceptors is relatively unchanged.

peak separations remain constant, but the peak energies shift with the laser excitation energy, as expected for SE of DAP transitions. Figure 6.7 shows the PL spectra resulting from 5K selective excitation at 1.5126 eV (the energy of A°X). As can be seen there are PL peaks at 18.3 meV and 15.1 meV below the excitation energy, an energy pattern characteristic of carbon acceptors [258]. While ME128 shows no significant difference in the intensity of the peaks associated with the excited states of acceptors regardless of hydrogenation status, in ME122 the excited peaks in the hydrogenated sample are only 25% to 40% as intense as in the as grown sample. Note also that the broadband DAP luminescence is hardly changed relative to the peaks excited by selective excitation when the sample is hydrogenated. Since the broadband continuum is due to neutral acceptors this is another indication of little change in the neutral acceptor concentration after hydrogen passivation. PLE spectra of both samples were also taken at various excitation energies. Patterns of excited states characteristic of Carbon acceptors were observed, similar to those seen in PL spectra resulting from selective excitation into the DAP band.

6.5 CONCLUSION

The main questions raised by these samples relate to (1) the lack of detectable donor related excitonic lines in the As Grown samples, but the appearance of strong D°X and D°h lines after hydrogen passivation; (2) the clear presence of substantial DAP PL in the As Grown samples, indicating the presence of neutral donors that nevertheless do not trap excitons; (3) the contradiction between the LO phonon replica intensity results indicating an approximately constant isolated shallow acceptor concentration before and after hydrogenation and the strong reduction in room temperature hole concentration revealed by C-V measurements; and (4) the lack of change in the eA°/DAP ratio and the ratio of the selective excitation peaks in the DAP

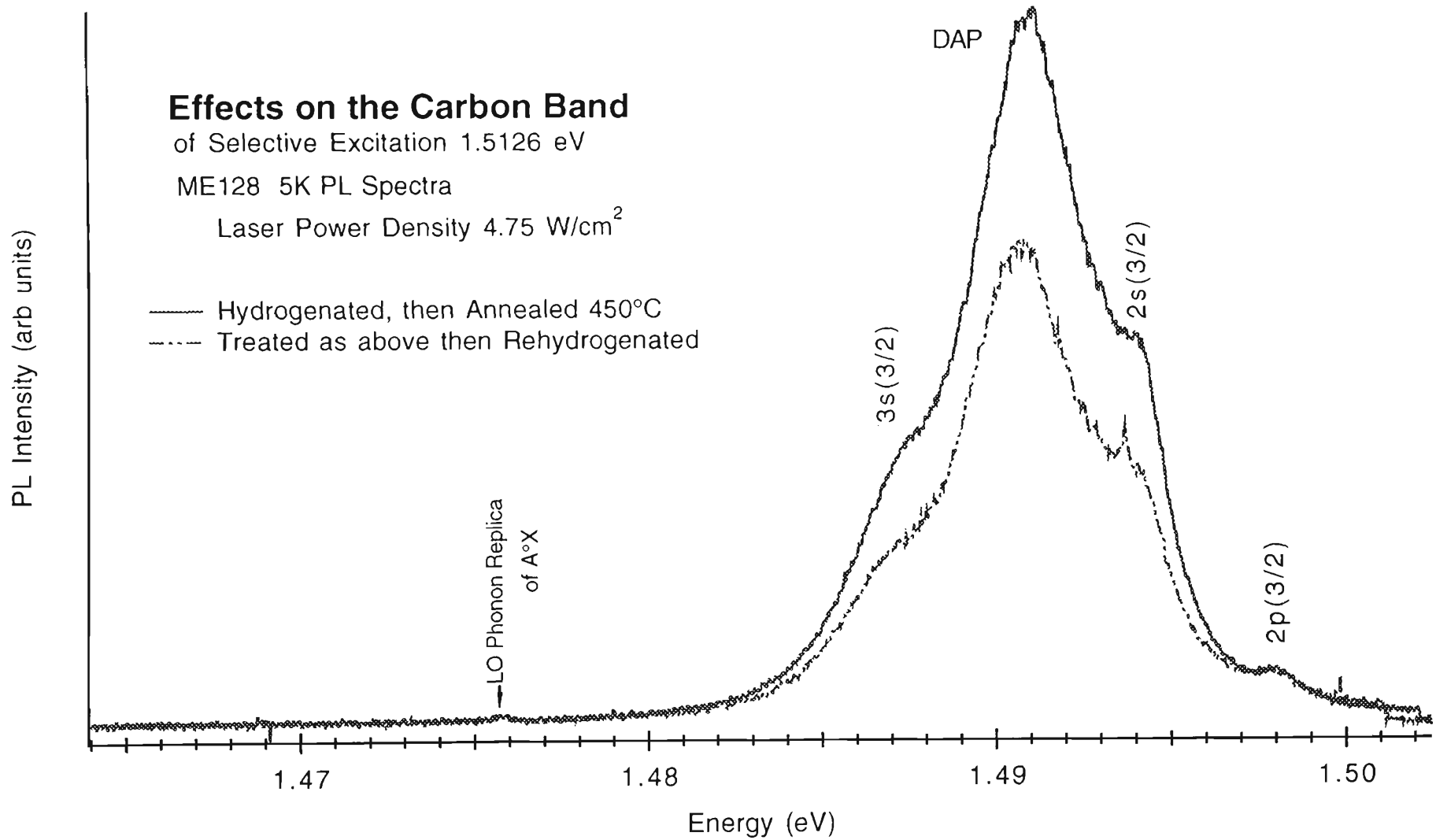

Figure 6.7 Selective excitation of A°X results in a LO phonon replica and (due to coincidence in energy of a set of excited DAP states) a pattern of peaks whose energy separations are characteristic of Carbon acceptors. Peak identifications are from Ashen et al. [258].

band relative to the background after hydrogen passivation; such lack of change suggesting relatively constant donor and acceptor concentrations, despite (1) and (3). These questions can be answered at least in part by assuming a model in which the samples are not homogeneous, and hydrogen passivation only has strong effects on the KP and g-line defect complexes, which are probably clustered around dislocations, with little or no hydrogen passivation of isolated single shallow acceptors.

6.5.1 Evidence for sample inhomogeneity

Dislocations are well known to concentrate defects and impurities, as is discussed in Section 2.1.2. The defects include the KP and g-line defects [54]. Dislocations are also known to act as conduits for hydrogen during the hydrogenation process [51,89]. There is no direct evidence for a high dislocation concentration in the present work, but the temperature dependent photoluminescence measurements do give evidence of sample inhomogeneity. PL spectra at lower power densities show a marked increase in total integrated PL intensity with temperature below 10K. According to Jiang, Jung and Ploog [263] such an increase is the signature of a 'grainy' inhomogeneous sample. The mobility of excitons and free carriers increases with temperature, enabling them to move from where they have been generated to areas of the sample where radiative recombination is more probable.

The absence of significant photoluminescence from the substrate indicates that as expected it is well supplied with nonradiative defects, and it would be expected that the same would be true of the uncapped surface [113]. It can be questioned whether hydrogen passivation of bulk deep nonradiative defects plays any sort of major role in the changes observed in the PL spectra after hydrogenation. The hydrogen passivation of deep defects commonly found

in epitaxial GaAs is expected to be stable under annealing at temperatures below 500C as discussed in Section 2.2.3.3. The spectra of the hydrogenated bulk $Al_xGa_{1-x}As$ samples discussed in Chapter 7 remained unchanged after annealing at 400C for 5 min, annealing conditions which produced marked changes in the present hydrogenated samples. Indeed, after an annealing at 450C it was impossible to discern from the PL spectra alone whether or not a given sample had ever been previously hydrogenated.

6.5.2 Evidence for no significant donor passivation

The passivation of shallow donors is not a serious issue in these samples, which the C-V measurements have clearly shown to be *p*-type. The LDA (Local Density Approximation) studies of Pavesi and Giannozzi [101,102] and related work discussed in Section 2.2.2 provide a good model with experimental support for how hydrogen passivates defects and impurities in GaAs. In a *p*-type sample the hydrogen diffuses in an H+ charge state and is thus unable to passivate donors, although it can do this in a *n*-type sample where the charge state is different [96]. There are several experimental studies of passivation of heavily compensated samples that show that only the majority dopant can be passivated regardless of the conditions [85,130]. These conclusions are also supported by the lack of change in the eA°/DAP ratio and the lack of significant change in the strength of SE and PLE peaks related to the DAP band after hydrogen passivation, both of which are sensitive to the donor concentration.

6.5.3 Evidence for no significant simple acceptor passivation

There is no question that hydrogen can passivate single carbon acceptors, at least at high concentrations. This has been confirmed by infrared absorption lines from localized vibrational modes from passivated $H\text{-}C_{As}$ pairs which closely match theoretical predictions [121,122,123]. It should be noted

that this infrared work has only been done with heavily doped *p*-type samples (carbon concentration $> 1 \times 10^{19}$ cm^{-3}). Pearton, Dautremont-Smith et al. [96] took SIMS depth profiles of passivated Zn-doped *p*-type GaAs using deuterium as a surrogate for hydrogen and found a strong dependence of D concentration on the initial doping level of Zn acceptors. On the other hand, Pan et al. [118] did report photoluminescence experiments claiming to show hydrogen passivation of shallow carbon acceptors in moderately high-purity *p*-type GaAs. Some of their spectra appear quite similar to the present ones, with some of the same changes seen on hydrogenation such as reduction of the g-line. However, they report a reduction in the intensity of the carbon impurity band of 3.5 times and a change in the eA°/DAP ratio, neither of which was observed here. In the present measurements hydrogenation always increases the integrated PL intensity of the carbon impurity band in relative and absolute terms, although the extent of brightening is sample dependent. This observation suggests that significant passivation of isolated cabon acceptors does not take place in the present samples.

Strong evidence for the lack of passivation of the shallow carbon impurities seen in A°X and the carbon impurity band is given by the present results from selective excitation of the LO phonon replica of A°X which shows little change in intensity after hydrogenation and thus no evidence of any substantial change in the neutral acceptor concentration. There was no evidence of excitonic recombination originating in the substrate when it was exposed by turning the sample on edge and PL spectra taken, so it is reasonable to assume that the A°X replica results relate to the epitaxial layer. If there were substantial acceptor passivation this would also have an effect on the eA°/DAP ratio as was reported (but only weakly) by Pan et al. [118], since the concentration of donors would be unaffected. In the magnetophotoluminescence spectra the eA° and DAP bands are well

separated and no such change in ratio is seen, as would be expected if there were a substantial passivation of isolated acceptors.

6.5.4 Passivation of KP and g-line defects and their relationship to free carrier and exciton concentrations.

While C-V measurements on ME122 showed a hole concentration on the order of 1×10^{15} cm^{-3} and a reduction of this by at least an order of magnitude on hydrogenation, the photoluminescence and selective excitation spectra give unequivocal evidence only for passivation of the KP and g-line defects. The excitonic PL lines associated with these defects are strongly reduced. sometimes virtually eliminated after hydrogenation and reappear upon annealing.

As discussed in section 3.4.5 there are a number of research papers by M. Skolnick and others [250,251,252,299] indicating that the KP defects contain pairs of acceptors, so passivation of the KP defects could indeed reduce hole concentrations. There is also evidence that the g-line defect contains a carbon acceptor. Since passivation of the KP and g-line defects clearly occurs in the present samples, it is reasonable to assume that the holes measured by the C-V experiments (and strongly reduced after hydrogenation) are primarily associated with them. There are several possible explanations as to why the KP and g-line defects are passivated but not the isolated carbon acceptors. One possibility is that hydrogen might simply bind to them more strongly. Preferential passivation of deep defects rather than shallow impurities has been claimed for $Al_xGa_{1-x}As$, [129] and references in [138]. Another is that the KP and g-line defects might be concentrated near dislocations, as was shown for their samples by Petroff et al. [54]. Dislocations are known to act as conduits for hydrogen as was discussed above. Regions distant from the dislocations might not be

passivated. A third possibility arises from the model for the axial KP defects put forward by M. Skolnick and his collaborators. If pairs of acceptors are involved in the defects then passivation of just one of the pair would eliminate the particular form of defect that gives rise to the KP excitonic PL.

The KP and g-line defects in these samples act as strong traps for excitons, being responsible for a high proportion of the radiative recombination in the as grown samples. It is not clear whether they trap the excitons directly, or first trap a free carrier of one type and then another to form an exciton on the defect. In any case the effects of hydrogen passivation on the carbon band in PL spectra of the present samples appear very similar to those seen in the case of impurity bands in $Al_xGa_{1-x}As$ when deep defects are passivated: the impurity band increases in intensity without much change in shape [129]. Such an increase of intensity is due to increased availability of free carriers necessary for the recombinations seen in the impurity band as the traps, which are deep defects in the $Al_xGa_{1-x}As$ and KP and g-line defects in the present samples, are eliminated by the hydrogenation. The sample dependent differences in the PL intensity increases seen in the carbon impurity band would thus depend on the concentration and distribution of the KP and g-line defects in the individual samples.

6.5.5 The question of the donor related exciton lines

The strength of donor bound excitonic PL lines is not generally directly proportional to the donor concentration. Because the transition probabilities are greater, the donor bound exciton lines are often stronger than the acceptor bound line even in *p*-type samples. The intensity ratios are also known to be affected by interaction between crystal defects [237], so the explanation for the appearance of donor related exciton lines after hydrogenation is not necessarily an actual increase in donor concentration.

One possibility is that these donor related lines are directly suppressed by the KP or g-line defects. Figure 6.3 shows that the donor bound exciton peaks decrease with annealing as the KP and g-line defects increase. It is known that the incorporation of acceptors can encourage the incorporation of donors [180,239]. Silicon donors have been shown to be concentrated around dislocations [53]. It is possible that many donors located near the KP and/or g-line defects are "hidden" in photoluminescence either because they are part of the defect complexes or simply because they are less efficient at trapping excitons. A difficulty with the above explanation is that selective excitation measurements of the DAP band do not indicate an increase in the ionized donor population after hydrogenation, but as mentioned above it is difficult to be sure that we are not mostly seeing transitions in the substrate. (SE intensity is a measure of ionized donor concentration.) It is also difficult to see why there is no evidence of donor bound excitons arising from the same population of donors that is responsible for the carbon DAP band. It is possible that a small donor bound exciton peak does exist before hydrogenation, but is obscured by the background PL.

6.5.6 The proposed model

The photoluminescence spectra of the present MBE GaAs samples before and after hydrogenation can be largely explained by the preferential passivation of KP and g-line defects located in distinct regions of the samples, probably near dislocations. On such a picture the KP and g-line defect complexes are responsible for trapping excitons and free carriers, causing reduced PL arising from other types of transition. This mechanism is similar to the suppressive effect on all types of PL transitions resulting from recombination through a high concentration of deep defects. The KP and g-line defects also appear to be responsible for the suppression of donor bound exciton lines. In regions separated from those containing the KP and g-line

defects there is little or no hydrogen passivation. Nevertheless there is increased eA°/DAP PL intensity (with the extent depending on the sample) after the KP and g-line defects are passivated, with a resultant increase in the free carrier population.

CHAPTER 7

HYDROGEN PASSIVATION STUDIES OF BULK AND LAYERED GaAs AND $Al_xGa_{1-x}As$ STRUCTURES

7.1 GENERAL INTRODUCTION

It is well known that hydrogen passivation of bulk and layered semiconductors can result in greater PL efficiency and other improvements in optical and electrical properties. Since hydrogen passivation operates on defects and impurities at the interfaces and surfaces and in the bulk, the effect on individual samples is highly variable. Improvements in PL efficiency have been observed which range from two orders of magnitude in some quantum well and superlattice samples and some bulk $Al_xGa_{1-x}As$, to no improvement at all, and even to an actual deterioration of PL efficiency of $Al_xGa_{1-x}As$ and GaAs epilayers [138] and quantum well samples [140] which were initially of very high quality. (A certain degree of damage due to the ion implantation or rf plasma used in hydrogenation is well known, usually at the surface, e.g. [89,92,87]). Such variability of sample response is abundantly observed in the present samples, involving $Al_xGa_{1-x}As$ epilayers, $GaAs/Al_xGa_{1-x}As$ quantum wells and $GaAs/Al_xGa_{1-x}As$ short period superlattices, and some new findings have been made, which are detailed in the sections devoted to the different sample types. An overview of the whole subject of hydrogen passivation of impurities and defects is given in Chapter 2.

7.2 CHARACTERISTICS OF THE SAMPLES

Table 7.1 contains those details of structure and growth that are known for all of the main samples examined, grouped into sections by whether they are (a) $Al_xGa_{1-x}As$ epilayers (b) quantum well samples or (c) short period superlattice samples. Hydrogenation and annealing of samples was carried

Table 7.1(a). **Structure of Bulk $Al_xGa_{1-x}As$ Samples. MBE Samples grown by Drs. P. Kemeny and B. Usher at Telecom Research Laboratories and Dr. Grant Griffiths at CSIRO**

Sample Name (as referred to in text) x for $Al_xGa_{1-x}As$ layers	TRL A x = 0.3	TRL B x = 0.3	TRL C x = 0.3
$Al_xGa_{1-x}As$ layer thickness	2 µm	2 µm	2 µm
nominal doping (carriers cm^{-3})	*n*-type (Si dopant) 1×10^{18} cm^{-3}	*n*-type (Si dopant) 1×10^{18} cm^{-3}	undoped
carrier concentration (measured)	*n*-type 1×10^{16} cm^{-3}	Semi-Insulating	Semi-Insulating
GaAs buffer	1 µm, undoped	0.5 µm, undoped	0.5 µm, undoped
GaAs substrate	semi-insulating	semi-insulating	semi-insulating
Growth Temperature/Conditions	610°C, As_2 source	640°C, As_2 source	615°C, As_4 source

Sample Name (as referred to in text) x for $Al_xGa_{1-x}As$ layers	CSIRO A x = 0.255±0.005	CSIRO B x=0.42
$Al_xGa_{1-x}As$ layer thickness	2 µm	1.5 µm
nominal doping (carriers cm^{-3})	undoped	undoped
GaAs buffer	undoped	undoped
GaAs substrate	semi-insulating	semi-insulating

Table 7.1(b). Structure of Quantum Well Samples. MBE Samples on Semi-insulating substrates grown at Nottingham University (NU) by Dr. M. Henini, at CSIRO by Dr. G. Griffiths and by Drs. M.T. Emeny and G.W. Smith of DRA, Malvern, UK (GWS)

Sample Name	NU84 Modulation Doped QW	NU98 Undoped QW Sample	NU211 Modulation Doped QW
x for $Al_xGa_{1-x}As$ layers	x = 0.3	x = 0.3	x = 0.33
GaAs capping layer	100Å, undoped	50Å, undoped	254Å, undoped
$Al_xGa_{1-x}As$ top barrier	400Å *n*-doped to 1×10^{18} cm^{-3} 400Å undoped spacer	800Å, undoped	305Å *n*-doped to 1×10^{18} cm^{-3} 305Å undoped spacer
GaAs QW	58Å	58Å	102 Å
$Al_xGa_{1-x}As$ barrier	0.5 µm, undoped	0.5 µm, undoped	102 Å, undoped
Buffer	3.5µm undoped GaAs	3.5 µm undoped GaAs	SHORT PERIOD SL 7 REPEATS 34 Å undoped GaAs 102Å undoped AlGaAs 2 µm undoped GaAs

Sample Name	GWS28 (undoped, Structure Assumed Same as Other GWS)	CSIRO 62 (undoped QW)
x for $Al_xGa_{1-x}As$ layers	x = 0.33	x = 0.3
GaAs capping layer	200Å, undoped	none
$Al_xGa_{1-x}As$ top barrier	500 Å undoped	400Å, undoped
Quantum Well Section	10 REPEATS 50Å GaAs Well 500Å AlGaAs barrier	80Å GaAs (QW A) 140Å AlGaAs barrier 140Å GaAs (QW B) 140Å AlGaAs barrier 300Å GaAs (QW C)
$Al_xGa_{1-x}As$ bottom barrier	-	2 µm, undoped
Buffer	1 µm undoped GaAs	1 µm undoped GaAs

Table 7.1(c). Structure of Superlattice Samples. MBE Samples grown by Drs. M.T. Emeny and G.W. Smith of DRA, Malvern, UK. Barriers AlAs in GWS97 and $Al_{0.33}Ga_{0.67}As$ in all other samples.

Sample Name	GWS148	GWS151	GWS180
GaAs capping layer	240Å, undoped	240Å, undoped	240Å, undoped
Top Barrier	none	none	500Å undoped AlGaAs
Superlattice	100 REPEATS (undoped layers) 9 ml (25.5Å) AlGaAs 12 ml (34Å) GaAs 9 ml (25.5 Å) AlGaAs	100 REPEATS (undoped layers) 9 ml (25.5Å) AlGaAs 12 ml (34Å) GaAs 9 ml (25.5 Å) AlGaAs	12 ml (25.5Å) GaAs 100 REPEATS (undoped layers) 9 ml (25.5Å) AlGaAs 12 ml (34Å) GaAs
Bottom Barrier	none	none	500Å undoped AlGaAs
Buffer	200Å undoped GaAs 1µm GaAs, *n*-doped to 1 × $10^{18}/cm^3$ with Si	200Å undoped GaAs 1µm GaAs, *n*-doped to 1 × $10^{18}/cm^3$ with Si	1µm GaAs, *n*-doped to 1 × $10^{18}/cm^3$ with Si
Growth Temperature/Conditions	bottom 0.75µm of buffer grown at 600C, rest of sample at 620C	bottom 0.75µm of buffer grown at 600C, rest of sample at 650C	bottom 0.75µm of buffer grown at 600C, rest of sample at 650C

Sample Name	GWS47	GWS97
GaAs capping layer	240Å, undoped	240Å, undoped
Top Barrier	none	none
Superlattice	100 REPEATS (layers undoped) 8 ml (22.6Å) AlGaAs 12 ml (34Å) GaAs 8 ml (22.6 Å) AlGaAs	100 REPEATS (layers undoped) 8 ml (22.6Å) AlAs 10 ml (28.3Å) GaAs 8 ml (22.6 Å) AlAs
Bottom Barrier	none	none
Buffer	200Å undoped GaAs 1µm GaAs, *n*-doped to 1 × $10^{18}/cm^3$ with Si (note that PL spectrum of buffer appears undoped)	1µm GaAs, *n*-doped to 1 × $10^{18}/cm^3$ with Si

out by the methods detailed in Chapter 4. In all the sections that follow, H after the sample name refers to the hydrogenated version, while AsG means the As Grown version of the sample. When Hann follows the sample name, it refers to a sample piece that has been hydrogenated and then annealed under conditions known to reactivate shallow impurities, but not common deep defects in GaAs.

7.3 EXPERIMENTAL RESULTS ON HYDROGENATED MBE $Al_xGa_{1-x}As$ EPITAXIAL LAYERS

7.3.1 Introduction

Some poor quality bulk $Al_xGa_{1-x}As$ samples grown by Telecom Research Laboratories under non-optimal conditions were obtained to determine the effects of hydrogenation, along with higher quality samples from CSIRO for comparison. The main samples are described in Table 7.1(a). Note that some of the TRL samples were *n*-doped, but later measured as semi-insulating or of much lower carrier concentration than the nominal value. The samples were characterized by 5K photoluminescence (PL) measurements between 0.91 and 2.07 eV, before and after hydrogenation by the process described in Chapter 4. After the initial characterization the hydrogenated pieces of TRL B and CSIRO A were sent to ANSTO for annealing for 5 minutes at 400C, a temperature sufficient to reactivate shallow donors, but not most deep levels in MBE GaAs. As shown from the normalized results in Table 7.2, the TRL samples exhibited large increases and the CSIRO samples modest increases in the integrated photoluminescence intensity. This increase occurred for every peak or band in the PL spectra, and the changes were not reversed on annealing. Further evidence is presented that these changes, similar to ones previously descibed [129,300] should be attributed to the hydrogen passivation of deep defects in the bulk $AlGa_xAl_{1-x}As$. The involvement of DX

centers and defects emitting in the infrared are ruled out as a cause of the changes with hydrogen passivation.

7.3.2 5K Photoluminescence Results

TRL A showed no photoluminescence at all in its as grown state, even at high laser intensities. CSIRO B showed a dominant bound exciton peak and a single smaller broad peak at energies characteristic of a broad eA°/DAP band. All of the other As Grown spectra were dominated by extrinsic recombination involving donor/acceptor pairs (DAP) as described by Henning and Ansems [301] and Pavesi [94]. In all of the TRL samples (apart from TRL A) only one broad band was visible, with its peak at energies consistent with DAP recombination at the bandgap determined by the Al mole fraction x of the sample. The TRL spectra are similar to those shown in Bosacchi et al. [300], as representative of $Al_xGa_{1-x}As$ samples grown without incorporation of hydrogen during growth. Figure 7.1 shows typical spectra for the low and higher quality samples. For both CSIRO samples the positions of the bound exciton peaks are consistent with x, according to the charts in Kuech et al. [302]. As can be seen from Table 7.2, apart from TRL A, both the other TRL As Grown samples were of similar brightness, about an order of magnitude less than that of the brighter CSIRO sample.

Photoluminescence was insignificant between 0.91 eV and 1.45 eV, regardless of hydrogenation status. Spectra were taken in this energy range because certain workers [303,304] had reported strong photoluminescence in the infrared in MOCVD, MOVPE and MBE $Al_xGa_{1-x}As$ samples between 1.1 eV and 0.8 eV associated with midgap traps.

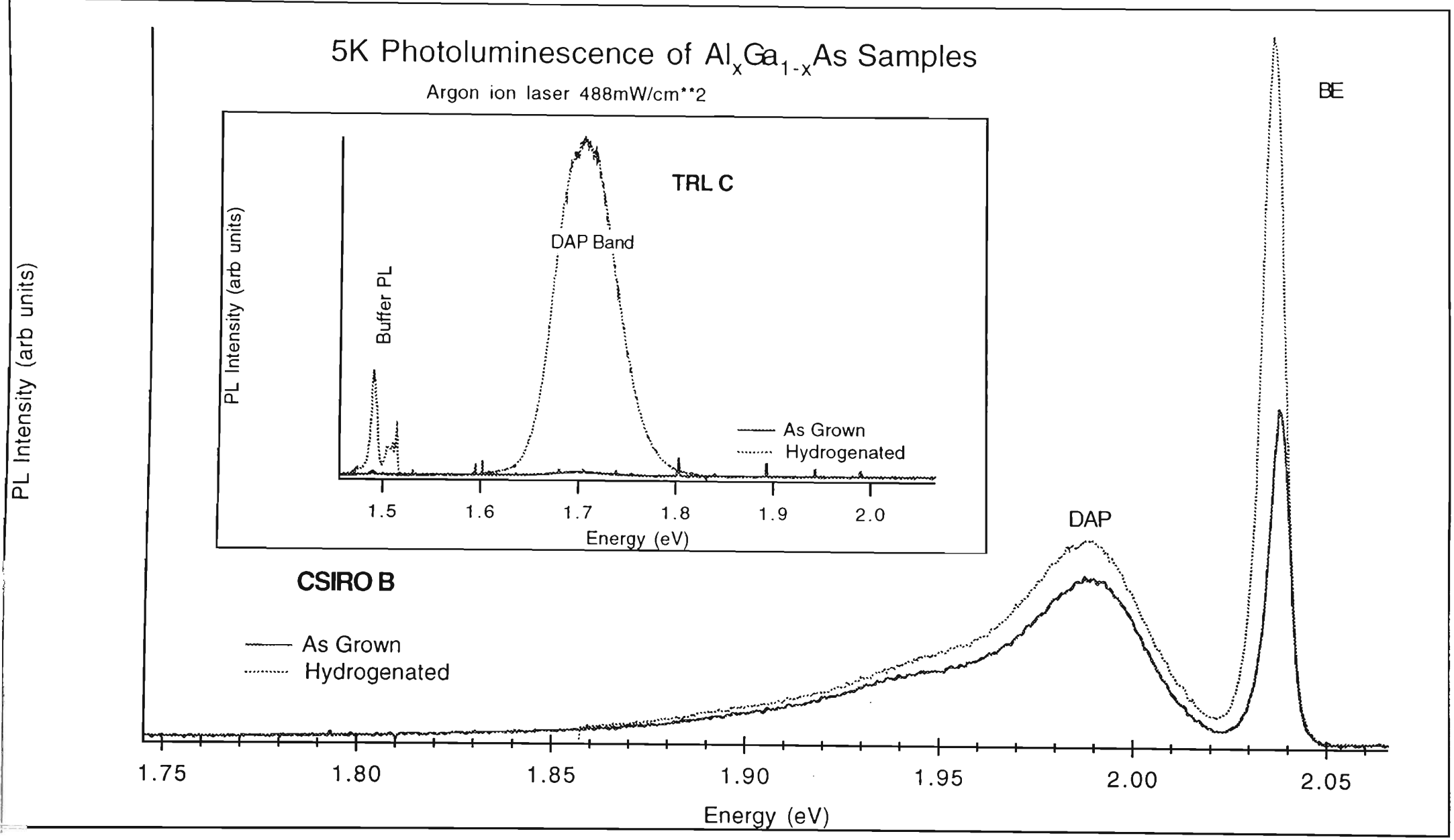

Figure 7.1. **5K PL spectra of typical high and low quality (inset) samples.**

Table 7.2 Integrated PL intensity between 600 and 850 nm of $Al_xGa_{1-x}As$ samples. Excitation with 488 nm line of Argon Ion laser at 480 mW/cm^2. Samples at 5K. Integrated intensity normalized to 1 for TRL C AsG to facilitate direct comparison of samples. There was approximately 20% variation between spots on the sample for the TRL samples and 10% for the CSIRO samples. Hydrogenated pieces of TRL B and CSIRO A were annealed for 5 min at 400C.

Sample Name	Integrated PL As Grown Sample (arb units)	Integrated PL Hydrogenated Sample (arb units)	Factor of Increase
TRL A	undetectable	13	>50×
TRL B	1.6	10	6.2×
TRL B after annealing	1.6*	11*	7×
TRL C	1	34	34×
CSIRO A	4.6	12	2.7×
CSIRO A after annealing	4.6	8.6	1.8×
CSIRO B	17	23	1.3×

*Estimated from spectrum taken at 4.8 W/cm^2. Spectral intensities were approximately linear over this range.

7.3.3 Effects of Hydrogenation and Annealing

As is shown in Figure 7.1, hydrogenation increases the PL intensity of every peak or band, including those due to GaAs in the buffer. In the TRL samples the single broad DAP peak arising from the $Al_xGa_{1-x}As$ layer becomes greatly magnified in intensity with hydrogenation, but without any other significant changes in the spectrum, as was observed for their samples by Bosacchi et al. [300]. In the case of the CSIRO samples, hydrogenation produced a modest increase in PL efficiency in CSIRO B and a small increase overall of 2 to 3 times in CSIRO A, with the increase particularly noticeable for the bound exciton peak, with the lesser improvement in PL efficiency relative to the TRL samples attributable to the CSIRO samples being of greater initial quantum efficiency [138]. There were no significant differences between the hydrogenated and annealed samples, although the annealing temperature was sufficient to produce recovery of shallow donor activity and of DX centers, as discussed in Section 2.2.3.3.

7.3.4 Conclusions on $Al_xGa_{1-x}As$ Samples

The main results are consistent with those observed by Pavesi et al. [129,305], Mehta et al. [132] and Bumai et al. [138]. The 'good quality' CSIRO samples showing excitonic activity in the As Grown condition showed little gain in PL efficiency with hydrogenation. By contrast the lower quality TRL samples showed massive gains in PL efficiency, of at least 7 times (in TRL B), and of more than an order of magnitude in TRL A and TRL C. These gains were similar to those observed by Pavesi et al. [129] and the other references and were far greater than those reported in the literature for uncapped GaAs samples [129].

The results in the present case are consistent with the Pavesi et al. [129] view that massive increases in the quantum efficiency of bulk $Al_xGa_{1-x}As$ samples

is associated with the preferential passivation of deep defects rather than shallow impurities. In support of this view, they noted the absence of changes in relative intensities of different parts of their PL spectra after hydrogenation, as is also the case with the present TRL samples. Deep defects are further implicated in the present work by the fact that there were no significant changes in the hydrogenated TRL B and CSIRO A samples as a result of annealing under conditions known to reactivate previously passivated shallow impurities.

It was also possible to draw some conclusions on the nature of these deep defects. There was no evidence of involvement of centers emitting in the infrared down to 0.91 eV. There is also strong reason to doubt the conclusion of Bosacchi et al. [300] that DX centers are the killer centers responsible for poor PL efficiency in samples such as the TRL ones. Oelgart et al. [306] point out that DX centers have a small thermally activated capture cross section so that their population of trapped carriers would be insignificant at low temperature under strong illumination. DX centers also exhibit the same response to hydrogen passivation and annealing as shallow donors [116]. In fact DX centers are strongly associated with a high shallow donor concentration (e.g. Bhattacharya [307]), and probably in fact arise from a deep impurity state induced by a simple donor impurity [308]. This allows a further argument in relation to our samples. The TRL samples that showed the greatest improvement in PL efficiency after hydrogenation were tested for donor activity and were found to have low carrier concentrations or to be semi-insulating. TRL C showed a big improvement with hydrogenation although it was not deliberately doped and measured as semi-insulating. In TRL B and CSIRO A there were no significant differences in hydrogenated samples before and after annealing at 400C, and therefore no evidence of any sort of recovery in defects or impurities.

There is no inconsistency in the present results with the main defect(s) being the Al-O-C complexes claimed by Mehta et al. [132] and Dallesasse et al. [309] to be responsible for the degradation of PL efficiency in exposed $Al_xGa_{1-x}As$. In the case of the TRL samples there was an actual suspicion of oxygen contamination during growth [310] which would account for the discrepancy between the nominal doping and measured carrier concentrations in some of the samples. Mehta et al. observed huge improvements with hydrogenation in the PL efficiency of samples that had been degraded after storage under humid conditions for more than a year. The improvements were only reversed by annealing at 500C.

7.4 EXPERIMENTAL RESULTS ON HYDROGENATED MBE GaAs/$Al_xGa_{1-x}As$ QUANTUM WELL SAMPLES

7.4.1 Introduction

Modulated and undoped single and multi- quantum well samples of varying quality were examined by photoluminescence (PL) and photoluminescence excitation (PLE) spectroscopy before and after hydrogenation and annealing at 400C for 5 minutes, a temperature sufficient to reactivate shallow impurities but not deeper defects. The structure of the individual samples is described in Table 7.1(b). The PLE spectra associated with the quantum wells, with detection on the low energy side of the E_{1hh1} transition tended to be weak and difficult to interpret apart from those associated with the MQW sample GWS28.

5K photoluminescence results were consistent with those reported in the literature, where response to hydrogenation was shown to vary strongly

with sample quality and to involve both the $Al_xGa_{1-x}As$ barriers and the wells themselves [129,138]. New results include (1) evidence from annealing that improvements in PL efficiency following hydrogen passivation are predominantly associated with shallow impurities, but with some improvement remaining after annealing due presumably to deeper defects associated with the wells; (2) an improved response at elevated temperatures after hydrogenation due to passivation occurring in the barriers even in samples where there was no apparent increase in PL efficiency at 5K; and (3) a demonstration of the elimination of the effects of modulation doping by hydrogen passivation of donors in the barrier.

7.4.2 Low Temperature Photoluminescence of the As Grown Samples

Figure 7.2 shows the 5K PL spectra of two modulation doped samples before and after hydrogenation. These include (a) the good quality sample NU211 and (b) the low quality sample NU84. Note that the quantum well photoluminescence in NU211AsG shows the typical asymmetrical modulation doped shape, caused by recombination of photo-created holes with the equilibrium free electron gas in the well, which has an electron sheet density n_s on the order of 5×10^{11} cm^{-2}. The excess electrons are supplied by heavy donor doping in the barrier. Exciton formation is suppressed as a result of screening and so called 'phase space filling' by the free electrons [7,311,312]. After hydrogenation, this characteristic lineshape is replaced by the typical Gaussian/Lorentzian lineshape seen in the case of excitonic recombination in undoped good quality quantum wells. The spectra of the quantum wells in all versions of the good quality undoped samples CSIRO62 and GWS28 strongly resemble the spectrum of the quantum well in NU211H although intensities and positions vary (according to well width, as described in Section 1.2.3), while the peak position of the quantum well PL from all

(a)

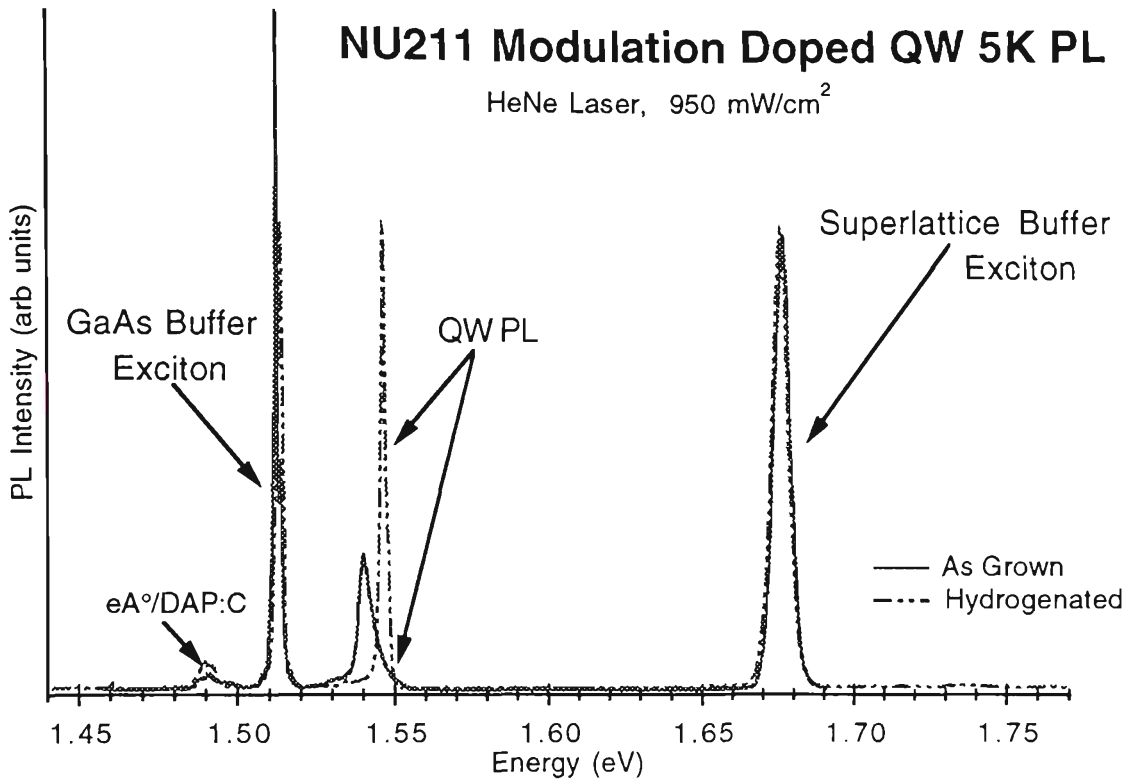

(b)

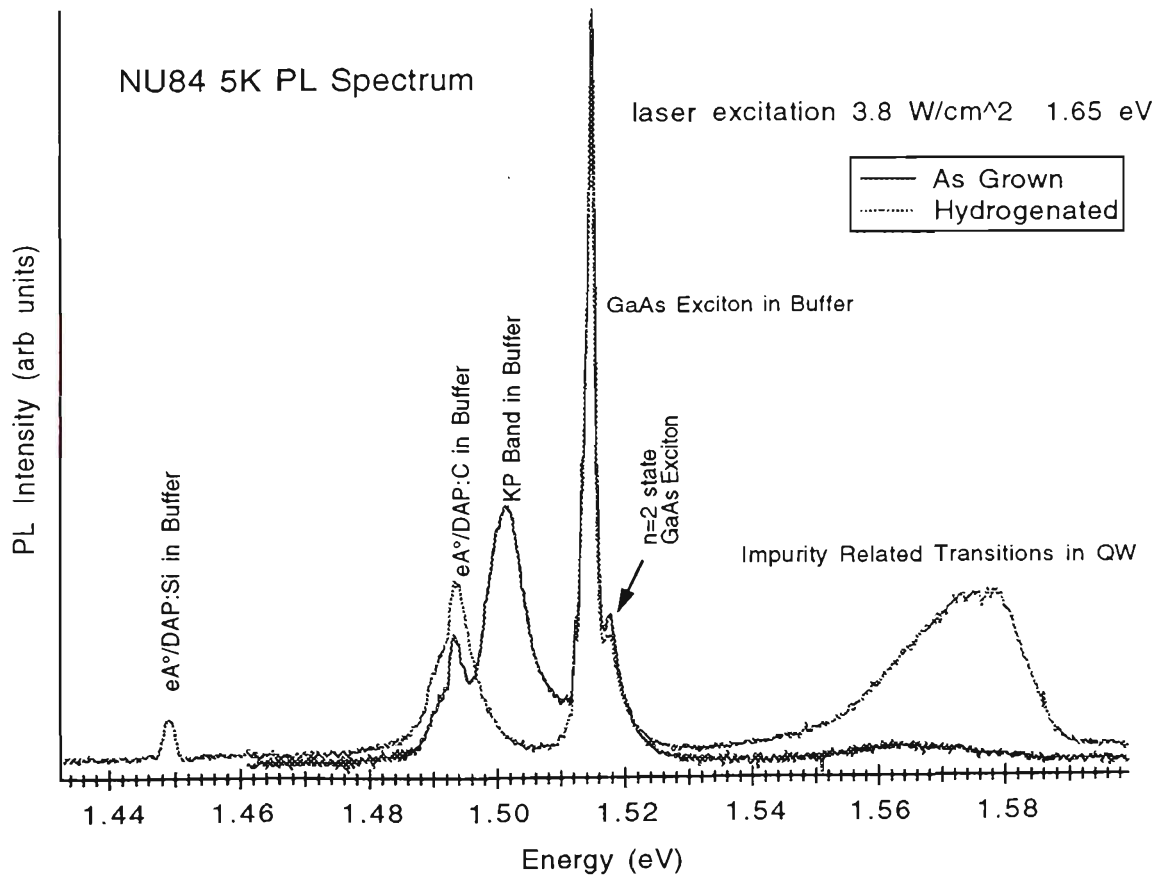

Figure 7.2. (a)NU211 Note the reversal of modulation doping and appearance of excitonic recombination with hydrogenation. (b)NU84 is of lower quality. Hydrogenation increases PL efficiency but excitonic PL is not seen from the quantum well. The increase in PL with hydrogen is greater when the laser excitation is above the $Al_xGa_{1-x}As$ bandgap.

samples is in fair agreement with the positions expected for E_{1hh1} recombination. All the samples, good and poor. show recombination from the buffer in their PL spectra and varying amounts of impurity related recombination in the PL from the $Al_xGa_{1-x}As$ barriers.

NU98 and NU84 are of much lower quality, probably due to non-optimum growth conditions and possibly also the absence of a superlattice buffer to trap impurities and defects, as described in Section 2.1.3. For NU98AsG and NU84AsG photoluminescence associated with the quantum well is weak. asymmetrical and very broad (<23 meV HWHM), and in a position consistent with extrinsic recombination in the well. Intrinsic recombination only occurs at very high laser intensities. At power densities less than $10W/cm^2$ such as are used in the present measurements there is no suggestion of modulation doping in the QW lineshape of NU84. although it is nominally modulation doped to the same donor density as NU211. All the samples show recombination from the buffer in their PL spectra and varying amounts of impurity related recombination in the PL from the $Al_xGa_{1-x}As$ barriers.

7.4.3 Effects of Hydrogenation and Annealing

Table 7.3 contains the integrated QW PL intensities taken under different conditions for the various samples. There are no significant changes in quantum well PL lineshape or intensity after hydrogenation in the good quality samples (apart from the modulation doped sample NU211). An increase in the intensity of barrier recombination seen in the PL spectra and the passivation of the KP band in the GaAs buffer, such as is discussed for the samples in Chapter 6, indicates that the samples were in fact effectively hydrogenated. For NU211H the QW photoluminescence shows a complete loss of the characteristic modulation doped lineshape as mentioned above. The

Table 7.3 **Integrated PL intensity of Quantum Wells for Paired As Grown and Hydrogenated Versions. Integrated intensity normalized to 1 for NU84AsG. This column was included to indicate the initial relative brightness of each sample. Annealing was for 5 minutes at 400C**

Sample Name	Temperature	Laser Line (eV)	Laser Power Density	Integrated QW PL in As Grown Sample (arb units)	Factor of Increase for Hydrogenated Sample
NU84 (mod. doped)	5K	1.958	11 W/cm^2	1	43×
	5K	1.653	3.8W/cm^2	0.8*	6.2×
after annealing	5K	1.958	11 W/cm^2	1.2	3.6×
	5K	1.746	19W/cm^2	7.8*	3.9×
NU98 (undoped)	5K	1.958	2.3W/cm^2	1.2	20.6×
	5K	1.653	3.8W/cm^2	0.7*	16.2×
after annealing	5K	1.958	19W/cm^2	0.5	3.9×
	5K	2.540	140mW/cm^2	0.6	1.6×
NU211 (mod. doped with SL buffer)	5K	1.653	3.8W/cm^2	1.9*	2.6×
	5K	1.958	950mW/cm^2	4.0	1.3×
	77K	1.958	950mW/cm^2	1.2	2.4×
CSIRO62 QW A	5K	1.653	3.8W/cm^2	1.3*	0.69×
QW B	5K	1.653	3.8W/cm^2	2.5*	0.49×

*Estimated from spectrum taken at 4.8 W/cm^2. Spectral intensities were approximately linear over this range.

lineshape is narrower and peaks at higher energy after hydrogenation. A modest increase in PL intensity also occurs, as can be seen from Figure 7.2(a).

The low quality samples NU84H and NU98H show a dramatic increase in PL intensity over the As Grown situation, of the order of 20 to 40×. In NU84, which was nominally modulation doped, the increase in PL intensity after hydrogenation is much greater when the laser excitation is above the $Al_xGa_{1-x}As$ bandgap, rather than when there is direct excitation of the quantum well. After annealing for 5 minutes at 400C most of the improvement in PL efficiency in these low quality samples is reversed, with spectra the same regardless of whether laser excitation is above or below the $Al_xGa_{1-x}As$ bandgap, suggesting that the remaining improvement is associated with the wells or interfaces rather than the bulk barrier layers.

7.4.4 Effects of Hydrogenation on the Temperature Dependence of a Good Quality QW Sample

A detailed study of CSIRO62 showed that quenching of PL intensity with increasing temperature is weaker when the laser excitation is below the $Al_xGa_{1-x}As$ bandgap, with QW A and QW B of CSIRO62 still showing an integrated PL intensity at 70K that is 70% to 90% of the integrated PL intensity at 5K. QW C is largely obscured at lower temperatures by excitonic recombination from the GaAs buffer. When the laser excitation is above the $Al_xGa_{1-x}As$ bandgap, the 70K/5K ratio of the integrated PL intensities for QW A and QW B in the As Grown sample is only of the order of 3% to 10%. After hydrogenation the 70K/5K ratio is of the order of 30%, even though there is no significant difference between the PL intensities of the As Grown and hydrogenated versions of the sample at 5K. The observed improvement in PL efficiency at higher temperatures after hydrogenation is reversed after

annealing for 5 minutes at 400C, as can be seen in Figure 7.3. Similar effects were observed in the good quality MQW sample GWS28.

7.4.5 Conclusions on Hydrogenated Quantum Wells

The present samples showed a wide variation in response to hydrogenation, from apparently none at all to manyfold increases in integrated PL intensity. It is known that the extent of the response to hydrogen passivation or indeed whether there are any visible effects at all is highly dependent on the initial quality of the well and barriers [138]. It is also well established that changes in the PL spectrum of a quantum well after hydrogenation can be caused not only by the direct passivation of defects or impurities in the well itself (especially at the interfaces) but also by the passivation of defects or impurities in a wide adjoining barrier. This is due to the resulting increase in diffusion length leading to an additional flood of photo-created carriers falling into the well from the barrier [129,138]. The lack of this flood of carriers can result in much smaller improvements in PL efficiency when the laser excitation is below the $Al_xGa_{1-x}As$ bandgap than above, as was observed in NU84. In this modulation doped sample the extra improvement due to passivation in the barriers was reversed by annealing at a temperature just sufficient to reactivate shallow impurities. This extra improvement with excitation above the $Al_xGa_{1-x}As$ bandgap was not evident in the sister undoped sample NU98, suggesting that the modulation doping in this low quality sample might somehow be involved in defect complexes.

The effects of modulation doping on the PL spectrum of NU211 were completely eliminated by hydrogenation, providing clear evidence of donor passivation in this sample. This reversal suggests that hydrogenation and annealing at various temperatures could be used to control the electron concentration in *n*-type modulation doped quantum wells, so that a uniform

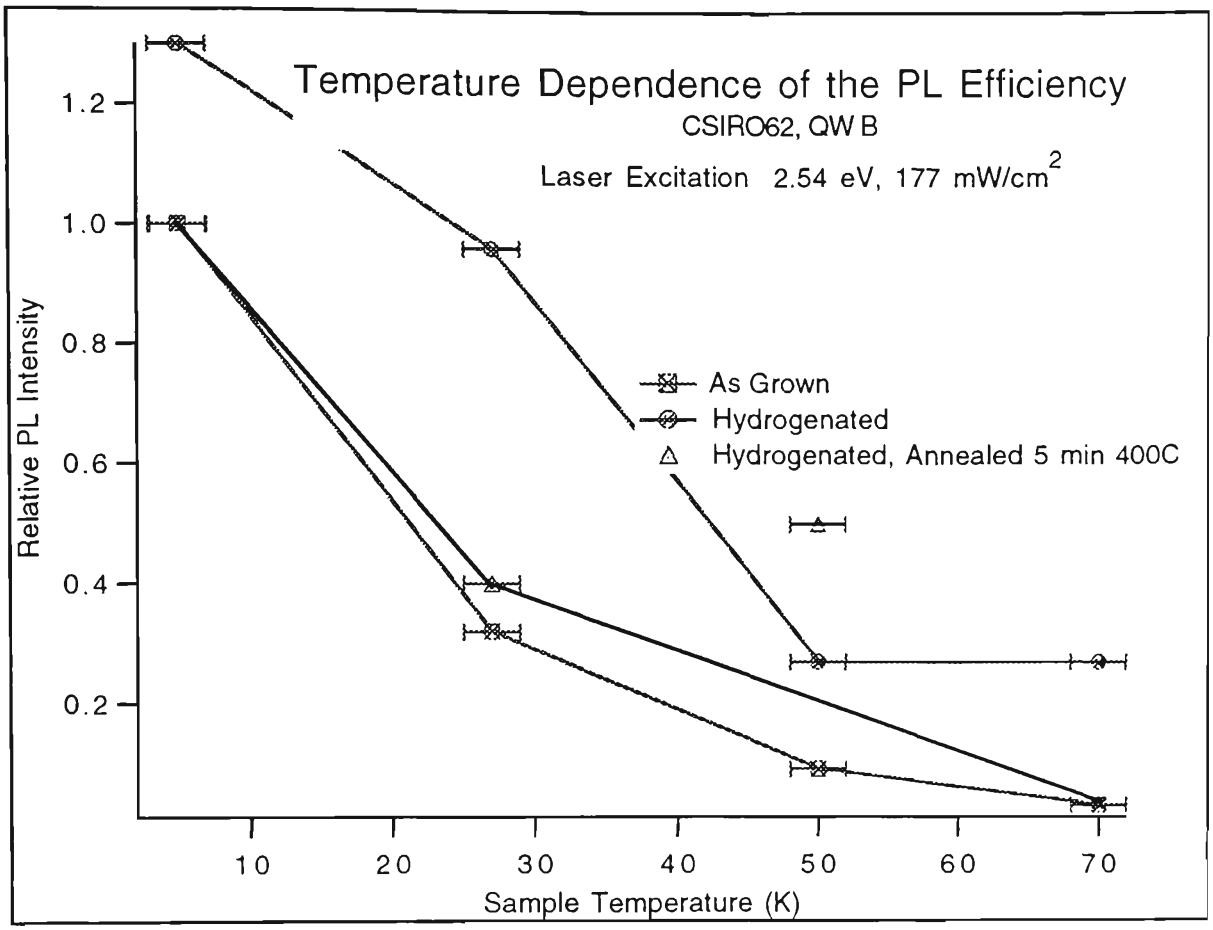

Figure 7.3. **Hydrogenation causes a reduction in PL quenching with temperature, a reduction which is reversed by annealing. The lines are merely a guide for the eye. The 50K value for the annealed sample appears anomalous.**

single heavily doped layer in a single wafer could produce a wide variety of modulation doped samples.

Thermal quenching of PL intensity from the quantum wells as the sample temperature was raised was reduced by hydrogenation in the good quality samples CSIRO62 and GWS28, but only when the excitation was above the $Al_xGa_{1-x}As$ bandgap, suggesting that the effect is due to passivation of defects or impurities occurring in the (nominally undoped) barriers. This reduction in quenching was reversed by annealing under conditions just sufficient to reactivate shallow impurities. Such a weakening in thermal quenching is not unexpected if non-radiative defects in the barrier with thermally activated capture cross sections are being passivated.

7.5 EXPERIMENTAL RESULTS ON HYDROGENATED MBE SHORT PERIOD SUPERLATTICES

7.5.1 Introduction

Short period superlattices, with their extended miniband states in the growth direction giving them a definite 3D character, show some optical properties intermediate between those of bulk semiconductors and quantum well systems, such as reduced heavy hole/light hole splitting and reduced exciton and impurity binding energies relative to those typically observed in quantum wells. Other properties, such as the appearance of saddle point excitons, are only seen in superlattices [313]. The present work shows that the response to hydrogenation of the PL spectra is strongly affected by one such intermediate property, the rapid transport of free carriers and excitons with excess kinetic energy to nonradiative recombination centers in the surface and substrate.

Temperature dependent PL measurements of the present samples indicate that much of the PL intensity arising from the superlattices in these samples is associated with weakly localized excitonic states in the low energy side of the superlattice minibands. Photocreated carriers which occupy miniband states apparently have a high probability of tunneling or hopping to nonradiative recombination centers as the temperature is raised. PL spectra exhibit little response to hydrogenation unless the rapid transport of delocalised carriers and excitons (to a lesser extent) out of the superlattice is suppressed by enclosure of the superlattice in a double heterostructure or by substantial disorder. The short period superlattices studied are of variable quality and show a variable response to hydrogenation, from none of any significance to a manyfold increase in PL intensity. The same variability was also seen in some of the bulk and quantum well samples discussed in the previous sections. Details of the sample structure and growth are given in Table 7.1(c).

7.5.2 Overview of the Samples

As a brief overview, all samples have 100 periods of GaAs/$Al_xGa_{1-x}As$, x=0.33 (except GWS97, x=1). GWS151, GWS148 and GWS180 are all 12/9 ml (12 monolayers of GaAs followed by 9 monolayers of $Al_xGa_{1-x}As$ in each period), with the superlattice in GWS180 enclosed in a double heterostructure and GWS148 grown at a lower temperature than the other two. GWS47 is a 12/8 ml sample. GWS97 contains a 10/8 ml superlattice whose E_{1hh1} exciton is expected [314] and found [315] to be pseudo-direct. A pseudo-direct transition is an indirect transition that appears direct because the main peak in PL is the zero-phonon peak, a phenomenon caused by X-Γ mixing by the potential discontinuity across the interface [316].

Pieces of the samples were hydrogenated at 307C for 1 hour as described in Chapter 4. The As Grown and Hydrogenated versions were studied using photoluminescence and photoluminescence excitation (PLE) at 5K and higher temperatures. A piece of the hydrogenated version of GWS47, the sample which showed the largest response to hydrogenation, was also annealed at 400C for 5 minutes as described in the experimental methods section.

7.5.3 Photoluminescence Results at 5K

Figure 7.4 shows spectra of three of the main samples before and after hydrogenation. The spectra of GWS148 and GWS97 (apart from the expected differences in superlattice peak position and intensity) resemble those of GWS151. Apart from recombination associated with the GaAs buffers, the spectra consist of a sharp symmetrical peak whose position is reasonably consistent with the E_{1hh1} recombination of superlattice excitons and a lower energy shoulder or separate peak(s) probably involving recombination through impurities in the superlattice. The poor quality of the 12/8 ml superlattice sample GWS47 is revealed by very low PL efficiency as is shown in Figure 7.4. There is up to a 10 fold variation in PL efficiency when identical spectra are taken of different spots on this particular sample. There were also small anomalous peaks in some spectra of this sample appearing at the correct position for recombination in a 12/9 ml superlattice, giving evidence of at least some period fluctuation. In GWS47, the excitonic PL is roughly two orders of magnitude weaker (depending on the excitation level) relative to the other samples, while the extrinsic contribution to the PL is larger than for the other samples, and the superlattice exciton peak broader, indicating lower quality. Buffer recombination is consistent with the nominal *n*-doping, apart from GWS47 where the buffer appears undoped.

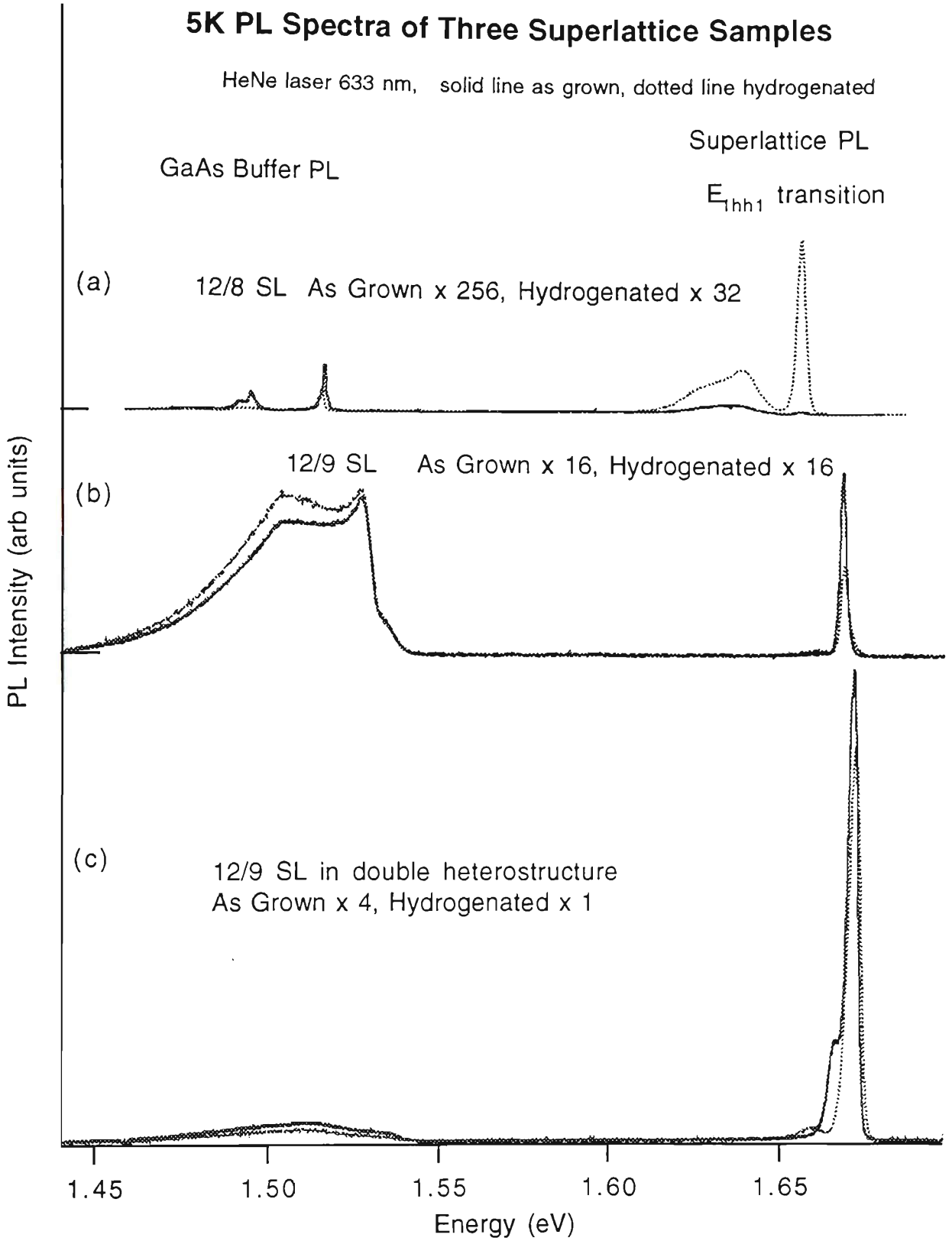

Figure 7.4. Three superlattice samples, x=0.33 (a) GWS47 190 mW/cm^2 (b) GWS151 570mW/cm^2 (c) GWS180 570mW/cm^2 Solid lines show the as grown, dotted lines the hydrogenated versions of each sample. The spectra of GWS148 (x=0.33) resembles that of GWS151, as does GWS97 (x=1), apart from the position and intensity of the superlattice PL.

Detailed PLE spectra of superlattice excitonic transitions for GWS151AsG and GWS180AsG are reported in Peggs et al. [317]. The Stokes shift for the E_{1hh1} peak between the reported PLE spectra and PL spectra is ≤ 1 meV, giving evidence of the presence of weakly localized states. A similar shift to lower energy of the peak of the excitonic resonant Raman excitation profile (relative to the absorption peak) also indicates the importance of localized states [205]. It is also notable in connection with the Peggs et al. results that the PLE spectrum of GWS151AsG, a good quality sample where the superlattice was grown without confinement in a double heterostructure, shows strong suppression of higher energy continuum transitions. Such suppression is attributed to carrier migration out of the superlattice [313,317]. The continuum transitions do appear in the sister sample GWS180AsG grown with superlattice confinement. PLE spectra of GWS148 and GWS47 taken by the present author with detection on peaks in the GaAs buffer show sharp dips corresponding to transitions in the superlattice, as is shown in Figure 7.5 for GWS148. Stokes shifts are ≤ 1 meV for the E_{1hh1} transition in PL and PLE for both samples. These quasi-absorption spectra also show the true relative intensities of the lowest light and heavy hole transitions, in contrast to PLE spectra with detection on the low energy side of the E_{1hh1} exciton, where transport of photocreated particles out of the superlattice can cause the E_{1lh1} peak to appear very weak.

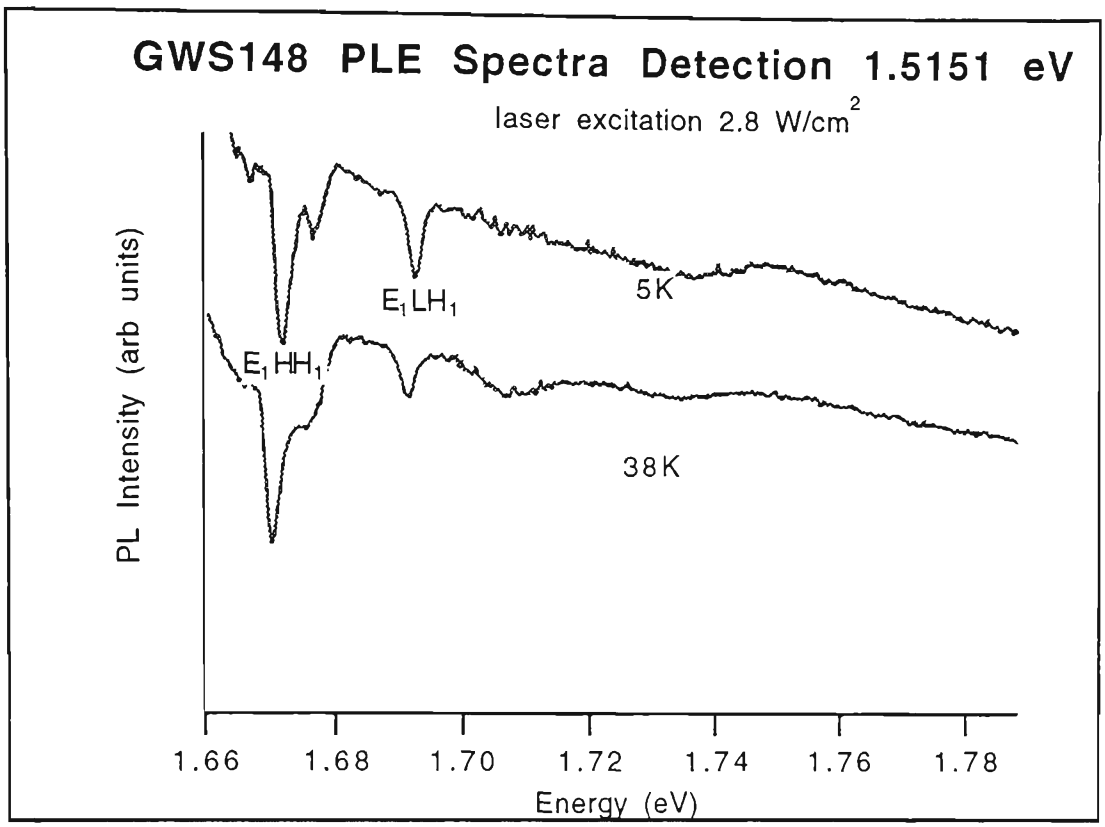

Figure 7.5. Quasi-absorption spectrum of GWS148AsG shows SL transitions. Detection is set within the PL band of the buffer layer. The lack of change with temperature indicates that carriers migrating out of the superlattice do no tmake a large contribution to the buffer PL. The spectrum of GWS47 is similar, regardless of hydrogenation status.

The rate of increase of integrated SL exciton PL intensity with laser excitation is approximately linear in GWS151 indicating good quantum efficiency [298], slightly superlinear in GWS97 and definitely superlinear in the other samples, especially GWS47. Such superlinearity indicates that impurity or defect transitions are being saturated as the laser excitation is raised. As an example of the magnitude of the superlinearity, the ratio of the integrated PL intensities of the superlattices in GWS180AsG to GWS151AsG (its sister sample grown without superlattice confinement), increases from less than 3× at a laser intensity of 20mW/cm^2 to 17× at 570mW/cm^2. The intensities of the superlattice impurity PL peak and the GaAs buffer extrinsic and intrinsic PL peaks in GWS47 show a roughly linear dependence on laser excitation, while the superlattice exciton shows a strongly superlinear behaviour.

7.5.4 Effects of Hydrogenation

The response of the PL spectra to hydrogenation varied from sample to sample. The energy of the laser excitation made no significant difference, provided only that it was above the superlattice energy levels. This is in contrast to the situation observed for some of the quantum well samples discussed in Section 7.4. This lack of sensitivity to the laser excitation energy is expected because none of the superlattice samples apart from GWS180 contain $Al_xGa_{1-x}As$ layers outside of the superlattice, and the volume of barrier material in the double heterostructure in GWS180 is only one sixth the volume of the superlattice.

As suggested in Figure 7.4, the samples fit naturally into two groups in their response to hydrogenation. The PL spectra of GWS151, GWS97 and GWS148, the good quality samples grown without superlattice confinement, all show a modest response (GWS148, grown at a lower temperature than the others) or no significant response (GWS151 and GWS97) to hydrogenation in terms of increased intensity due to recombination from the superlattice.

In GWS180 (superlattice confinement), hydrogenation increases the integrated intensity of the main SL peak by a factor of approximately 6×, depending on the laser excitation. GWS47, the sample showing the greatest improvement, showed increases in integrated intensity of the E_{1hh1} peak after hydrogenation of 50 to 100× depending on the spot on the sample. The superlattice impurity peak is brightened and shifted to higher energies, but the percentage improvement is not as great as for as the E_{1hh1} peak. The GaAs buffer is also brightened at high laser power, but only when excitation is above the superlattice energy levels. Annealing at 400C for 5 minutes almost completely reverses the improvements in PL efficiency caused by

hydrogenation, unlike the situation in some quantum well samples where there was some residual improvement in the quantum well PL.

7.5.5 Temperature Dependence of PL Intensity

PL spectra of all the superlattice samples show the integrated PL intensity emitted from the superlattices falling off rapidly with increasing temperature. Such PL is almost completely quenched by 35-45 K. Detailed measurements of superlattice PL intensity as a function of temperature were made for some of the samples. It became clear from the temperature dependence of superlattice photoluminescence intensity that PL intensity is well described by a $\exp(T/T_o)$ dependence, with T_o fitted between 6K and 10.5K. An Arrhenius or $\exp(-T_o/T)$ form would be expected if the temperature dependence were activated. (Temperature dependence of PL intensity is discussed in Sections 3.4.7 and 3.4.8) In GWS47, the temperature dependence was studied before and after hydrogenation. In this case PL intensity decreased more sharply with increasing temperature after hydrogenation. Nevertheless it was found that a higher temperature was required for complete quenching of PL due to the greater low temperature PL efficiency after hydrogenation. The $\exp(T/T_o)$ temperature dependence remained after hydrogenation. Figure 7.6 shows qualitative fits of the PL temperature dependence for this sample and for GWS148AsG.

7.5.6 Conclusions on Hydrogenated Short Period Superlattices

Some $GaAs/Al_xGa_{1-x}As$ short period superlattices studied show dramatic improvements in PL efficiency after hydrogenation, while hydrogenation resulted in little or no effect on other samples. A similar improvement was observed by Fischer et al. [139] after hydrogenation of GaAs/AlAs superlattices with much shorter periods than those of the present samples. Fischer et al. found from time resolved photoluminescence that the

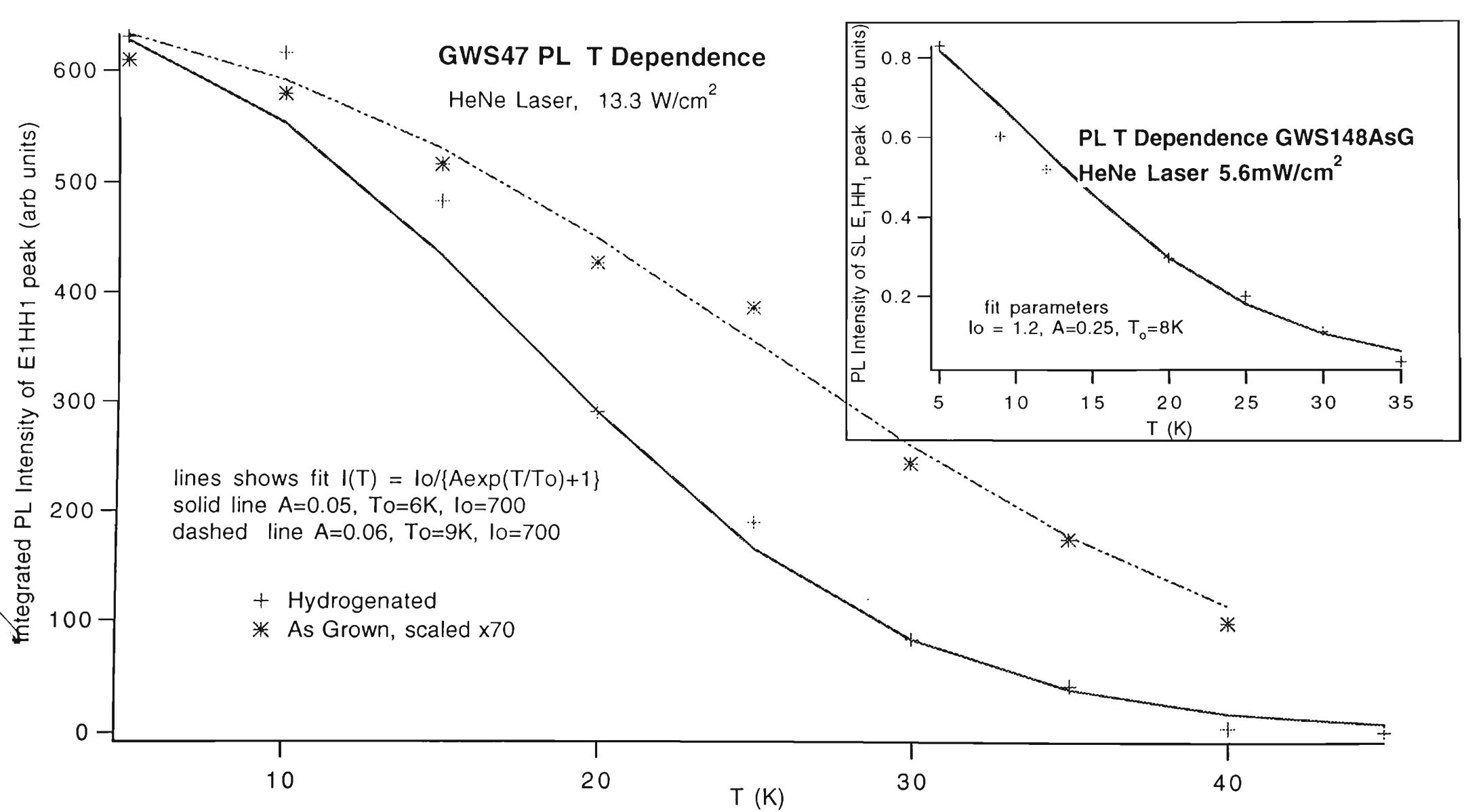

Figure 7.6. **Superlattice PL intensities show $\exp(T/T_o)$ temperature dependence as expected for tunneling or hopping transport of carriers to nonradiative centers [266]. GWS180AsG resembles GWS47AsG.**

recombination lifetime doubled to 400 ps in their very short period (3/1 ml) superlattice after hydrogenation. They found no significant effect on a 15/15 ml superlattice where the recombination time was already 400 ps. They explained their results through Kronig-Penney calculations that estimated the probability of finding electrons in the AlAs and at the interfaces, and found a correlation with low quantum efficiency when this probability was high. They concluded that hydrogenation achieves its effects by passivating defects in the AlAs and at the interfaces.

The present samples are quite similar to each other in period, and increases in PL efficiency are strongly correlated with confinement of carriers or excitons within the superlattice for the duration of their lifetimes. Such confinement is either due to a double heterostructure, as in GWS180, or because the poor quality of the sample means that there are many centers where carriers or excitons can be localized, as in GWS47. It is clear from work using enlarged quantum wells [284,318,319,320] and using time resolved measurements on coupled quantum wells [6] that the main recombination channel for good quality superlattices involves rapid migration of carriers and excitons out of the superlattice. Transport is reduced when disorder is introduced into a superlattice and states are localized. Where there is such rapid transport, as was established for GWS151 by Peggs et al. [317], hydrogenation would be expected to (and in this case did) have little effect on PL efficiency. Where an identical superlattice grown under identical conditions (GWS180) was confined in a double heterostructure, there was a significant increase in superlattice PL intensity after hydrogenation. This would occur because of longer exposure of carriers and excitons to any nonradiative centers associated with defects that were present. Such centers are passivated by hydrogenation.

As was discussed above, disorder relating to nonradiative recombination centers is high in GWS47 (the unconfined superlattice sample that also shows very strong increases in PL efficiency after hydrogenation). There is an increased flow of carriers out of the superlattice after hydrogenation which is manifested by increases in the buffer PL, which only appear when excitation is above the superlattice energy levels. It is worth noting that despite the increases in PL efficiency GWS47H showed PL intensities from the superlattice that were an order of magnitude less than those from the superlattices in GWS151 and GWS148, the good quality unconfined superlattice samples. The annealing results indicate that the defects involved in reducing PL efficiency in this sample behave like shallow centers, since the improvement is reversed after annealing at 400C.

In a pair of superlattices (GWS151 and GWS148) identical except for a 30K difference in growth temperature, the sample grown at the higher temperature (GWS151) was of somewhat better quality with less impurity related superlattice PL and a linear response to laser excitation. GWS151 showed no significant improvement in PL efficiency with hydrogenation, while the sister sample grown at a lower temperature did improve modestly with hydrogen. It has long been known that lower growth temperatures are correlated with increased defect concentrations both in bulk materials and at interfaces [38,74,321,322], so that the difference in growth temperatures is likely to be responsible for the difference in response.

The $\exp(T/T_o)$ PL temperature dependence results give evidence [266,267] that quenching of PL intensity as the temperature is raised occurs due to phonon assisted tunneling or hopping of localized excitons or carriers to sites where nonradiative recombination is likely to occur. An Arrhenius type or activated $\exp(-T_o/T)$ temperature dependence on the other hand is associated

with delocalization and diffusion of excitons and carriers at a standard mobility edge separating extended and localized states, as is discussed in Section 3.4.7. The same $\exp(T/T_o)$ temperature dependence observed here was also observed in 7/5 ml GaAs/AlAs superlattices by Minami et al. [208] and was attributed to phonon assisted tunneling of indirect excitons localized at the GaAs/AlAs interfaces. Minami et al. deduced T_o to be 10K, similar to the present results for GWS180AsG and GWS47AsG. As can be seen from Figure 7.7, hydrogenation reduces T_o to the neighborhood of 6K for the poor quality sample GWS47.

The overall conclusion is that hydrogen passivation of defects and impurities in superlattices is only manifested in improved PL efficiency when photo-created carriers or excitons are prevented from migrating out of the superlattice prior to recombination. Migration can be prevented either by superlattice confinement in a double heterostructure, or the localization of a large proportion of the carriers by various forms of disorder in the superlattice (including trapping by defects).

REFERENCES

[1] C. Kittel *Introduction to Solid State Physics* 6th ed. New York, Wiley, 1986.

[2] Omar, M. Ali *Elementary Solid State Physics: Principles and Applications* Reading, Mass., Addison-Wesley, 1975.

[3] J. Singh, *Physics of Semiconductors and their Heterostructures.* New York, McGraw-Hill, 1993.

[4] J.R. Chelikowsky and M.L. Cohen, *Phys. Rev.* **B14**, 556 (1976).

[5] R. Gupta in *Properties of Aluminium Gallium Arsenide,* Sadao Adachi, ed. (London, INSPEC, 1993), p. 186.

[6] F. Clérot, B. Deveaud, A. Chomette and A. Regreny, *Phys. Rev.* **B41**, 5756 (1990).

[7] G. Bastard, *Wave Mechanics Applied to Semiconductor Heterostructures* Paris, Les Éditions de Physique, [1990].

[8] M. El Allali, C.B. Soerensen, E. Veje and P. Tidemand-Petersson, *Phys. Rev.* **B48**, 4398 (1993).

[9] C. Herring, *Phys. Rev.* **57**, 119 (1940).

[10] C. Herring and A.G. Hill *Phys. Rev.* **58**, 152 (1940).

[11] J.C. Slater, *Phys. Rev.* **51**, 846 (1937).

[12] J.C. Slater *Quantum Theory of Molecules and Solids,* **2**, *Symmetry and Energy Bands in Crystals* New York, McGraw-Hill, 1965.

[13] E.O. Kane in *Semiconductors and Semimetals* , **1**, *Physics of III-V Compounds,* R.K. Willardson and A.C. Beer, eds. (New York, Academic Press, 1973) p. 75.

[14] E.O. Kane *J. Phys. Chem. Solids* **1**, 249 (1957).

[15] M. Heiblum *Phys. Rev. Lett.* **58**, 816 (1987).

[16] S. Adachi in *Properties of Aluminium Gallium Arsenide,* S. Adachi, ed. (London, INSPEC, 1993), p. 58, 66.

[17] Li, Ming-Fu *Modern Semiconductor Quantum Physics* Singapore, World Scientific, 1994.

[18] E. Grilli, M. Guzzi, R. Zamboni and L. Pavesi *Phys. Rev.* **B45**, 1638 (1992).

[19] L. Viña, S. Logothetidis and M. Cardona *Phys. Rev.* **B30**, 1979 (1984).

[20] D.D. Sell, *Phys Rev.* **B6**, 3750 (1972).

[21] D. Cherns in *Properties of Aluminium Gallium Arsenide,* S. Adachi, ed. (London, INSPEC, 1993), p. 3.

[22] M. Missous in *Properties of Aluminium Gallium Arsenide,* S. Adachi, ed. (London, INSPEC, 1993), p. 73.

[23] C. Weisbuch and B. Vinter *Quantum Semiconductor Structures.* New York, Academic Press, 1991.

[24] O. Brandt, H. Lage and K. Ploog *Phys. Rev.* **B43**, 13 285 (1991)

[25] K.W. Goossen, J.E. Cunningham and W.Y. Jan *Appl. Phys. Lett.* **57**, 2582 (1990).

[26] J. Feldmann, K.W. Goossen, D.A.B. Miller, A.M. Fox, J.E. Cunningham and W.Y. Jan *Appl. Phys. Lett.* **59**, 66 (1991).

[27] S.B. Nam, D.C. Reynolds, C.W. Litton, R.J. Almassy, T.C. Collins and C.M. Wolfe, *Phys. Rev.* **B13**, 761 (1976).

[28] L.C. Andreani and A. Pasquerello *Europhys. Lett.* **6**, 259 (1988).

[29] L.C. Andreani and A. Pasquerello *Phys. Rev.* **B42** 8928 (1990).

[30] L.C. Andreani and F. Bassani *Phys. Rev.* **B41** 7536 (1991).

[31] R.C. Miller and D.A. Kleinman *J. Lumin.* **30**, 520 (1985).

[32] R.G. Green, K.K. Baja and D.E. Phelps *Phys. Rev.* **B29**, 1807 (1984).

[33] B. Zhu and K. Huang *Phys. Rev.* **B36**. 8102 (1987).

[34] G.D. Sanders and Y.C. Chang *Phys. Rev.* **B32**, 5517 (1985).

[35] D.A. Broido and L.J. Sham *Phys. Rev.* **B34**, 3917 (1986).

[36] M.R. Brozel in *Properties of Gallium Arsenide*, 2d ed. (London, INSPEC, 1990). p. 309.

[37] C.E.C. Wood in *The Technology and Physics of Molecular Beam Epitaxy*, E.H.C. Parker, ed. (New York, Plenum Press, 1985) p. 61.

[38] N. Chand *Thin Solid Films* **231**, 143 (1993).

[39] M. Illegems in *The Technology and Physics of Molecular Beam Epitaxy*, E.H.C. Parker, ed. (New York, Plenum Press, 1985) p. 83.

[40] K. Huang and A. Rhys, *Proc. Roy. Soc.* **A204**, 406 (1950).

[41] J.M. Baranowski in *Properties of Gallium Arsenide*, 2d ed. (London, INSPEC, 1990) p. 304

[42] S. Yasuami in *Properties of Gallium Arsenide*, 2d ed. (London, INSPEC, 1990) p. 318

[43] A.R. Peaker and J. Nicholas in *Properties of Gallium Arsenide*, 2d ed. (London, INSPEC, 1990) p. 334

[44] A.R. Peaker and F. Saleemi in *Properties of Aluminium Gallium Arsenide*, S. Adachi, ed. (London, INSPEC, 1993), p. 269

[45] R.D. Schnell, S. Gisdakis and H. Ch. Alt *Appl. Phys. Lett.* **59**, 668 (1991).

[46] S.J. Pearton, M.P. Ianuzzi, C.L. Reynolds Jr. and L. Peticolas *Appl. Phys. Lett.* **52**, 395 (1988).

[47] G. Wicks, W.I. Wang, C.E.C. Wood, L.F. Eastman and L. Rathbun *J. Appl. Phys.* **52**, 5792 (1981).

[48] P.D. Augustus in *Properties of Gallium Arsenide*, 2d ed. (London, INSPEC, 1990) p. 285

[49] J.L. Weyher and L.J. Giling in *Proceedings of the International Symposium on Defect Recognition and Image Processing in III-V Compounds, Montpellier, France July 2-4, 1985* , J.P. Fillard, ed. Amsterdam, Elsevier, 1985 p. 63

[50] P.L. Gourley, T.J. Drummond and B.L. Doyle *Appl. Phys. Lett.* **49**, 1101 (1988).

[51] S.J. Pearton, C.S. Wu, M. Stavola, F. Ren, J. Lopata and W.C. Dautremont-Smith *Appl. Phys. Lett.* **51**, 496 (1987).

[52] H. Kressel and J.K. Butler in *Semiconductors and Semimetals* , **14**, *Lasers, Junctions, Transport* R.K. Willardson and A.C. Beer, eds. (New York, Academic Press. 1979) p. 66.

[53] D. Araujo, G. Oelgart, J.D. Ganiere and F.K. Reinhart *J. Appl. Phys.* **74**, 1997 (1993).

[54] P.M. Petroff, C. Weisbuch, R. Dingle, A.C. Gossard and W. Wiegmann *Appl. Phys. Lett.* **38**, 965 (1981).

[55] S. Clark, M.R. Brozel and D.J. Stirland in *Proceedings of the International Symposium on Defect Recognition and Image Processing in III-V Compounds, Montpellier, France July 2-4, 1985* , J.P. Fillard, ed. Amsterdam, Elsevier, 1985 p. 201.

[56] M. Dussac, M. Dupuy and E. Molva in *Proceedings of the International Symposium on Defect Recognition and Image Processing in III-V Compounds, Montpellier, France July 2-4, 1985* , J.P. Fillard, ed. Amsterdam, Elsevier, 1985 p. 209.

[57] M. S. Skolnick in *Proceedings of the International Symposium on Defect Recognition and Image Processing in III-V Compounds, Montpellier, France July 2-4, 1985* , J.P. Fillard, ed. Amsterdam, Elsevier, 1985 p. 165.

[58] R. Mitdank, H. Haefner, E. Schulze and G. Oelgart *Journal de Physique IV, Colloque C6* (supplement to *Journal de Physique III*) **1**, 143 (1991).

[59] R. Leonelli, D. Morris, J.L. Brebner, D. Jiaqi, A.P. Roth and C. Lacelle *Can. J. Phys.* **69**, 456 (1991).

[60] B.L. Sharma in *Semiconductors and Semimetals* , **15**, *Contacts, Junctions, Emitters* R.K. Willardson and A.C. Beer, eds. (New York, Academic Press, 1980) p. 1.

[61] E.S. Aydil and R.A. Gottscho *Materials Science Forum* **148-149**, 159 (1994).

[62] F. Pérez-Rodríguez and P. Halevi *Phys. Rev.* **B45**, 11 854 (1992).

[63] F. Pérez-Rodríguez and P. Halevi *Phys. Rev.* **B48**, 2016 (1993).

[64] R.J. Nelson and R.G. Sobers *J. Apl. Phys.* **49**, 6103 (1978).

[65] C.H. Henry and R.A. Logan *J. Apl. Phys.* **48**, 3962 (1977).

[66] J.M. Moison, K. Elcess, F. Houzay, J.Y. Marzin, J.M. Gérard, F. Barthe and M. Bensoussan *Phys. Rev.* **B41**, 12 945 (1990).

[67] F. Houzay, J.M. Moison, K. Elcess and F. Barthe *Superlattices and Microstructures* **9**, 507 (1991).

[68] R.C. Miller, W.T. Tsang and O. Munteneau *Appl. Phys. Lett.* **41**, 374 (1982).

[69] J.M. Gérard, B. Sermage, L. Bergomi and J.Y. Marzin *Superlattices and Microstructures* **8**, 417 (1990).

[70] P. Dawson and K. Woodbridge *Appl. Phys. Lett.* 45, 1227 (1984).

[71] H. Iwata, H. Yokoyama, M. Sugimoto and N. Hamao *Appl. Phys. Lett.* **54**, 2427 (1989).

[72] T. Sajoto, M. Santos, J.J. Heremans, M. Shayegan, M. Heiblum, M.V. Weckwerth and U. Meirav *Appl. Phys. Lett.* **54**, 840 (1989).

[73] P. Krispin, R. Hey and H. Kostial *J. Appl. Phys.* **77**, 5773 (1995).

[74] C.S. Hong and W.I. Wang *Inst.Phys.Conf.Ser.* **65**, 297 (1982) Int[76] International Symposium on GaAs and related compounds, Albuquerque 1982.

[75] T. Achtnich, G. Burri, M.A. Py and M. Illegems *Appl. Phys. Lett.* **50**, 1730 (1987).

[76] O. Brandt, K. Kanamoto, M. Gotoda, T. Isu and N. Tsukuda *Phys. Rev.* **51**, 7029 (1995).

[77] N. Chand and S.N.G. Chu *Appl. Phys. Lett.* **57**, 1796 (1990).

[78] M.H. Meynadier, J.A. Brum, C. Delalande, and M. Voos *J. Appl. Phys.* **58**, 4307 (1985).

[79] M.A. Herman, D. Bimberg and J. Christen *J. Appl. Phys.* **70**, R1 (1991).

[80] A. Van Wieringen and N. Warmoltz *Physica* **22**, 849 (1956).

[81] J. Chevallier, W.C. Dautremont-Smith, C.W. Tu and S.J. Pearton *Appl. Phys. Lett.* **47**, 108 (1885).

[82] N.M. Johnson, R.D. Burnham, R.A. Street and R.L. Thornton *Phys. Rev.* **B33**, 1102 (1986).

[83] J.I. Pankove and N.M. Johnson in *Semiconductors and Semimetals* , **34**, *Hydrogen in Semiconductors* J.I. Pankove and N.M. Johnson, eds. (Boston, Academic Press, 1991) p. 1.

[84] C.R. Abernathy *Materials Science Forum* **148-149**, 3 (1994).

[85] R. Murray in *Properties of Gallium Arsenide*, 2d ed. (London, INSPEC, 1990) p. 298.

[86] C.H. Seager in *Semiconductors and Semimetals* , **34**, *Hydrogen in Semiconductors* J.I. Pankove and N.M. Johnson, eds. (Boston, Academic Press, 1991) p. 17.

[87] M. Capizzi, C. Coluzza, P. Frankl, A. Frova, M. Colocci, M. Gurioli, A. Vinattieri and R.N. Sacks *Physica* **B70**, 561 (1991).

[88] G.S. Jackson, J. Beberman, M.S. Feng, K.C. Hsieh, N. Holonyak, Jr. and J. Verdeyen *J. Appl. Phys.* **64**, 5175 (1988).

[89] K.C. Hsieh, M.S. Feng, G.E. Stillman, N. Holonyak, Jr., C.R. Ito and M. Feng *Appl. Phys. Lett.* **54**, 341 (1989).

[90] K. Saarinen, P. Hautojärvi, J. Keinonen, E. Rauhala and J. Räisänen *Phys. Rev.* **B43**, 4249 (1991).

[91] R. Rahbi, B. Pajot, J. Chevallier, A. Marbeuf, R.C. Logan and M. Gavand *J. Appl. Phys*, **73**, 1723 (1993).

[92] C. Shwe and M. Gal *Appl. Phys. Lett.* **62**, 516 (1993).

[93] F. Ren *Materials Science Forum* **148-149**, 141 (1994).

[94] L. Pavesi in *Properties of Aluminium Gallium Arsenide*, S. Adachi, ed. (London, INSPEC, 1993), p. 303.

[95] J. Chevallier *Materials Science Forum* **148-149**, 219 (1994).

[96] S.J. Pearton, W.C. Dautremont-Smith, J. Lopata, C.W. Tu and C.R. Abernathy *Phys. Rev.* **B36**, 4260 (1987).

[97] A.J. Tavendale, S.J. Pearton, A.A. Williams and D. Alexiev *Appl. Phys. Lett.* **56**, 1457 (1990).

[98] M.H. Yuan, L.P. Wang, S.X. Jin, J.J. Chen and G.G. Qin *Appl. Phys. Lett.* **58**, 925 (1991).

[99] A.W.R. Leitch, Th. Prescha and J. Weber *Phys. Rev.* **B44**, 1375 (1991).

[100] B. Clerjaud, F. Gendron, M. Krause and W. Ulrici *Mod. Phys. Lett.* (Singapore) **B5**, 877 (1991).

[101] L. Pavesi and P. Giannozzi *Phys. Rev.* **B43**, 2446 (1991).

[102] L. Pavesi and P. Giannozzi *Phys. Rev.* **B46**, 4621 (1992).

[103] L. Pavesi, P. Giannozzi and F.K. Reinhart *Phys. Rev.* **B42**, 1864 (1990).

[104] Y.-C. Pao, D. Liu, W.S. Lee and J.S. Harris *Appl. Phys. Lett.* **48**, 1291 (1986).

[105] B.H. Yang, H.P. Gislason and M. Linnarsson *Phys. Rev.* **B48**, 12 345 (1993).

[106] D. Yang, J.W. Garland, P.M. Raccah, C. Coluzza, P. Frankl, M. Capizzi, F. Chambers and C. Devane *Physica* **B170**, 557 (1991).

[107] S.J. Pearton *Materials Science Forum* **148-149**, 393 (1994).

[108] J. Lagowski, M. Kaminska, J.M. Parsey, Jr., H.C. Gatos and M. Lichtensteiger *Appl. Phys. Lett.* **41**, 1078 (1982).

[109] E.M. Omel'yanovskii, A.V. Pakhomov and A.Ya. Polyakov *Sov. Phys. Semicond.* **21**, 514 (1987).

[110] E.M. Omel'yanovskii, A.V. Pakhomov, A.Ya. Polyakov and L.V. Kulikova *Sov. Phys. Semicond.* **21**, 1068 (1987).

[111] A.B. Conibear, A.W.R. Leitch and C.A.B. Ball *Phys. Rev.* **B49**. 5069 (1994).

[112] H.Y. Cho, E.K. Kim, S. Min, J.B. Kim and J. Jang *Appl. Phys. Lett.* **53**, 856 (1988).

[113] W.C. Dautremont-Smith, J.C. Nabity, V. Swaminathan, M. Stavola, J. Chevallier, C.W. Tu and S.J. Pearton *App. Phys Lett* **49**, 1098 (1986).

[114] S.J. Pearton, W.C. Dautremont-Smith, C.W. Tu, J.C. Nabity, V. Swaminathan, M. Stavola and J. Chevallier *Inst. Phys. Conf. Ser.* **83**, 289 (1987) Paper presented at International Symposium on GaAs and Related Compounds, Las Vegas, Nevada 1986.

[115] S.J. Pearton and A.J. Tavendale *Electronics Lett.* **18**, 715 (1982).

[116] J.C. Nabity, M. Stavola, J. Lopata, W.C. Dautremont-Smith, C.W. Tu and S.J. Pearton *Appl. Phys. Lett.* **50**, 921 (1987).

[117] S.J. Pearton, W.C. Dautremont-Smith, J. Chevallier, C.W. Tu and K.D. Cummings *J. Appl. Phys.* **59**, 2821 (1986).

[118] N. Pan, S.S. Bose, M.H. Kim, J.S. Hughes, G.E. Stillman, K. Arai and Y. Nashimoto *Appl. Phys. Lett.* **51**, 596 (1987).

[119] N. Pan, S.S. Bose, M.H. Kim, J.S. Hughes, G.E. Stillman, K. Arai and Y. Nashimoto *Appl. Phys. Lett.* **50**, 1832 (1987).

[120] A. Jalil, J. Chevallier, R. Azoulay and A. Mircea *J. Appl. Phys.* **59**, 3774 (1986).

[121] M.J. Ashwin, B.R. Davidson, L. Woodhouse, R.C. Newman, T.J. Bullough, T.B. Joyce, R. Nicklin and R.R. Bradley *Semicond. Sci. Technol.* **8**, 625 (1993).

[122] B.R. Davidson, R.C. Newman, T.J. Bullough and T.B. Joyce *Phys. Rev.* **B48**, 17 106 (1994).

[123] B.R. Davidson, R.C. Newman, R.E. Pritchard, T.J. Bullough, T.B. Joyce, R. Jones and S. Öberg *Mat. Res. Soc. Symp. Proc.* **325**, 241 (1994) Presented at Symposium on Physics and Applications of Defects in Advanced Semiconductors, Boston 1993.

[124] R.C. Newman in *Proceedings of the 22nd International Conference on the Physics of Semiconductors , Vancouver, 1994* **1**, D. J. Lockwood, ed. (Singapore, World Scientific, 1995) p. 19.

[125] J. Chevallier, A. Jalil, J.C. Pesant, R. Mostafaoui, B. Pajot, P. Murawala and R. Azoulay *Revue Phys. Appl.* **22**, 851 (1987).

[126] B. Pajot, A. Jalil, J. Chevallier and R. Azoulay *Semicond. Sci. Technol.* **2**, 305 (1987).

[127] B. Pajot, R.C. Newman, R. Murray, A. Jalil, J. Chevallier and R. Azoulay *Phys. Rev.* **B37**, 4188 (1988).

[128] P.S. Nandhra, R.C. Newman, R. Murray, B. Pajot, J. Chevallier, R.B. Beall and J.J. Harris *Semicond. Sci. Technol.* **3**, 356 (1988).

[129] L. Pavesi, F. Martelli, D. Martin and F.K. Reinhart *Appl. Phys. Lett.* **54**, 1522 (1989).

[130] J. Chevallier, B. Pajot, A. Jalil, R. Mostefaoui, R. Rahbi and M.C. Boissy *Mat. Res. Soc. Symp. Proc.* **104**, 337 (1988).

[131] I. Szafranek, S.S. Bose and G.E. Stillman *Appl. Phys. Lett.* **55**, 1205 (1989).

[132] S.K. Mehta, T. Srinavasan, G.C. Dubey and R.K. Jain *J. Appl. Phys.* **77**, 6058 (1995).

[133] E. Yoon, R.A. Gottscho, V.M. Donnelly and H.S. Luftman *Appl. Phys. Lett.* **60**, 2681 (1992).

[134] M. Aucouturier *Physica* **B170**, 469 (1991).

[135] M. Gal, A. Tavendale, M.J. Johnson and B.F. Usher *J. Appl. Phys.* **66**, 968 (1989).

[136] S.J. Pearton and A.J. Tavendale *J. Appl. Phys.* **54**, 1154 (1983).

[137] A.Y. Polyakov, A.V. Pakhomov, M.V. Tishkin, O.M. Borodina, A.V. Govorkov and B.M. Leiferov *Solid State Comm.* **76**, 761 (1990).

[138] Yu. A. Bumai, B.S. Yavich, M.A. Sinitsyn et al. *Semiconductors* **28**, 166 (1994).

[139] R. Fischer, G. Peter, E.O. Göbel, M. Capizzi, A. Frova, A. Fischer and K. Ploog *Appl. Phys. Lett.* **60**, 2788 (1992).

[140] J.R. Botha and W.T. Leitch *Appl. Phys. Lett.* **63**, 2534 (1993).

[141] J. Chevallier, B. Clerjaud and B. Pajot in in *Semiconductors and Semimetals*, **34**, *Hydrogen in Semiconductors* J.I. Pankove and N.M. Johnson, eds. (Boston, Academic Press, 1991) p. 447.

[142] M. Stavola *Materials Science Forum* **148-149**, 251 (1994).

[143] P.R. Briddon and R. Jones *Inst. Phys. Conf. Ser.* **95**, 459 (1989).

[144] J. Chevallier, A. Jalil, R. Mostafoui, R. Rahbi and M.C. Boissy *Mat. Res. Soc. Symp. Proc.* **104**, 337 (1988).

[145] D.S. Citrin *Phys. Rev.* **B50**, 5497 (1994).

[146] L.C. Andreani *Phys. Lett.* **A192**, 99 (1994).

[147] L.C. Andreani *Phys. Stat. Sol.* **B188**, 29 (1995).

[148] Y. Chen, R. Cingolani, L.C. Andreani, F. Bassani and J. Massies *Nuovo Cimento* **10D**, 847 (1988).

[149] F. Tassone, F. Bassani and L.C. Andreani *Phys. Rev.* **B45**, 6023 (1992).

[150] R.D. Guenther *Modern Optics* New York, Wiley, 1990.

[151] D.S. Citrin *Phys. Rev.* **B47**, 3832 (1993).

[152] L.C. Andreani, V. Savona, P. Schwendimann and A. Quattropani *Superlattices and Microstructures* **15**, 453 (1994).

[153] G. Burns *Solid State Physics* Boston, Academic, 1990.

[154] R. Winkler *Phys. Rev.* **B51**, 14 395 (1995).

[155] B. Gil, Y. El Khalifi, H. Mathieu, C. de Paris, J. Massies, G. Neu, T. Fukunaga and H. Nakashima *Phys. Rev.* **B41**, 2885 (1990).

[156] B.P. Zhang, S.S. Kano, Y. Shiraki and R. Ito *Phys. Rev.* **B50**, 7499 (1994).

[157] M. Born and E. Wolf *Principles of Optics: Electromagnetic Theory of Propagation, Interference and Diffraction of Light* London, Pergamon, 1959.

[158] P.E. Simmonds, M.J. Birkett, M.S. Skolnick, W.I.E. Tagg, P. Sobkowicz, G.W. Smith and D.M. Whittaker *Phys. Rev.* **B50**, 11 251 (1994).

[159] J. Humlíček, L. Bočánek, K. Navrátil, P. Pánek and R. Svehla *Solid State Comm.* **93**, 725 (1995).

[160] Y. Chen *Nuovo Cimento* **11D**, 993 (1989).

[161] A.J. Shields and P.C. Klipstein *Phys. Rev.* **B43**, 9118 (1991).

[162] F. Evangelisti, J.U. Fischbach and A. Frova Phys. Rev. **B9**, 1516 (1974).

[163] X.L. Zheng, D. Heiman, B. Lax and F.A. Chambers *Appl. Phys. Lett.* **52**, 287 (1988).

[164] J.J. Hopfield and D.G.Thomas *Phys. Rev.* **132**, 563 (1963).

[165] F. Bassani, Y. Chen, G. Czajkowski and A. Tredicucci *Phys. Stat. Sol.* **B180**, 115 (1993).

[166] J.U. Fischbach, W. Ruehle, D. Bimberg and E. Bauser *Solid State Comm.* **18**, 1255 (1976).

[167] C. Weisbuch and R.G. Ulbrich in *Light Scattering in Solids, 3, Recent Results* M. Cardona and G. Guntherodt, eds. (Berlin. Springer-Verlag, 1982) p. 207.

[168] L.C. Andreani, F. Tassone and F. Bassani *Solid State Comm.* **77**, 641, (1991).

[169] S. Jorda, U. Rössler and D. Broido *Phys. Rev.* **B48**, 1669 (1993).

[170] D.S. Citrin *Solid State Comm.* **89**, 139 (1994).

[171] A. Tredicucci, Y. Chen, F. Bassani, J. Massies, C. Deparis and G. Neu *Phys. Rev.* **B47**, 10 348 (1993).

[172] V.A. Kosobukin *Sov. Phys. Solid State* **34**, 1662 (1992).

[173] E.L. Ivchenko, A.V. Kavokin, V.P. Kochereshko, P.S. Kop'ev and N.N. Ledentsov *Superlattices and Microstructures* **12**, 317 (1992).

[174] A.F. Terzis, X.C. Liu, A. Petrou, B.D. McCombe, M. Dutta, H. Shen, D.D. Smith, M.W. Cole, M. Taysing-Lara and P.G. Newman *J. Appl. Phys.* **67**, 2501 (1990).

[175] M. Haraguchi, Y. Nakagawa, M. Fukui and S. Muto *Jpn. J. Appl. Phys.* **30**, 1367 (1991).

[176] R. Atanosov, F. Bassani and V.M. Agranovitch *Phys. Rev.* **B49**, 2658 (1994).

[177] M. Sigrist, G. Chassaing and A. Hameury *J. Appl. Phys.* **75**, 5316 (1994).

[178] E.L. Ivchenko, V.P. Kochereshko, P.S. Kop'ev, V.A. Kosobukin, I.N. Uraltsev and D.R. Yakovlev *Solid State Comm.* **70**, 529 (1989).

[179] E.L. Ivchenko, V.P. Kochereshko, I.N. Uraltsev and D.R. Yakovlev Phys. Stat. Sol. **B161**, 217 (1990).

[180] H.B. Bebb and E.W. Williams in *Semiconductors and Semimetals* , **8**, *Transport and Optical Phennomena* R.K. Willardson and A.C. Beer, eds. (Boston, Academic Press. 1972) p. 181.

[181] Y. Masumoto, M. Matsuura, S. Tarucha and H. Okamoto *Phys. Rev.* **B32**, 4275 (1985).

[182] W.T. Masselink, P.J. Pearah, J. Klem, C.K. Peng, H. Morkoç, G.D. Sanders and Y.-C. Chang *Phys. Rev.* **B32**, 8027 (1985).

[183] V. Srinivas, J. Hryniewicz, Y.J. Chen and C.E.C Wood *Phys. Rev.* **B46**, 10 193 (1992).

[184] O. Heller, J. Tignon, J. Martinez-Pastor, Ph. Roussignol, G. Bastard, M. Maaref, V. Thierry-Mieg and R. Planel *Nuovo Cimento* **17D**, 1493 (1995).

[185] A.V. Kavokin *Phys. Rev.* **B50**, 8000 (1994).

[186] P.E. Simmonds personal communication.

[187] R. Grousson, V. Voliotis, P. Lavallard, M.L. Roblin and R. Planel *Semicond. Sci. Technol.* **8**, 1217 (1993).

[188] R.C. Iotti and L.C. Andreani *Nuovo Cimento* **17D**, 1505 (1995).

[189] D.S. Citrin *Solid State Comm.* **97**, 1009 (1996).

[190] A.J. Shields, M. Cardona, R. Noetzel and K. Ploog *Phys. Rev.* **B46**, 10 490 (1992).

[191] D. Birkedal, V.G. Lyssenko, K.-H. Pantke, J. Erland and J.M. Hvam *Phys. Rev.* **B51**, 7977 (1995).

[192] T. Ruf, J. Spitzer, V.F. Sapega, V.I. Belitsky, M. Cardona and K. Ploog *Phys. Rev.* **B50**, 1792 (1994).

[193] J. Humlíček, E. Schmidt, L. Bočanek, R. Svehla and K. Ploog *Phys. Rev.* **B48**, 5241 (1993).

[194] T. Takagahara *Phys. Rev.* **B31**, 6552 (1985).

[195] I. Aksenov, J. Kusano, Y. Aoyagi, T. Sugano, T. Yasuda and Y. Segawa *Phys. Rev.* **B51**, 4278 (1995).

[196] P.S. Kop'ev, V.D. Kulakovsii, B. Ya. Mel'tser and B.N. Shepel' *Sov. Phys. Semicond.* **20**, 748 (1986).

[197] I. Brener, M. Olszakier, E. Cohen, E. Ehrenfreund, A. Ron and L. Pfeiffer *Phys. Rev.* **B46**, 7927 (1992).

[198] A. Frommer, E. Cohen, A. Ron, A. Kash and L.N. Pfeiffer *Phys. Rev.* **B49**, 2935 (1994).

[199] H. Jeong, I.-J. Lee, J.-C. Seo, M. Lee and D. Kim *Solid State Comm.* **85**, 111 (1993).

[200] D.S. Citrin *Solid State Comm.* **84**, 281 (1992).

[201] D.S. Citrin *Phys. Rev.* **B47**, 3832 (1993).

[202] H. Stolz, D. Schwarze, W. von der Osten and G. Weimann in *Proceedings of the Eighteenth International Conference on the Physics of Semiconductors, Stockholm, 1986.* O. Engstrom, ed. (World-Scientific, Singapore, 1987) p. 691

[203] R. Klann, H.T. Grahn and K. Fujiwara *Phys. Rev.* **B51**, 10 232 (1995).

[204] B.M. Ashkinadze, E. Linder, E. Cohen, A. Ron and L.N. Pfeiffer *Phys. Rev.* **B51**, 1938 (1995).

[205] A.J. Shields, G.O. Smith, E.J. Mayer, R. Eccleston, J. Kuhl, M. Cardona and K. Ploog *Phys. Rev.* **B48**, 17 338 (1993).

[206] J. Hegarty, L. Goldner and M.D. Sturge *Phys. Rev.* **B30**, 7346 (1984).

[207] J. Hegarty, M.D. Sturge, C. Weisbuch et al. *Phys. Rev. Lett.* **49**, 930 (1982).

[208] F. Minami, K, Hirate, K. Era, Y. Yao and Y. Masumoto *Phys. Rev.* **B36**, 2875 (1987).

[209] G. Bastard, C. Delalande, M.H. Meynadier, P.M. Frijlink and M. Voos *Phys. Rev.* **B29**, 7042 (1984).

[210] C. Delalande, M.H. Meynadier and M. Voos *Phys. Rev.* **B31**, 2497 (1985).

[211] E.-X. Ping and V. Dalal *J. Appl. Phys.* **74**, 5349 (1993).

[212] M. Gurioli, J. Martinez-Pastor, A. Vinattieri and M. Colocci *Solid State Comm.* **91**, 931 (1994).

[213] V. Srinivas, Y.J. Chen and C.E.C. Wood *Phys. Rev.* **B47**, 10 907 (1993).

[214] V. Srinivas, Y.J. Chen and C.E.C. Wood Phys. Rev. **B48**, 12 300 (1993).

[215] T. Takagahara *J. Lumin.* **44**, 347 (1989).

[216] J. Lee, E.S. Koteles and M.O. Vassell *Phys. Rev.* **B33**, 5512 (1986).

[217] J.V.D. Veliadis, J.B. Khurgin, Y.J. Ding, A.G. Cui and D.S. Katzer *Phys. Rev.* **B50**, 4463 (1994).

[218] D. Oberhauser, K.-H. Pantke, J.M. Hvam, G. Weimann and C. Klingshirn *Phys. Rev.* **B47**, 6827 (1993).

[219] B. Deveaud, F. Clérot, N. Roy, K. Satzke, B. Sermage and D.S. Katzer *Phys. Rev. Lett.* **67**, 2355 (1991).

[220] M. Gurioli, A. Vinattieri, M. Colocci, C. Deparis, J. Massies, G. Neu, A. Bosacchi and S. Franchi *Phys. Rev.* **B44**, 3115 (1991).

[221] L. Schultheis, J. Kuhl, A. Honold and C.W. Tu in *Proceedings of the 18th International Conference on the Physics of Semiconductors, Stockholm, 1986* O. Engstrom, ed. (Singapore, World Scientific, 1987) p 1397.

[222] L. Schultheis, A. Honold, J. Kuhl, K. Köhler and C.W. Tu *Phys. Rev.* **B34**, 9027 (1986).

[223] T. Takagahara *Phys. Rev.* **B31**, 8171 (1985).

[224] T. Takagahara *Phys. Rev.* **B32**, 7013 (1985).

[225] T. Takagahara *J. Lumin.* **38**, 64 (1987).

[226] S. Rudin and T.L. Reinecke *Phys. Rev.* **B41**, 3017 (1990).

[227] E. Hanamura *Phys. Rev.* **B38**, 1228 (1998).

[228] R. Eccleston, B.F. Feuerbacher, J. Kuhl, W.W. Rühle and K. Ploog *Phys. Rev.* **B45**, 11 403 (1992).

[229] B. Sermage, B. Deveaud, K. Satzke, F. Clérot, C. Dumas, N. Roy, D.S. Katzer, F. Mollot, R. Planel, M. Berz and L. Oudar *Superlattices and Microstructures* **13**, 271 (1993).

[230] J. Martinez-Pastor, A. Vinattieri, L. Carraresi, M. Colocci, Ph. Roussignol and G. Weimann *Phys. Rev.* **B47**, 10 456 (1993).

[231] C. Weisbuch *Solid State Electronics* **21**, 179 (1978).

[232] M. Colocci, M. Gurioli, and A. Vinattieri *J. Appl. Phys.* **68**, 2809 (1990).

[233] J.V.D. Veliadis, Y.J. Ding, J.B. Khurgin and D.K. Wickenden *J. Lumin.* **63**, 55 (1995).

[234] A. Vinattieri, J. Shah, T.C. Damen, D.S. Kim, L.N. Pfeiffer, M.Z. Maialle and L.J. Sham *Phys. Rev.* **B50**, 10 868 (1994).

[235] T.C. Damen, Jagdeep Shah, D.Y. Oberli, D.S. Chemla, J.E. Cunningham and J.M. Kuo *J. Lumin.* **45**, 181 (1990).

[236] L. Pavesi in *Properties of Aluminium Gallium Arsenide*, Sadao Adachi, ed. (London, INSPEC, 1993) p. 245.

[237] M.T. Ramsbey, I. Szafranek, G. Stillman and J.P. Wolfe *Phys. Rev.* **B49**, 16 427 (1994).

[238] D.M. Eagles *J. Phys. Chem. Solids* **16**, 76 (1960).

[239] P.J. Dean in *Progress in Solid State Chemistry*, **8**, J.O. McCalid, G. Somarjaj, eds. (Oxford, Pergamon, 1973) p. 1.

[240] P.J. Dean and D.C. Herbert in *Excitons,* K. Cho, ed. (Berlin, Springer-Verlag, 1979) p. 55.

[241] B. Hamilton in *Properties of Gallium Arsenide*, 2d ed. (London, INSPEC, 1990). p. 252.

[242] H. Künzel and K. Ploog *Appl. Phys. Lett.* **37**, 416 (1980).

[243] E.V.K. Rao, F. Alexandre, J.M. Masson, M. Allovaon and L. Goldstein *J. Appl. Phys.* **57**, 503 (1985).

[244] F. Briones and D.M. Collins *J. Electronic Materials* **11**, 847 (1982).

[245] B.J. Skromme, S.S. Bose, B. Lee, T.S. Low, T.R. Lepkowski, R.Y. DeJule and G.E. Stillman *J. Appl. Phys.* **58**, 4685 (1985).

[246] D.C. Reynolds, K.K. Bajaj, C.W. Litton, G. Peters, P.W. Yu, R. Fischer, D. Huang and H. Morkoç *J. Appl. Phys.* **60**, 2511 (1986).

[247] A.C. Beye, B. Gil, G. Neu and C. Vèrié *Phys. Rev.* **B37**, 4514 (1988).

[248] M.S. Skolnick, C.W. Tu and T.D. Harris *Phys. Rev.* **B33**, 8468 (1986).

[249] S. Charbonneau and M.L.W. Thewalt *Phys. Rev.* **B41**, 8221 (1990).

[250] L. Eaves and D.P. Halliday *J. Phys.* **C17**, L705 (1984).

[251] M.S. Skolnick, D.P. Halliday and C.W. Tu *Phys. Rev.* **B38**, 4165 (1988)

[252] M.S. Skolnick, T.D. Harris, C.W. Tu, T.M. Brennan and M.D. Sturge *Appl. Phys. Lett.* **46**, 427 (1985).

[253] Y. Cheng, M. Stavola, C.R. Abernathy, S.J. Pearton and W.S. Hobson *Phys. Rev.* **B49**, 2469 (1994).

[254] Y.M. Cheng, M. Stavola, C.R. Abernathy and S.J. Pearton *Mat. Res. Soc. Symp. Proc.* **325**, 273 (1994). Paper presented at the Symposium on Physics and Applications of Defects in Advanced Semiconductors, Boston, 1993.

[255] K. Akimoto, M. Dohsen, M. Arai and N. Watanabe *Appl. Phys. Lett.* **45**, 922 (1984).

[256] Y. Makita, T. Nomura, M. Yokota, T. Matsumore, T. Izumi, Y. Takeuchi and K. Kudo *Appl. Phys. Lett.* **47**, 623 (1985).

[257] D.C. Reynolds and T.C. Collins *Excitons: Their Properties and Uses* New York. Academic, 1981.

[258] D.J. Ashen, P.J. Dean, D.T.J. Hurle, J.B. Mullin, A.M. White and P.D. Greene *J. Phys Chem. Solids* **36**, 1041 (1975).

[259] M. Leroux, G. Neu, J.P. Contour, J. Massies and C. Vèrié *J. Appl. Phys.* **59**, 2996 (1986).

[260] P.J. Dean, H. Venghaus and P.E. Simmonds *Phys. Rev.* **B18**, 6813 (1978).

[261] H. Tews, H. Venghaus and P.J. Dean *Phys. Rev.* **B19**, 5178 (1979).

[262] H. Hillmer, A. Forchel, S. Hansmann, M. Morohashi, E. Lopez, H.P. Meier and K. Ploog *Phys. Rev.* **B39**, 10 901 (1989).

[263] D.S. Jiang, H. Jung and K. Ploog *J. Appl. Phys.* **64**, 1371 (1988).

[264] D.V. Korbutyak, A.I. Bercha, L.A. Demchina, V.G. Litovchenko and A.V. Troshchenko *Sov. Phys. Solid State* **34**, 1793 (1992).

[265] J.E. Zucker, A. Pinczuk, D.S. Chemla and A.C. Gossard *Phys. Rev.* **B35**, 2892 (1987).

[266] R.A. Street *Adv. Phys.* **30**, 593 (1980).

[267] R.W. Collins, M.A. Paesler and W. Paul *Solid State Comm.* **34**, 833 (1980).

[268] W.Y. Jan, J.E. Cunningham, K.W. Goossen and W. Knox *J. Vac. Sci. Technol.* **B10**, 972 (1992).

[269] J.D. Grange and D.K. Wickenden in *The Technology and Physics of Molecular Beam Epitaxcy* E.H.C. Parker, ed. New York, Plenum Press, 1985 p. 629.

[270] G.J. Davies and D. Williams in *The Technology and Physics of Molecular Beam Epitaxcy* E.H.C. Parker, ed. New York, Plenum Press, 1985 p. 15.

[271] G.W. Smith, personal communication.

[272] SPEX Industries, Inc. Manual to SPEX 1704 Spectrometer.

[273] Model 3900 CW Ti:Sapphire Laser Instruction Manual, Spectraphysics.

[274] Tutorial in 1988 Newport Catalog.

[275] Designed and built by Dale Hughes of the University of Wollongong Physics Department.

[276] W.I. Tagg, *PhD Thesis - Optical and Electrical Studies of Low Dimensional Structures*, University of Sheffield, 1993.

[277] P.J. Pearah, J. Klem, T. Henderson, C.K. Peng, H. Morkoç, D.C. Reynolds and C.W. Litton *J. Appl. Phys.* **59**, 3847 (1987).

[278] A.B. Novikov, H. Röppischer, N. Stein and B.V. Novikov *J. Appl. Phys.* **78**, 4011 (1995).

[279] D.D. Sell, S.E. Stokowski, R. Dingle and J.V. DiLorenzo *Phys. Rev.* **B7**, 4568 (1973).

[280] S. Park and O'D. Kwon *J. Appl. Phys.* **79**, 3267 (1996).

[281] S. Schmitt-Rink, D.S. Chemla, D.A.B. Miller, *Adv. Physics* **38**, 89 (1989).

[282] Y. Chen, G.P. Kothiyal, J. Singh and P.K. Bhattacharya, *Superlattices and Microstructures* **3**, 657(1987).

[283] A.M. Fox, D.A.B. Miller, J.E. Cunningham, W.Y. Jan, C.Y.P. Chao and S.L. Chuang *Phys. Rev.* **B46**, 15 365 (1992).

[284] B. Deveaud, J. Shah, T.C. Damen, B. Lambert, A. Chomette and A. Regreny *IEEE J. Quantum Electronics* **24**, 1641 (1988).

[285] P.M. Young, H. Ehrenreich, P.M. Hui and N.F. Johnson *J. Appl. Phys.* **74**, 7369 (1993).

[286] M. Krahl, J. Christen, D. Bimberg, G. Weimann and W. Schlapp *Appl. Phys. Lett.* **52**, 798 (1988).

[287] T.A. Fisher, University of Wollongong Physics Department, unpublished reports.

[288] C-V measurements were carried out by P.E. Simmonds, University of Wollongong Physics Department.

[289] E.S. Koteles, J. Lee, J.P. Salerno and M.O. Vassell *Phys. Rev. Lett.* **55**, 867 (1985).

[290] S.S. Bose, B. Lee, M.H. Kim, and G.E. Stillman *Appl. Phys. Lett.* **51**, 937 (1987).

[291] M.R. Lorenz, T.N. Morgan and G.D. Pettit in *Proceedings of the International Conference on the Physics of Semiconductors,* S.M. Ryvkin, ed. (Leningrad, Nauka, 1968) p. 495.

[292] W. Schairer and M. Schmidt *Phys. Rev.* **B10**, p. 2501 (1974).

[293] Y.I. Nissim and J.F. Gibbons in *Semiconductors and Semimetals* , **17**, *CW Beam Processing of Silicon and other Semiconductors,* J.F. Gibbons, ed., (New York, Academic Press, 1973) p. 397.

[294] D. Bimberg, M. Sondergeld and E. Grobe *Phys. Rev.* **B4**, 3451 (1971).

[295] Magnetophotoluminescence measurements were carried out for the author by P.E. Simmonds at the University of Sheffield where the necessary facilities were available.

[296] T.W. Steiner, Y. Zhang, M.L.W. Thewalt, M. Maciaszek and R.P. Bult *Appl. Phys. Lett.* **56**, 647 (1990).

[297] R.A. Lewis, P.E. Simmonds, T.M. Silver, T.S. Cheng, M. Henini and J.M. Chamberlain in *Proceedings of a Conference on Shallow-Level Centers in Semiconductors, Amsterdam, 1996,* C.A.J. Ammerlaan and B. Pajot, eds. (Singapore, World Scientific, 1997) p. 257.

[298] T. Schmidt, K. Lischka and W. Zulehner *Phys. Rev.* **B45**, 8989 (1992).

[299] M.S. Skolnick in *Proceedings of the Eighteenth International Conference on the Physics of Semiconductors, Stockholm, 1986* , O. Engstrom, ed. (World-Scientific, Singapore, 1987) p. 1389.

[300] A. Bosacchi, S. Franchi, L. Vanzetti, P. Allegri, E. Grilli, M. Guzzi, R. Zamboni and L. Pavesi *Physica* **B170**, 540 (1991).

[301] J.C.M. Henning and J.P.M. Ansems *Semicond. Sci. Technol.* **2**, 1 (1987).

[302] T.F. Kuech, E. Veuhoff, D.J. Wolford and J.A. Bradley *Inst. Phys. Conf. Ser.* **74**, p. 181 Paper presented at the International Symposium on GaAs and Related Compounds, Biarritz, 1984.

[303] M. Fockele, B.K. Meyer, J.M. Spaeth, M. Heuken and K. Heime *Phys. Rev.* **B40**, 2001 (1989).

[304] E. Calleja, C. Fontaine, E. Muñoz, A. Muñoz-Yagüe, M. Fockele and J.M. Spaeth *Semicond. Sci. Technol.* **8**, 1006 (1991).

[305] L. Pavesi, D. Martin and F.K. Reinhart *Appl. Phys. Lett.* **55**, 475 (1989).

[306] G. Oelgart, G. Grumml, G. Lippold, R. Pickenhain, R. Schwabe and L. Lehmann *Semicond. Sci. Technol.* **5**, 894 (1990).

[307] P. Bhattacharya *Semicond. Sci. Technol.* **3**, 1145 (1988).

[308] L. Dobaczewski, A.R. Peaker and J.M. Langer in *Properties of Aluminium Gallium Arsenide,* Sadao Adachi, ed. (London, INSPEC, 1993), p. 278.

[309] J.M. Dallesasse, N. El-Zein, N. Holonyak, Jr., K.C. Hsieh, R.D. Burnham and R.D. Dupuis *J. Appl. Phys.* **68**, 2235 (1990).

[310] private communication P. Kemeny, 1990.

[311] A. Pinczuk, J. Shah, R.C. Miller, A.C. Gossard and W. Wiegmann *Solid State Comm.* **50**, 735 (1984).

[312] M.K. Saker, M.S. Skolnick, P.A. Claxton, J.S. Roberts and M.J. Kane *Semicond. Sci. Technol.* **3**, 691 (1988).

[313] A. Chomette, B. Deveaud, F. Clérot, B. Lambert and A. Regreny *J. Lumin.* **44**, 265 (1989).

[314] L.J. Sham and Y.-T. Lu *J. Lumin.* **44**, 207 (1989).

[315] I.L. Spain, M.S. Skolnick, G.W. Smith, M.K. Saker and C.R. Whitehouse *Phys. Rev.* **B43**, 14 093 (1991).

[316] K.J. Moore, G. Duggan, P. Dawson and C.T. Foxon *Phys. Rev.* **B38**, 5535 (1988).

[317] D.W. Peggs, P.E. Simmonds, M.S. Skolnick, G.W. Smith, D.M. Whittaker, A.N. Forshaw, D.J. Mowbray and T.A. Fisher *Superlattices and Microstructures,* **15**, 317 (1994).

[318] A. Nakamura, K. Fujiwara, Y. Tokuda, T. Nakayama and M. Hirai *J. Lumin.* **40&41**, 719 (1988).

[319] E. Tuncel, L. Pavesi. D. Martin and F.K. Reinhart *Phys. Rev.* **B38**, 1597 (1988).

[320] F. Piazza, L. Pavesi, A. Vinattieri, J. Martinez-Pastor and M. Colocci *Phys. Rev.* **B47**, 10 625 (1993).

[321] P. Blood and J.J. Harris *J. Appl. Phys.* **56**, 993 (1984).

[322] K. Akimoto, M. Kamada, K. Taira, M. Arai and N. Watanabe *J. Appl. Phys.* **59**, 2833 (1986).